ÇUKUROVA UNIVERSITY
INSTITUTE OF NATURAL AND APPLIED SCIENCES

PhD THESIS

İlyas KARASU

EFFECT OF YAW ANGLE ON VORTEX FORMATION OVER A SLENDER DELTA WING

DEPARTMENT OF MECHANICAL ENGINEERING

ADANA, 2015

ÇUKUROVA UNIVERSITY
INSTITUTE OF NATURAL AND APPLIED SCIENCES

EFFECT OF YAW ANGLE ON VORTEX FORMATION OVER A SLENDER DELTA WING

İlyas KARASU

PhD THESIS

DEPARTMENT OF MECHANICAL ENGINEERING

We certify that the thesis titled above was reviewed and approved for the award of degree of the Doctor of Philosophy by the board of jury on 11/23/2015.

…….....	…….	…….....
Prof. Dr. Beşir ŞAHİN	Prof. Dr. Hüseyin AKILLI	Prof. Dr. M. Sami AKÖZ
SUPERVISOR	MEMBER	MEMBER

…….....	…….....
Assoc. Prof. Dr. M. Metin YAVUZ	Assoc. Prof. Dr. M. Serdar GENÇ
MEMBER	MEMBER

This dissertation for the Degree of Doctor of Philosophy is written at the Department of Institute of Natural And Applied Sciences of Çukurova University.
Registration Number:

Prof. Dr. Mustafa GÖK
Director
Institute of Natural and Applied Sciences

This thesis was supported by the Çukurova University Scientific Research Unit under contract number MMF2013D9 and the Scientific and Technological Research Council of Turkey TÜBİTAK under contract number 114M497.

ÖZ

DOKTORA TEZİ

SAPMA AÇISININ YÜKSEK SÜPÜRME AÇILI BİR DELTA KANAT ÜZERİNDE GİRDAP OLUŞUMUNA ETKİSİ

İlyas KARASU

ÇUKUROVA ÜNİVERSİTESİ
FEN BİLİMLERİ ENSTİTÜSÜ
MAKİNE MÜHENDİSLİĞİ ANABİLİM DALI

Danışman : Prof. Dr. Beşir ŞAHİN
Yıl:2015, Sayfa: 181
Jüri : Prof. Dr. Beşir ŞAHİN
: Prof. Dr. Hüseyin AKILLI
: Prof. Dr. M. Sami AKÖZ
: Doç. Dr. M. Metin YAVUZ
: Doç. Dr. M. Serdar GENÇ

Bu çalışmada sapma açısının, süpürme açısı $\Lambda=70°$ olan bir delta kanat üzerindeki girdaplı akışa olan etkisi nitel ve nicel deneysel yöntemlerle incelenmiştir. Deneyler, kanat hücum açısı $25°\leq\alpha\leq35°$ aralığında ve sapma açısı $0°\leq\beta\leq20°$ aralığında gerçekleştirilmiştir.

Girdap kırılma noktaları, girdapların kanat üzerinde hareket ettiği yörüngeler ve girdapların etkileşimi boya görselleştirme deneyleri ile incelenmiştir. Stereo parçacık görüntülemeli hız ölçme yöntemi (Stereo-PIV) ile akış alanında anlık hızlar ölçülerek zaman ortalama hız vektörleri, akım çizgileri, çevrinti eşdeğer eğrileri Reynolds gerilmeleri, hız çalkantıları ve türbülans kinetik enerjisi gibi değişkenlerin türbülans istatistikleri incelenmiştir. Gaz yağı ile yüzey görselleştirme deneyinde ise akışın kanat yüzeyindeki ayrılma ve tutunma noktaları görselleştirilmiştir. Yüzey basınç deneylerinde ise kanat yüzeyindeki basınç katsayısı, C_p dağılımı incelenmiştir.

Deneysel sonuçlara göre sapma açısı, β olmadığı durumda delta kanat üzerinde simetrik bir akış yapısı oluşmakta fakat delta kanada sapma açısı, , β verilmesiyle akış yapısı önemli ölçüde değişmekte ve asimetrik bir akış yapısı oluşmaktadır. Sapma tarafındaki girdabın çökme noktası kanattan oldukça uzağa doğru hareket etmekte ve kanat üzerindeki izlediği yol hücum kenarına doğru kaymaktadır. Sapmanın tersi tarafındaki girdap çökme noktası kanat ucuna doğru hareket etmekte ve kanat üzerindeki izlediği yol kanat merkez çizgisine doğru kayarak kanat yüzeyine yayılmaktadır. Ayrıca, sapma açısının, β; hız bileşenleri, türbülans istatistikleri ve basınç katsayısı, C_p dağılımları üzerinde oldukça etkili olduğu görülmüştür.

Anahtar Kelimeler: Delta kanat, Girdap çökmesi, Sapma açısı, Stereo PIV

ABSTRACT

PhD THESIS

EFFECT OF YAW ANGLE ON VORTEX FORMATION OVER A SLENDER DELTA WING

İlyas KARASU

ÇUKUROVA UNIVERSITY
INSTITUTE OF NATURAL AND APPLIED SCIENCES
DEPARTMENT OF MECHANICAL ENGINEERING

Supervisor : Prof. Dr. Beşir ŞAHİN
Year:2015, Pages: 181
Jury : Prof. Dr. Beşir ŞAHİN
: Prof. Dr. Hüseyin AKILLI
: Prof. Dr. M. Sami AKÖZ
: Assoc. Prof. Dr. M. Metin YAVUZ
: Assoc. Prof. Dr. M. Serdar GENÇ

In this study, effects of yaw angle, β on the vortical flow over a delta wing which has a 70° sweep angle, Λ were investigated qualitatively and quantitatively by means of different experimental techniques. Experiments were performed as a function of angles of attack, in the range of $25°\leq\alpha\leq35°$ and yaw angles in the range of $0°\leq\beta\leq20°$. Leading edge vortex breakdown locations, trajectories of these vortices and their interactions were observed using dye visualizations. Time-averaged velocity vectors, pattern of streamlines, velocity components, contour of vorticity distributions, turbulence statistics such as Reynolds stress correlations, distribution of fluctuating velocities and turbulent kinetic energy were determined using instantaneous velocities measured by Stereo Particle Image Velocimetry (Stereo PIV). Separation and reattachment lines on the surface of the delta wing were also observed using surface oil visualization. Distribution of pressure coefficients C_p over the surface of the delta wing were calculated using pressure measurements.

Results revealed that in the absence of the yaw angle, β symmetrical flow structure forms over the delta wing but when delta wing is yawed symmetrical flow structure is altered considerably. Windward side vortex breakdown location moves upstream, close to the apex of delta wing. Trajectories of the vortices moved towards the central axis of the delta wing. Disordered vortices are observed to spread over the surface of the delta wing. Leeward side vortex breakdown location moves downstream of the delta wing and its trajectory slips towards the leading edge. Furthermore, variation of yaw angles, β are observed to have significant effects on the distribution of velocity components, turbulence statistics and distribution of pressure coefficients, C_p over the surface of the delta wing.

Key Words: Delta Wing, Stereo PIV, Vortex Breakdown, Yaw Angle

ACKNOWLEDGEMENTS

First of all, I would like to express my gratitude to my advisor, Prof. Dr. Beşir ŞAHİN for his guidance, support and encouragement during my studies. I sincerely thank. Prof. Dr. Hüseyin AKILLI for valuable advises during my studies. I sincerely thank Serkan ÇAĞ, Assist. Prof. Dr. Bülent YANIKTEPE, Mehmet Oğuz TAŞCI, Sedat DOĞRU, Ferdi BESNİ, Research Assistant Erhan FIRAT and Sefa MERAL for their help during my experiments. I would like to thank Assist. Prof. Dr. Çetin CANPOLAT for his support and help during dye visualization experiments.

I am grateful to Assoc. Prof. Dr. Mustafa Serdar GENÇ for great support in the wind tunnel experiments. I would like to thank Prof. Dr. Hüseyin YAPICI head of Erciyes University Energy Systems Engineering and all academic personnel for their support. I am grateful Research Assistant Halil Hakan AÇIKEL, Mustafa ÖZDEN, Sadık KIRIŞ and Mert TAŞ for their help during wind tunnel experiments. I am grateful to Dr. Muhammet ÇELİK for his invaluable contributions.

I want to thank to dean of the Gaziantep University Faculty of Aeronautics and Astronautics, Prof. Dr. İ. Halil GÜZELBEY for his supports. I am grateful to all personnel of Gaziantep University Faculty of Aeronautics and Astronautics who support me during my studies.

I want to thank Scientific and Technological Research Council of Turkey (TÜBİTAK) and Çukurova University Scientific Research Unit (BAP) for their supports.

For great patience and support during my studies I want to thank my dear wife Merve KARASU. I would like to express my gratitude my mother and all family members who have great trust and support up to now.

TABLE OF CONTENTS **PAGE**

LIST OF FIGURES **PAGE**

NOMENCLATURE

A	: Area (m^2)
AR	: Aspect ratio
BR	: Blockage ratio
c	: Chord (m)
C	: Coefficient
D	: Drag Force (N)
f	: Frequency (Hz)
F	: Force (N)
H	: Height of the tunnel test section or water level (m)
L	: Length or Lift (m or N)
max	: Maximum
min	: Minimum
x, y, z	: Streamwise, transverse and vertical coordinate directions
Re	: Reynolds number
s	: Span (m)
St	: Strouhal number
t	: Time (s)
T	: Temperature or Torque (°C or N·m)
TKE	: Turbulent kinetic energy
Tu	: Turbulence intensity
u, v, w	: Streamwise, transverse and vertical components of velocity (m/s)
U	: Freestream velocity (m/s)
V	: Vector
Acronyms	
CCD	: Charge Coupled Device
CTA	: Constant Temperature Anemometry
DAQ	: Data Acquisition
FOV	: Field Of View
Nd:YAG	: Neodymium-doped Yttrium Aluminum Garnet

PIV : Particle Image Velocimetry

RMS : Root-Mean-Square

SPIV : Stereoscopic PIV

Operators

<…> : Time-averaged

[…] : Magnitude

Greek symbols

α : Angle of attack (°)

β : Yaw angle (°)

γ : Scheimflug angle (°)

Δ : Difference in the value of a physical quantity

θ : Roll angle (°)

λ : Wavelength (m)

μ : Viscosity of fluid (kg/m/s)

ρ : Density of fluid (kg/m^3)

υ : Kinematic viscosity of fluid (m^2/s)

ϕ : Amplitude of wave (m)

ω : Vorticity (1/s)

Superscripts

′ : Fluctuating component

1. INTRODUCTION

Especially wings used in high speed aircraft have similar shape with Greek letter Δ. For this reason, these types of wings are called delta wing. Contrary to classical aircrafts, fuselage and wings can be together and these types wings are defined as flying wings. Delta wings are advantageous in both structural and aerodynamics perspectives. After World War II delta wings have gained increasing popularity, they have been being used for combat aircrafts, bombardment aircrafts and unmanned aircrafts technologies. Recent Advancements in the design of delta wings lead them to reach higher angles of attack, high maneuverability, higher stealth capability and superior aerodynamic performance at high speeds. In addition, they have a lower cross-section areas and more stiff structures.

Figure 1.1. Examples of delta wing aircrafts (Wikipedia, 2015).

Figure 1.1 shows different types of delta wing aircrafts used ; B-2 Spirit (a) is stealth bomber, F-16 XL (b) is a fighter jet, F-35 (c) is the one of the newest jet fighter, Su T-50 (d) is still-continuing to test jet, X-47A (e) and X-47B (f) unmanned jets (Wikipedia, 2015). In addition these current delta wing projects, there is hybrid project that NASA and Boeing collaboration's blended wing body which combines delta and classical aircrafts to reduce fuel consumption by means of reducing drag force caused by aircraft shape.(NASA, 2015).

Figure 1.2. Blended Wing,X-48B (NASA,2015).

Figure 1.3 shows important definitions of a typical delta wing. Sweep angle (Λ) can be defined as an angle between leading edge and trailing edge. The most important parameter of delta wing geometry is sweep angle, Λ, because delta wings are classified with this parameter. If sweep angle, Λ is equal or greater than 65°, the delta wing is called slender delta wing, otherwise it is called non-slender delta wing (Munro et al., 2005). Bevel angle can be defined as angle of leading edge according to upper surface of the delta wing. Instead of beveling, leading edge can be fillet too.

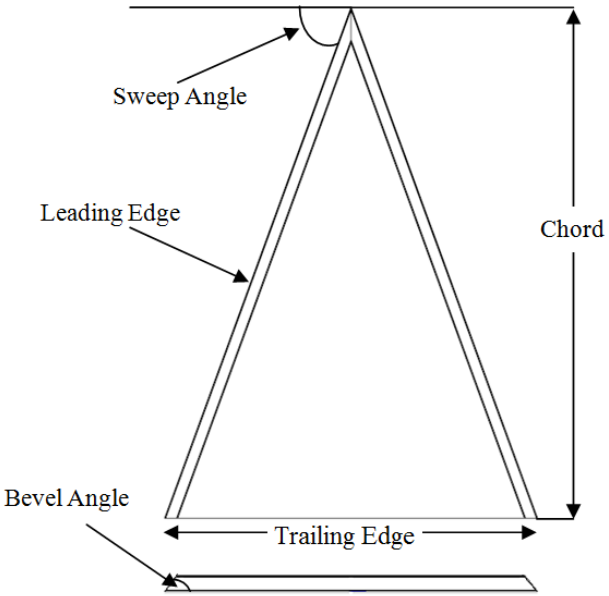

Figure 1.3. Geometry of a delta wing.

Delta wings may have different configurations such as double delta, cropped delta wing, compound delta wing, cranked delta wing, ogival delta wing, lamda delta wing, diamond delta wing as shown in figure 1.4.

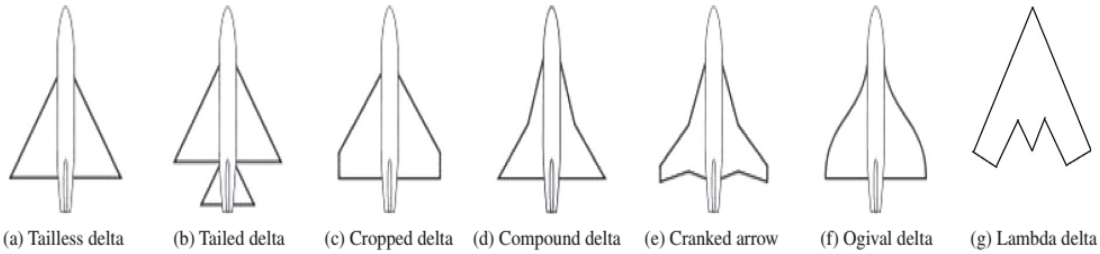

Figure 1.4. Some of the delta wing planforms (Pevit and Alam, 2014).

The flow structure of a delta wing consists of two counter-rotating leading edge vortices. Separated flow from the leading edge form a curved free shear layer rolling up into a core (Gursul et al., 2007). Earnshaw (1962) showed that leading edge vortexes of a delta wing could be divided to 3 different regions; vortex core, viscous sub-core and outside of vortex core (free shear layer). Figure 1.5 shows flow structure over a delta wing.

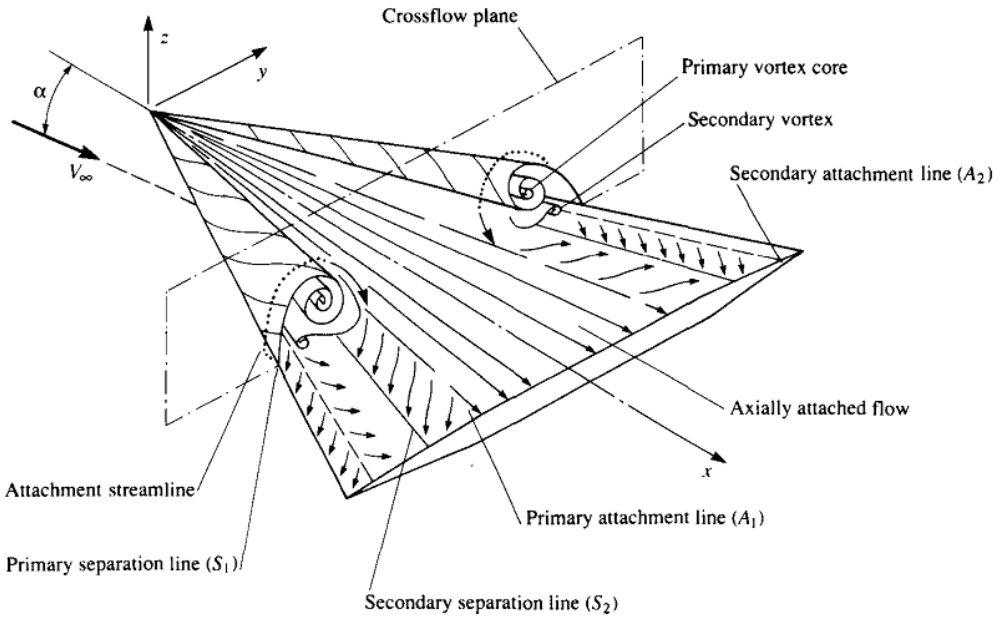

Figure 1.5. Sketch of flow over delta wings (Anderson, 1991).

The leading edge vortices induce a flow in the spanwise direction the upper surface and this outward flow separates from the surface forming a smaller secondary vortex outboard and below primary vortex (Nelson and Pelletier, 2003). Leading edge vortices in a fully developed stable stage cause extra lift and increase maximum angle of attack, α (stall angle) and this improves maneuver capabilities of aircraft (Breitsamter, 2008). As angle of attack, α of the delta wing is increased, leading edge vortices expand suddenly and this is called vortex breakdown or vortex bursting (Gursul et al., 2005). Vortex breakdown can be defined as; sudden deceleration of in axial velocity, formation of a small recirculatory flow region, a decrease in the circumferential velocity and increase in size of the vortex and bursting of the vortex (Payne and Nelson, 1986).

Vortex breakdown location depends on some parameters such as, sweep angle, Λ of the wing, angle of attack, α, sideslip (yaw) angle, β, roll angle, θ, the Reynolds number, Re, thickness of the wings, t and shape of the wing etc. (Nelson and Pelletier, 2003). The most important parameters on vortex breakdown are sweep angle, Λ of the wing and angle of attack, α and the Reynolds number, Re for non-slender wings. When angle of attack, α is increased vortex location moves upstream, when sweep angle, Λ decreases vortex breakdown location moves upstream too.

Figure 1.6 demonstrates vortex breakdown over a F-18 aircraft at angles of attack α=20° and α=42°.

Vortex breakdown causes changes in lateral and longitudinal forces, moments and stability derivates since vortex breakdown near apex leads decline in lift force, F_L (Nelson and Pelletier, 2003). Vortex breakdown is a limiting parameter of aerodynamic of the delta wing because it causes some adverse effects such as decreasing of the lift and pitching moment (Gursul et al., 2005). If the angle of attack, α increases extensively, this leads to asymmetric shedding of the vortices into the flow and this vortex shedding produces asymmetric distribution of lift force, F_L that leads to develop wing rock. Due to the roll and yaw coupled oscillations of these unbalanced forces; delta wings can encounter nose slicing and loss of control as well (Walker, 2011).

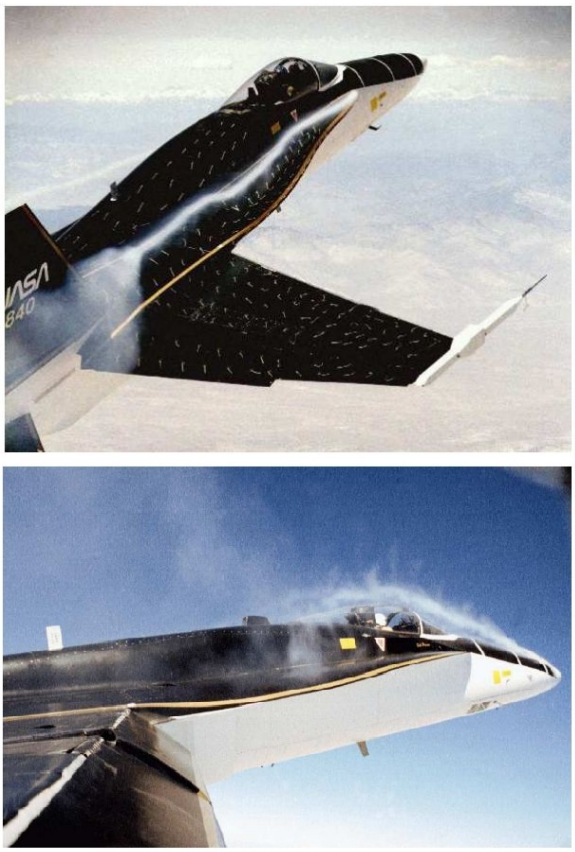

Figure 1.6. Vortex breakdown over NASA's F-18 aircraft at angle of attack α=20° and 42° (Görtz, 2005).

Vortex structure and breakdown can be visualized in a tube in which fluid can be swirled. However there are different types of vortex breakdown in the nature spiral and bubble types breakdown seen on the delta wings (Nelson and Pelletier, 2003). Figure 1.7 shows main vortex breakdown types; spiral, bubble and double helix type vortex breakdown. While one of the vortex breakdown is spiral the other one can be bubble type as seen figure 1.8. Vortex breakdown is an unsteady event so one can't talk about a stationary vortex breakdown location but it fluctuates over a mean value (Mitchel et al. 2000).

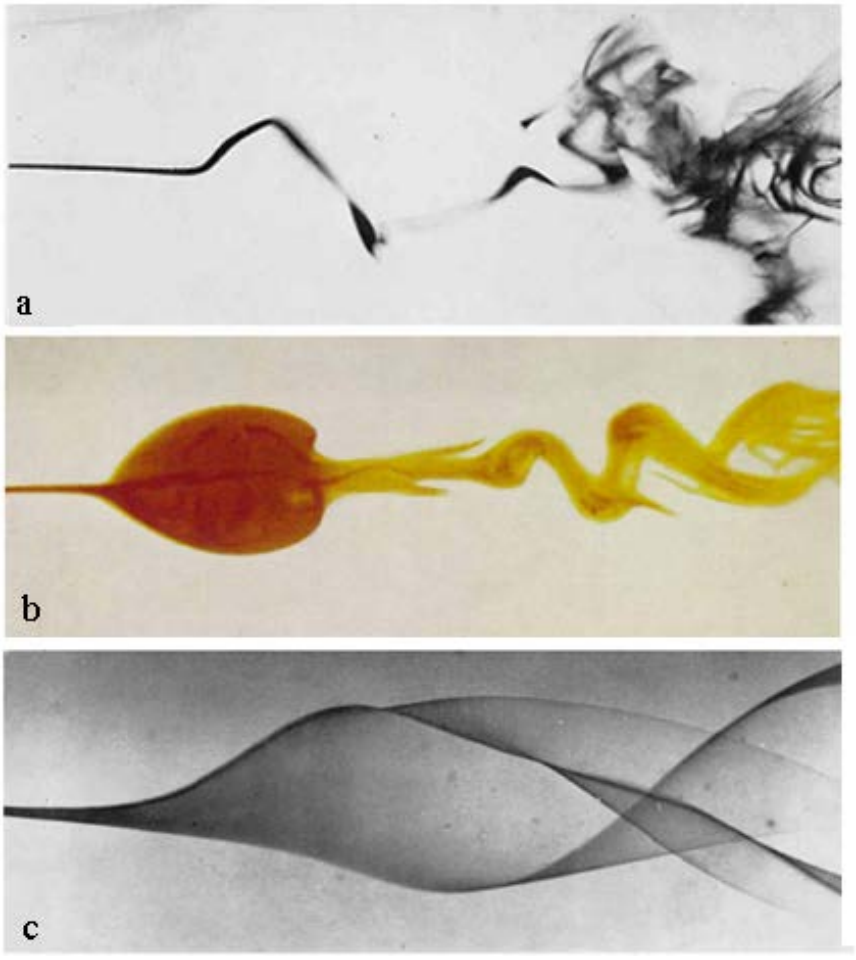

Figure 1.7. Types of common vortex breakdown: spiral (a), bubble (b) and double helix (c) breakdown types (Sarpkaya, 1971).

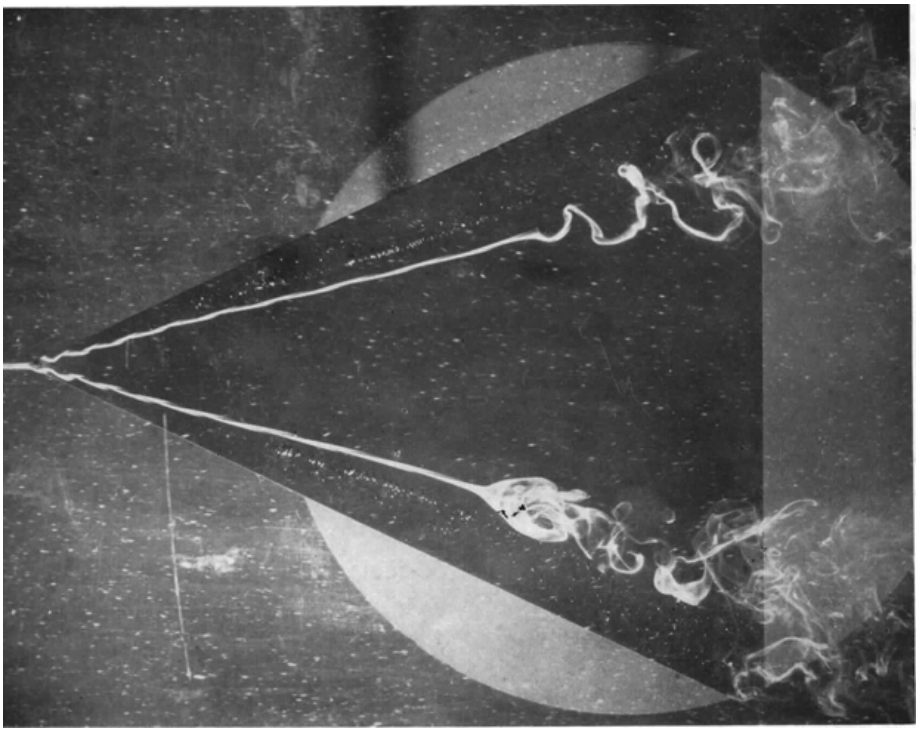

Figure 1.8. Spiral and bubble vortex breakdown over a flat plate delta wing (Lambourne and Bryer ,1961).

2. PREVIOUS STUDIES

2.1. Structure of Vortical Flow over Delta Wings

Earnshaw (1962) indicated that leading edge vortices of a delta wing could be divided into 3 different regions; vortex core, viscous sub-core and outside of vortex core (free shear-layer). Nelson and Visser (1990) performed an experimental investigation on the vorticity in breakdown phenomena. They concluded that spanwise vorticity distributions based on a single traverse through the core of the vortex was scaled with the local geometry in the pre-breakdown state and the vorticity distribution was severely altered as the vortex breakdown took place and appeared to indicate that there was vorticity distribution with maximum magnitude that may occur in the region just preceding the vortex breakdown location. Moreover maximum azimuthal vorticity also maintained more or less constant value in the leading edge vortex before upstream of vortex breakdown, but it becomes negative upon entering the breakdown zone. Gursul (1994) performed an experimental survey to investigate unsteady flow over 60°-75° delta wings at Reynolds numbers $2.5x10^3$-$1x10^5$ using surface pressure measurement, velocity measurement and smoke visualizations in wind tunnel. Some of his findings; if the vortex breakdown took place over the delta wing comprehensive pressure fluctuations were detected; instability of the wake flow of breakdown leaded these fluctuations. Another important finding is that; unsteady loading on the delta wing is as a result of the helical mode instability not vortex shedding and however effect of the vortex shedding on pressure fluctuations was negligible, in the wake comprehensible velocity oscillations were detected. Figure 2.1 shows variation of dimensionless frequency fc/U as a function of streamwise distance, x/c and angle of attack, α obtained from this survey. Honkan and Andreopoulus (1995) conducted on experimental study to investigate flow structures over delta wing having 45° sweep angle, Λ. They concluded that vorticity reached a maximum value in primary vortex where velocity was 1.3U and hence a secondary vortex was formed. Turbulent activities occurred along the shear layer over delta wing, peaks of vorticity and

velocity fluctuations took place low speed side of the shear layer close to the vortex core.

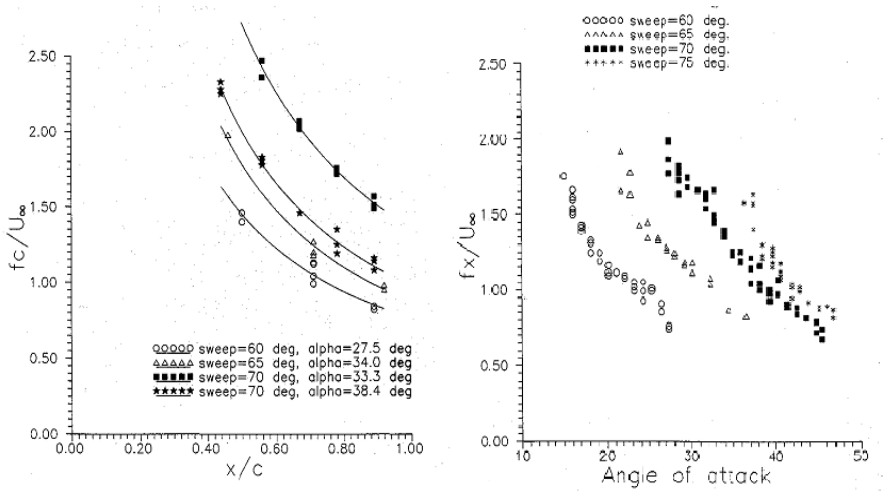

Figure 2.1. Variation of dimensionless frequency fc/U as a function of streamwise distance, x/c and angle of attack, α. (Gursul (1994).

Gad el-Hak and Blcakwelder (1985) conducted an experimental survey over 2 delta wings with 45° sweep angle, Δ having NACA0012 profile in spanwise and flat plate 60° sweep angle, Λ. In this survey, important findings can be summarized as; frequency, f_s of shedding near leading edge is independent of sweep angle, Λ and leading edge shape, at constant free-stream velocity, if the angle of attack, α was increased the shedding frequency, f_s decreased and ant constant angle of attack, α the shedding frequency, f_s was proportional to square root of the free-stream velocity. Redinioits et al. (1993) performed an experimental survey over a delta wing with 76° sweep angle, Λ at very high angles of attack ($30°\leq\alpha\leq90°$) at moderate Reynolds numbers. They demonstrated that , up to angle of attack, α of 35°, breakdown of leading edge vortices took place outside of the delta wing, when angles of attack vary with the range of $35°\leq\alpha\leq70°$ leading edge vortices shed simultaneously, however $\alpha>70°$ a second type of vortex shedding having higher frequency were detected. This vortex shedding occurred near the trailing edge of the delta wing then spread out as an angle of attack increased further more shedding frequency was depended on the angle of attack and nonlinear dependence were detected. Shih and Ding (1996) performed an experimental survey to investigate flow structures of delta wings

having 75° and 60° sweep angle at low Reynolds numbers (9,000 and 9,800) via dye visualisations and PIV experiments in towing tank. They concluded that a quasi-periodic shedding of Kelvin-Helmholtz (K-H) eddies occurred from separated shear layer and this shedding was related with interaction of the primary vortex and delta wing and eruption of secondary vortices. While delta wing/vortex interaction played important role for 60° sweep angle delta wing, for 75° delta wing this interaction was not very important on vortex development. Alsayed at al. (2007) performed an experimental survey to investigate flow structure over 76° sweep angle, Δ delta wing at Reynolds numbers $0.2x10^6$ and $0.6x10^6$ using dye visualization and the stereo PIV technique. They concluded that due to interaction of primary and secondary vortices in the free shear layer co-rotating substructures took place. Quite unsteady flow was observed on the rear section of the delta wing and this unsteadiness could be related with the Reynolds number. Gursul and Xie (2000) performed an experimental survey over the Δ=75° delta wing to investigate origin of the vortex wandering. They concluded that at low the Reynolds number, Re rms of swirl velocity in the vortex core lower as shear-layer does not exhibit Kelvin-Helmholtz instability but after a critical Reynolds number, Re shear-layer was dominated the vortical flow structures due to Kelvin-Helmholtz instability, so it can be concluded that after a critical value of Reynolds number, Re, Kelvin-Helmholtz instability has certain effects on vortex wandering. Özgeren et al. (2002) conducted an experimental study to investigate flow over slender delta wings at high angles of attack, α via PIV. They defined the existence of three different vorticity concentrations. First of them was concentrations of azimuthal vorticity because of a centrifugal instability of vortices which have comparatively lower values of wavelength and circulation. Second concentrations occurred due to vortex breakdown and had significantly higher values of circulation and wavelength and they were related with the classical helical mode instability. The last concentrations were due to an unsteady instability from the leading-edge, it had moderate circulation and relatively large values of wavelength, and they arise from reorientation of the unsteady layer of vorticity shed from the leading edge.

When vortex breakdown takes place on the wing surface, pressure difference of suction and pressure side of the delta wing decreases because extra pressure

decrease due to vortex decreases. When vortex breakdown starts to take place over de the delta wing, if the angle of attack is increased more lift goes on increasing but slope of the increase decreases. If the angle of attack was increased more vortex breakdown takes place on the apex and stall finally (Nelson and Pelletier, 2003). Figure 2.2 summarizes flow structure over a delta wing.

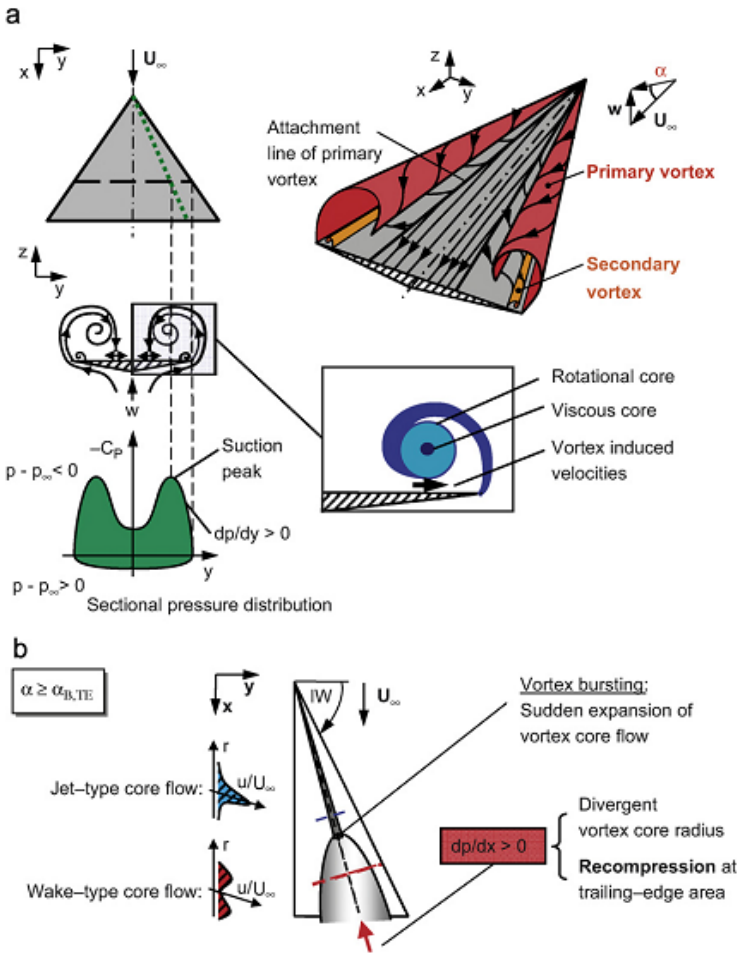

Figure 2.2. Flow over delta wing (Breitsamter, 2012)

2.2. Parameters Affecting Vortex Breakdown

Main parameter affecting vortex breakdown location over a delta wing are; sweep angle Λ, Reynolds number, Re, angle of attack, α, thickness/chord, t/c ratio of the delta wing, leading edge shape, yaw (sideslip) angle, β, roll angle, ϕ (Nelson and Pelletier, 2003). The necessary information about angles of attack, α have provided in earlier section of the text.

2.2.1. Sweep angle

Payne and Nelson (1986) conducted an experimental survey over delta wings with different sweep angles, Δ. In this survey, LDA (Laser Doppler Anemometry) and smoke flow visualization were used to determine vortex breakdown characteristics. They found that, when sweep angle, Δ was increased, the location of vortex breakdown moved aft of the delta wing, and velocity of the vortex core could reach up to 3 times of the free-stream velocity, so behaved jet-like flow and after breakdown velocity breakdown became wake-like flow. Payne et al. (1988) performed an experimental survey to investigate vortical flow over delta wings having 70°, 75°, 80° and 85° sweep angles, Δ. They stated that at constant angle breakdown point moved aft when the sweep angle, Λ increased, especially with delta wings having high sweep angle, Δ vortex breakdown location oscillated in a large distance, bubble and spiral type of breakdown and transformation of these each other were observed moreover flow behaved jet-like in pre-breakdown region but it behaved as a wake-like in post-breakdown location. Figure 2.3. shows effect of the sweep angle, Λ, on vortex breakdown location over slender delta wings.

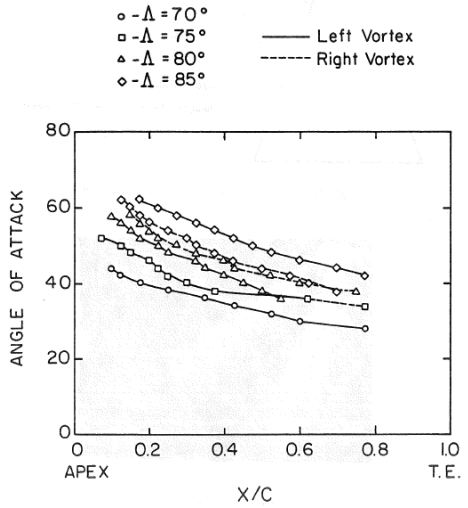

Figure 2.3. Effect of the sweep angle, Λ, on vortex breakdown location over slender delta wings (Payne and Nelson (1986).

2.2.2. Reynolds Number

Lee et al. (1989) performed an experimental study about a delta wing response of steady and unsteady flow. They showed that since separated leading edge vortices controlled by inviscid shear layer dynamics; viscosity does not play an important role in delta wing aerodynamics. They compared the coefficient of lift, C_L of this survey based on the Reynolds number, Re=2.3 x 10^4 with another experimental investigation which was performed at the Reynolds number Re=6 x 10^6 and they found that experimental results for different Reynolds numbers, Re had very close values at same angle of attacks, α. Furthermore, the locations of vortex breakdown were also compared and found that locations are not the same but difference were not significant for these two different experimental works based on two different Reynolds numbers, Re. Figure 2.4 shows steady lift coefficients, C_L variation with angle of attack at different Reynolds numbers .Erickson (1981) performed experiments in water tunnel for determining vortex core trajectory and core stability characteristics obtained on different delta wings having sweep angles, Λ ranging from 60° to 80°. Experimental results showed that flow of at high of angels of attack slender delta wing having sharp leading edge, thin and flat structure was independent of Reynolds number so water channel experiments could be used to investigate flow structure because in these circumstances potential flow were dominant.

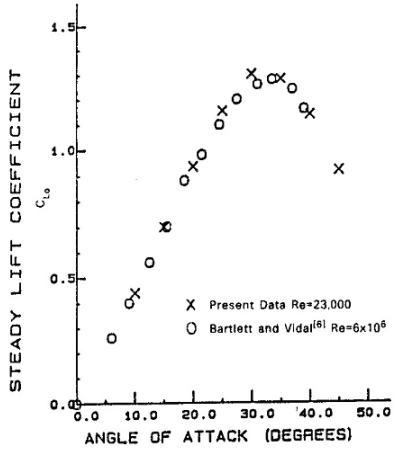

Figure 2.4. Steady lift coefficients, C_L versus angle of attack at different Reynolds numbers (Lee et al. 1987).

Coton et al. (2008) investigated the flow structure over delta wings with 65° sweep angle, Λ having sharp and rounded leading edges at Reynolds numbers, $Re=1x10^6$ and $Re=2x10^6$ via flow visualisation and force measurements. They concluded that when leading edge was rounded, flow topology and forces were dependent on the Reynolds number however at higher angles of attack, α this dependency was less, but on pitching moment and tangential force Reynolds number has important influence. Traub et al. (1998) conducted an experimental survey to investigate aerodynamics characteristics of 60° and 70° sweep angles delta wings at Reynolds numbers ranging 20.000 to 60.000. Pressure taps on the 60° sweep angle delta wing were placed along the 60% of the delta wing. Results revealed that the Reynolds number in this range did not play important role on lift coefficient C_L, but with increased Reynolds numbers maximum C_L and stall angle were increased. For 60° sweep angle delta wing, the Reynolds number had effect on vortex trajectory and pressure distributions but these variations were gradual. Figure 2.5 shows effect of the Reynolds number, Re on the pressure coefficient, C_p of the 60° sweep angle delta wing used in the investigation.

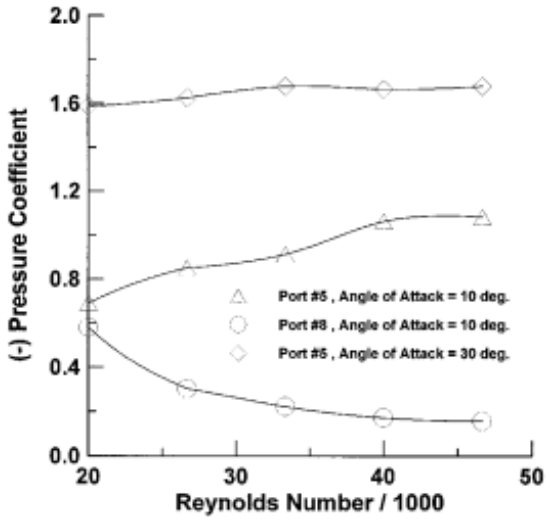

Figure 2.5. Effect of the Reynolds number on the pressure coefficient, C_p of the 60° sweep angle delta wing (Traub et al 1998).

2.2.3. Wing Shape

Kawazoe et al. (1994) conducted an experimental survey to investigate effect of thickness of delta wing on flow structures over delta wings with 45° sweep angle, Λ having 20 mm and 6 mm thickness. Their conclusion can be summarized as; for the thin and thick delta wings strongest vortex is observed at angles of attack, α of 15°, at 5°, but, angle of attack, α on the lower surface of the thick delta wing flow separated and reattached just as laminar separation bubble, stall angle was found as 25° for the thick delta wing but for the thin delta wing the stall angle was lower than 25° furthermore, due to spreading wider area leading edge vortices of thin delta wing, they collided each other at lower angles of attack, α causing early stall. Figure 2.6 shows effect of the t/c on C_L, C_D and L/D. Roosenboom et al. (2012) performed and experimental investigation over the static and pitching modified delta wing used for unmanned combat air vehicle (UCAV) using stereo PIV. Static experiments revealed patterns of the 3-D structure of the flow over the delta wing having apex vortex, thickness-caused vortex and tip vortex which are depended on angles of attack, α as shown in figure 2.7. Although low pitch amplitude had minor influence flow topology especially when passing dead regions of motions, high pitch-amplitude had strong influence on strength and size of the vortices in all phase of the pitching motion.

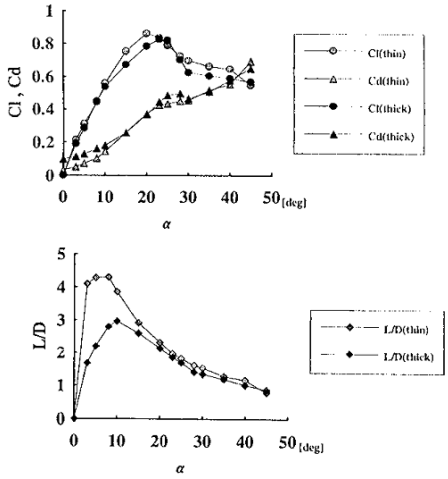

Figure 2.6. Effect of the thickness of the nonslender delta wing on C_L, C_D and L/D Kawazoe at al.(1994)

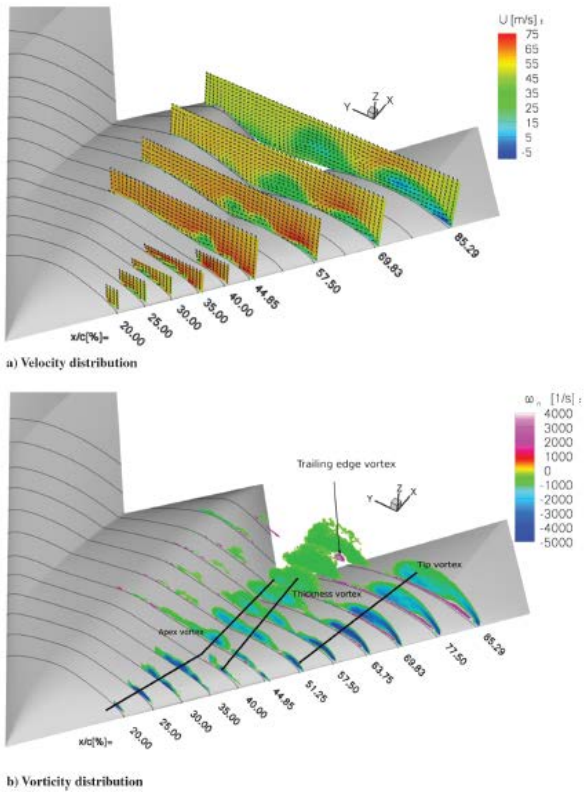

Figure 2.7. Flow structure over a UCAV model (Roosenboom et al. 2012).

Wang and Tu (2010) performed an experimental survey over cropped delta wing modified rectangular planform. They concluded that when $\Lambda=0°$ (rectangular planform) a spanwise vortex was dominant, for the cropped delta wing having the sweep angle as $\Lambda \geq 26°$ dual vortices were observed in a range of angles of attack, this dual vortices were visible at relatively low angles of attack, when $\Lambda \geq 56$ with increasing sweep angle, Λ vortices were visible in a wider range of angles of attack, α. Furthermore vortex breakdown of primary vortex took place later than the outer vortex.Verhagen (2010) performed and experimental investigation over 50° nonslender delta wing to investigate effects of leading edge shape and the Reynolds number on the aerodynamic characteristics of delta wings. He concluded that larger leading edge radius reduces the size and strength of the primary vortex and this vortex moved outboard and closer to the wing and larger leading edge radius delayed the outward secondary separation line and this caused delay of vortex breakdown. He also found that leading edge geometry has influence in level and slope of force, but, the Reynolds number, Re has small influence. Furman and Breitsamter (2013)

performed an experimental survey over 65° using oil flow visualization, SPIV, laser sheet flow visualization, surface pressure measurement and hot wire anemometry at different angles of attack, α and at Reynolds numbers $Re=0.5x10^6$ and $Re=2x10^6$. In this survey they concluded that for medium angle of attack, α flow structure over straight edged delta wing depends on the Reynolds number, Re and an extra inboard vortex which is stronger for rounded leading edge than sharp leading edge occurred. Yaniktepe and Rockwell (2005) investigated flow structure of lambda and diamond delta wing planforms. They showed that different flow structures than simple delta wing were seen at these planforms. Streamline topology shows that for these planforms angle of attack, α has strong effect on flow structure of these planforms moreover trailing edge configuration also have effect of on the flow structure. One of the important finding of this work is contours of rms velocity fluctuation nearby wing planfom have maximum points on the outer regions of the vorticity layers. Spectral analysis obtained from instantaneous images is given in figure 2.8.

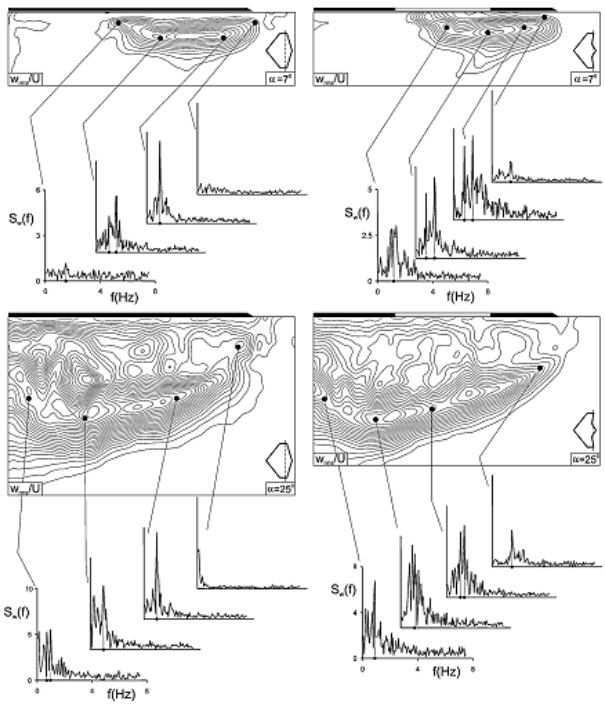

Figure 2.8. Spectra $S_w(f)$ of the vertical velocity fluctuations on different delta wing planforms(Yaniktepe and Rockwell, 2005).

Woodiga and Liu (2009) conducted on an experimental study to investigate skin friction fields on different delta wing configuration at different flight conditions. For the 65° delta wing, when the angle of attack, α is set below 15° no breakdown was observed but as the angle of attack, α was increased lines of reattachment, L_R moved inboard, when the angle of attack, α is set above 15° vortex breakdown was observed and in breakdown location reattachment line, L_R expanded and moved outboard. Whereas for the baseline 76°/40° double delta wing configuration highly curved reattachment lines, L_R and having angles of attach values above 15° spirals vortices near junctions were observed, for the diamond and parabolic fillet configurations rather straight reattachment lines, L_R were observed and no apparent spiral vortices near junction were observed. Figures 2.9 shows skin friction lines on 65° delta wing and figure 2.10 shows skin friction lines on $76°/40^0$ delta wing.

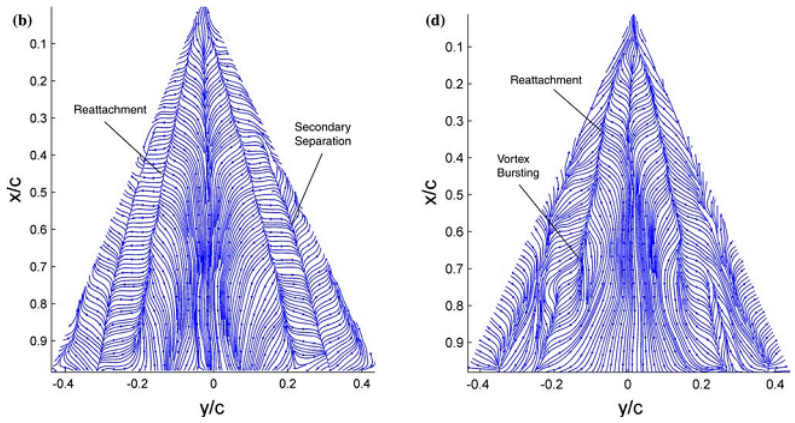

Figure 2.9. Skin friction lines on 65° delta wing (Woodiga and Liu, 2009).

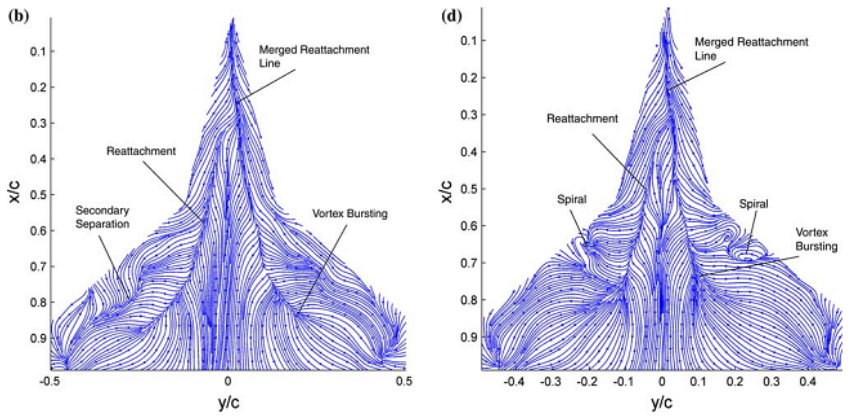

Figure 2.10. Skin friction lines on 76°/40° delta wing (Woodiga and Liu, 2009).

2.2.4. Roll Angle

The experimental results of Taylor at al. (2003) revealed that vortical flow structure and location of the vortex breakdown over low sweep angle, Λ delta wing was highly depended on the Reynolds number. As shown Figure 2.10 at low roll angle, effect of the roll angle, ϕ on vortex breakdown location was not so significant but at high angles of attack, α especially at leeward side was considerable. Large fluctuations of the vortex breakdown were originated from unsteadiness of the flow at low Reynolds numbers. At low Reynolds numbers weak vortical structure was observed. Cipolla and Rockwell (1998) conducted an experimental work to investigate flow structure of a rolling of 65° sweep angled, Λ delta wing having cylindrical centerbody. Flow structure in cross plane was investigated by means of PIV. Experiments revealed vortex breakdown location and flow topology that could change with self-excited excursions. Transformations could take place in streamline or vorticity independently. Furthermore coupling of leading edge vortices took place as shown figure 2.12.

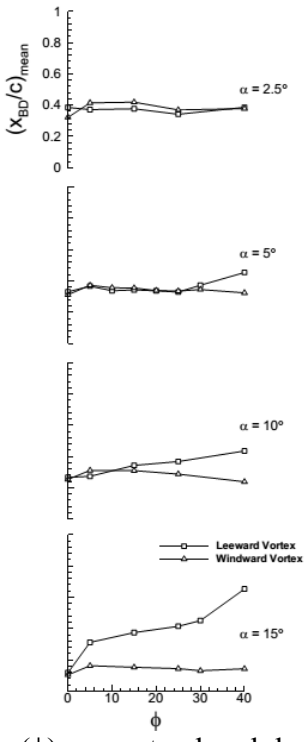

Figure 2.11. Effect of roll angle (ϕ) on vortex breakdown locations of 50° sweep angle (Λ) delta wing at the Reynolds number of 26.700 at different angles of attack (α) Taylor et al. (2003).

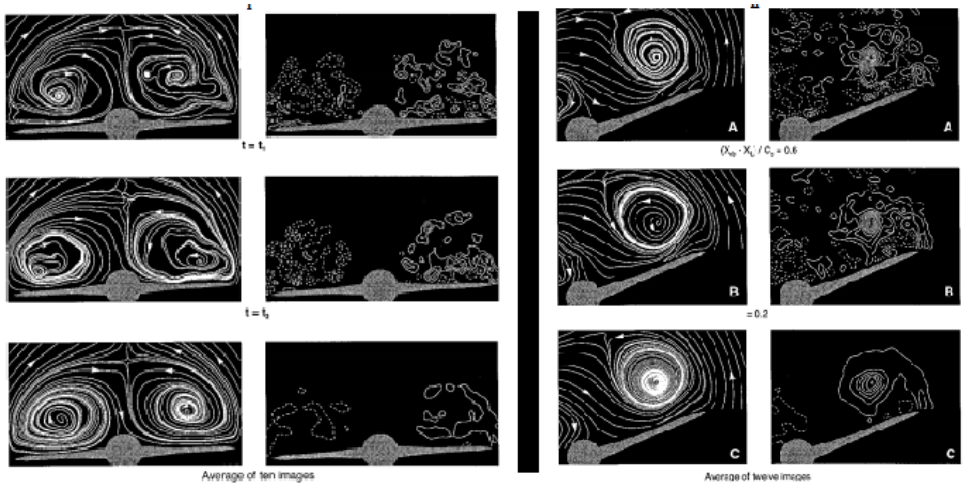

Figure 2.12. Streamline and vorticity patterns of unrolled and rolled delta wing (Cipolla and Rockwell 1998).

2.2.5. Yaw Angle

Johnson et al. (1980) performed and experimental investigation about effect of yaw angle, θ on a delta wing having 70° sweep angle, Λ. They stated that a fundamental difference in the variation of the lift coefficient C_L and rolling-moment coefficient C_M with the angle of yaw, β between low and high angle-of-attack conditions. Furthermore, at low angles of attack,α the lift coefficient, C_L showed a small decrease with increasing yaw angle, β while at higher angles of attack, α this coefficient initially decreased strongly and then more gradually with having yaw angle, β. They also concluded that C_M shows a linear variation with increased yaw angle, θ at a low angle of attack, α but a strong non-linear variation with yaw angle, β at a high angle of attack, α. Yayla et al. (2010) performed an experimental investigation over a nonslender diamond wing which has 40° sweep angle. They investigated effect of yaw angle on vortex breakdown by using the dye visualization technique. They concluded that up to 4° yaw angle, β there were no clear change on the location of vortex breakdown, but at higher yaw attack, β than 4°, the vortex breakdown point moved towards the leading edge on windward side, while this location took place further downstream on leeward side namely, asymmetrical vortex breakdown locations were seen over the delta wing in plain view plane. Canpolat et al. (2009) investigated the flow structures on the delta-wing surface with a

nonslender delta wing having 40° sweep angle, Λ. They concluded that when the delta wing had a yaw angle, β the symmetrical flow structure disappeared; vortex breakdown occurred earlier on the windward side of the delta wing, as compared with the leeward side. They also found that main vortices in cross flow planes took place in the inner side close to the central axis of the delta wing. Sohn and Chang (2010) investigated effect of centerbody on a yawed double delta wing by using off-surface flow visualization and wing-surface pressure measurements. They concluded that up to 24° angle of attack, α the presence of the centerbody had a small influence on the suction pressure distribution on the wing upper surface, even at the large yaw angle of α=20°. They also concluded that at higher angle of attack like 28°-32°, presence of centerbody caused decrease in the magnitude of pressure coefficient, C_p when compared with 0° yaw angle, β. Sohn et al. (2004) performed an experimental study about vortex flow visualization of a yawed delta wing with leading edge extension (LEX). Interaction between LEX and delta wing were investigated at some angle of attacks, α and yaw angles, β. They concluded that the wing vortex and the LEX vortex coiled around each other while maintaining comparable strength and identity when yaw angle, β was 0° and the increase of angle of attack, α intensified the coiling and shifted the cores of the wing and LEX vortices inboard and upward. It was also concluded that when the wing is yawed, the coiling, the merging and, the diffusion of the wing and LEX vortices increased on the windward side, whereas they became delayed significantly on the leeward side and movement of vortices on the windward and leeward sides of the wing changed significantly. Some of the results were presented in figure 2.13. Nakamura and Yamada (2002) investigated aerodynamic characteristics of spin over a delta wing. It was reported that when the wing was yawed, asymmetric pressure distribution over two halves of the wing took place and this pressure difference caused different lift forces, F_L on the two sides of the wing and finally rotation called spin. They also stated that at low angles of attack, α when the wing had a yaw angle, β the upper surface pressures on the windward wing-half became lower than those on the leeward wing-half but near the stall angle the upper surface pressures of the leeward wing-half become lower than those in the windward wing-half.

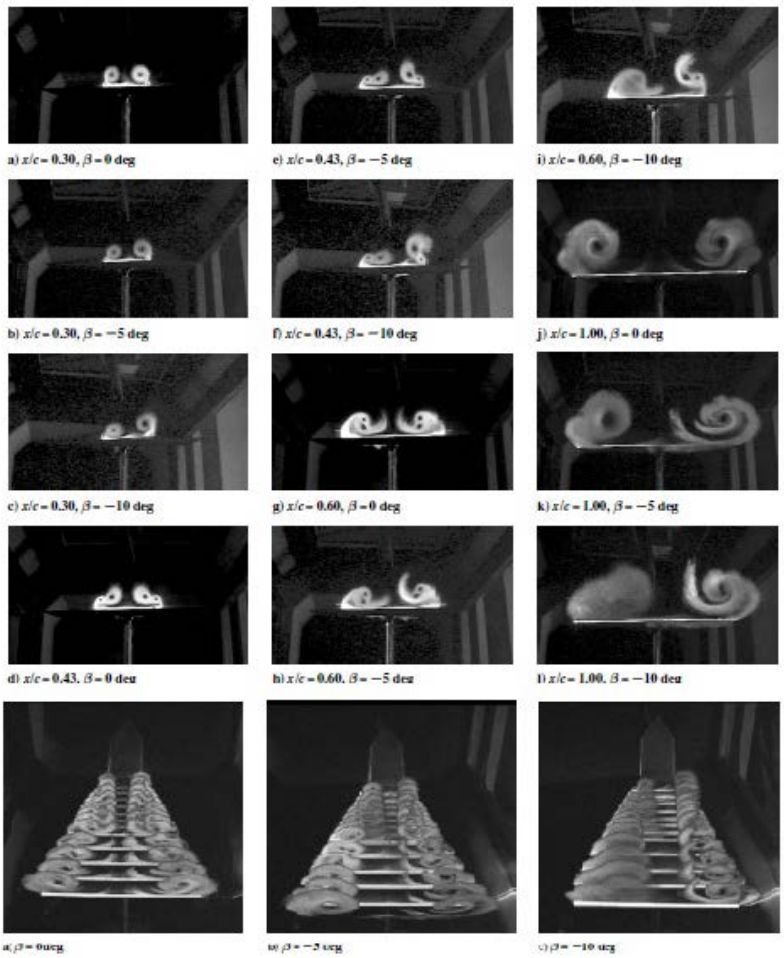

Figure 2.13. Visualization of the vortices over double delta wing with and without yaw angle (Sohn et. Al, 2004).

Verhaagen (1999) conducted an experimental survey to investigate of the effect of sideslip (yaw),β over a 65° delta wing having a constant angle of attack, α=30° by using different experimental techniques. According to his results, when β has 0°, the flow over the delta wing is dominated by two primary and secondary vortices, but, with yaw, β vortices were observed to move towards the leeward edge with increasing sideslip angle, β vortex burst taken place on the windward side moved towards the apex, the vortex burst on the other side moved in the opposite direction. In additions, on the windward side the reduction of the suction on upper surface was seen causing the amplitude of the oscillation of the burst along the vortex axis to increase with yaw angle, β. Effect of yaw angle, β on pressure distribution over a delta wing was shown in figure 2.14. Effects of sideslip (yaw

angle, β) on the sharp edged biconvex delta wing at angle of attack, α=21.1 degree, Reynolds number of $2.5x10^6$ and varying yaw angle, β from 0^0 to 20^0 were investigated by Verhagen and Naarding (1989). They concluded that up to 12^0 with yaw angle, β owing to boundary layer transition, chances the leading edge vortex strength and location of the vortex breakdown, pressure distributions and crossflow structure, but, at a higher yaw angle, β vortex breakdown has extra effect on the flow structures and pressure distributions

In the investigation of Shields ad Mohseni (2012), effects of aspect ratio, planform of wing, the low Reynolds number, Re, and sideslip (yaw) angle, β and winglet configuration on aerodynamic characteristics were investigated. They concluded that at increased angle of attack, α, leading edge vortices and tip vortices coupled leading to complex flow structures which delayed separation, increased stall angle and brought the C_L lift coefficient to a maximum value. It was also shown that sideslip angle, β decreased C_L, increased C_D and decreased C_M furthermore sideslip angle, β had more influence on C_M than C_L and C_D.

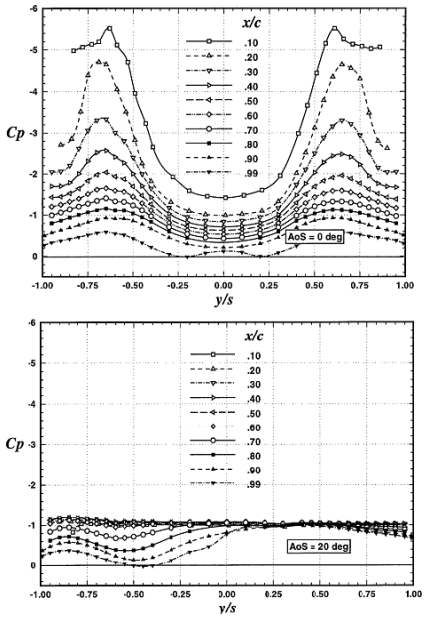

Figure 2.14. Effect of yaw (sideslip) angle on surface pressure distribution at β=0° and β=20° (Verhaagen, 1999)

Lee and Sohn (2003) conducted on an experimental study over a delta wing with LEX (Leading Edge Devices). They concluded that leading edges devices

(LEX) could stabilize and delayed leading edge vortex breakdown even high angles of attack, α., sideslip (yaw) angle, β had significant in both LEX and delta wing vortices; with sideslip, breakdown location moved forward both the LEX and delta wings of the windward side vortices, leeward side of LEX and leading edge vortices coiled each other and kept their identities, breakdown took place later. Jeans et al. (2008) performed a numerical study to investigate aerodynamic characteristics of fuselage/delta wing which can be used for unmanned aerial vehicles. In this study delayed Detached-Eddy Simulation method were used. At 0° yaw angle,α for all angles of attack, α lift and drag predictions were outstanding. At 30° angle of attack, up to 5° yaw angle prediction of the rolling moment outstanding also, at 1° yaw angle, β good prediction was also obtained nonlinear aerodynamic behaviour. In this investigation showed that nonlinear aerodynamic characteristics was due to abrupt vortex breakdown over windward side. Investigation showed that vortex trajectories of 1° and 2° yaw angles, β showed minor differences. At 2° yaw angle in windward side vortex increase in total pressure depreciation an adverse pressure gradient were detected which are not detected on leeward side vortices at 1° and 2° yaw angles or windward side vortex at 1° yaw angle.

2.3. Vortex Breakdown Control

2.3.1. Passive Control

Akilli et al. (2001) conducted an experimental work to investigate sensitivity of vortex breakdown on a delta wing at high angle-of-attack, α, via placing slender wire orthogonally to the center of the leading-edge vortex. It was reported that a slender wire could move the onset of the vortex breakdown by as much as fifteen vortex diameters in the upstream direction. The movement of the vortex breakdown depended on the dimensionless diameter of the wire and place of the wire. Vortex breakdown onset could occur either upstream or downstream of the located wire. It was also reported that patterns of instantaneous vorticity in the presence of slender wire typically exhibited a form characteristic of either a spiral or bubble-like mode of

vortex breakdown that occurred in the absence of wire. Kawazoe and Kato (2006) performed and experimental investigation over hard and flexible delta wings with 60° sweep angle, Λ. They concluded that at low angles of attack, Δ winding-up leaded stronger leading edge vortices and higher C_L and C_D, but, excessive winding-up of the leading edges causes adverse effect on the performance of the delta wing because of weaker leading edge vortices. Cai et al. (2014) performed an experimental and numerical investigation about effect of the vortex flap over flow structure and aerodynamic performance over a 50° sweep angle delta wing. They concluded however upward vortex flap increased C_L because of stronger vortices at low and moderate angles of attack, it decreased maximum C_L and stall angle at higher angles of attack so at high angles of attack upward deflection flap was not good at aerodynamic performance. Although downward deflected flap leaded poor aerodynamic performance at low angles of attack, at high angles of attack it increased the aerodynamic performance considerably. Downward deflected flap increased the maximum angle of attack, maximum lift coefficient C_L moreover it increased C_L even in post-stall region and optimum deflection angle was found as -70°, figure 2.15 and 2.16 summarizes results.

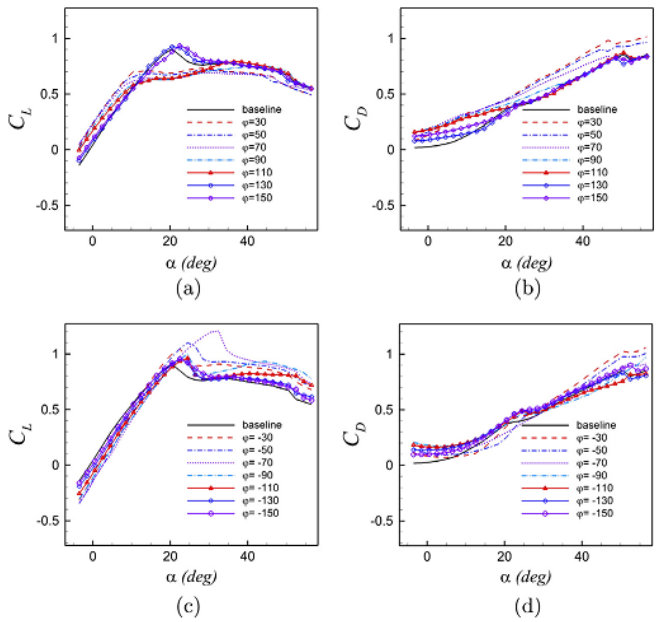

Figure 2.15. Effects of positive and negative vortex flap angles, γ with experimental C_L and C_D. (Cai et al. 2014).

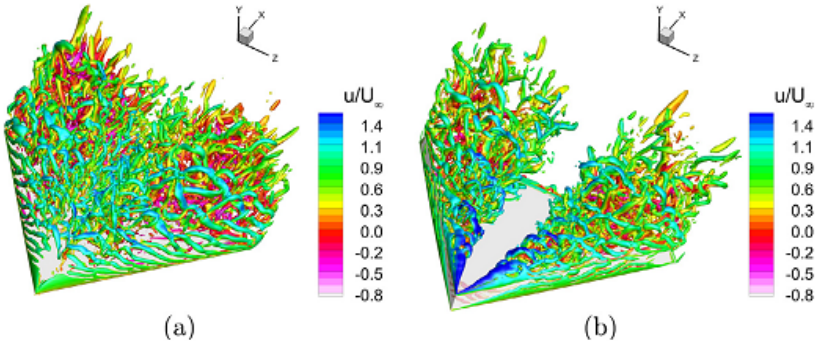

Figure 2.16. Numerical results of nondimensional streamwise velocity compononet (Cai et al. 2014).

Goruney and Rockwell (2009) performed and experimental study to investigate effect of the sinusoidal leading edges on the flow structure over a delta wing having Λ=50° at 25° angles of attack, α at the Reynolds number, 15000. Some of the finding can be summarized as follows. When sinusoidal leading edges were used flow structure near surface was drastically changed if appropriate wavelength and amplitude were chosen. For small wavelength/amplitude λ/ϕ values if amplitude/chord ratio ϕ /c of the leading edges was increased focus of the separation moved toward to leading edge, if this value was set a 0.02 % the focus of the separation replaced with focus of attachment moreover if λ/c was larger (0.08) focus of the separation moved near apex of the delta wing.

2.3.2. Active Control

Guy et al. (1999) performed experimental surveys to investigate effect of suction and blowing on flow over 70° delta wing via water channel and wind tunnel experiments. They found that periodic blowing and suction delayed vortex breakdown occurrence and increased lift force, F_L frequency of the excitation, f_e which is important ,for example, at right frequency, f vortex breakdown could be delayed by almost 0.2 chord length. Instantaneous and time-averaged flow topologies were investigated over delta wing having 38.7° sweep angle by Yavuz et al. (2004). In this study, effects of pitching motion were investigated via the PIV technique at the Reynolds number of $Re=1x10^4$. Experiments demonstrated that critical points of

time-averaged and instantaneous flow patterns were considerably different. Beneath the vortex breakdown rms of the velocity fluctuations showed unsteadiness of the flow topology. When the delta wing was pitched, significant changes on the flow topology were detected; less critical point were detected furthermore significant reduction in magnitude surface-normal vorticity at certain locations of the delta wing. Timescale of the motion was also important to form critical points. Ozgoren et al. (2001) performed an experimental investigation on a 75° sweep angle, Λ delta wing. The delta wing was perturbed with low-amplitude over a low range of periods. Experiments were conducted on both with and without impingement plate, to determine effect of the impingement plate on the flow pattern of the delta wing. Considerable changes of the instantaneous and averaged flow pattern of the leading-edge vortex were detected, both with and without a downstream impingement plate. Another main finding of this study was the onset of vortex breakdown could either be advanced or delayed, and the modifications in structures vortices played significant role on buffeting of the plate. In their study, one can also see that the using the plate leaded important modifications on the vortex structures downstream of the breakdown as shown in figure 2.17. Delay in the onset of vortex breakdown could be provided, when the leading edge of the delta wing was perturbed at a natural frequency of vortex breakdown as reported by Sahin et al. (2001). They also found that onset of upstream movement of vortex breakdown could be attained when the period of excitation frequency f_e was sufficiently large. Sidorenko et al. (2013) performed and experimental survey to control leading edge vortices of a 65° sweep angle delta wing by means of Dielectric barrier discharge (DBD) plasma actuator. Dielectric barrier discharge (DBD) plasma located surface of the delta wing was used for vortex flow control; they concluded that in range of Reynolds numbers, $1.4x10^5 \leq Re \leq 2.5x10^5$, not only DBD plasma delayed leading edge vortices, it could stabilize them as well at high angles of attack. Furthermore, mode of excitation, location and angle of the DBD plasma actuator are crucial to control of vortex breakdown. As a mode the optimum mode was found burst mode, highest efficiency was reached when DBD plasma actuator was placed perpendicularly to the leading edge across the vortex flow.

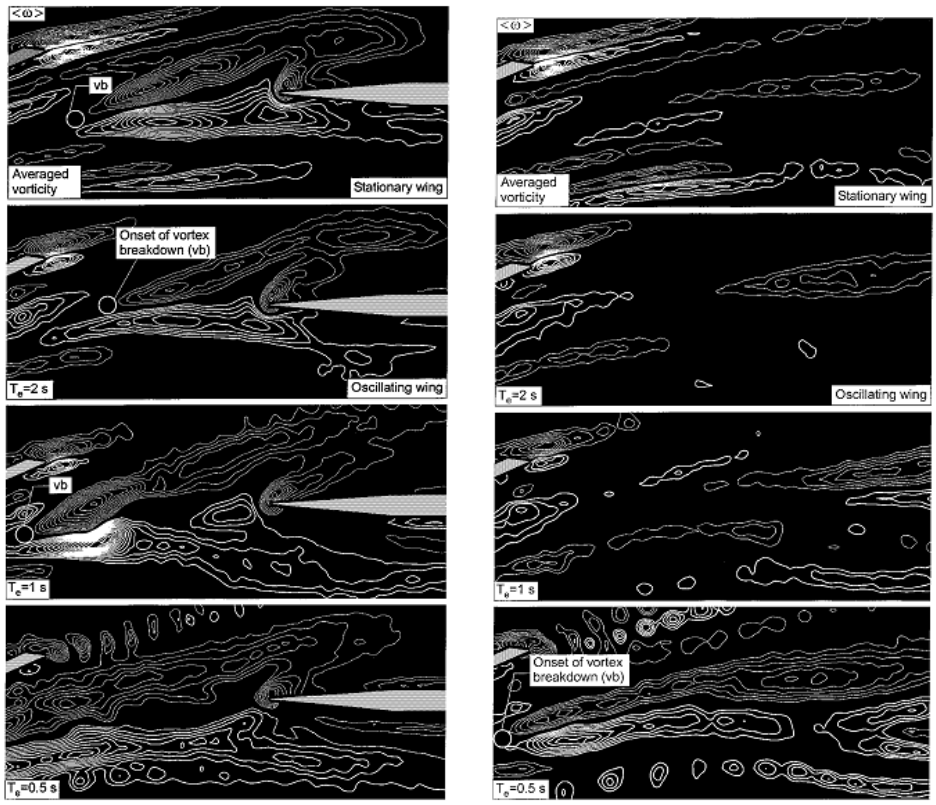

Figure 2.17. Effect of perturbation and impigiment plate on flow structure over a slender delta wing (Ozgoren et al. 2001).

Kanstantin et al. (2010) performed an experimental survey to control of vortex breakdown by means of dielectiric barrier discharge (DBD) plasma actuator using stereo PIV, LDA, surface pressure measurements and force measurements. Findings of this investigation are; using plasma actuator could control vortex breakdown and increase aerodynamic performance. Yavuz and Rockwell (2006) performed and experimental survey to investigate effect of trailing edge blowing on near surface patterns of a delta wing having 35° sweep angle delta wing. When there was no control, at a critical angle of attack, 3D dimensional separation was detected. This separation had a focus center of the inward spiralling downstream of the apex existed and in this pattern near-surface had considerable velocity fluctuations. At lower angles of attack, α lower blowing from trailing edge leaded considerable changes in flow topology, especially, if the magnitude of the blowing was sufficiently large, structures and locations of critical points alter along the surface of

the delta wing and the near the wake. Beyond critical angles of attack, α blowing from the trailing edge moved focus of the separation toward the apex of the delta wing. At a critical value of blowing the focus of the separation was eliminated completely. Furthermore the blowing at a high angles of attack, α leads a similar flow structure with flow structure without blowing at lower angles of attack. If the angle of attack considerably was higher than the critical angle of attack flows structure was less sensitive to blowing and larger blowing coefficient were required. Not only trailing edge blowing from a slot located at the center of trailing edge was performed, but also blowing from dual slots located at a symmetrical point with respect to the center of the delta wing was employed. At the lower blowing coefficients the dual configuration was more effective than the single configuration, at higher blowing coefficients the single configuration was considerably effective than the dual configuration. Figure 2.18 demonstrates streamline topology at different blowing configurations. Calderon et al. (2012) performed and experimental survey over plunging 50° sweep angle, Λ delta wing in a water channel. Double helix pattern in the post-stall region was observed over the delta wing plunging with small amplitude at angle of attack of 27° and in a region reverse axial flow existed along the centre of the double helix flow structure. In this survey by means of 3-D particle-tracking method double helix mode over plunging could be shown which could not be shown easily by classical methods. Gordiner et al. (2009) performed a computational and experimental investigation over 50° sweep angle delta wing at angle of attack 15° at Reynolds numbers $2x10^5$, $6.2x10^5$ and $2x10^6$. Computational and PIV experimental results were compared. Good agreements between experimental and computational results of time-averaged and instantaneous flow data were observed at the lower Reynolds number. However dissimilarity at location and structure of the vortex breakdown was observed. A qualitative agreement was seen for $Re=6.2x10^5$, also. Vortex breakdown took place in two stages, such as in a diffuse region and wake-like flow region for $Re=6.2x10^5$. In cross-plane, secondary vortices were observed moreover downstream of the vortex breakdown shape of the vortex were more oval and includes small-scale structures. It was observed that when the Reynolds number was increased the small scale structures increased and got more

different flow structures with increasing the Reynolds number, in additions, helical substructures co-rotating with primary vortex were also observed. Wavelength of these helical substructures decreases and develops gradually in upstream region with increasing the Reynolds number.

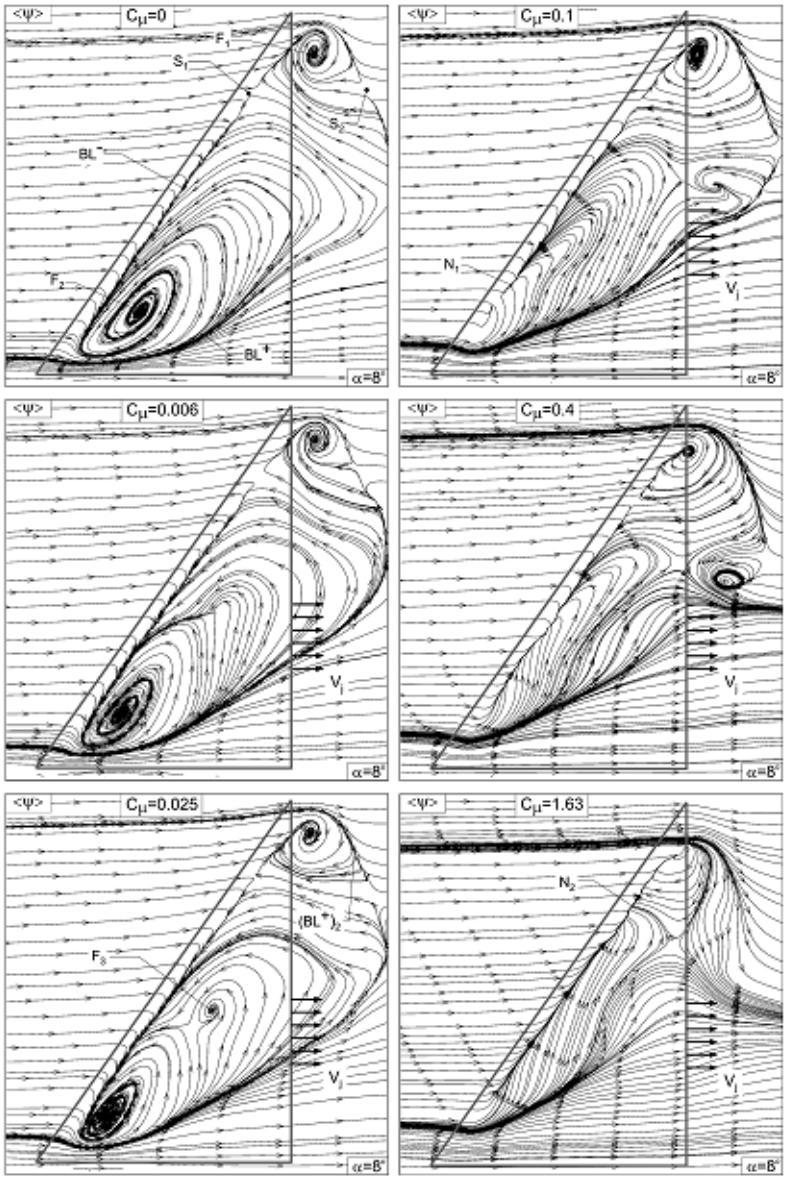

Figure 2.18. Effect of trailing edge blowing at different blowing coefficient C_μ (Yavuz et al., 2006)

Süchtte and Lüdeke (2013) performed CFD simulation over a 65 ° delta wing having rounded leading edge at an angle of attack of α=13.1° and Reynolds numbers,

Re=$2x10^6$ and $3x10^6$. Results of the CFD simulation were compared with experimental investigation performed within NATO RTO project. Main features of the flow field predicted well by the Spalarat-Allmaras turbulence model but inner and outer vortices were predicted at further upstream region. Wilcox k–ω turbulence model predicted the vortex at a location further downstream region and this model is more sensitive to angle of attack, α. However predicted and experimental pressure distribution showed small differences, several numerical and physical sensitivities were detected. Both of the turbulence models showed effect of Reynolds number on the flow structure. Fully turbulent assumption was made for both of the turbulence models and it was concluded this assumption which would affect flow patterns.

Elkhoury (2015) performed a numerical investigation flow structure over 50° and 70° sweep angle delta wings. In this numerical investigation LES with dynamic Smagorinsky coefficient, k_T-k_L-ω transition model, SST Transition models were used. LES with dynamic Smagorinsky coefficient predicted precisely the onset of vortex breakdown and transition for all the test cases. Predictions at the surface flow patterns of the SST-TR and the k_T-k_L-ω models were different and differences were more in turbulent flow regions. For the 70° sweep angle delta wing, k_T-k_L-ω transition model predicted point of transition to turbulence comparatively better than SST-TR. For the 50° sweep angle delta wing, LES with dynamic SGS model gave better prediction than other models. SST-TR model predicted better than k_T-k_L-ω transition onset of the breakdown, low-speed conical shaped region and surface limiting streamline for the same delta wing. Vortex wandering was detected by SST-TR and LES models, but both of two models were not good in predicting the mean turbulent kinetic energy values.

3. MATERIAL AND METHOD

3.1. Water Channel

The water channel experiments were performed in a closed-circuit free-surface water channel in the Fluid Mechanics Laboratory at Çukurova University. Dimensions of the water channel; length of 800 cm, width of 100 cm, and height of 75 cm and plexiglass transparent test section of the water tunnel has thickness of 1.5 cm.

The water channel has two reservoirs in upstream and downstream of the channel, water is pumped from downstream reservoir to upstream reservoir, before reaching test section the water is passed through a settling chamber then a honeycomb located before 2:1 contraction. The water is pumped by a 15 kW electric driven pump which has a frequency controller sets speed of the flow. Turbulence intensity was kept below 0.5 % due to the design of the channel and the honeycomb. Figure 3.1 shows schematic of the water channel.

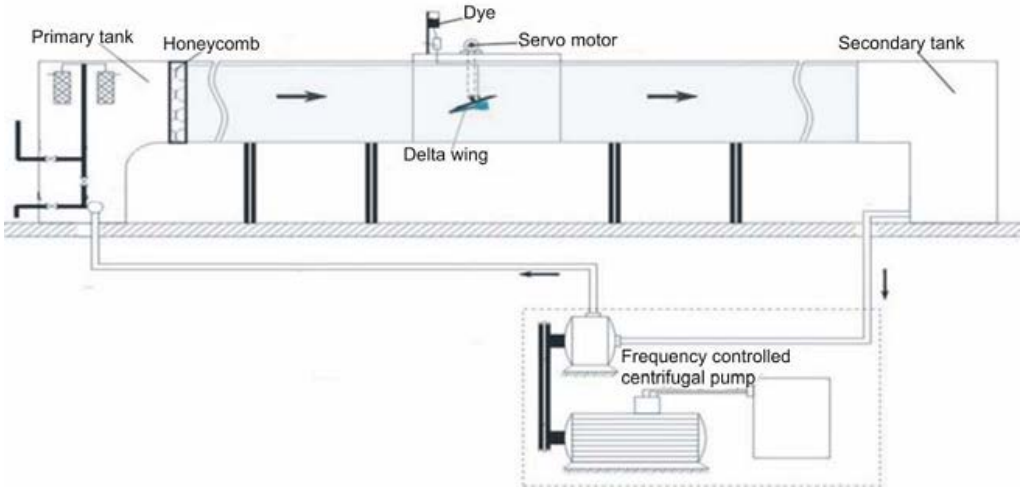

Figure 3.1. Schematic of the water channel (Yayla, 2009).

3.2. Wind Tunnel

The wind tunnel experiments were performed in an open-circuit suction type wind tunnel located in Energy Systems Engineering in Erciyes University.

Contraction ratio is of the contraction cone of the wind tunnel is 9:1. Test section of the wind tunnel is 50 cm x 50 cm x 200 cm and walls of the test section have a 0.3 to minimize effects of the boundary layer and maintain constant static pressure. Velocity of the flow can be set by means of frequency controller. A honeycomb in the inlet section of the wind tunnel was used to reduce the turbulence level. Turbulence intensity on the central axis of wind tunnel was measured by a one dimensional hot-wire probe of which are shown in Figure 3.2. The schematic drawing of the wind tunnel and experimental system are presented in Figure 3.3.

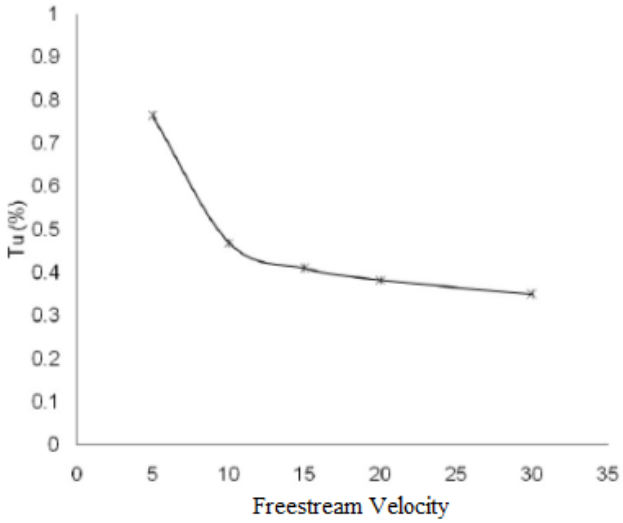

Figure 3.2. Turbulence intensity of the wind tunnel (Karasu, 2011).

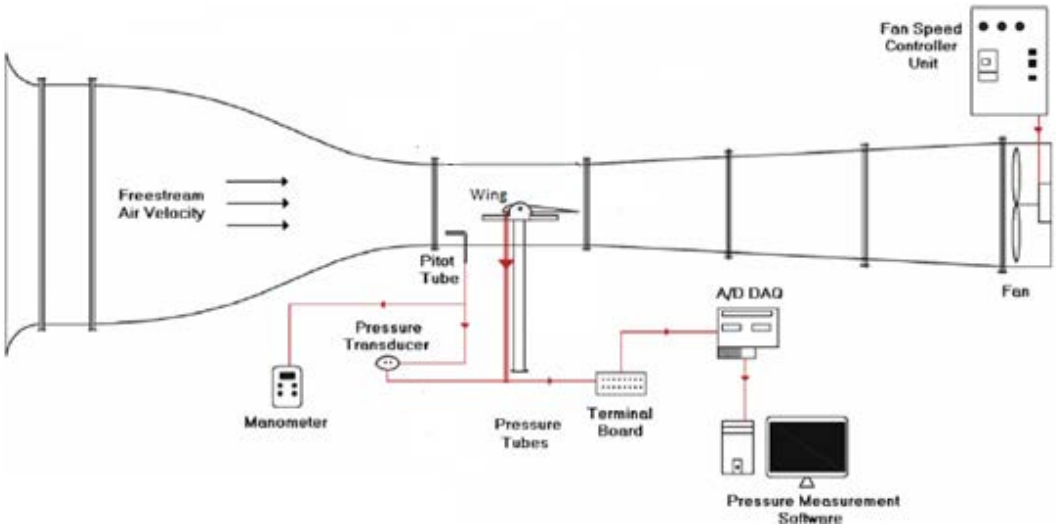

Figure 3.3. Schematic diagram of wind tunnel (Genç et al. 2012a).

3.3. Experimental Apparatuses

The delta wing was located to the water channel by means of an angle apparatus which can set both angle of attack, α and yaw angle, β. Angle of attack,α is set by means of a servo motor while yaw angle, β is set manually. The delta wing is maintained by means of streamlined strut which has insignificant effect on the flow structure over the measurement plane. For the wind tunnel experiments delta wings were maintained via an apparatus which kept the wing from span of the delta wing.

3.4. General Principles of the Experimental Systems

3.4.1. Particle Image Velocimetry (PIV)

Particle Image Velocimetry (PIV) is a non-intrusive velocity measurement technique used to simultaneously determine the instantaneous velocities at many points in a flow field. The technique involves seeding, illumination and capturing two images in a certain time interval. Since displacement of the particles between 2 images in the captured is known, velocity vector field can be determined from basic velocity formula given below.

$$U = \frac{\Delta x}{\Delta t}$$

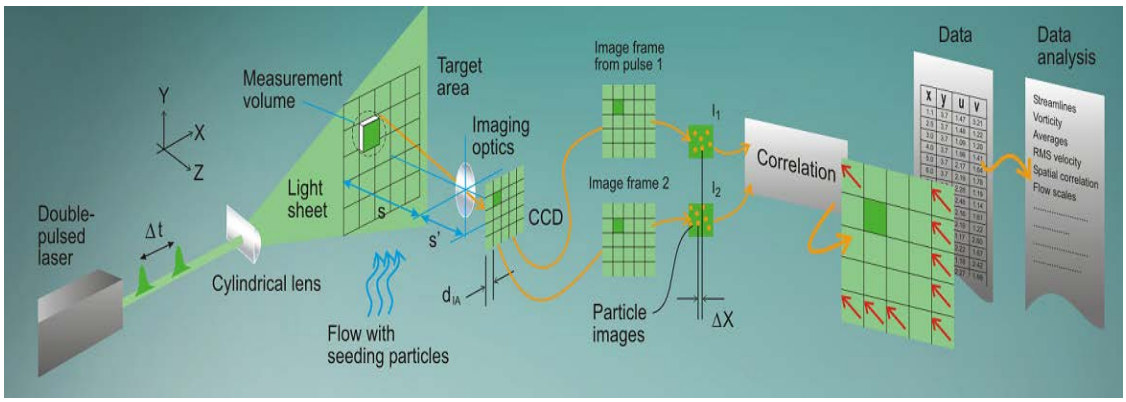

Figure 3.4. PIV Measurement Principle (Dantec Dynamics, 2015).

To obtain displacement of the particles in the captured images, enough particles are needed to obtain displacement of the particles in the measurement plane. Homogenous seeding of particle is one of the requirements of the PIV system, to see particle clearly laser illumination is another requirement of PIV system. Laser illumination system illuminates the particles in the measurement plane, illumination is not continuous but pulsed, illumination system is synchronized with image capturing system, time between pulses is determined the time interval used in the velocity formula given above. CCD (Charge Coupled Device) camera is used to capture illuminated images, if the camera capture double frame images, frame 1 and 2 are used to determine velocity vector map.

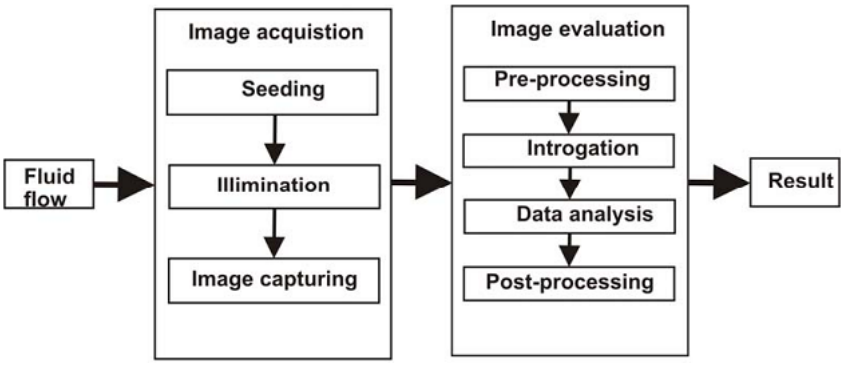

Figure 3.5. General PIV Process (Yayla, 2009).

If camera captures single frame images successive images are used and time interval in the double frame is lower than single frame so more accurate results can be obtained. Acquired raw images must be evaluated to obtain velocity vector fields and related physical properties such as velocity, vorticity, turbulence kinetic energy etc.

Choosing appropriate seeding tracer particles is very critical for PIV measurement because PIV measurement is based on tracking particles acquired images in a certain time interval. Particles must have almost same density with the fluid flow to provide same motions of particles with fluid otherwise particle may move upstream or downstream free to fluid due to buoyancy. Size of the particle should be enough to be detected by the camera; while highly reflective particles such

as silver coated particles are used for water tunnels, olive oils or alcohol droplets are used for wind tunnels (Tunay, 2011). Amount of the particle in the measurement plane is very crucial because every pixel of the image must contain certain amount of particle for the correlation process; around 35 particles for each interrogation area otherwise measurements can have high errors (Öztürk et al., 2008).

Particles must be illuminated by an external source synchronized with the camera to be detected by the cameras or the PIV system. However different sources such as laser diodes Xeon lamps can be used for illumination pulsed laser systems are the most common for the PIV systems. Illumination source must provide sufficient energy level and thickness and also it must illuminate the entire measurement plane and must be synchronized with camera. Nd:YAG (Neodymium-Doped Yttrium Aluminum Garnet) lasers is the most widely used in PIV because of performing required conditions mentioned above. (Tunay, 2011).

Illuminated particles by the laser source are captured by a camera. Generally CCD (Charged Couple Device) cameras are used which formed series of detectors called pixel. Cameras must work synchronal with laser system.

3.4.2. Stereo PIV

In the PIV technique, to compensate optical problems such as refraction, prisms can be used. In some circumstances, camera cannot be set as perpendicular to the measurement plane of the PIV system. In the present study, when the delta wing has an angle of attack as well as yaw angle optical problems arise such as refraction and parallax effect etc. For this reason, the stereo PIV technique was used to eliminate optical problems in the present study. Measurement principle of stereo PIV is based on same principle with human eyesight. When one looks at an object, however right and left eyes see similar things, they are not completely same. Left and right images are compared and interpreted in the brain; finally 3-Dimensional image is generated (Dantec Dynamics, 2006). However other parts of the system are same, in the stereoscopic PIV system there are 2 cameras as distinct from the traditional PIV system. 3-D vectors are obtained by means of processing 2-D vectors obtained

from each camera located with angle according to the object. However the best results are obtained while the angle between cameras, reasonable results can be obtained at much less angles. (Dantec Dynamics, 2006).

Due to the parallax effect, if cameras are located to measurement plane with angle, different velocity component is obtained since the cameras see different magnitude and direction of the vectors as shown in figure 3.6. To reconstruct true velocity field vectors, new correlation is performed using 2 adaptive correlations of the cameras taken into account calibrations by this way not parallax effects and misalignment of the laser sheet are corrected.

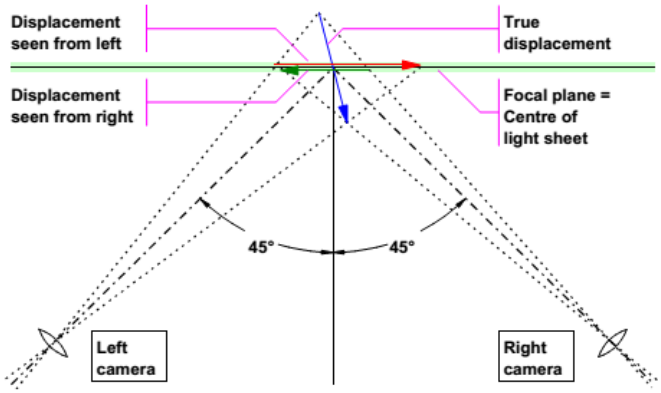

Figure 3.6. Principle of stereo-vision (Dantec Dynamics, 2006)

Stereo PIV is required a calibration process to construct 3-D image from 2 2-D images. Calibration process is performed as follow;

- Calibration target is aligned with laser sheet in the measurement plane; the surface of the target is located in the center of laser sheet.
- The target is traversed in Z axis through laser sheet thickness in the measurement plane. Center of the laser sheet is accepted as Z=0, 3 or 5 points must be traversed through entire of laser sheet thickness.
- Single frame images are recorded at every Z points.
- Calibration process is performed separately for each camera.

Calibration can be performed with different techniques; linear and non-linear techniques. Linear models are pin-hole model and direct linear transformation (DLT); linear models are used if the target is moved linearly and if there is nothing breaking non-linearity such as low quality of lenses or complex refractions. If non-linearity is expected 3 ordered XYZ polynomial model must be used. (Dantec Dynamics, 2011).

To be able to perform calibration process, Scheimpflug condition for each camera condition must be ensured. The Scheimpflug principle describes the orientation of the plane of focus of an optical system when the lens plane is not parallel to the image plane (Wikipedia, 2015). If the Scheimpflug condition is not satisfied entire of the image or some part of the image focus becomes inadequate (blur) to form appropriate vector map.

Stereo PIV camera has Scheimpflug mount to tilt camera to satisfy Scheimpflug condition. To be sure satisfying Scheimpflug condition different techniques may be used; Scheimpflug angle is set by means of tilting camera according the calibration target. Setting light in the environment has great importance to set Scheimpflug condition also. Figure 3.7 shows proper and improper Scheimpflug condition.

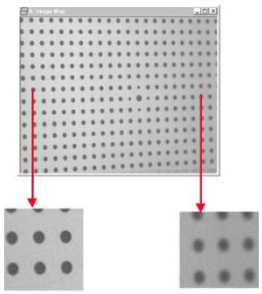

Figure 3.7. Image of the calibration target shows proper and improper Scheimpflug condition, the left is proper, the right is improper (Dantec Dynamics,2006).

Scheimpflug condition can be set via 3 different ways (Dantec Dynamics, 2006). The first one is calculating Scheimpflug condition angle according to given formula below.

$$\gamma=\text{ArcTan}[(f_{lens}\cdot\tan\theta)/(d_o-f_{lens})]$$

The second method to set Scheimpflug condition is to focus center of the image and tilting cameras until reach the best focus whole of the image. If this method is used on-line histogram can be used, in this histogram if 2 distinct peaks are detected as shown in figure 3.8 Scheimpflug condition is ensured. The last method to set right Scheimpflug condition is adjusting focus of the camera and Scheimpflug angle, γ until the obtain satisfactory vectors in entire of the plane.

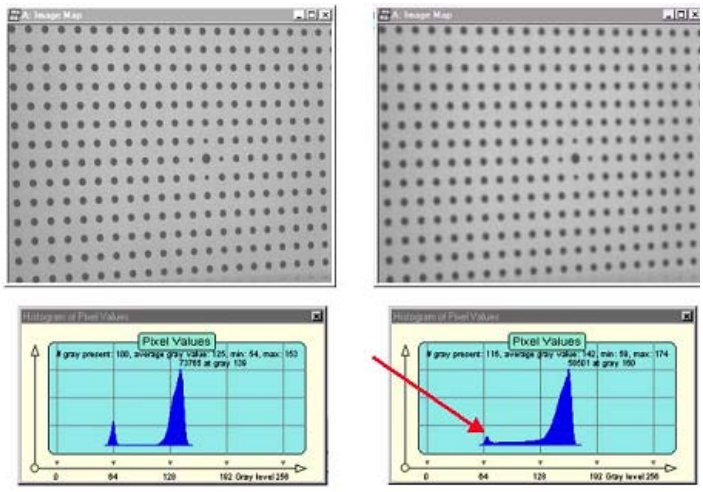

Figure 3.8. Two different adequate Scheimpflug conditions using online histogram which shows two distinct peaks (Dantec Dynamics, 2006).

Figure 3.9 shows reconstruction of the 3D stereo PIV image from a pair of 2D image. 3rd component velocity (w) is given as a contour drawing in the measurement plane and there is no z axis. Since the cameras are oriented to the measurement plane with angle and different positions, it is impossible they see identical areas; region where both 2 camera's views intersect which is generally trapezoidal area is used to form 3-D image and the regions outside the intersection called overlap can not be used to form accurate vectors. The best stereo PIV measurement is conducted when angle between camera axes is 90 but this is not an obligation, cameras can be placed asymmetrical as well as shown figure 3.9 (Dantec Dynamics,2002).

Raw images must be evaluated to obtain velocity vector. The first step of the evaluation is correlation process; however there are different types of correlation methods, in this investigation adaptive correlation is applied, in this analysis method velocity vectors are calculated with an interrogation area consisting m x n pixels. Vectors are recalculated using smaller interrogation area and recalculation is repeated until defined final interrogation area reached (Suástegui, 2012). Interrogation and overlap area are given in figure 3.11.

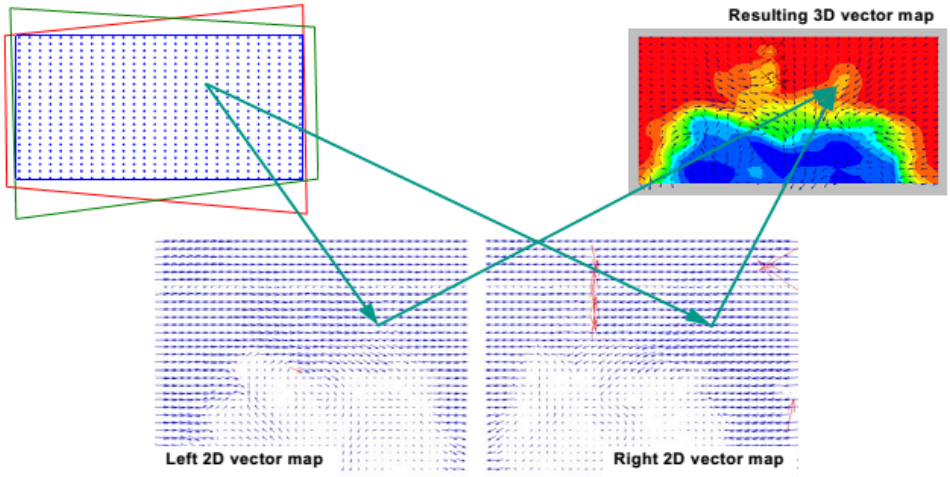

Figure 3.9. Reconstruction of the 3-D vector map from a pair of 2-D vector map (Dantec Dynamics, 2006).

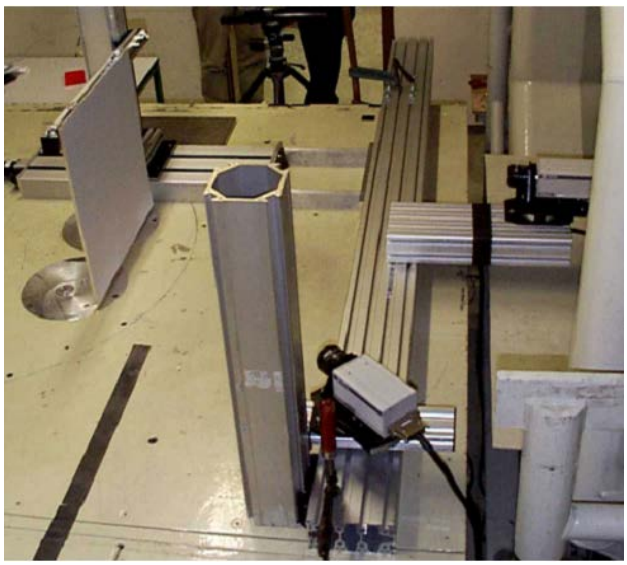

Figure 3.10. Example of a non-symmetric stero PIV experimental set-up (Dantec Dynamics, 2002).

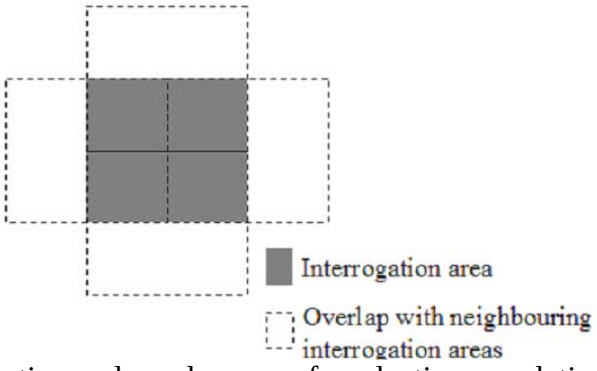

Figure 3.11. Interrogation and overlap areas for adaptive correlation (Dantec Dynamics, 2011).

After the instantaneous velocity fields are calculated for each image by means of the correlation process, post-processing is performed for deleting spurious vectors, replacing the deleted vectors, smoothing and filtering entire of the velocity fields. Spurious vectors can be formed due to noise or artifacts such as laser misalignment which cause improper peak detection (Yavuz, 2006).

To eliminate spurious vectors, a validation is required. Validation is performed by means of CLEANVEC software written by Meinhart and Soloff (1999) which has 4 methods; RMS tolerance filter method, magnitude difference filter, absolute range filter, quality filter methods. The software removes vectors below the defined threshold value of the mentioned methods. To fill deleted vectors by CLEANVEC, NFILVB software written by Lin (1994) which uses bilinear interpolation with least squares fit is used.

Finally obtained velocity field is smoothed using a Gaussian-weighted method proposed by Landreth and Adrian (1989) with smoothing parameter of 1.3. Physical quantities such as vector map, streamline, u_{rms} etc. are presented via data analysis software Tecplot and Surfer. Figure 3.12 shows steps of the stereo PIV process and post-processing. Formulations of PIV analyses are given in the appendix.

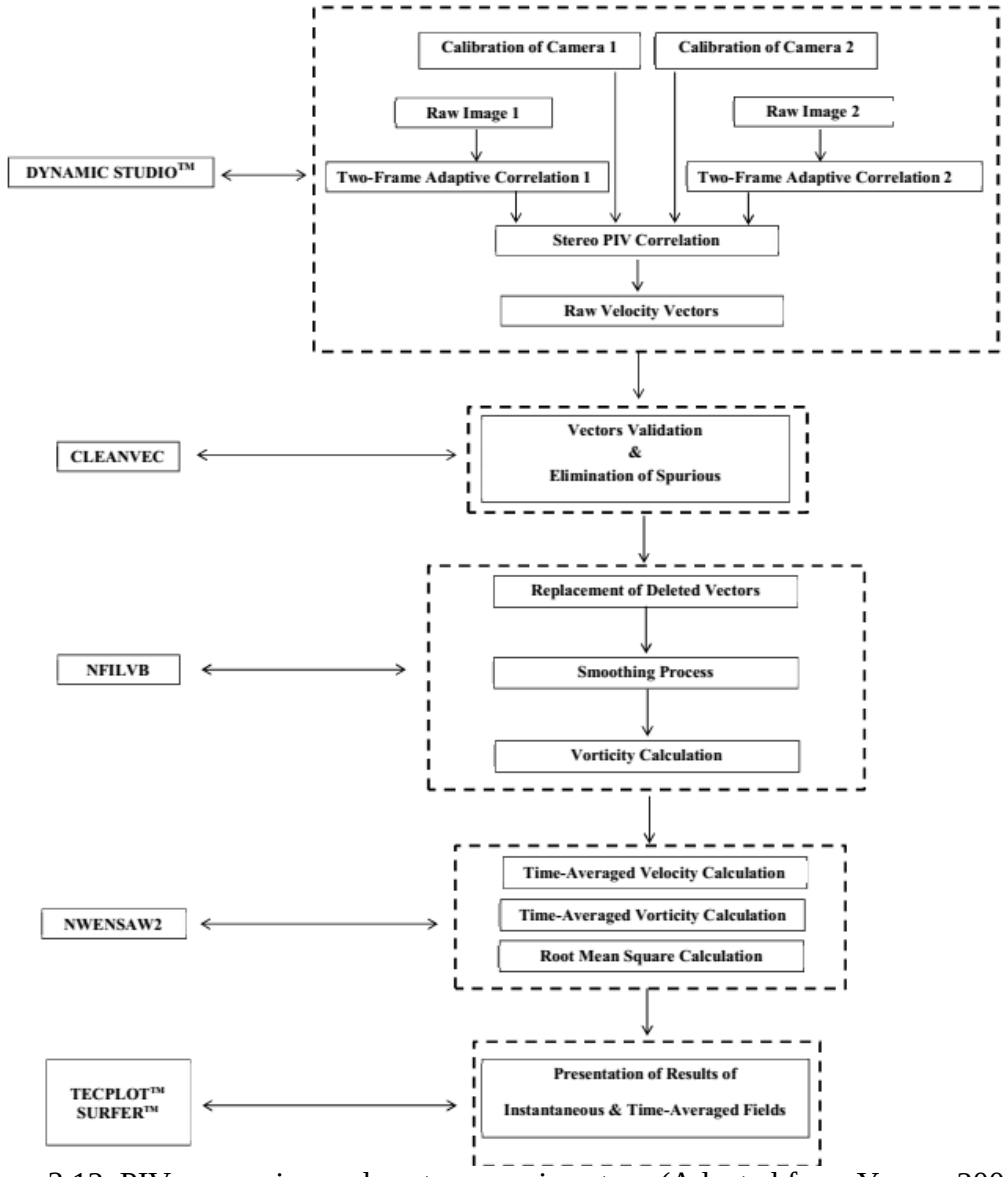

Figure 3.12. PIV processing and post-processing steps (Adapted from Yavuz, 2006).

3.4.3. Surface Pressure Measurements

Pressure measurements can be conducted on via different pressure measurement devices such as, U manometer, digital manometer etc. In this present research differential type electronic pressure transducer including strain gage and diaphragm which widely used differential pressure measurement device.

The pressure transducer consists of a strain gage and a membrane. Strain gage is an electrical circuit consists of 4 resistors of which 2 cross multiplying values are

equal. If the 3 of the 4 resistors are known the fourth can be calculated via formula given below.

$R_1 \times R_4 = R_2 \times R_3$

With applied pressure membrane moves and changes the resistor, output voltage changes with applied pressure also. Output voltage can be adjusted linearly with applied pressure; output voltage is transmitted to terminal board then computer via analog-digital data acquisition card. Acquired voltage data is converted to pressure values by means of a computer program. To be able to get corresponding pressure value, calibration process must be performed prior to the measurement. Calibration is performed via measuring pressure with another pressure device such as a manometer; 2 measured pressures by the manometer are entered to the software and the software converts output signals to pressure since output voltage varies linearly with applied pressure.

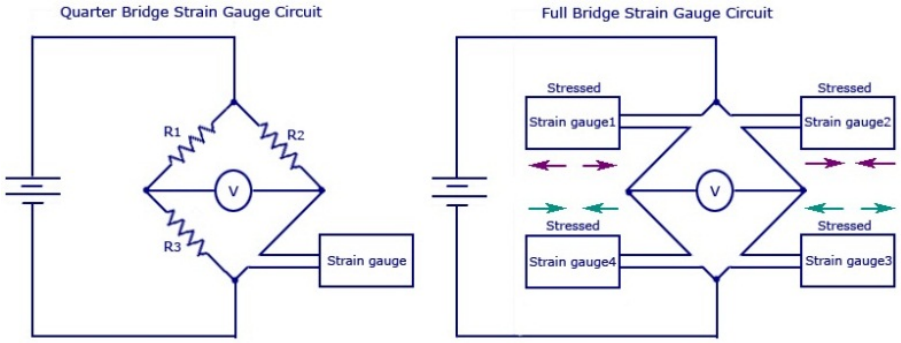

Figure 3.13. Different type Strain gauges (Instrumentation Today, 2015)

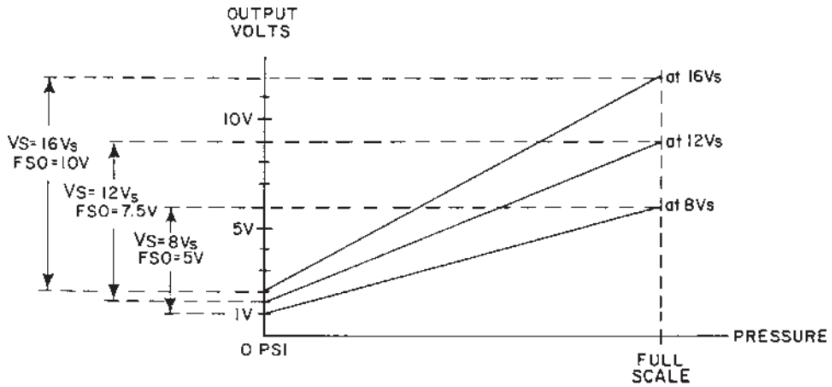

Figure 3.14. Relation of output voltage and pressure of the used pressure transducer (Honeywell, 2001).

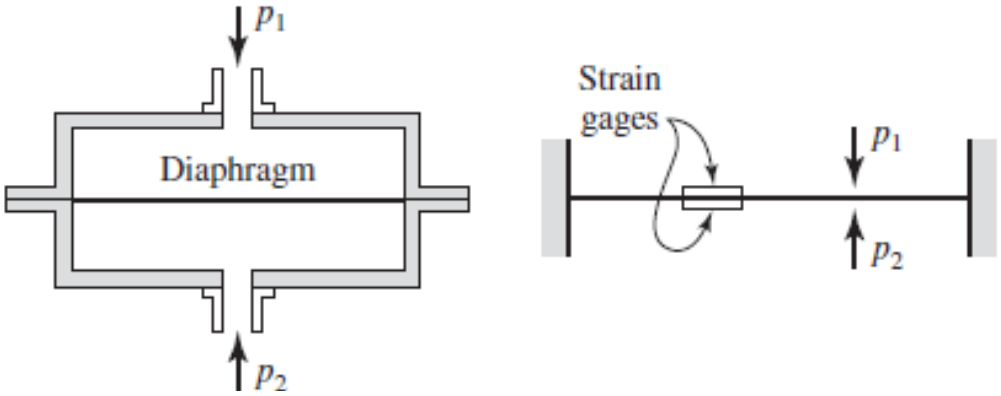

Figure 3.15. Schematic of differential pressure gage with diaphragm and with diaphragm (Holman, 2011).

3.4.4. Surface Oil Visualization

Surface oil visualization is qualitative technique to observe boundary layer transition, separation regions, surface flow direction, shock wave location and whether the flow is laminar or not. (Curry et al., 1983). In this technique a mixture is prepared and this mixture is applied to surface into flow direction while the tunnel is off, then the tunnel is operated until the applied mixture is dries then flow pattern can be recorded by a camera.

The mixture contains oil, pigment matter and extra additives to against dispersion (and pelletizing). Kerosene, light diesel oil, light transformer oil can be used and if the velocity is low, additives which reduces viscosity of the mixtures such as alcohol can be added also) titanium dioxide, china clay, lampblack can be used as pigment and against oleic acid can be used (Merzkirch, 1987). Fluorescent dye can be used if the ultraviolet illumination is provided. The inertia forces of the mixture should be lower than the viscous and surface tension forces in order to not affect the flow events on the surface (Genç et al., 2012b). Some examples of surface oil visualization is presented in figure 3.16 and 3.17.

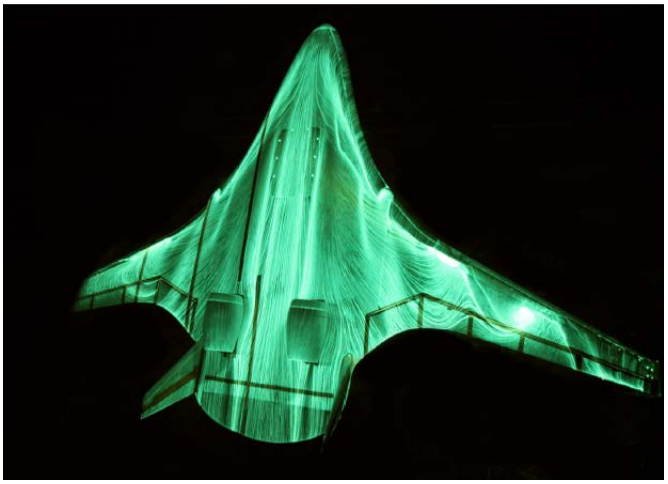

Figure 3.16. Oil visualization over surface of a delta wing with fluorescent oil under UV illumination (Gatlin et al. 2012).

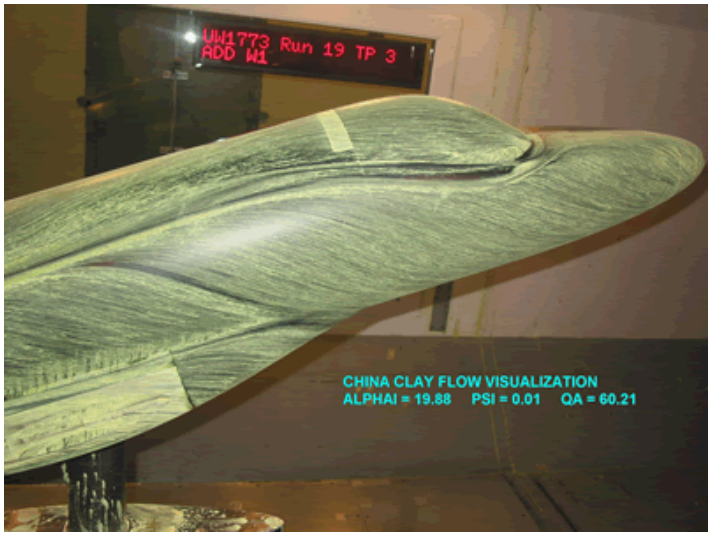

Figure 3.17. Oil visualization with China clay (UWAL, 2015).

3.4.5. Dye Visualization Experiments

Dye visualization is a qualitative method to observe flow pattern in the defined measurement plane. In the dye visualization technique a kind of dye is released to the water channel, released dye moves with the flow. Dye visualization technique in water channel is similar with smoke visualization with wind tunnel.

As dye, ink, food dye, rhodamine etc. can be used, dye mix with water and a solution is prepared and released to the flow by hoses furthermore if fluorescent dye

such as rhodamine is used a laser source is required for illumination in order to get higher quality observations. Figure 3.18 represents a dye visualization experiment.

Figure 3.18. Dye visualization of the wake of an oscillating fin (IHHR,2015).

3.4.6. Flow Topology

To analyze flow pattern topology of vortical flows is very crucial. In literature several works can be found such as Délery (1992, 2001, 2013), Tobak and Peake (1982).

Critical points in a plane are shown in figure 3.19. Types of critical points are determined with respect to eigenvalues of skin friction line equation. If the two eigenvalues are real and have the same sign, the singular point is a node. If the eigenvalues are distinct, the singular point is attachment node. If both of the eigenvalues are equal, the single point is isotropic node. If the eigenvalues are real and opposite signs singular point is a saddle point in which two trajectories go through the singular point and other trajectories form hyperbolic shape. If the eigenvalues are complex conjugates, the singular point is a focus. If p is zero for positive q, the critical point is center. Right side of the Figure 3.19 represents separation and left side of the figure represents attachment (Délery, 2001). Figure 3.20 represents surface flow pattern of a delta wing and flow pattern near the apex of the delta wing.

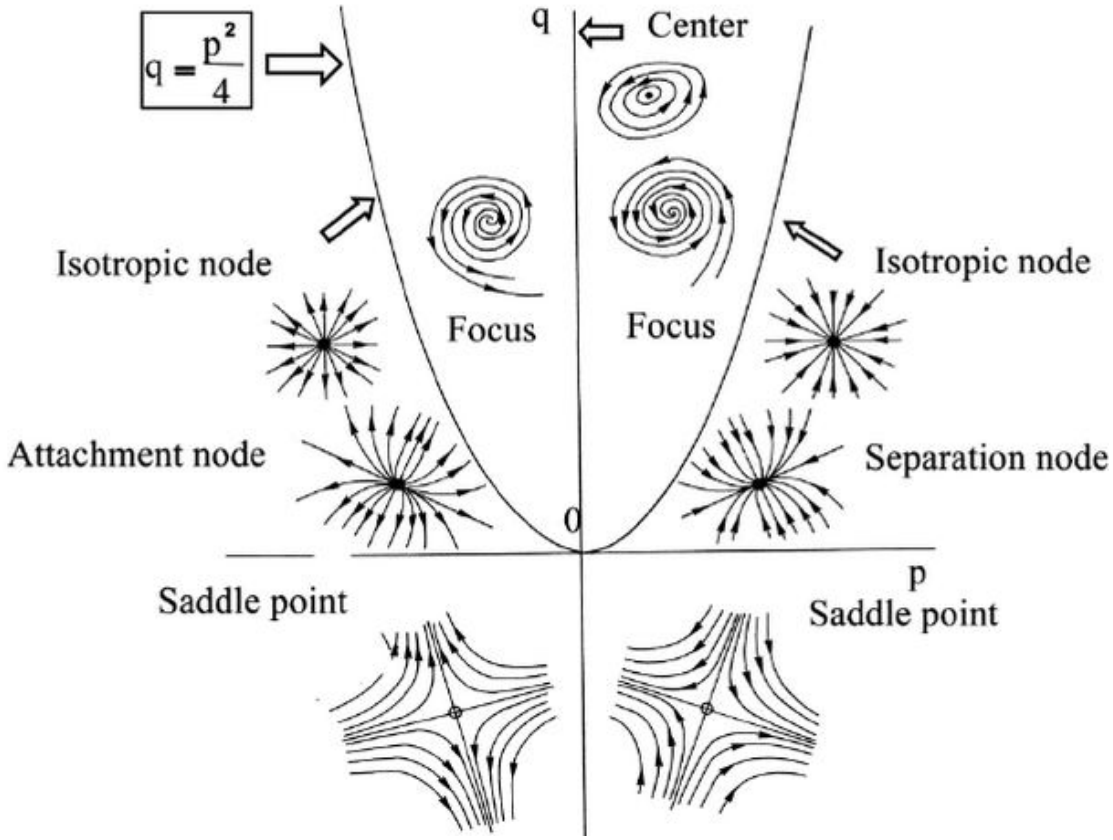

Figure 3.19. Critical points (Délery 2001)

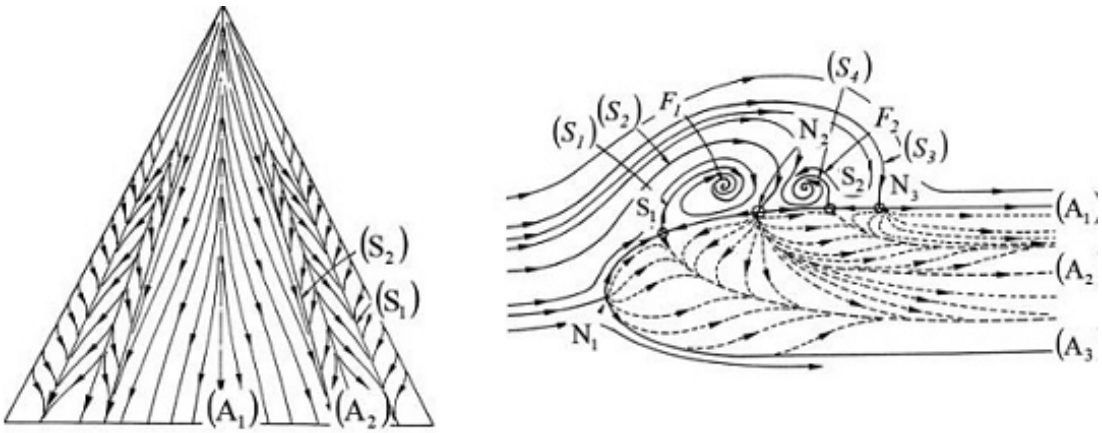

Figure 3.20. Surface flow pattern of a delta wing and flow pattern near the apex of the delta wing.(Délery, 2013)

3.5. Experimental Setup

3.5.1. Dye Visualization Experiments

The depth of the water was kept constant at 53 cm during all dye experiments, the pump frequency was kept at 20 Hz, and corresponding free-stream velocity was 80 mm /s. The delta wing with sweep angle, $\Lambda=70°$ made of plexiglass has a chord of 25 mm, 6 mm thickness and leading edges were bevelled 45°. There are 3 dye release points both side of the leading edges which were placed at 5%, 30% and 55% of the chord length. Temperature of the water, T inside channel was 22 C°, Reynolds number based on the delta wing chord was Re=20,000 as explained by Karasu et al. 2015.

Experiments were performed in both plan and side view planes, the laser sheet was passed from the center of leading edge vortex for side-view visualization; it was located parallel to surface of the delta wing for plan-view, but, in the case of measurements in side-view plane, laser sheet was located perpendicular to the surface of delta wing as shown in figure 3.21. A Rhodamine type dye is used to observe flow patterns by releasing a specified amount of dye that shines under the laser light sheet passing through the defined flow field. Dyes were received from a small tank place almost 1 meter higher from the delta wing via plastic hoses and needles and amount of the dye to be released is set by means of apparatus on the hoses. Magnitudes of velocity of dyes released from six different locations are almost same with the flow velocity. SONY HD-SR1 video camera was used to capture video of the vortical flow patterns, instantaneous images were taken by means of software.

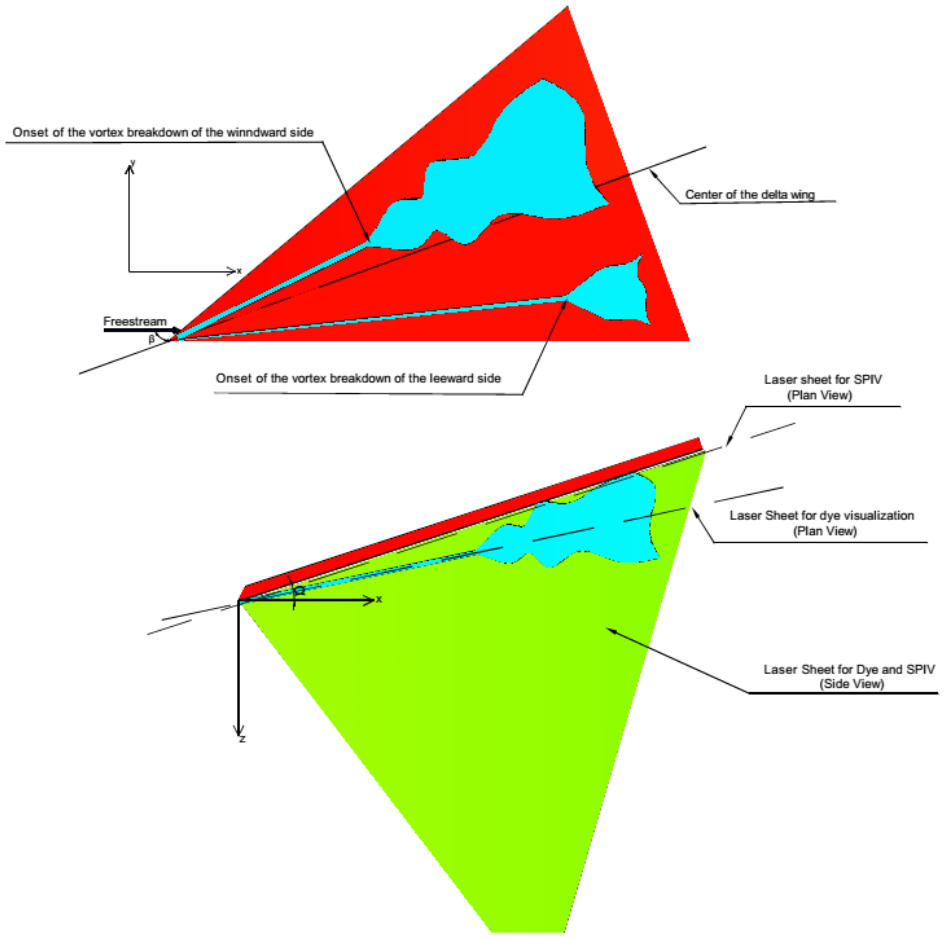

Figure 3.21. Schematic of the experimental set-up for dye visualization and Stereo PIV experiments for plan and side-view planes.

3.5.2. Stereo PIV Experiments

Images were acquired by 2 FlowSense 2M model CCD cameras equipped with 2 35 mm focal lenses. Silver coated hollow glass spheres with 10 µm diameter which is very close to buoyant were used for seeding. 12 double frame images per second acquired from both cameras. The measurement plane was illuminated by a double pulsed Nd:YAG laser has 120 mJ/pulse maximum energy output at 532 wavelength. Time between pulses was set as between 1750-5000 µs depending on flow structure. Thickness of the laser sheet in the measurement plane was almost 1.5 mm. The central axis of laser sheet is 1.25 mm far away from the surface of delta wing. Namely, the distance between laser light sheet and surface of the wing is 1.25 mm. The resolutions of the CCD cameras were 1176x1200 pixels. Dantec Dynamic

Studio 3.20 software was employed for acquiring images, synchronizing the system, getting adaptive and stereo correlations. Image processing were performed 32 x 32 pixel interrogation areas with 50 % to satisfy Nyquist criterion. 71x74= 5254 vectors were obtained for each image.

For the stereo PIV measurements a delta wing made of plexiglass has chord length of 17.7 cm, thickness of 6 mm and leading edges were bevelled 45°. Same aperture with the dye visualisation experiments to fix the delta wing in water channel. Free-stream velocity was kept at 120 mm/s and corresponding Reynolds number almost was $Re=20x10^3$. Since the size of field of view of cameras is not enough to capture whole area of the wing which is used in the dye visualization experiments, another delta wing having shorter chord length was used for velocity measurement using Stereo PIV. Before the stereo PIV experiments, vortex breakdown locations on this delta wing were observed by means of dye releasing and it was seen that the location of vortex breakdown was same for both delta wings.

Measurements in plan and side-view planes were conducted using a stereo PIV. For stereo PIV experiments; for the plan-view plane experiments angles of attack α=25°,30°,35°, and yaw angles β=0°,4°,8°,12°,16° and 20° were investigated. Due to the leeward side vortex breakdown takes place quite far from the measurement plane, only windward side vortex breakdown were investigated at angles of attack α=30°,35° and yaw angles of β=0°,4°,12° and 20°. Whereas laser sheet was oriented same with the dye visualization experiments in side-view plane by employing stereo PIV, for the plan-view plane experiments the laser sheet was oriented parallel to the delta wing and at a location 0.5 mm below the surface, then, measurements were performed at a location 1.25 mm below the delta wing.

In the present investigation 200 mm x 200 mm standard calibration target is used. This target has white background and black dots. Spacing between dots in both X and Y axis is 5 mm reference marker diameter is 2.7 mm and axis marker diameter 1.3. To be able to get appropriate light for the calibration, black curtains were used to block excess light. Direct linear transformation (DLT) method is used for the calibration via scanning laser sheet thickness with points; Z=0, Z=1, Z=-1. CCD cameras were located symmetrical to the measurement plane for the plan-view

experiments whereas they were located non-symmetrical to the measurement plane for the side-view experiments to prevent laser reflection. The uncertainty level of the velocity measurement is almost 2%. (Yayla, 2013). Figure 3.22 and 3.23 show experimental set-ups of stereo PIV in plan-view and side-view planes.

Figure 3.22. Experimental arrangement photo for plan-view stereo PIV experiments.

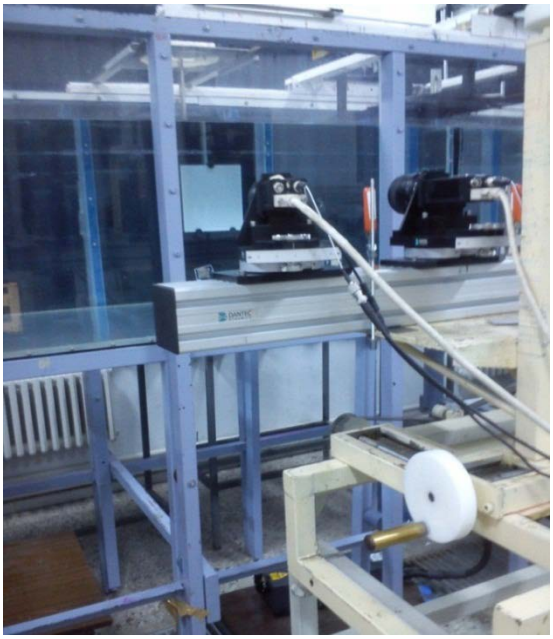

Figure 3.23. Experimental arrangement photo for side-view stereo PIV experiments.

3.5.3. Surface Pressure Measurements

For the pressure measurement a delta wing has chord length of 20 cm with 1 mm diameter 32 pressure taps on suction side. Pressure tabs locations shown in table 1. PVC hoses having 2.1 diameters inside the delta wing were used to transmit pressures to sensors. To minimize effect of the fixing apparatus on flow structures of delta wing, thin materials were used. Figure 3.24 shows locations of pressure taps over the surface of the delta wing and figure 3.25 shows the delta wing used for the pressure measurement experiments.

x/c	y/s								
0.2	-0.43			0			0.43		
0.3	-0.62		-0.31		0		0.31		0.62
0.5	-0.77	-0.51		-0.25		0	0.25	-0.51	0.77
0.7	-0.84	-0.63	-0.42		-0.21	0	0.21	0.42	0.63	0.84
0.9	-0.87	-0.70		-0.53		-0.35	0.35	0.53	0.70	0.87

Figure 3.24. Locations of the pressure taps over the delta wing.

Figure 3.25. The delta wing used for pressure measurement.

Pressure measurement system contains 32 pressure taps, a terminal board, an AD DAQ card, a Pitot tube, a digital manometer, a leakage free bottle and a hand pump. Differential type Honeywell 163PC01D75 pressure transducers were used to measure pressures over the surface of delta wing. Static pressure of the free-stream was received from static port of the Kimo TPL-03–300 Pitot tube located far from the delta wing.

By means of the software output voltage was converted to pressure values and instantaneous pressure values were saved. Calibration process was performed by means of calibrator system which includes, a hand-pump, leakage free a bottle and a CEM DT-8920 manometer. Minimum and maximum values of the pressure were set via hand pump and entered to house-made software which receives voltage values from the transducers and converts voltage values to pressure values. In order to calculate properties of the air in terms of pressure, humidity, temperature and altitude of the environment a house made software was used. Data of pressures, humidity and temperature were taken from the State Meteorological Service located almost 2 km away from the laboratory.

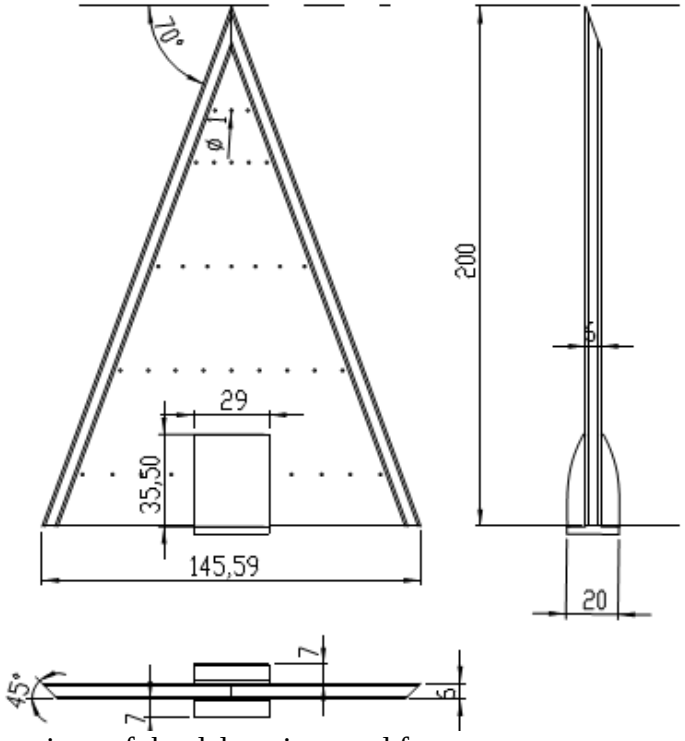

Figure 3.26. Dimensions of the delta wing used for pressure measurement.

Free-stream velocity was measured as U, 9.20 m/s and the corresponding Reynolds number was almost $10x10^4$. Uncertainty of this Reynolds number, Re is almost %.5.5 and the uncertainty of the pressure coefficient C_P is nearly 5% (Genç et al., 2012a).

After the calibration, pressure measurements are conducted for one minute and experiments were repeated by three runs 500 values are collected per second. To get dimensionless value pressure coefficients formula two is used and all results were presented as $-C_p$ to determine pressure coefficient.

$$C_p = \frac{\Delta P}{\frac{1}{2}\rho U^2}$$

ΔP is the difference of pressure of the corresponding pressure tapping and static pressure of the free-stream, ρ is the density of the air, U is the free-stream velocity. Dry air density was used to taking into account, atmospheric pressure, humidity and temperature of the environment. Velocity was calculated from pressure difference of total pressure and static pressure using dynamic pressure formula; after calculating density of the air, required velocity was determined then frequency of the tunnel of the was set until reaching required pressure differences from manometer and Pitot tube system. Static pressure of the air comes from static port of the Pitot-static tube located far from the delta wing.

Blockage ratio (BR) can be defined as frontal area of the delta wing to frontal area of the wind tunnel. Figure 3.26 shows 3 views of the delta wing in the wind tunnel.

$$BR = \frac{A_w}{A_T}$$

For the frontal view, maximum length in y direction is span of the delta wing 145.59 mm, for the maximum length z direction is 116.19 mm and frontal lengths of the tunnel are 500 mm as shown figure 3.27. The maximum blockage ratio without yaw is 6.76 %.

Since maximum blockage ratio is below than 10 %, blockage correction was not required, but when the delta wing was yawed since leading edge came closer to the side walls of the wind tunnel, the delta wing and apparatus were moved to the

opposite direction of the yaw using channels on wind tunnel to reduce walls on the flow structure of delta wing.

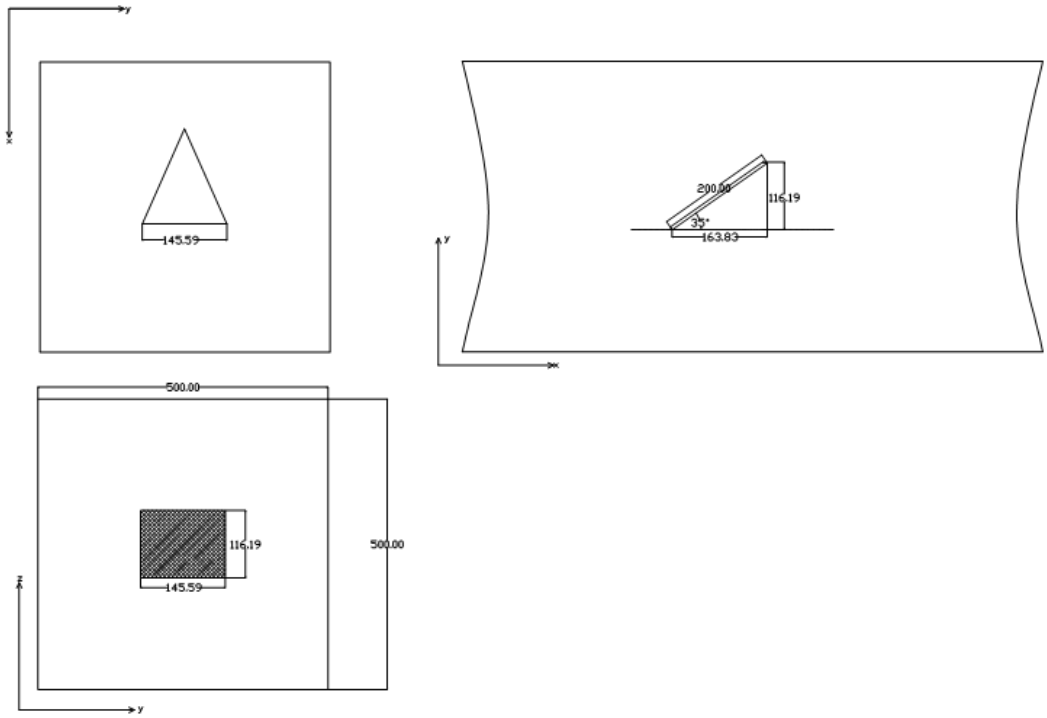

Figure 3.27. Dimensions of the delta wing inside the wind tunnel.

Figure 3.29 and 3.30 show the apparatus used for the wind tunnel experiments. Angle of attack, α was set by means of Stanley ST142919 water level and yaw angle, α was set with the apparatus. Figure 3.31 represents experimental set-up of the pressure measurement system.

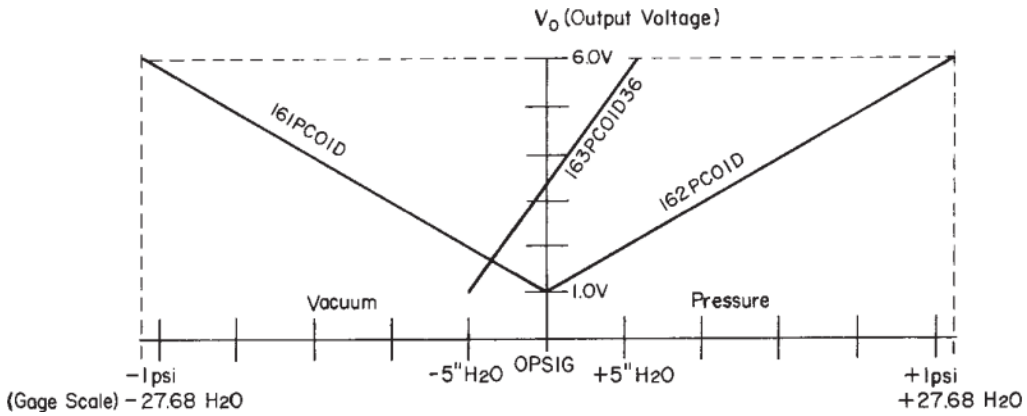

Figure 3.28. Output voltage variation with pressure (Honeywell, 2011).

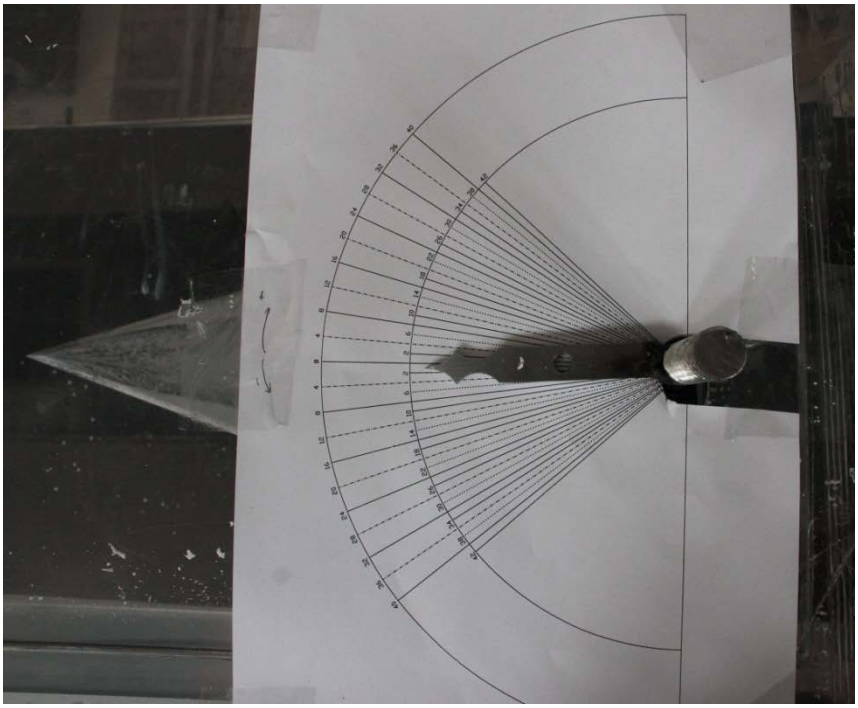

Figure 3.29. Top view of angle wind tunnel apparatus.

Figure 3.30. Channel on wind tunnel to move the delta wing to protect from wind tunnel wall's interference.

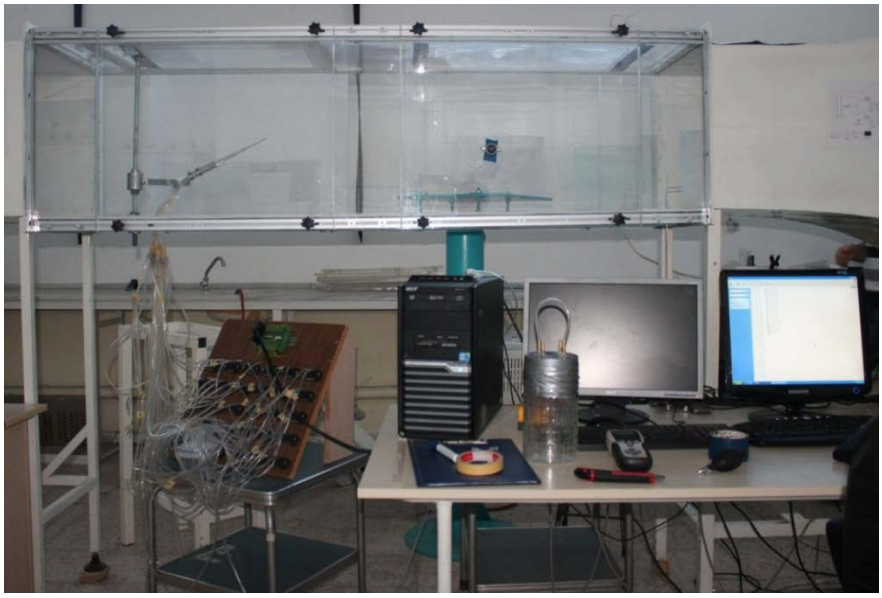

Figure 3.31. Image of the experimental set-up of the pressure experiments.

3.5.4. Oil Surface Visualization Experiments

For oil visualization experiment all experimental conditions were same, a delta wing having 20 cm chord length without pressure tabs were used. In the present investigation, gasoline-titanium dioxide-oleic acid mixture was applied to surface of the delta wing to observe flow pattern on the surface. The mixture was applied via in direction of the free-stream via a brush. Since magnitude of the velocity changed with angle of attack, α and yaw angle, β concentration of the mixture is changed; especially for higher yaw angle, β the diluted mixture were applied to allow flow to move with flow. Angle of attack, α was set by means of Stanley ST142919 water level and yaw angle, β was set with the apparatus. Experiments were conducted in the same conditions for the surface pressure measurements.

3.6. Aim of the Study

During a maneuvering, aircrafts are subjected to the crosswinds. Similarly, giving a yaw angle to the delta wing in the wind tunnel experiment free-stream flow

direction is not parallel to the central cord axis of the wing. That is to say, under high yaw angles delta wing is under effect of crosswinds causing nonsymmetrical flow structures over the wing surface.

In the present study, effect of yaw angle, β on the behavior of vortex breakdown and vortical flow structure over a slender delta wing is investigated via 4 different experimental techniques. Effects of yaw angle, β are observed in detail in order to understand yaw maneuver capability of a slender wing at a low Reynolds number, Re. The significance of this study is that the different experimental techniques are applied so as to understand in detail the effects of yaw angle, β on the aerodynamics of slender delta wings and offer control techniques.

4. RESULTS AND DISCUSSION

4.1. Dye Visualization

In this section, the dye visualization experiments in plan-view and side-view were performed at the Reynolds number, Re= 20.000. In terms of the dye visualization experiments; vortex breakdown locations, trajectories of the leading edge vortices, interactions of the leading edge vortices and interaction of leading edge vortices ad surface of the delta wing were observed.

Figures 4.2-4.4 represent variation of leading edge vortices structures with yaw angles β, at angles of attack 25°, 30° and 35° from plan-view plane. Blue lines representing dimensionless chord are placed with 0.1 x/c interval. These images are acquired from video records after careful observation, because vortex breakdown locations are not stationary. Maximum, minimum and mean locations of the vortex breakdown are determined observing these video records. In addition to vortex breakdown locations, interaction of the leading edge vortices and trajectories of the leading edge vortices were examined as well.

At 0° yaw angle β, pair of symmetrical leading edge vortices are observed. Vortex breakdown locations are not stationary, oscillations on the vortex breakdown location are observed as shown figure 4.1. Observations reveal that leading edge vortices do not breakdown simultaneously, one of them breakdown earlier than the other but breakdown location interchange and mean location of the vortex breakdown almost symmetrical at 0° yaw angle, β. When the yaw angle, β is constant at 0°, vortex breakdown location of the leading edge vortices moved toward to apex of the delta wing with increasing angle of attack, α.

At constant angle of attack α, when the delta wing is yawed gradually, observations reveal that while the vortex breakdown location of windward side comes near the apex of the delta wing, leeward side vortex breakdown moves further than the β=0° circumstance. Since the leeward side vortex breakdown location moves out of the visualization plane, only windward side of the vortex breakdown location is examined. When delta wing is yawed vortex breakdown locations of the windward

side move toward to apex gradually. Generally speaking, nonlinear decrease of windward side vortex breakdown with increasing yaw angle is observed. Figure 4.5 demonstrates vortex breakdown location as a function of yaw angle. For angle of attack α=25°, mean windward side vortex breakdown locations take place x/c=1 and x/c 0.5 at 0° and 20° yaw angle β respectively. At 30° angle of attack α, mean vortex breakdown locations take place x/c=0.8 and x/c= 0.35 for 0° and 20° yaw angle, β respectively and for 35° angle of attack, α, vortex breakdown occurred x/c 0.55 and 0.1 at 0° and 20° yaw angle, β respectively.

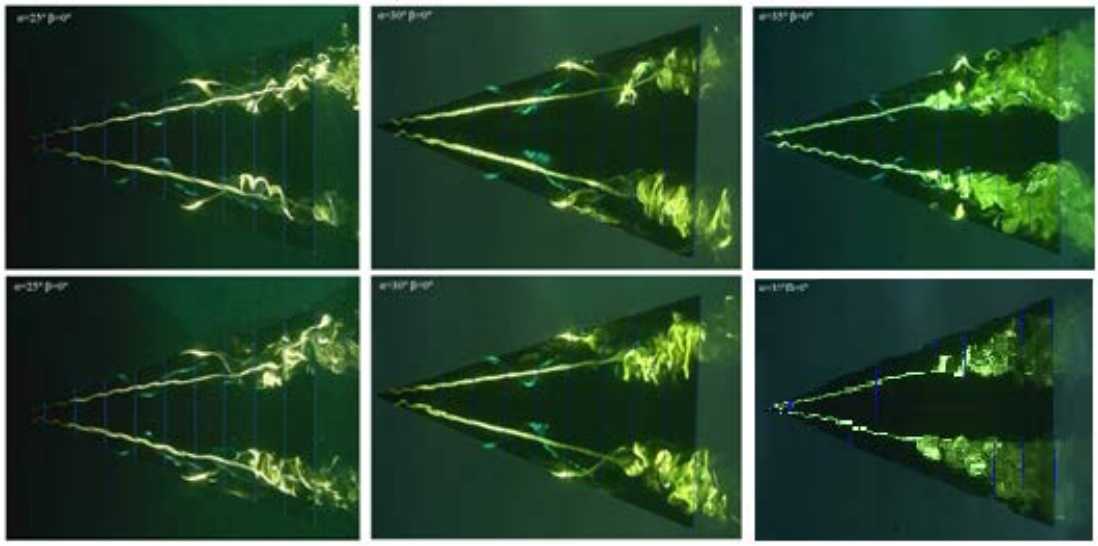

Figure 4.1. Dye visualization images showing maximum and minimum vortex breakdown locations at 0° yaw angle, β.

As shown figures, yaw angle, β has great influence on the trajectories of both leading edge vortices and this influence is much stronger on the leeward side leading edge vortex. With increasing yaw angle leeward side vortex moves toward to the leading edge and gets almost parallel to the leading edge while windward side vortex moves toward to the center of the delta wing.

Plan-view experiments reveal interactions of the leading edge vortices also. Interaction regions are not stationary just as vortex breakdown locations; figure 4.6 which include instantaneous images demonstrate vortex interactions. Experiments

reveal that the windward side vortex coil leeward side vortex moreover vortex interactions lead leeward side vortex to oscillate in streamwise direction.

As can be seen in figures disorganised windward side vortex covers the great portion of the surface of the delta wing which may lead decrease aerodynamic performance since low velocity caused less pressure distribution.

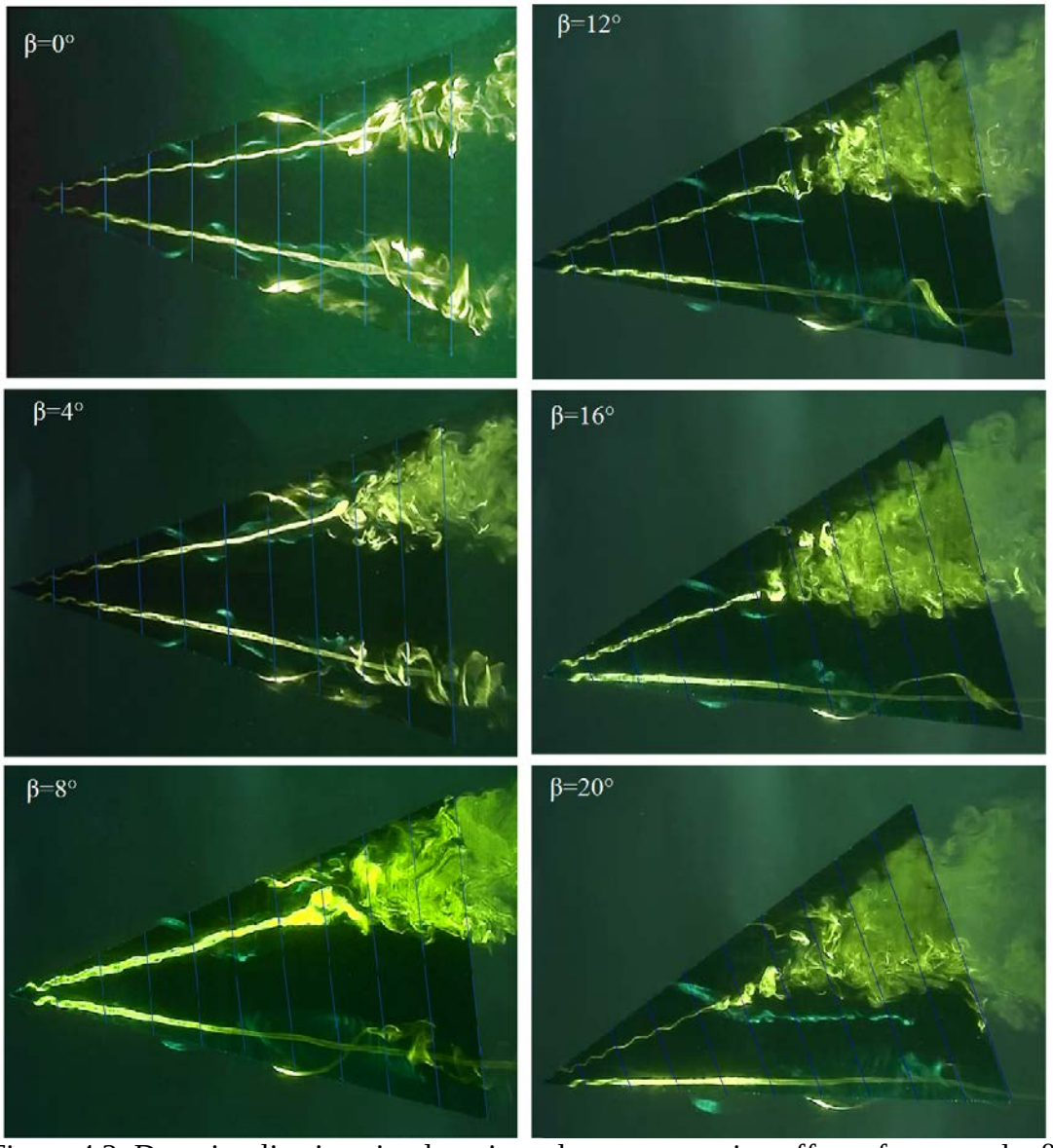

Figure 4.2. Dye visualizations in plan-view plane representing effect of yaw angle, β on vortical flow structure at angle of attack, α= 25° and yaw angles within the range of $0 \leq \beta \leq 20$.

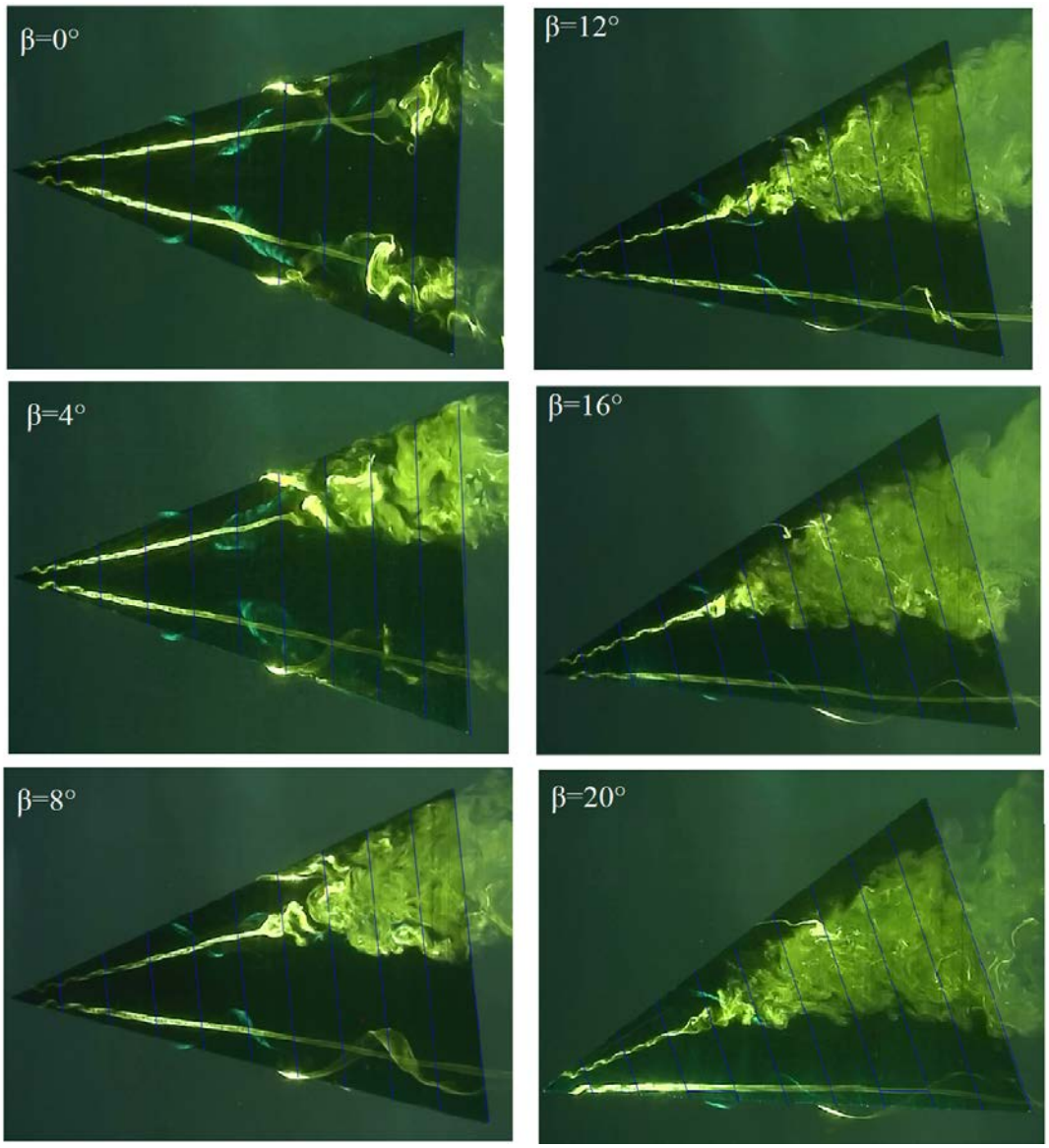

Figure 4.3. Dye visualizations in plan-view plane representing effect of yaw angle, β on vortical flow structure at angle of attack, α= 30° and yaw angles within the range of $0 \leq \beta \leq 20$.

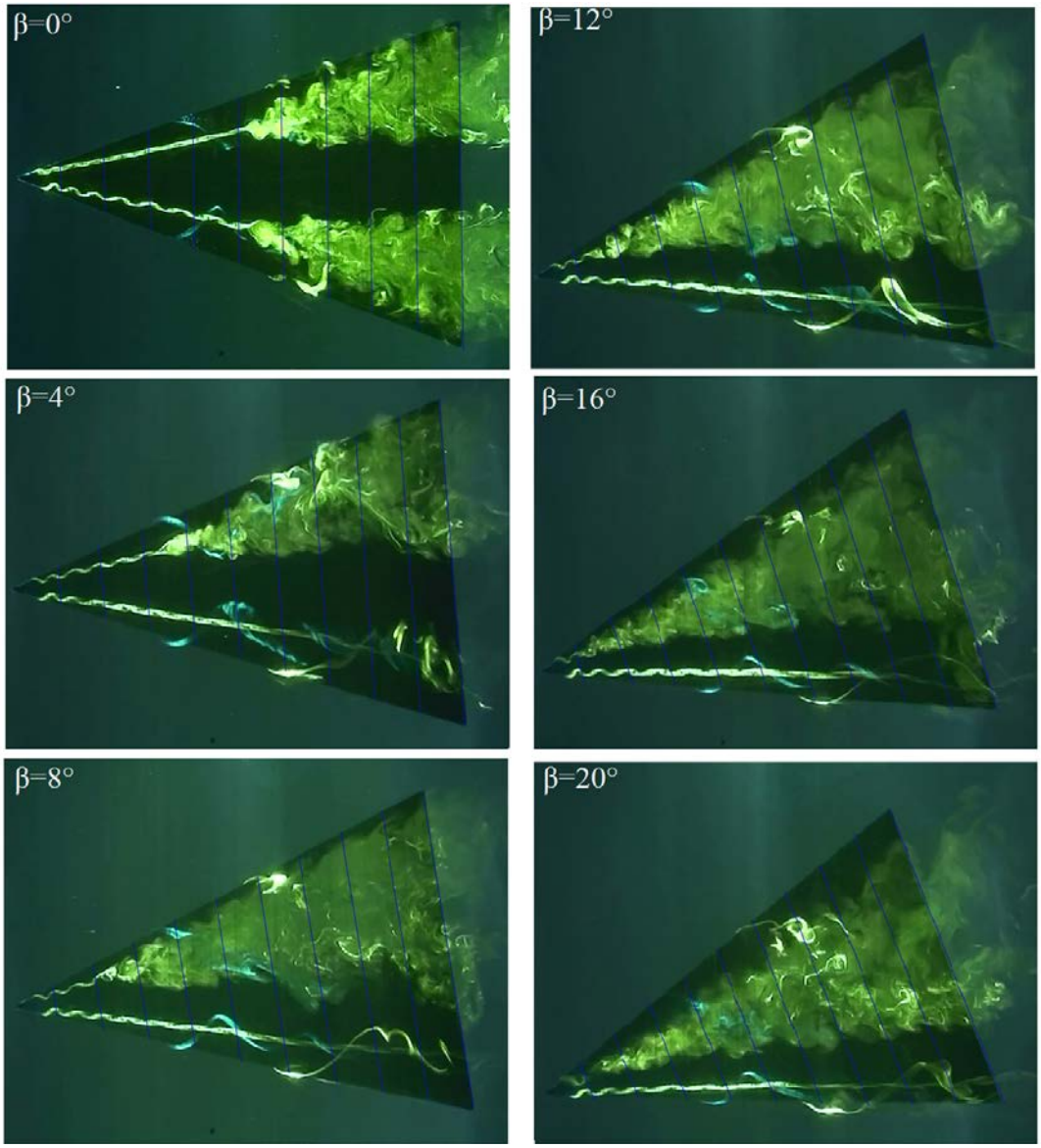

Figure 4.4. Dye visualizations in plan-view plane representing effect of yaw angle, β on vortical flow structure at angle of attack, α= 35° and yaw angles within the range of $0 \leq \beta \leq 20$.

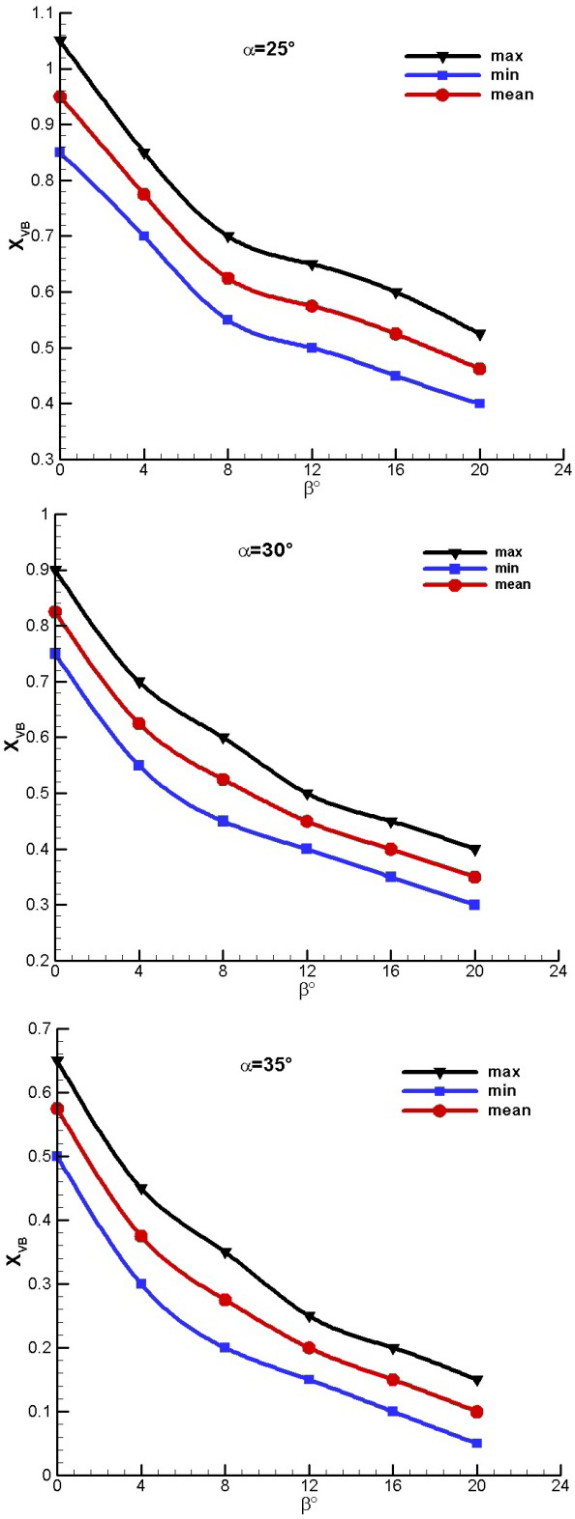

Figure 4.5. Vortex breakdown locations of windward side as a function of angle of attack α and yaw angle, β.

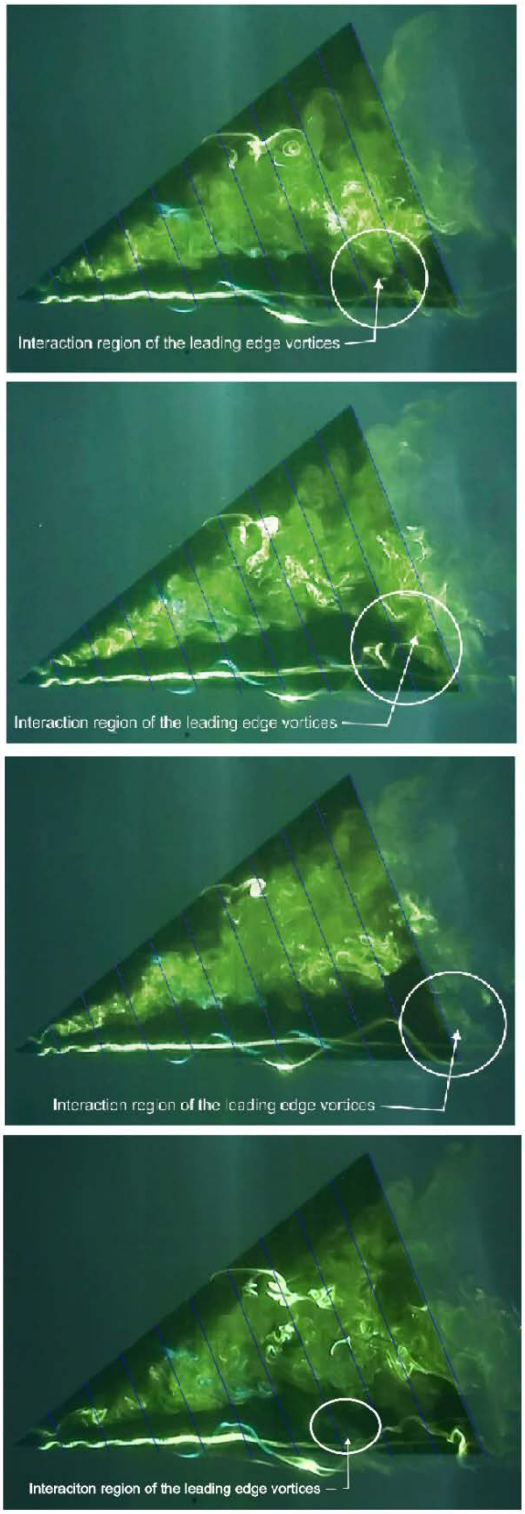

Figure 4.6. Leading edge vortices interaction regions at angle of attack α=35° and yaw angle β=20°.

Figure 4.7 shows the structures of the windward side leading edge vortices in side-view plane. As shown figures yaw angle has significant effects on the flow

structures in side-view plane. In this plane with increasing yaw angle, larger scale Kelvin-Helmholtz vortex structures take place and interactions of the leading edge vortex and the delta wing surface is observed moreover the interactions is increased with the yaw angle.

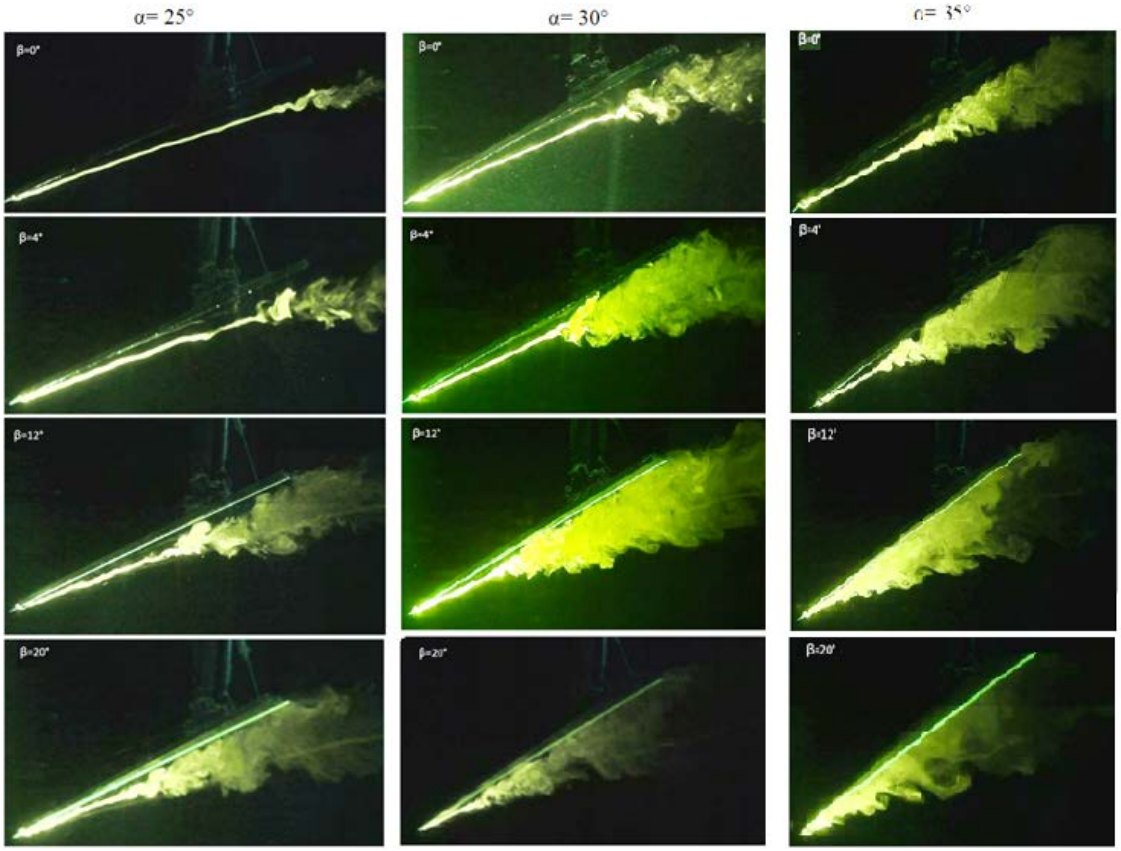

Figure 4.7. Dye visualizations in side-view plane representing effect of yaw angle, β flow structure at angle of attack within range of 25°≤α≤35° and yaw angles within the range of 0°≤β≤20°.

4.2. Surface Oil Visualization

Surface oil visualization experiments were performed at angles of attack with the range of $25° \leq \alpha \leq 35°$ and yaw angles with the range of $0° \leq \beta \leq 20°$ at the Reynolds number, $Re=10x10^4$. Surface oil visualization experiments reveal clearly formation of the leading edge vortices at a lower yaw angles, β. Figure 4.8 shows an example of oil visualization experiment.

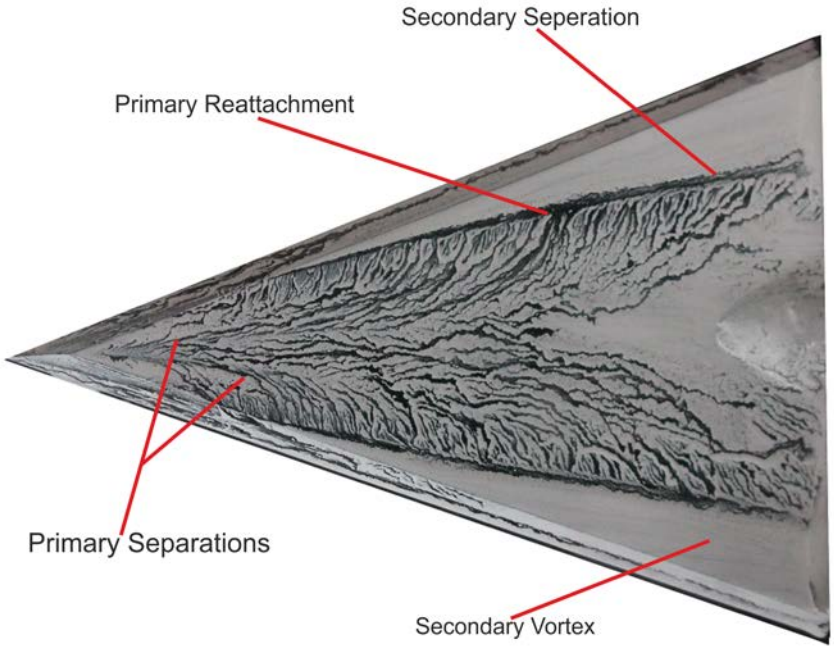

Figure 4.8. Flow patterns on the surface of the delta wing obtained oil surface visualization experiments.

Surface oil visualizations reveal that while reattachment points form a line at $\beta=0°$, with yaw angle they form a curve. Primary reattachment points come closer toward to center of the delta wing. At higher yaw angles β, flow cannot sweep oil mixture on the surface of the delta wing, because of low velocity of the delta wing. In the recirculation area momentum of the flow is not capable of sweeping the mixture however different diluted mixture was applied to the surface of the delta wing. If one examines separation and reattachment points of the leeward side leading edge vortices, with increasing yaw angle leeward side leading edge vortex both separation and reattachment points move toward to the leading edge moreover size of

the primary leading edge on leeward decrease. Furthermore visualizations reveal at higher yaw angles β, secondary vortices of the leeward side start to shrink and finally diminish. Figure 4.9 shows leeward side leading edge vortices at angle of attack, α=35° and yaw angles β=0° and β=12°. Figures 10-12 represent oil visualization experiment results.

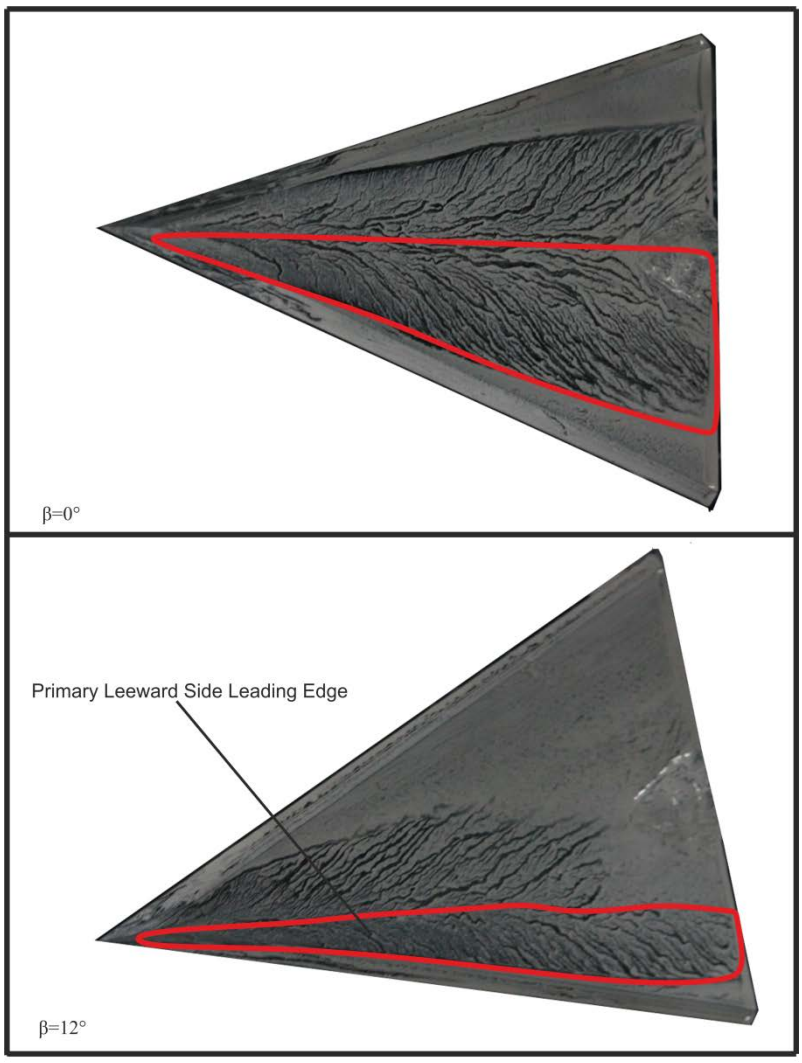

Figure 4.9. Leeward side leading edge vortices at angle of attack, α=35° and yaw angles β=0° and β=12°.

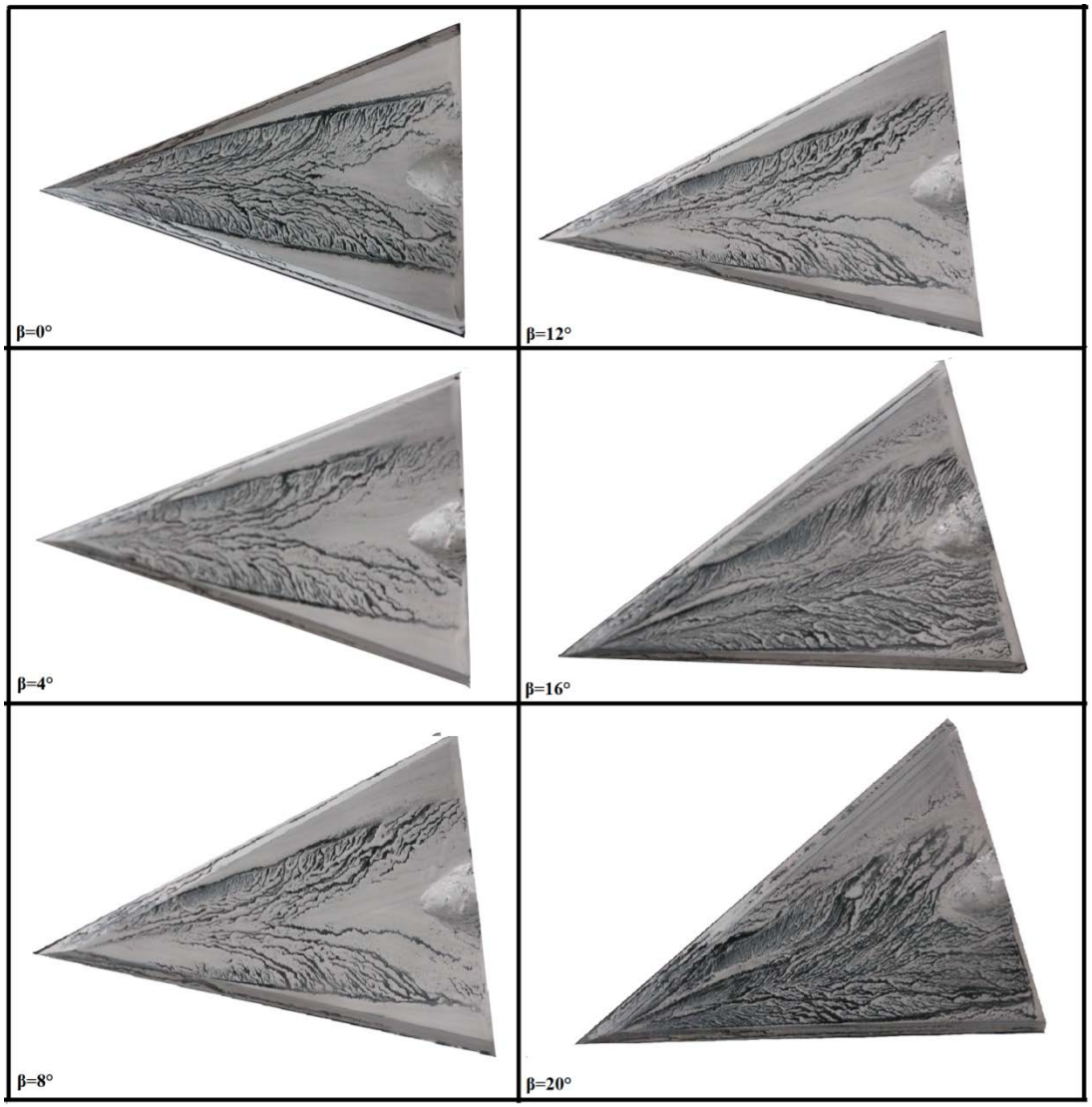

Figure 4.10. Surface oil visualization of the delta wing at angle of attack α=25° and yaw angle within range of $0° \leq \beta \leq 20°$.

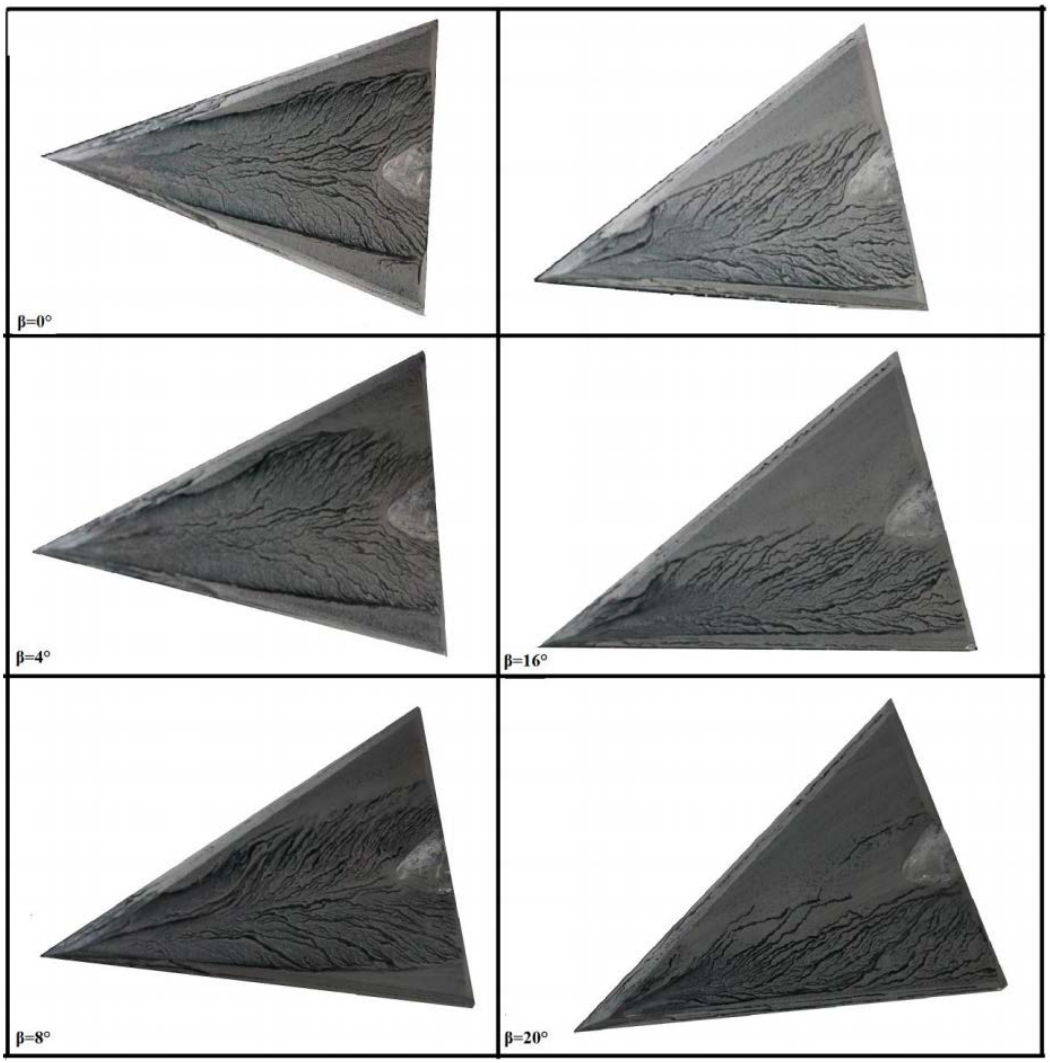

Figure 4.11. Surface oil visualization of the delta wing at angle of attack α=30° and yaw angle within range of $0° \leq \beta \leq 20°$.

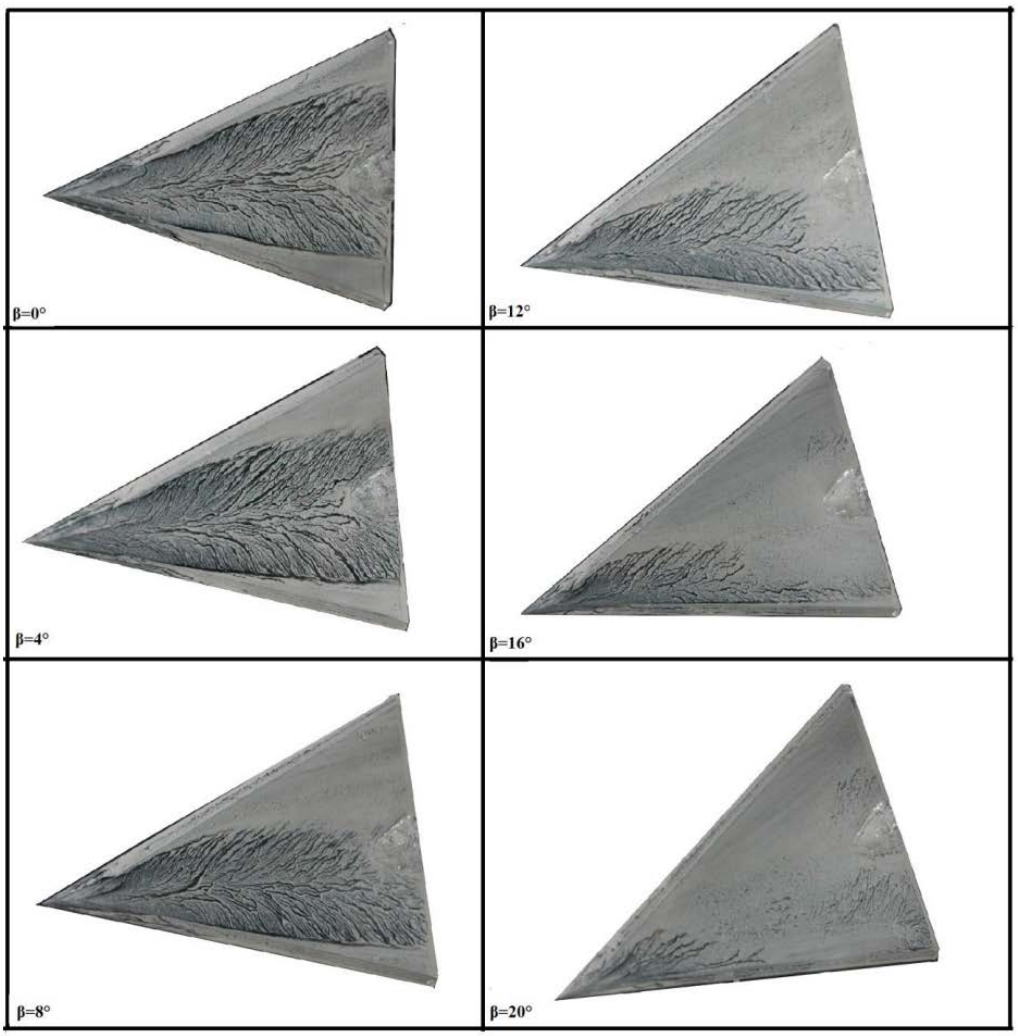

Figure 4.12. Surface oil visualization of the delta wing at angle of attack α=35° and yaw angle within range of 0°≤β≤20°.

4.3. Stereo PIV Experiments

4.3.1. Plan-View Plane Experiments

Near surface topology of the vortical flow over the surface of delta wing was experimentally examined in plan-view plane. In these experiments, angles of attack were taken as α=25°, 30° and 35° and yaw angles were varied in the range of $0° \leq \beta \leq 20°$ with step of 4°. The laser sheet which had 1.5 mm thickness was positioned at a plane 0.5 mm below the surface of the delta wing, that is to say, measurements were conducted at a plane which was 1.25 mm below from the delta wing surface.

In this section time-averaged vector, streamline, vorticity, u and v velocity components, velocity fluctuations, Reynolds stresses and turbulence kinetic energy values were examined.

4.3.1.1. Time-Averaged Vector, Streamline and Vorticity

Figures 4.13-4.15 represent time-averaged vectors <V> for angles of attack such as α=25°, 30° and 35 and yaw angles in the range of $0° \leq \beta \leq 20°$. At yaw angle, β=0° a pair of primary vortex V_p, and secondary vortex V_s which has smaller velocity vectors <V> are clearly visible. Secondary vortices, V_s start to diminish with increasing yaw angle, β on leeward side. Furthermore, since windward side has lower velocity vectors in this region it is hard to identify secondary vortices from time-averaged velocity vectors, <V>.

Figures 4.16-4.18 demonstrate time-averaged streamlines, <Ψ>. For angle of attack, α=25°, effect of yaw angle, β on time-averaged streamlines, <Ψ> is inherit but any important critical points could not be detected. Shape of streamlines are changed dramatically as a function of yaw angle, β especially on leeward the yaw angle, β is more dominant. Curvature and trajectories of the streamlines decreases with varying yaw angle, β, less curvature pattern is seen at higher yaw angles, β.

At 30° angle of attack up to 12° yaw angle, β any important critical points take place and same patterns are seen for angle of attack of α=25°. At yaw angle β=12° a foci F and bifurcation line L_0 downstream of this F on leeward side take place. When yaw angle, β is set at 16° the point of foci, F and bifurcation line L_0 take place in further upstream region comparing with β=12°, furthermore, a saddle point, S also appears after the bifurcation point, L_0 . At yaw angle, β=20° near the leading edge on leeward side bifurcation line, L_0, a saddle point, S, then the point of foci, F and finally second bifurcation line L_0 are seen. At angle of attack, α=35° up to 4° yaw angle, β important critical points do not occur. At yaw angle, β=8° and β=12° a bifurcation point L_0 takes place and flow starts to have more complex formation. At yaw angle, β=16° a bifurcation point, L_0 develops approximately at a location of x/c 0.3, a saddle point, S occurs at x/c 0.8 and also second bifurcation line, L_0 takes place at x/c 0.9. When yaw angle, β is set to 20° a point of foci, F appears at x/c 0.5 near centreline of the delta wing, a bifurcation line, L_0 near leading edge, a saddle point, S at x/c 0.8 and a bifurcation line L_0 take place. As can be seen from time-averaged streamline patterns, <Ψ> on windward side vortices form recirculation zone and spread over majority part of the delta wing surface while leeward side vortices move towards the leading edge and occupying smaller area. Time-averaged vector patterns, <V> and streamline patterns, < Ψ> demonstrate that attached flow near centreline of the delta wing moves towards the leeward side of the leading edge. These patterns also show the spreading of the windward leading edge vortices along the delta wing surface and interaction of the leading edge vortices.

Time-averaged vorticity, <ω> contours are demonstrated in figures 4.19-4.21. For easy comparison minimum and maximum values of the contours is set with the same numerical value for each angle of attack, α. When yaw angle is adjusted with β=0° three pairs vorticity is seen; outside vorticity O, main vorticity M and secondary vorticity S between O and M. When the delta wing is yawed these symmetrical patterns of flow change dramatically. At yaw angle, β=0° maximum vorticity $[<\omega>]_{max}$ takes place in outside vorticity O. With increasing yaw angle on windward side $[<\omega>]_{max}$ takes place around the apex of the delta wing, on leeward side $[<\omega>]_{max}$ takes place in outside of vorticity O. Especially on windward side, ,

vorticity magnitudes <ω> reach maximum value in the region close to the trailing edge since the flow orients towards the windward side as seen from streamline patterns . Streamline patterns demonstrate the spreading of the windward leading edge vortices along the delta wing surface and interactions take place between the leading edge vortices.

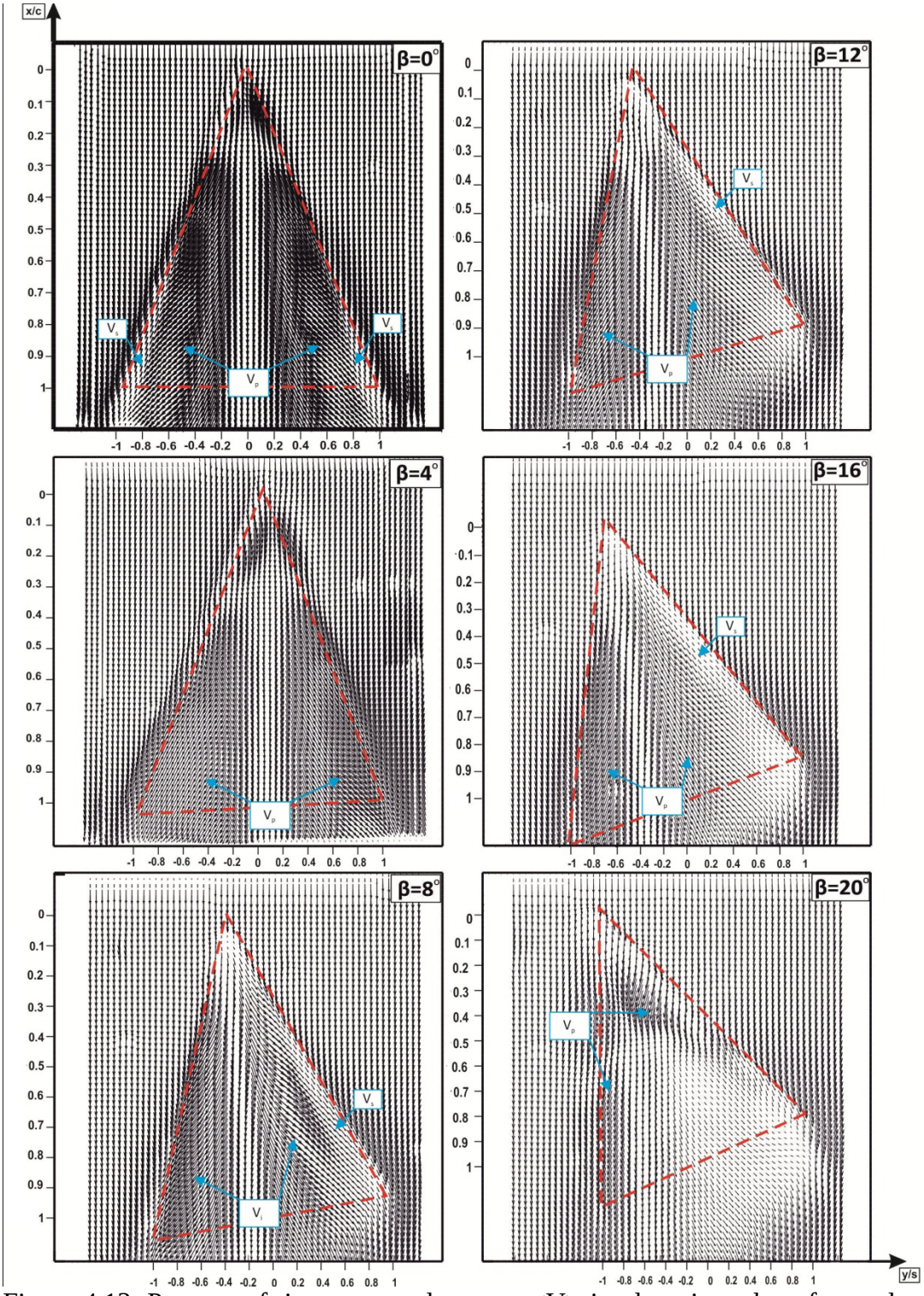

Figure 4.13. Patterns of time-averaged vectors <V> in plan-view plane for angle of attack α=25° and yaw angle within the range of $0° \leq \beta \leq 20°$.

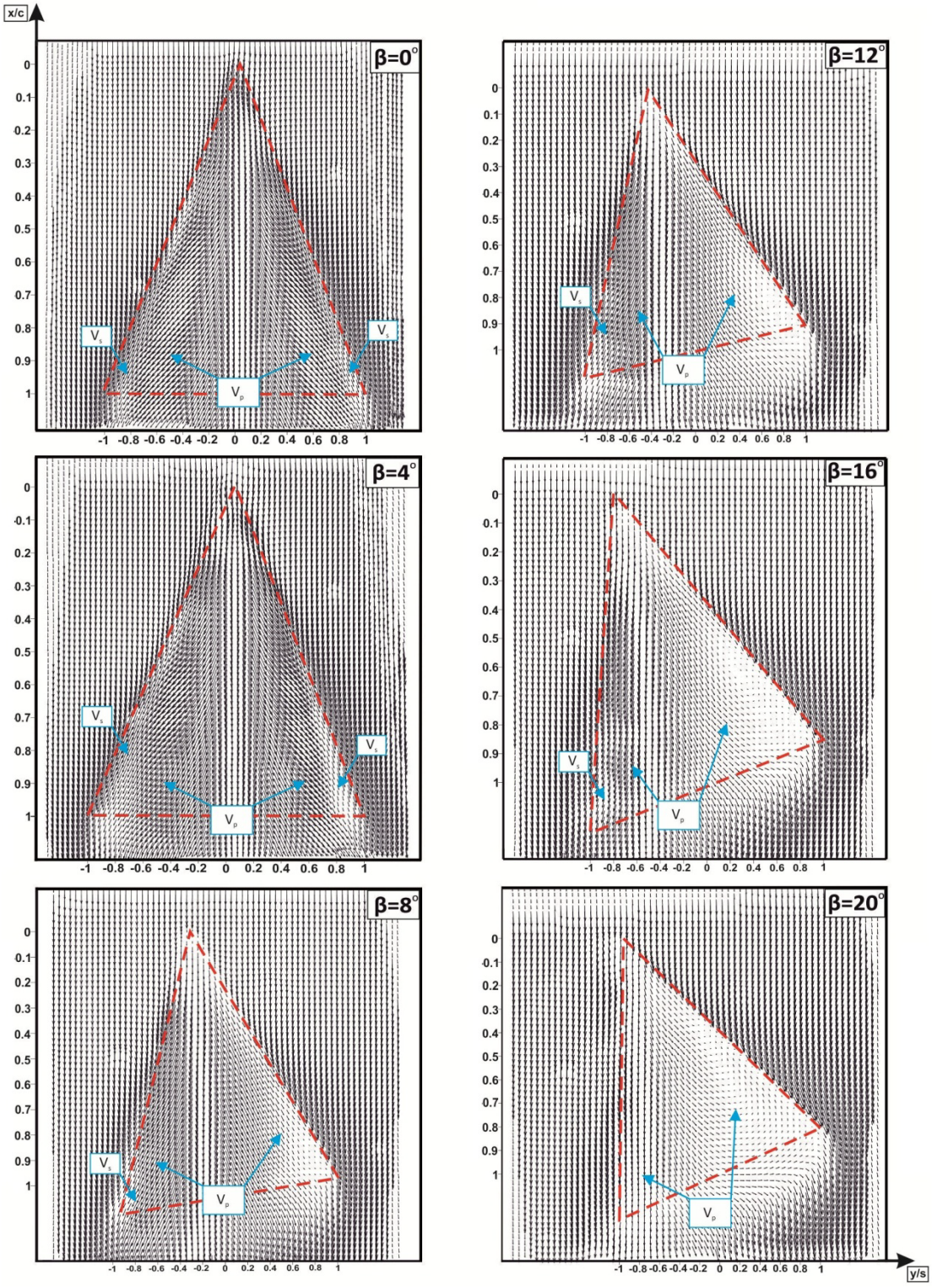

Figure 4.14. Patterns of time-avaraged vectors <V> in plan-view plane for angle of attack α=30° and yaw angle within the range of $0° \leq \beta \leq 20°$.

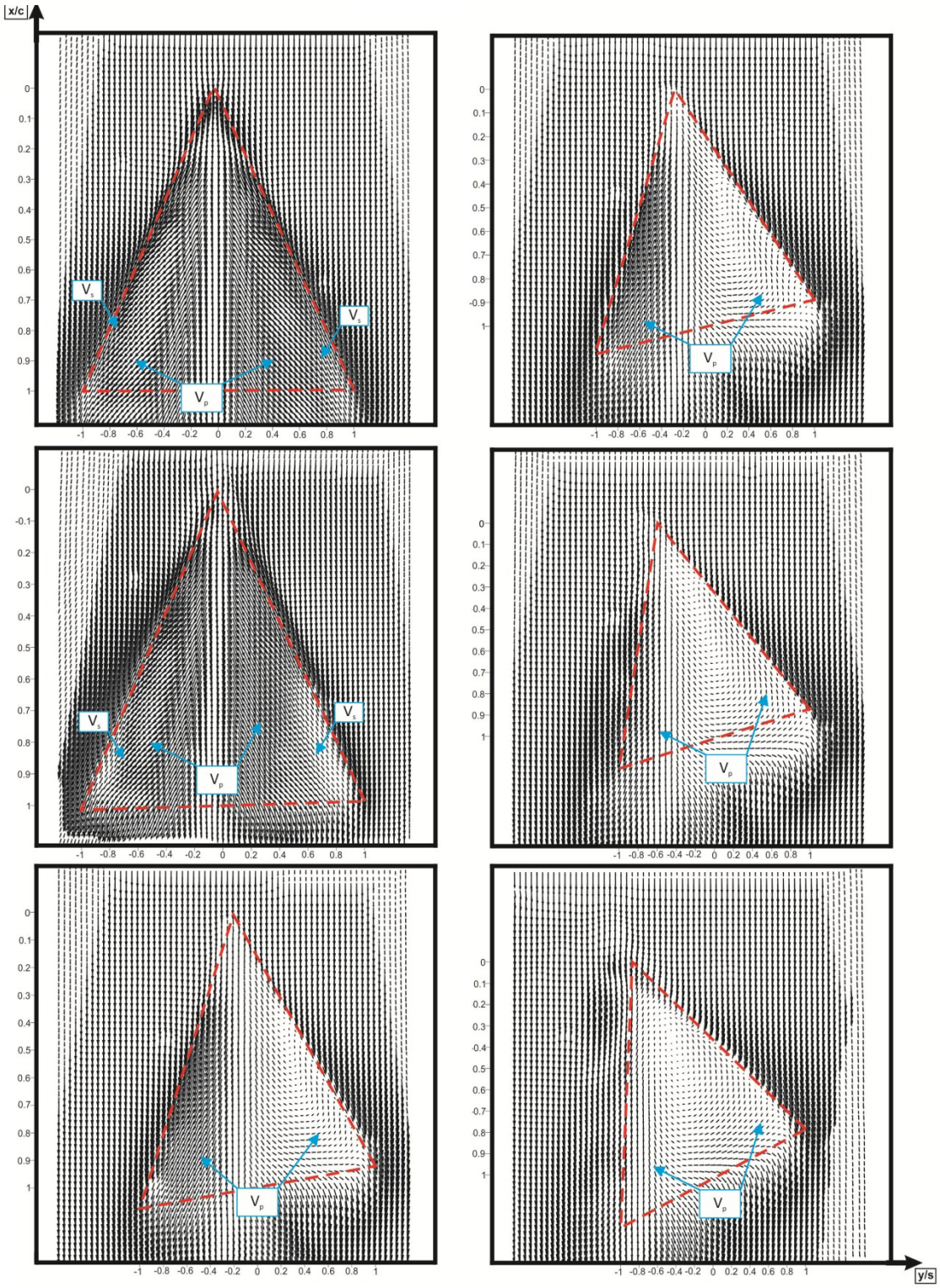

Figure 4.15. Patterns of time-averaged vectors <V> in plan-view plane for angle of attack α=35° and yaw angle within the range of $0° \leq \beta \leq 20°$.

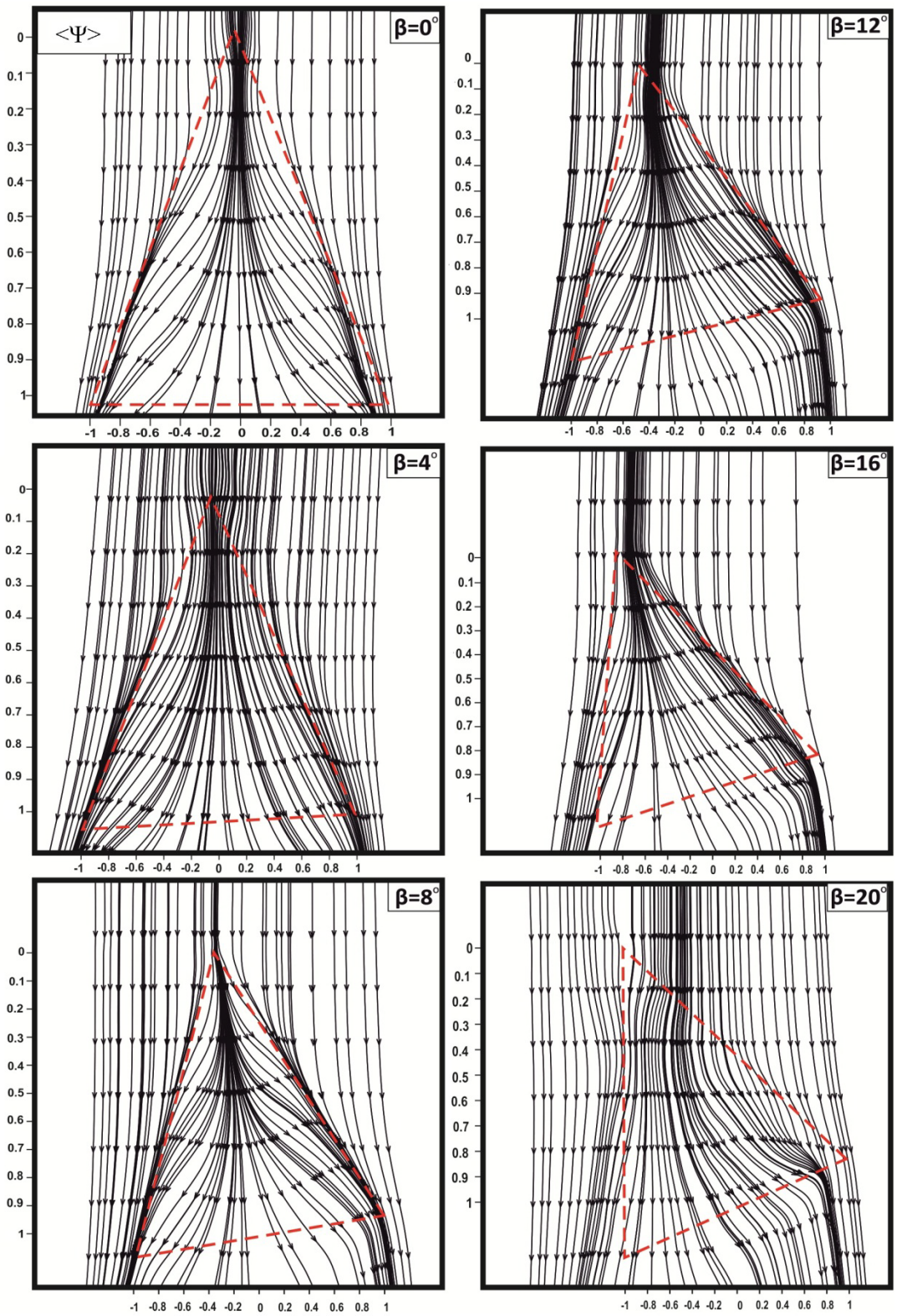

Figure 4.16. Patterns of time-averaged streamline <Ψ> in plan-view plane for angle of attack α=25° and yaw angle within the range of 0°≤β≤20°.

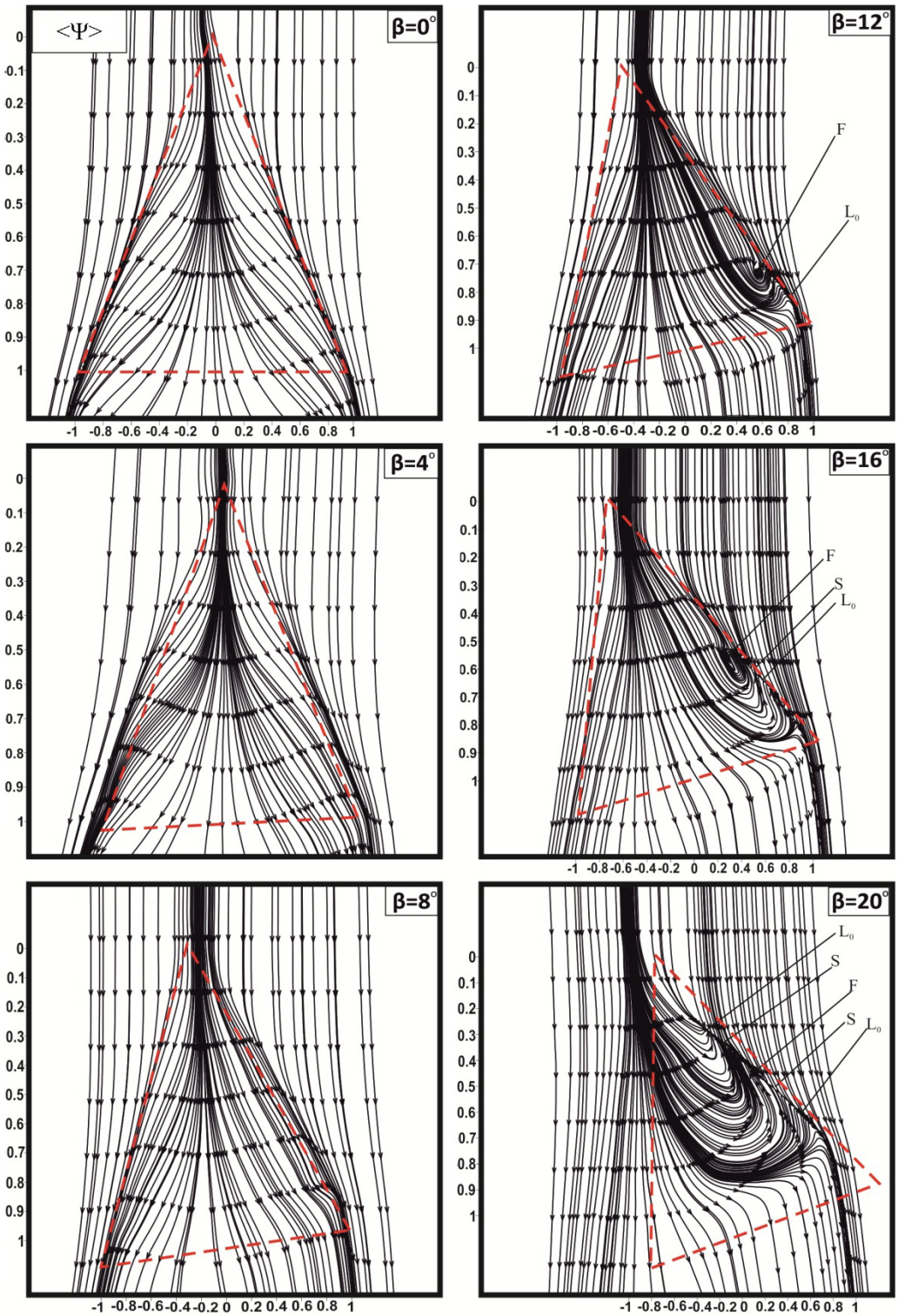

Figure 4.17. Patterns of time-averaged streamline <Ψ> in plan-view plane for angle of attack α=30° and yaw angle within the range of 0°≤β≤20°.

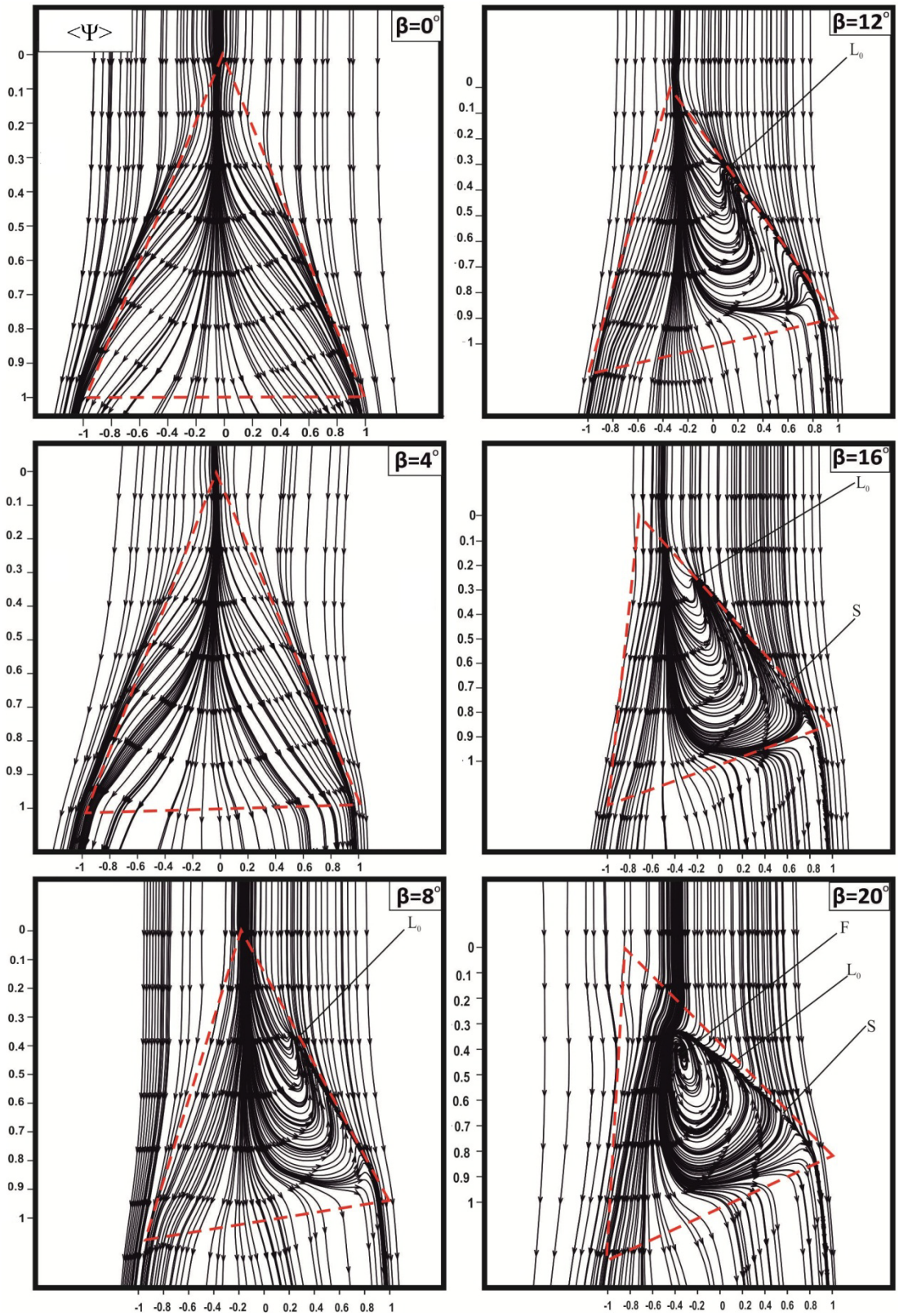

Figure 4.18. Patterns of time-averaged streamline <Ψ> in plan-view plane for angle of attack α=35° and yaw angle within the range of 0°≤β≤20°.

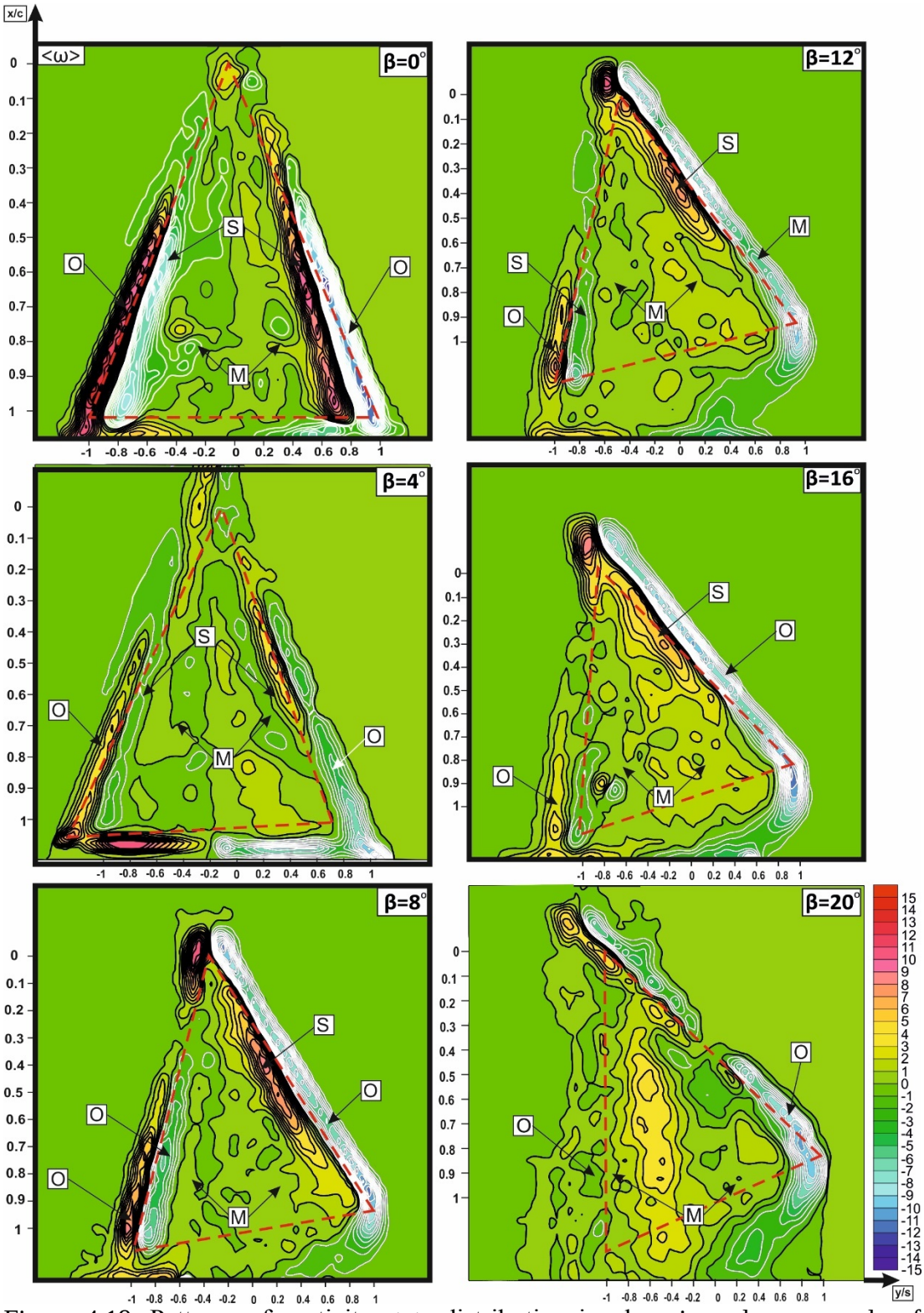

Figure 4.19. Patterns of vorticity <ω> distribution in plan-view plane at angle of attack α=25° and yaw angle within the range of 0°≤β≤20°. Minimum and incremental values $[<\omega>]_{min}$=1 and Δ[<ω>]=1 respectively.

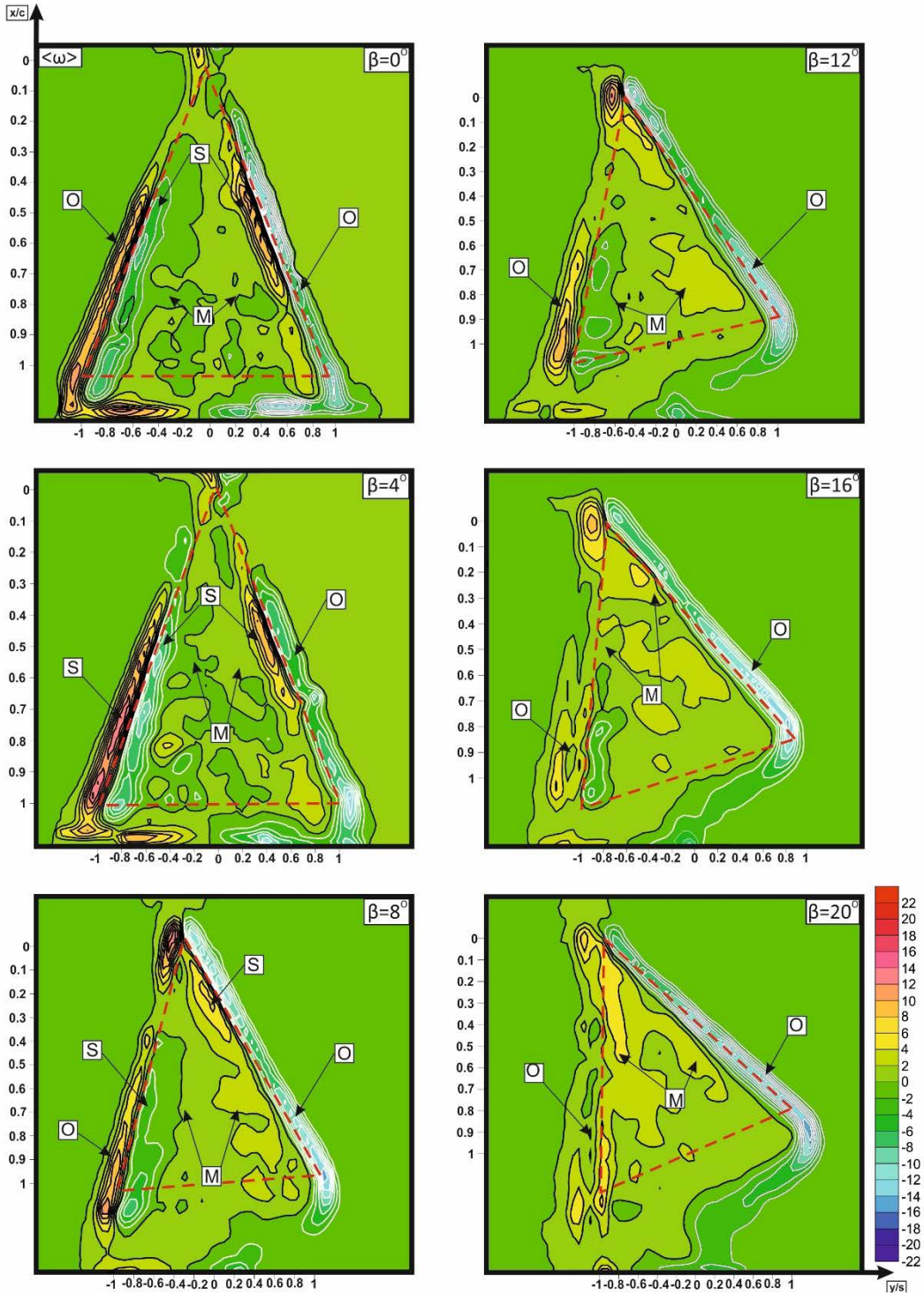

Figure 4.20. Patterns of vorticity <ω> distribution in plan-view plane at angle of attack α=30° and yaw angle within the range of 0°≤β≤20°. Minimum and incremental values $[<\omega>]_{min}=2$ and $\Delta[<\omega>]=2$ respectively.

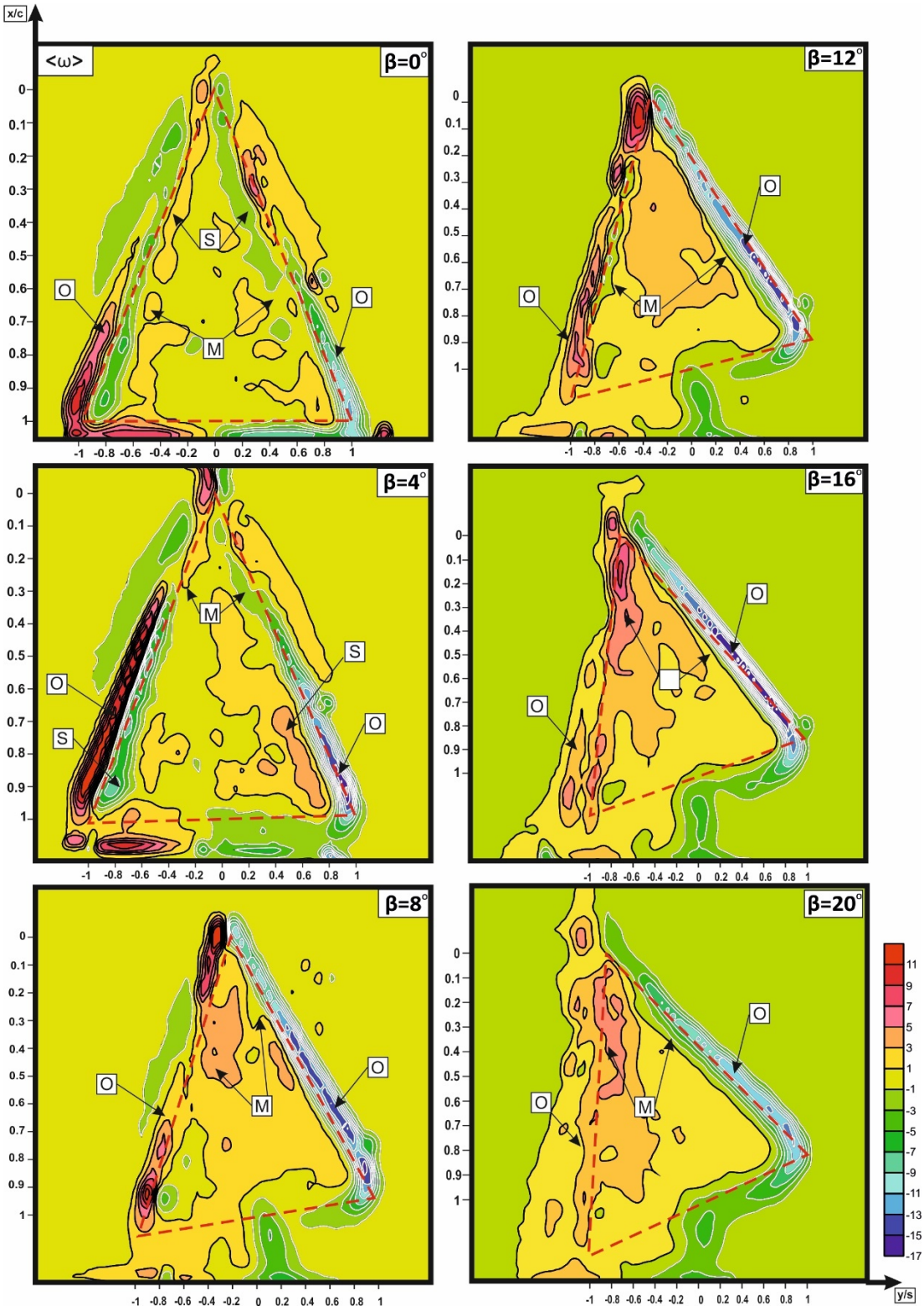

Figure 4.21. Patterns of vorticity <ω> distribution in plan-view plane at angle of attack α=30° and yaw angle within the range of 0°≤β≤20°. Minimum and incremental values are $[<\omega>]_{min}=1$ and $\Delta[<\omega>]=2$ respectively.

4.3.1.2. Time-Averaged Streamwise and Transverse Velocity Components

Figure 4.22-4.24 demonstrate contours of time-averaged dimensionless streamwise velocity, <u>/U for angles of attack, α=25°,30° and 35° and yaw angles with range of 0°≤β≤20°. Figures 4.25-4.27 show time-averaged dimensionless transverse velocity, <v>/U contour under same circumstances. Minimum and incremental values of the contours were kept same for each component for constant angle of attack, α. As seen from figures when the vortex breakdown takes place, streamwise component velocity, <u>/U decrease abruptly. On windward side however at angle of attack α=25° streamwise velocity component, does not take negative value. But increasing angles of attach to values of α=30° and α=35° streamwise velocity component, u takes negative value. This negative value of streamwise velocity component, u increase further with yaw angle β. For example, dimensionless absolute value of negative streamwise velocity component, [<u>/U] reach the value of 0.3 with the increasing yaw angle, β. On the leeward side, under all circumstances, negative <u>/U values do not take place, moreover, generally dimensionless negative streamwise velocity component, β=0° values increase with increasing angle of attack, α and yaw angle, β. As can be seen from figures with increasing yaw angle on windward side low velocity region spreads over the surface of the delta wing and on leeward side near the leading edge <u>/U increases.

In the figures in addition to colourful contours, black lines present positive values and white lines present negative values. As shown from transverse velocity component <v>/U, at yaw angle β=0° pair of well-defined cluster can be seen clearly. The symmetrical structure begins to change suddenly with the yaw angle β. Generally speaking, with the increasing yaw angle β, absolute values of the transverse velocity component, <v>/U on both windward and leeward sides decrease. At angle of attack α=25° and yaw angle β=0° transverse velocity component $[<v>/U]_{max}$, takes place between 0.9 and -0.9 when yaw angle β, is equal to 20°, these value takes place between -0.26 and 0.35. For angle of attack α=30° and yaw angle β=0°, transverse velocity component $[<v>/U]_{max}$, takes place between -0.9 and 0.9, moreover at yaw angle 20° -0.2, $[<v>/U]_{max}$ is between -0.2 and 0.6. As can be

seen in figures yaw angle, β has significant effects on velocity distribution in components, u and v. Reactions of the yaw angle, β on velocity distributions is more coherent on leeward side. At angle of attack α=35° for yaw angle, β=0°, Numerical values of transverse velocity components, $[<v>/U]_{max}$ vary between -1 and 1 and for yaw angle, β=20° values of $[<v>/U]_{max}$ take place between -0.2 and 0.2.

These results can help to understand the surface oil visualization experiments in more detail. Low velocity regions where oil could not be swept by the flow can be seen clearly. The momentum of the flow over the delta wing falls in this because of low velocity components.

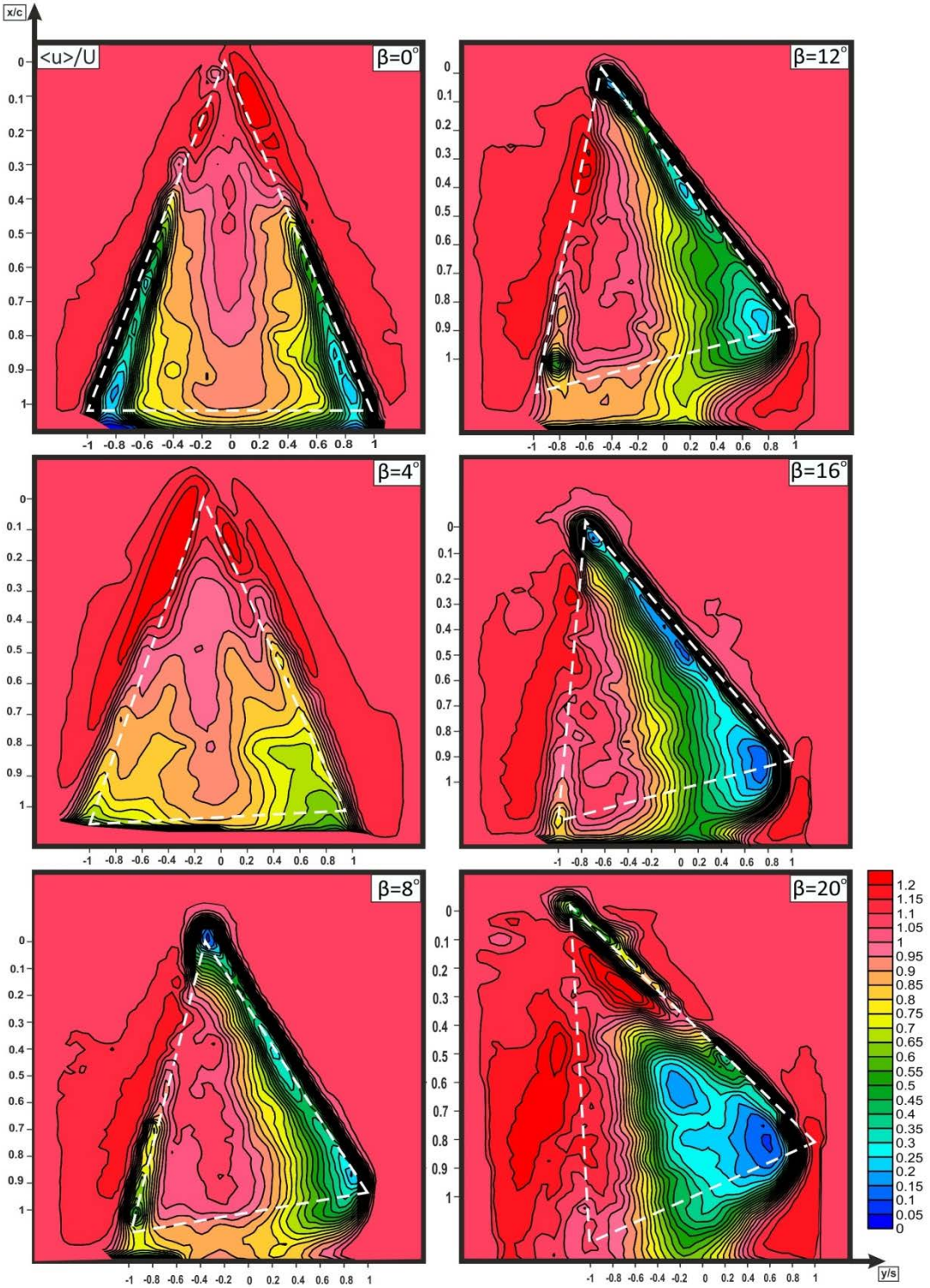

Figure 4.22. Patterns of time-averaged components of streamwise velocity, <u>/U in plan-view plan for the angle of attack α=25° and yaw angle within the range of 0°≤β≤20°. Minimum and incremental values are $[<u>/U]_{min}$=0.05, and Δ[<u>/U]= 0.05 respectively.

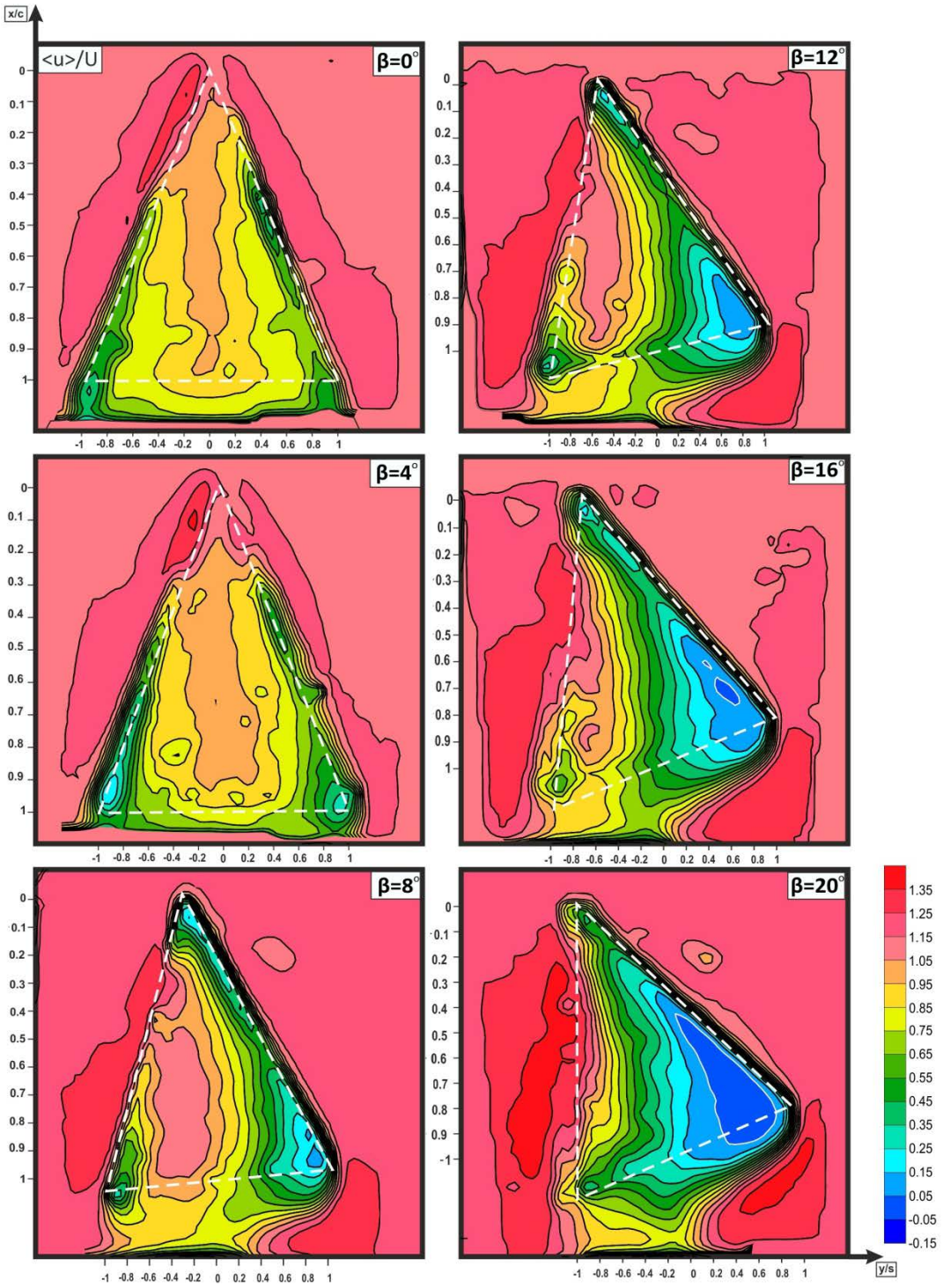

Figure 4.23. Contours of time-averaged components of streamwise velocity, <u>/U in plane-view plan for the angle of attack α=30° and yaw angle within the range of $0° \leq \beta \leq 20°$. Minimum and incremental values are $[<u>/U]_{min}=0.05$, and $\Delta[<u>/U]= 0.1$ respectively.

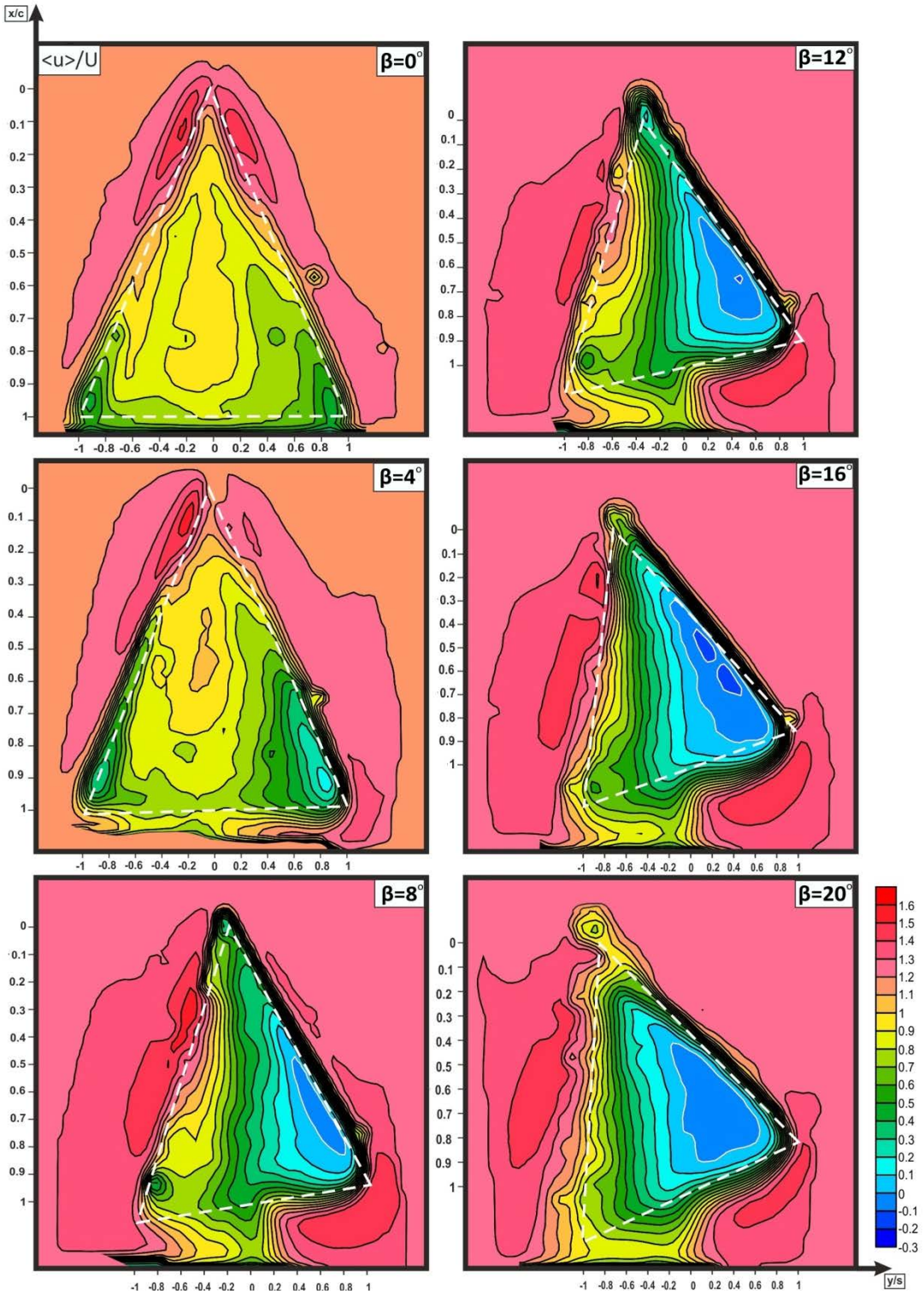

Figure 4.24. Contours of time-averaged components of streamwise velocity <u>/U in plan-view plane for the angle of attack α=35° and yaw angle within the range of 0°≤β≤20°. Minimum and incremental values are $[<u>/U]_{min}$=0.1, and Δ[<u>/U]= 0.1 respectively.

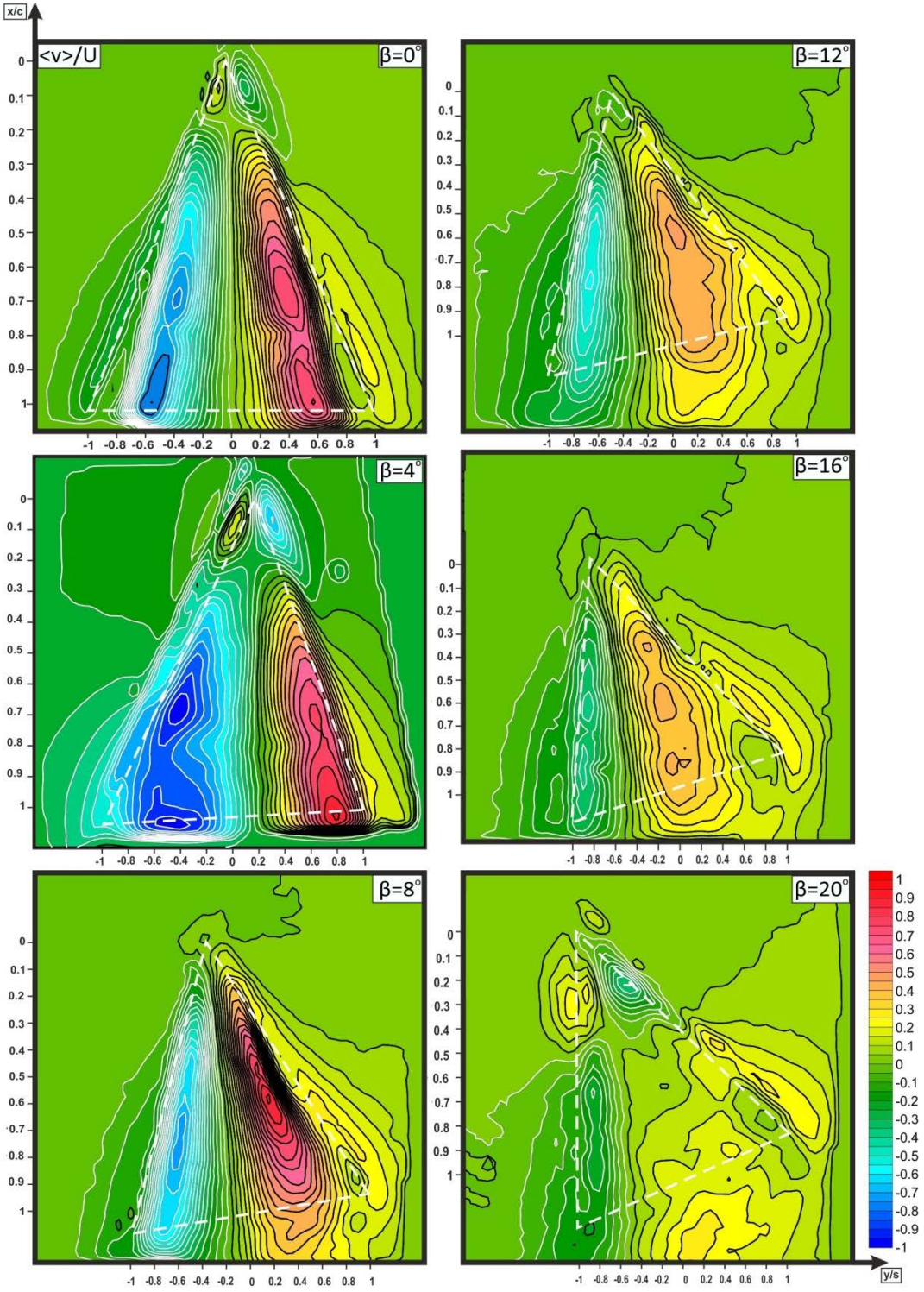

Figure 4.25. Contours of time-averaged components of transverse velocity, <v>/U in plan-view plane for angle of attack α=25° and yaw angle within the range of 0°≤β≤20°. Minimum and incremental values are $[<v>/U]_{min}$=0.05, and Δ[<v>/U]= 0.05 respectively.

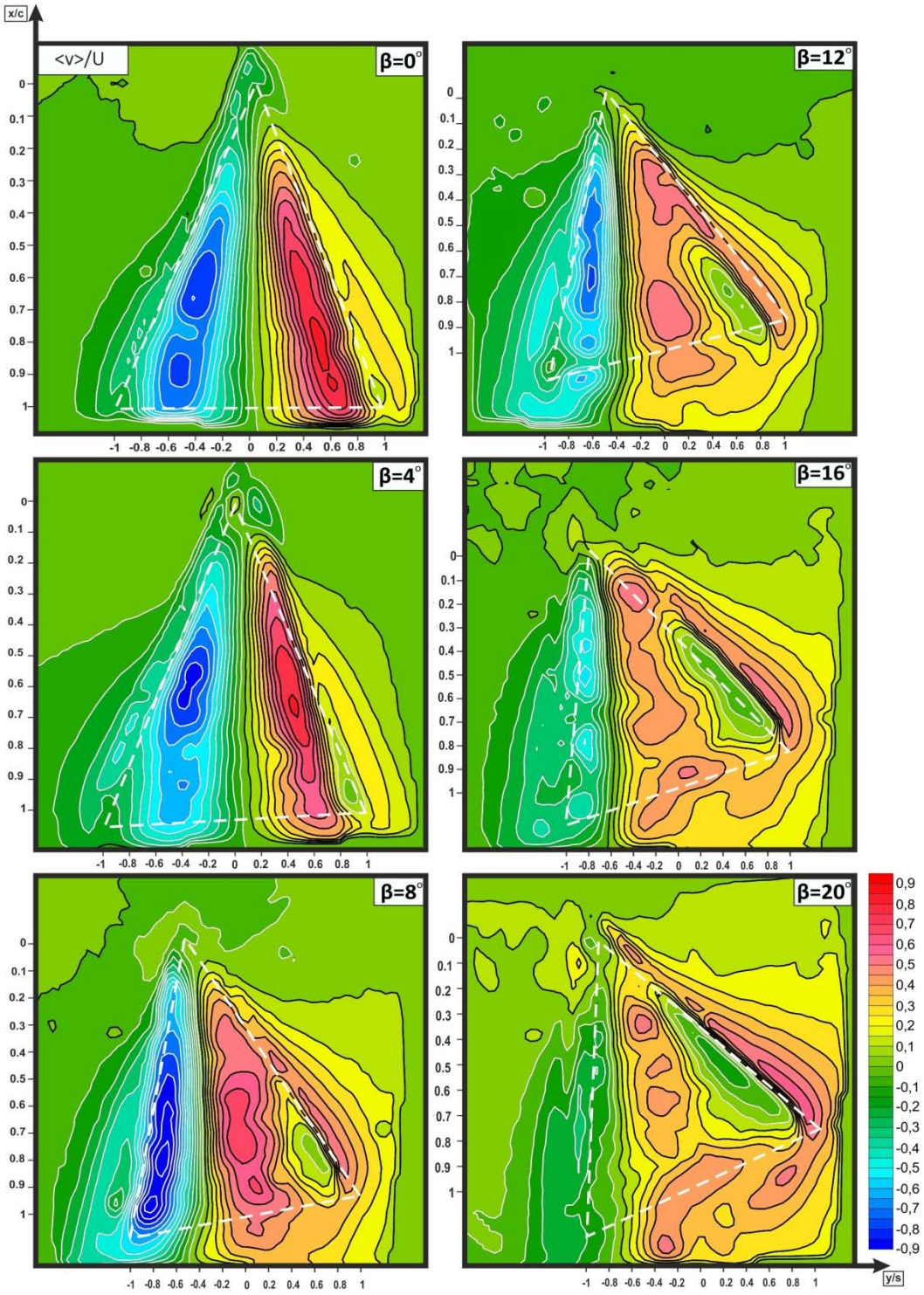

Figure 4.26. Patterns of time-averaged components of transverse velocity, <v>/U in plan-view plane for the angle of attack α=30° and yaw angle within the range of 0°≤β≤20°. Minimum and incremental values are $[<v>/U]_{min}$=0.05, and Δ[<v>/U]= 0.05 respectively.

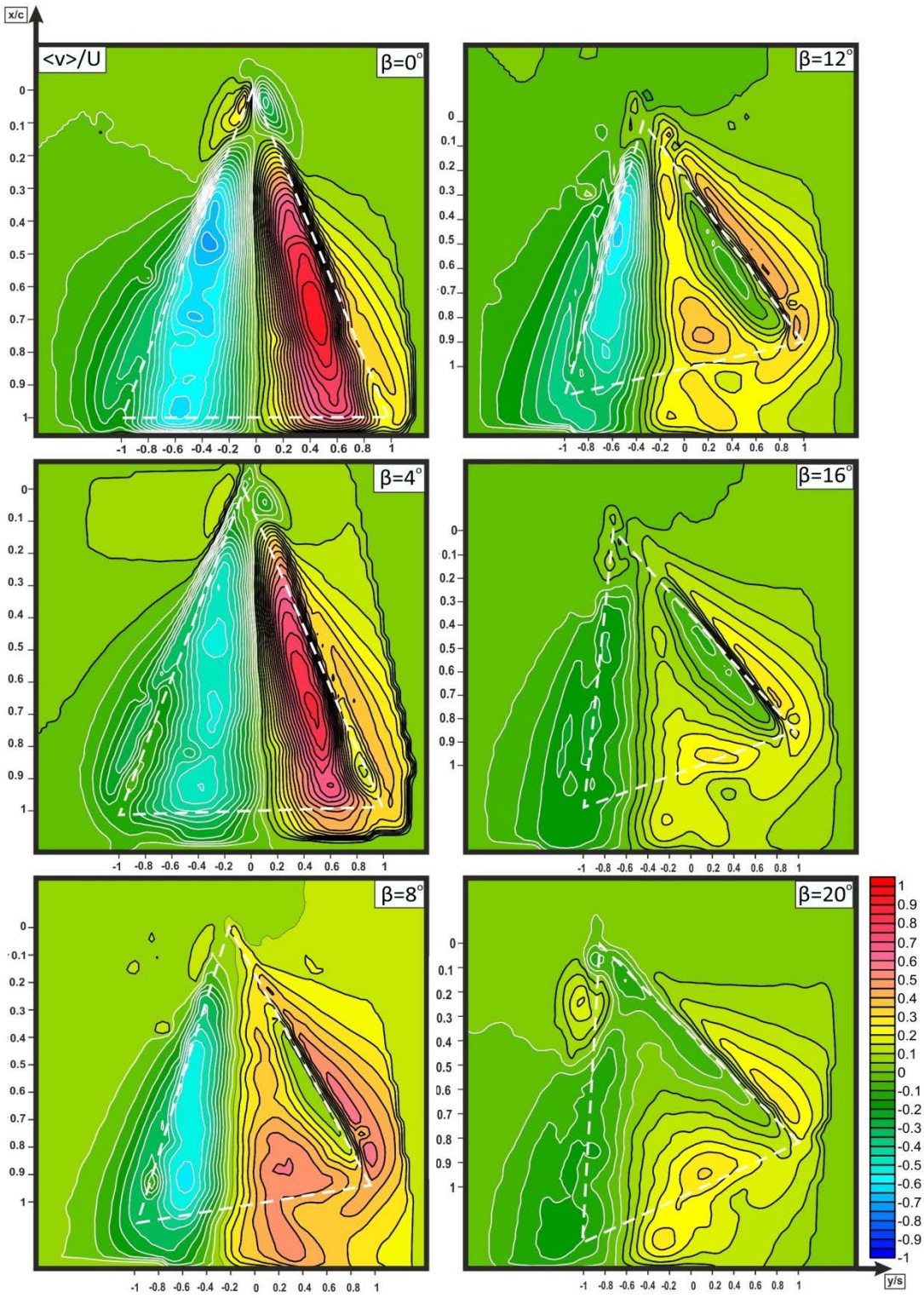

Figure 4.27. Patterns of time-averaged components of transverse velocity, <v>/U in plan-view plane for the angle of attack α=35° and yaw angle within the range of $0° \leq \beta \leq 20°$. Minimum and incremental values are $[<v>/U]_{min}=0.05$, and $\Delta[<v>/U]= 0.05$ respectively.

4.3.1.3. Velocity Fluctuations

Root mean squares (rms) of streamwise, transverse and vertical velocities, $<u_{rms}>/U$, $<v_{rms}>/U$ and $<w_{rms}>/U$ normalized by free-stream velocity, U are demonstrated in figures 4.28-4.30, figures 4.31-4.33 and figures 4.34-4.36 respectively. As shown in figures when delta wing is yawed, the magnitude of $[<u_{rms}>/U]_{max}$ increase gradually on leeward side while on windward sides' decrease gradually. In axially attached flow region, rms values of all velocity components are lower than vortical flow regions.

At an angle of attack $\alpha=25°$, the magnitude of $[<u_{rms}>/U\ ]_{max}$ is 0.34 for yaw angle $\beta=0°$. On the other hand, having yaw angle as $\beta=20°$ the magnitude of $[<u_{rms}>/U\ ]_{max}$, on windward side is 0.24 ,but, on leeward side is 0.6. Increasing angle of attack, α to a value of 30°, for yaw angle $\beta=0°$ the magnitude of $[<u_{rms}>/U]_{max}$ is equal to 0.38, but setting this yaw angle as $\beta=20°$ the magnitude of $[<u_{rms}>/U]_{max}$ becomes equal to 0.20 on windward side and this magnitude of $[<u_{rms}>/U]_{max}$ promotes to a value of 0.45 in the region of leeward side.

Magnitudes of $<v_{rms}>/U$ increase for a certain degree then decrease gradually, moreover, maximum values of $<v_{rms}>/U$ are seen on windward side. At an angle of attack $\alpha=25°$, dimensionless transverse velocity, $[<v_{rms}>/U]_{max}$ has a value of 0.27 for yaw angle $\beta=0°$, keeping the yaw angle, β at 8° dimensionless $[<v_{rms}>/U]_{max}$ takes maximum value such as 0.48. Setting this yaw angle, β to a value of 12°, dimensionless transverse velocity component, $[<v_{rms}>/U]_{max}$ falls to the lower values such as 0.38 and for yaw angle $\beta=16°$ and 20° it is almost 0.34. At an angle of attack, for example, $\alpha=30°$, for yaw angle $\beta=0°$ maximum value of $[<v_{rms}>/U]_{max}$ is 0.32, the maximum value is obtained at yaw angle $\beta=4°$ which is $[v_{rms}/U]_{max}=0.36$. Increasing the yaw angle, β beyond 8°, the maximum value of $[v_{rms}/U]_{max}$ falls around 0.24.

Magnitudes of maximum value of vertical velocity component $[<w_{rms}>/U]_{max}$ generally increase with yaw angle, β. At an angle of attack $\alpha=25°$, when the yaw angle,β is to 0° the magnitude of maximum value of dimensionless vertical velocity component, $[<w_{rms}>/U]_{max}$ is 0.3, at $\beta=16°$ it is 0.64, at $\beta=20°$ it is 0.48. Rising the angle of attack, α to a higher level, for example, 30° the magnitude of maximum

value of dimensionless vertical velocity component, $[<w_{rms}>/U]_{max}$ increases with yaw angle, β up to yaw angle β=8° then it falls gradually. At yaw angle β=0°, the magnitude of maximum value of dimensionless vertical velocity component, $[<w_{rms}>/U]_{max}$ is almost 0.35. On the other hand, when yaw angle, β is equal to 8° the magnitude of maximum value of dimensionless vertical velocity component, $[<w_{rms}>/U]_{max}$ reaches 0.5 and when yaw angle is β=20° it falls to 0.35. At an angle of attack of α=35°, $[<w_{rms}>/U]_{max}$ increases up to yaw angle of β=12° then it falls gradually. At yaw angle β=0° $[<w_{rms}>/U]_{max}$ is 0.38, at yaw angle β=12° it is 0.46 and at β=20° it is 0.36.

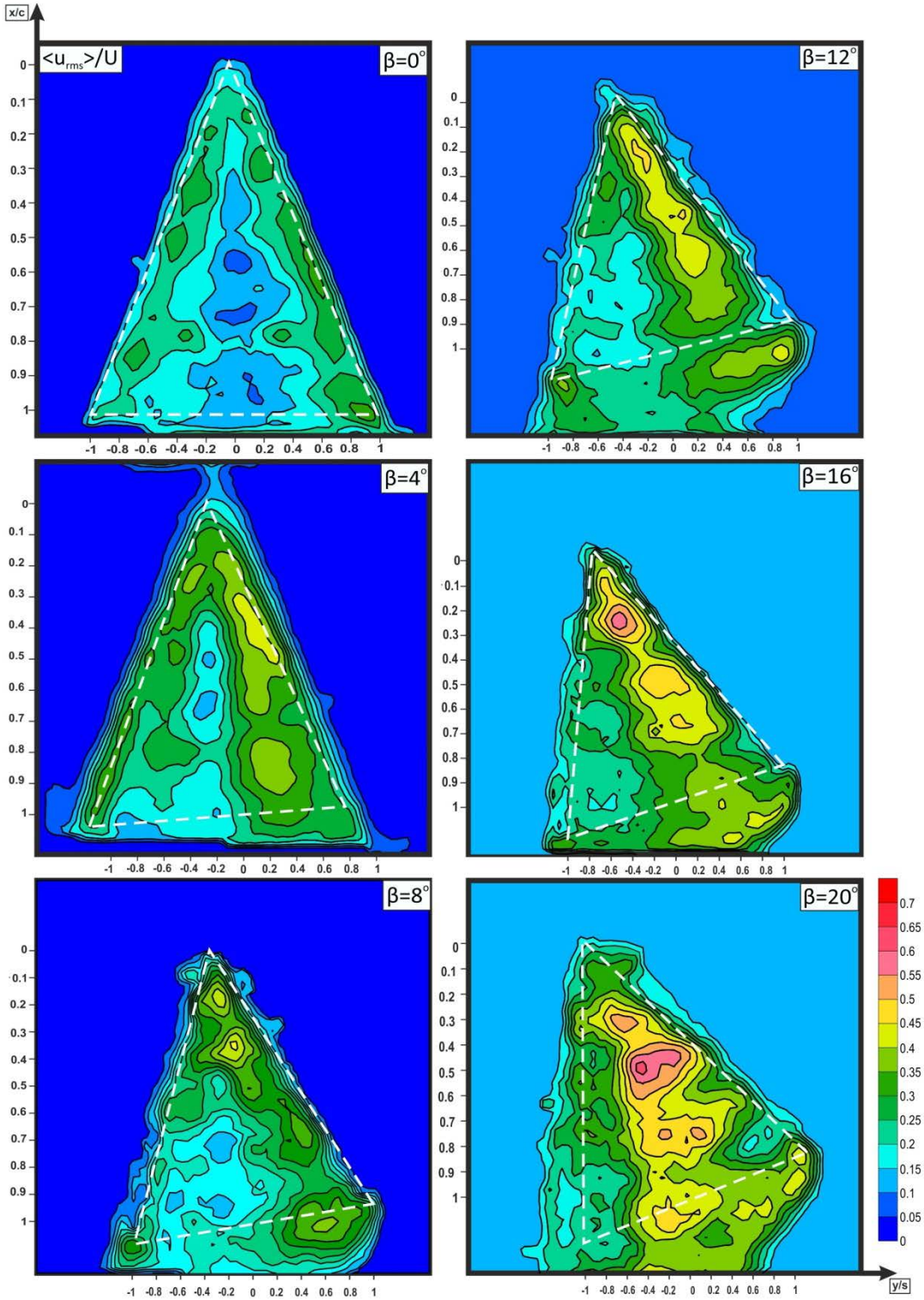

Figure 4.28. Contours of time-averaged components of rms of streamwise velocity, [$<u_{rms}>/U$] in plan-view plane for the angle of attack α=25° and yaw angle within the range of 0°≤β≤20°. Minimum and incremental values are $[<u_{rms}>/U]_{min}$=0.05, and $\Delta[<u_{rms}>/U]$= 0.05 respectively.

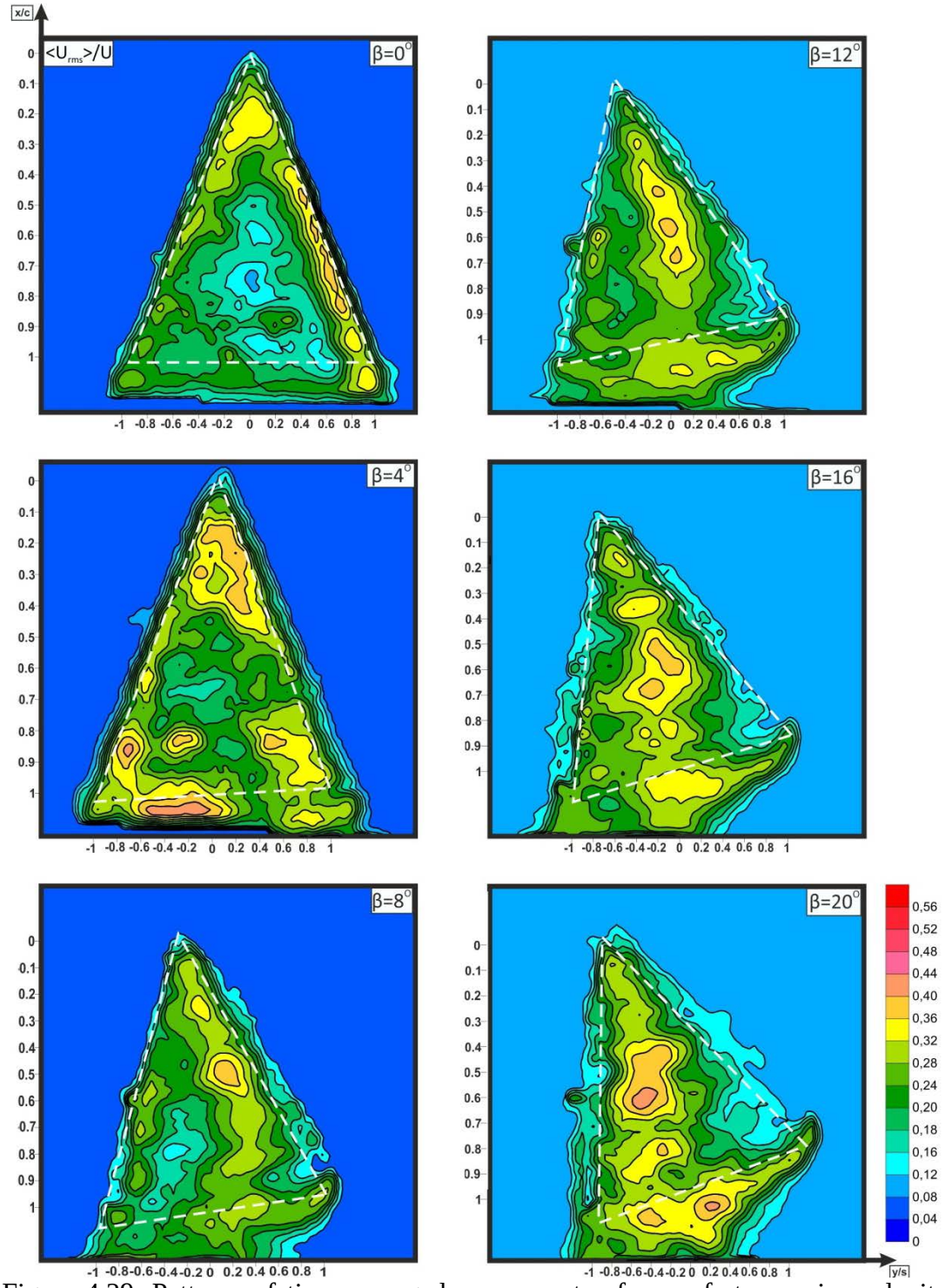

Figure 4.29. Patterns of time-averaged components of rms of streamwise velocity, $\langle u_{rms} \rangle / U$ in plan-view plane for the angle of attack $\alpha=30°$ and yaw angle within the range of $0° \leq \beta \leq 20°$. Minimum and incremental values are $[\langle u_{rms} \rangle / U]_{min}=0.04$, and $\Delta[\langle u_{rms} \rangle / U]= 0.04$ respectively.

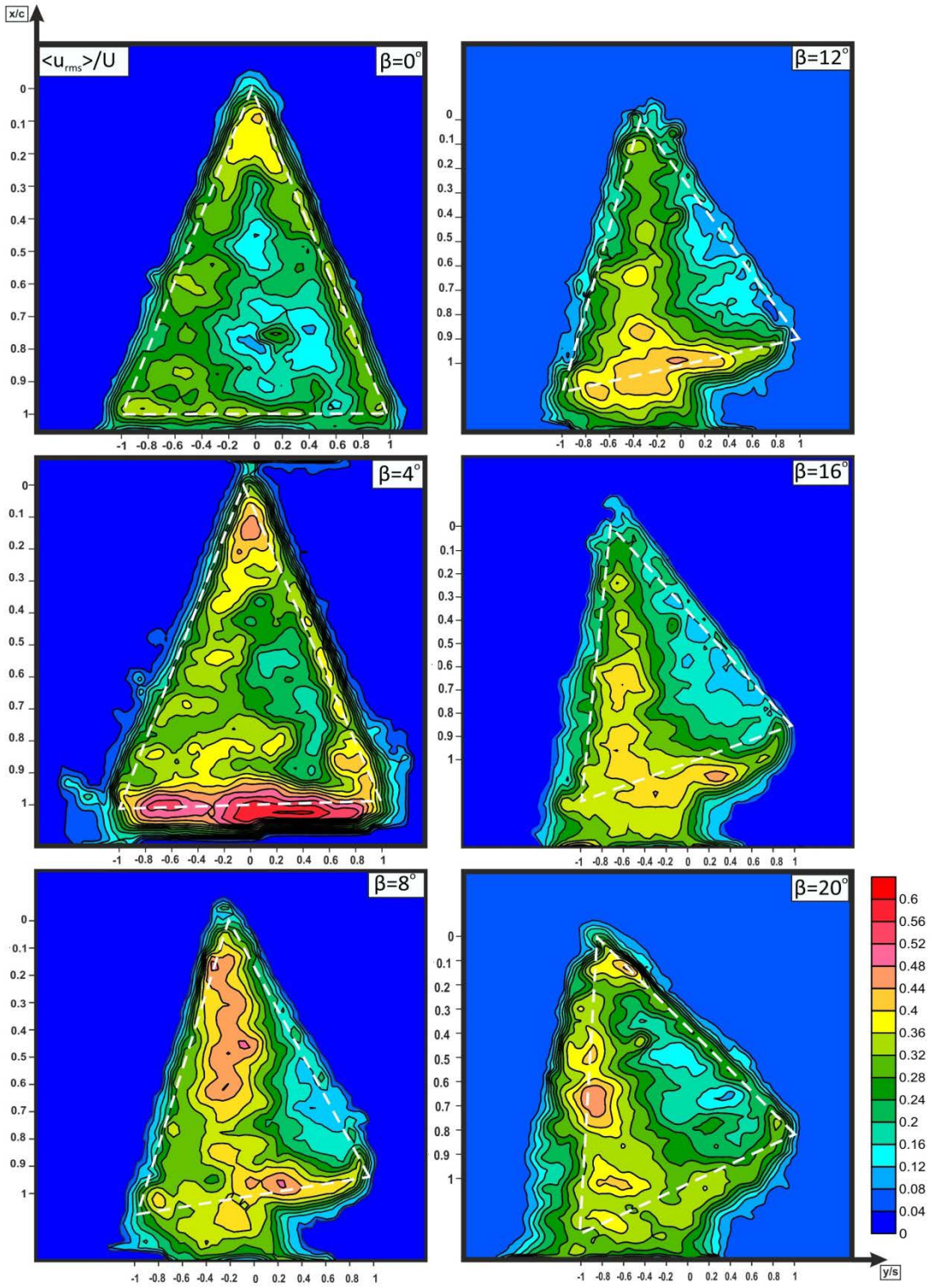

Figure 4.30. Patterns of time-averaged components of rms of streamwise velocity $\langle u_{rms} \rangle/U$ in plan-view plane for the angle of attack $\alpha=35°$ and yaw angle within the range of $0° \leq \beta \leq 20°$. Minimum and incremental values are $[\langle u_{rms} \rangle/U]_{min}=0.04$, and $\Delta[\langle u_{rms} \rangle/U]= 0.04$ respectively.

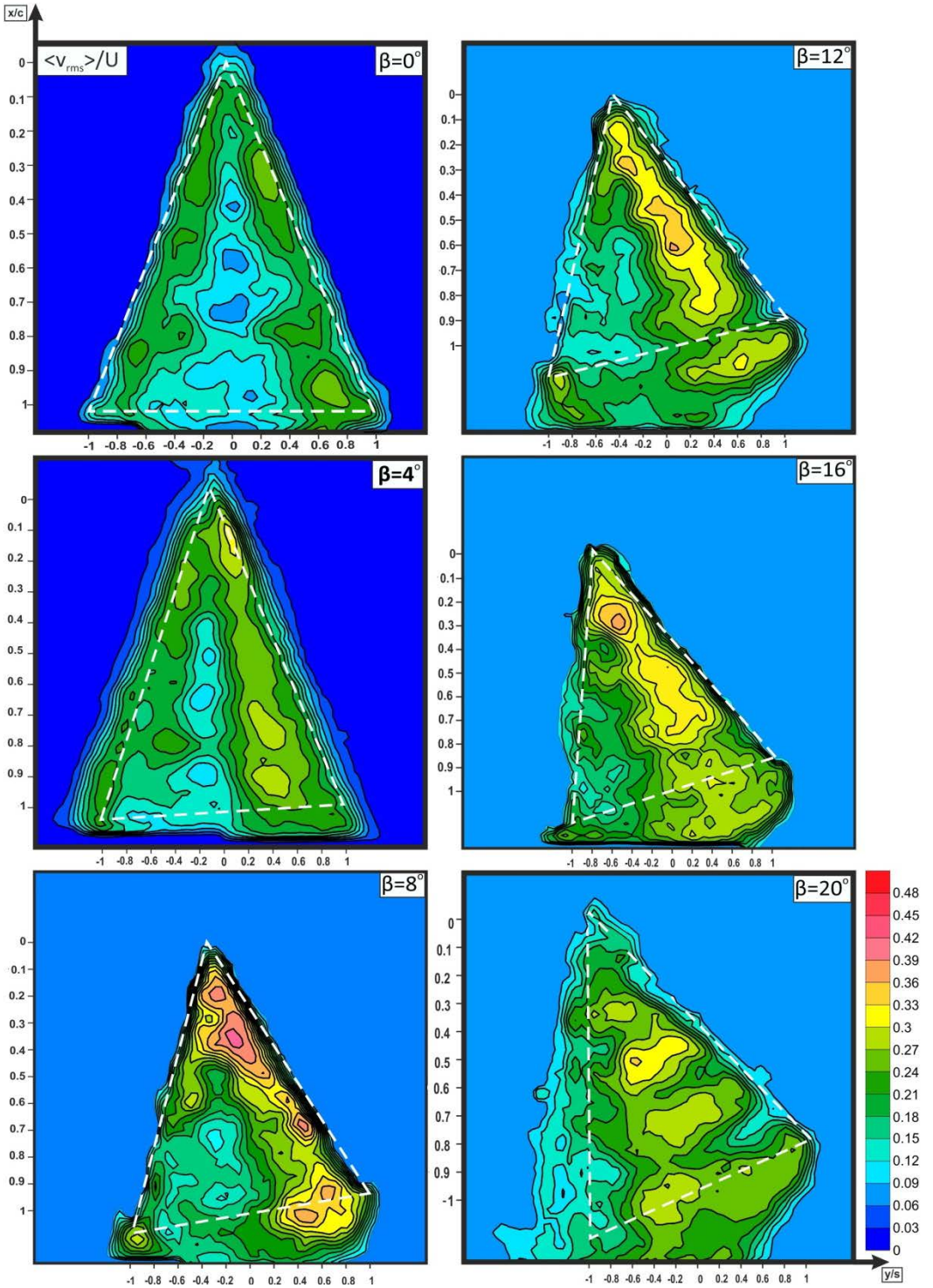

Figure 4.31. Patterns of time-averaged components of rms of transverse velocity, $\langle v_{rms} \rangle / U$ in plan-view plane for the angle of attack $\alpha=25°$ and yaw angle within the range of $0° \leq \beta \leq 20°$. Minimum and incremental values are $[\langle v_{rms} \rangle / U]_{min}=0.03$, and $\Delta[\langle v_{rms} \rangle / U]= 0.03$ respectively.

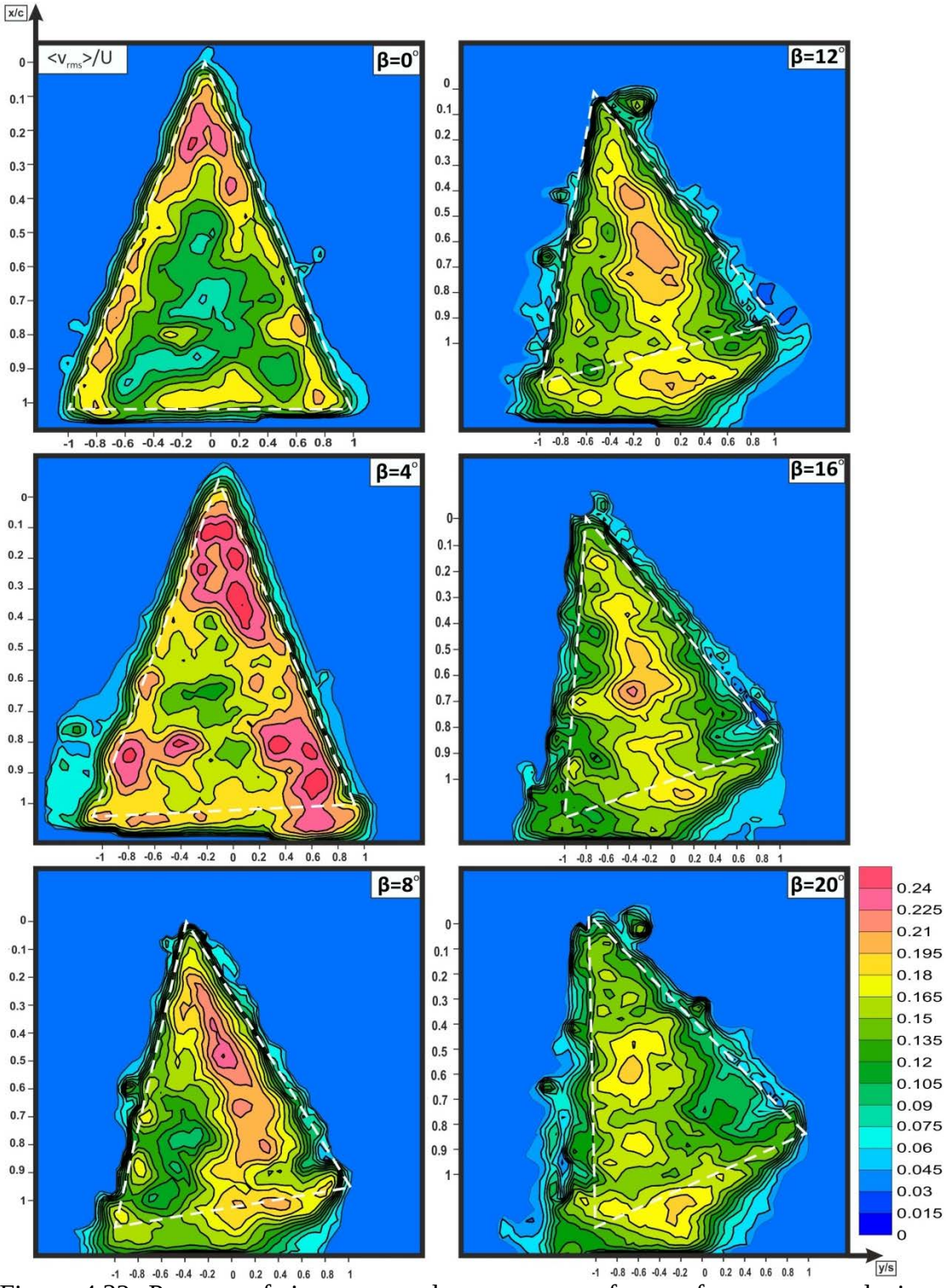

Figure 4.32. Patterns of time-averaged components of rms of transverse velocity, $<v_{rms}>/U$ in plan-view plane for the angle of attack α=30° and yaw angle within the range of 0°≤β≤20°. Minimum and incremental values are $[<v_{rms}>/U]_{min}$=0.015, and $\Delta[<v_{rms}>/U]$= 0.015 respectively.

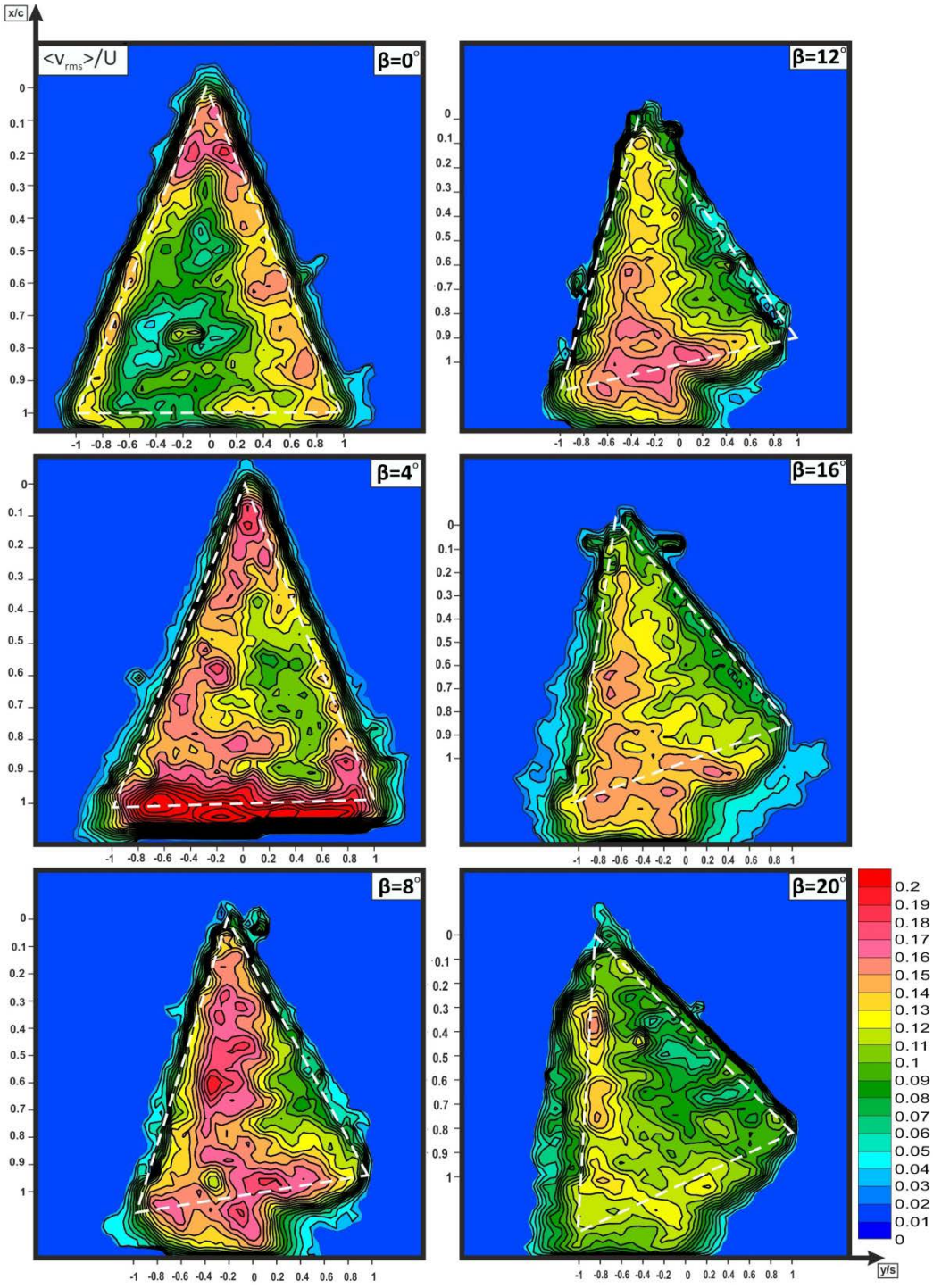

Figure 4.33. Patterns of time-averaged components of rms of transverse velocity, $\langle v_{rms} \rangle / U$ in plan-view plane for the angle of attack α=35° and yaw angle within the range of $0° \leq \beta \leq 20°$. Minimum and incremental values are $[\langle v_{rms} \rangle / U]_{min}=0.01$, and $\Delta[\langle v_{rms} \rangle / U]= 0.01$ respectively.

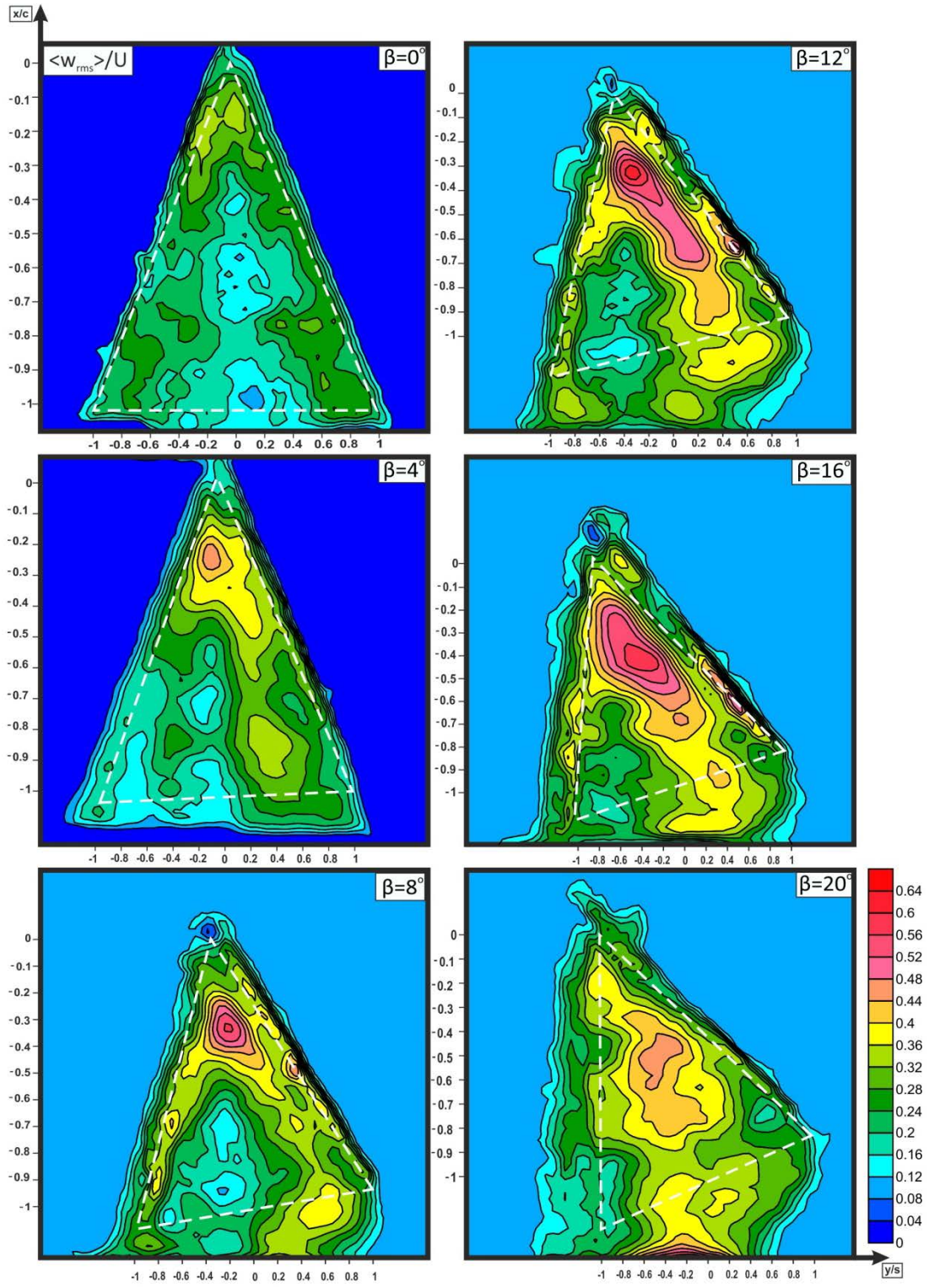

Figure 4.34. Patterns of time-averaged components of rms of vertical velocity, $\langle w_{rms} \rangle / U$ in plan-view plane for the angle of attack α=25° and yaw angle within the range of 0°≤β≤20°. Minimum and incremental values are $[\langle w_{rms} \rangle / U]_{min}$=0.04, and $\Delta[\langle w_{rms} \rangle / U]$= 0.04 respectively.

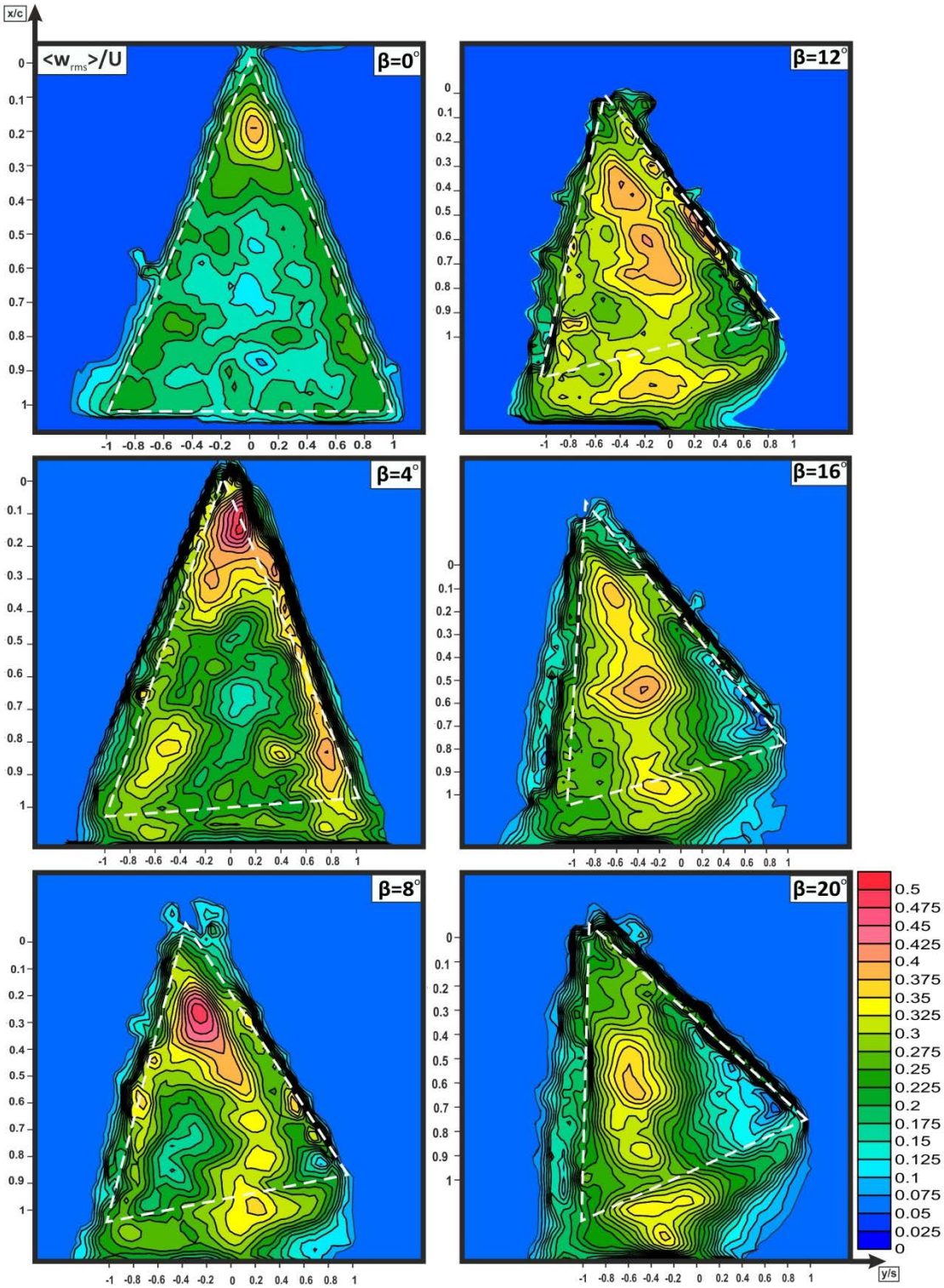

Figure 4.35. Patterns of time-averaged components of rms of vertical velocity, $\langle w_{rms} \rangle / U$ in plan-view plane for the angle of attack $\alpha=30°$ and yaw angle within the range of $0° \leq \beta \leq 20°$. Minimum and incremental values are $[\langle w_{rms} \rangle / U]_{min}=0.025$, and $\Delta[\langle w_{rms} \rangle / U]= 0.025$ respectively.

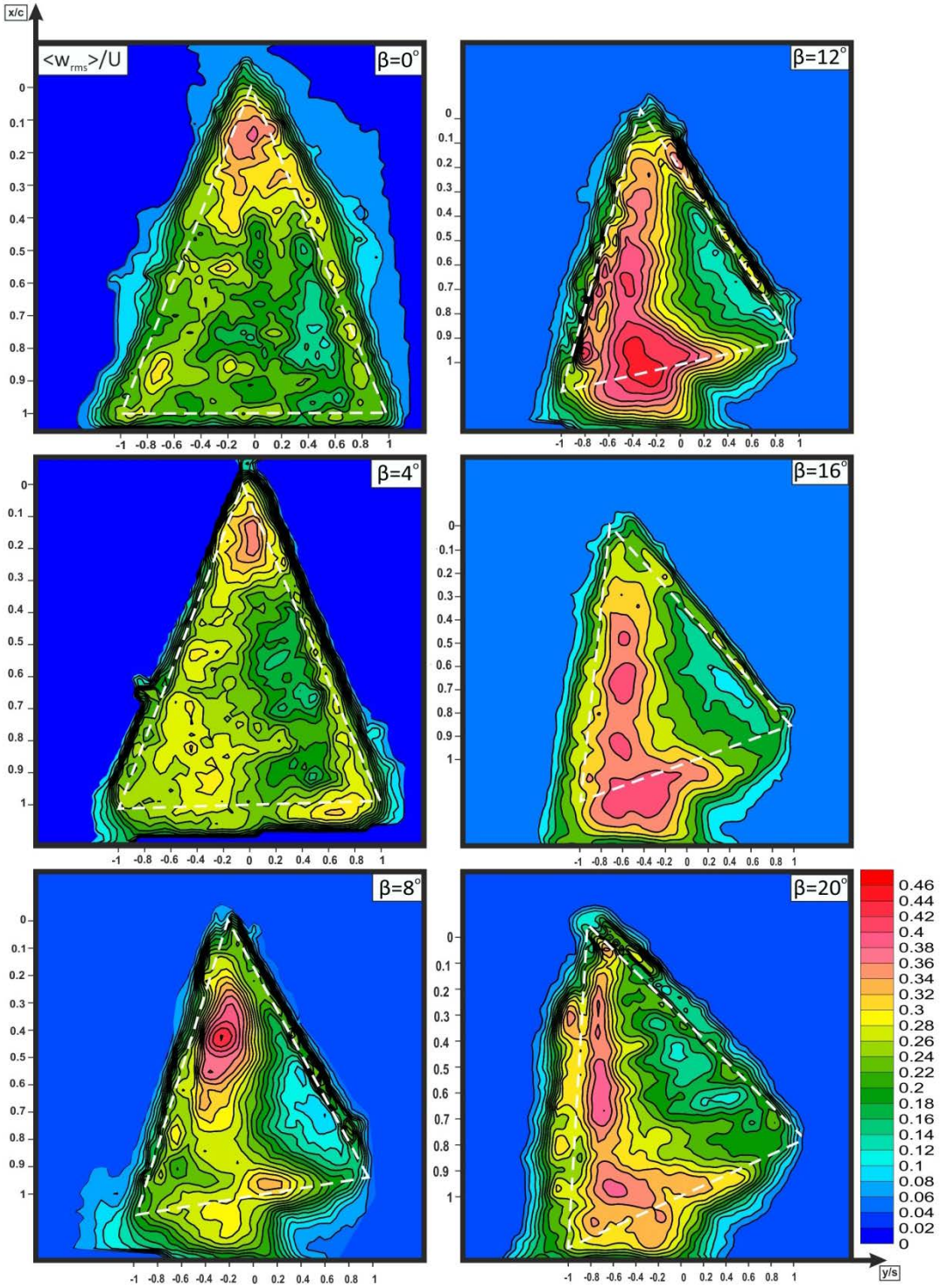

Figure 4.36. Patterns of time-averaged components of rms of vertical velocity, $\langle w_{rms} \rangle / U$ in plan-view plane for the angle of attack $\alpha=35°$ and yaw angle within the range of $0° \leq \beta \leq 20°$. Minimum and incremental values are $[\langle w_{rms} \rangle / U]_{min}=0.02$, and $\Delta[\langle w_{rms} \rangle / U]= 0.02$ respectively.

4.3.1.4. Spectral Analysis of the Streamwise Velocity Components

Figures 4.37-4.39 show the results of (Fast Fourier Transform) analysis of the u velocity components on u_{rms}/U contours. As seen from figures, there are a certain peak locations near vortex breakdown. Before and after vortex breakdown, peaks were complex which represent that the flow is very unsteady. Especially after vortex breakdown, flow becomes highly disordered and new small scale vortices take place and this leads complicated velocity distributions, moreover, the magnitude of peaks get lower values. For example, at an angle of attack α=25° and yaw angle β=20°, peak is almost 9.20 where $<u_{rms}/U>$ is maximum. Furthermore, on windward side after vortex breakdown, maximum value decreases but flow structures are more complex. Figures show that with increasing yaw angle, β flow gets more unsteady behavior. Moreover, since all frequencies lower than 12 Hz, this frequency is appropriate in order to acquire for PIV studies.

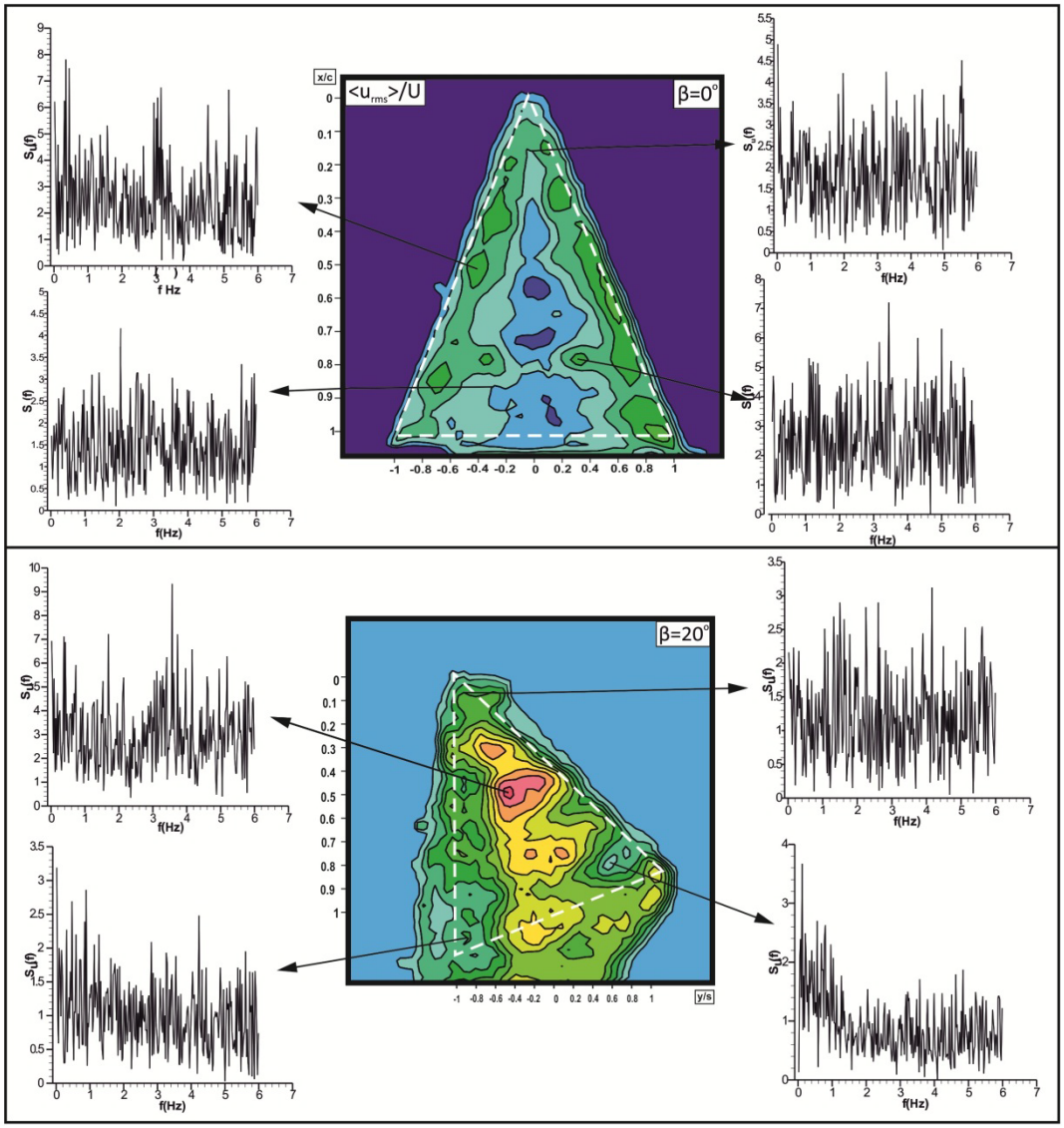

Figure 4.37. Spectra S_u of velocity fluctuations at selected locations, on $<u_{rms}>/U$ at angle of attack α=25° and yaw angles β=0° and β=20°.

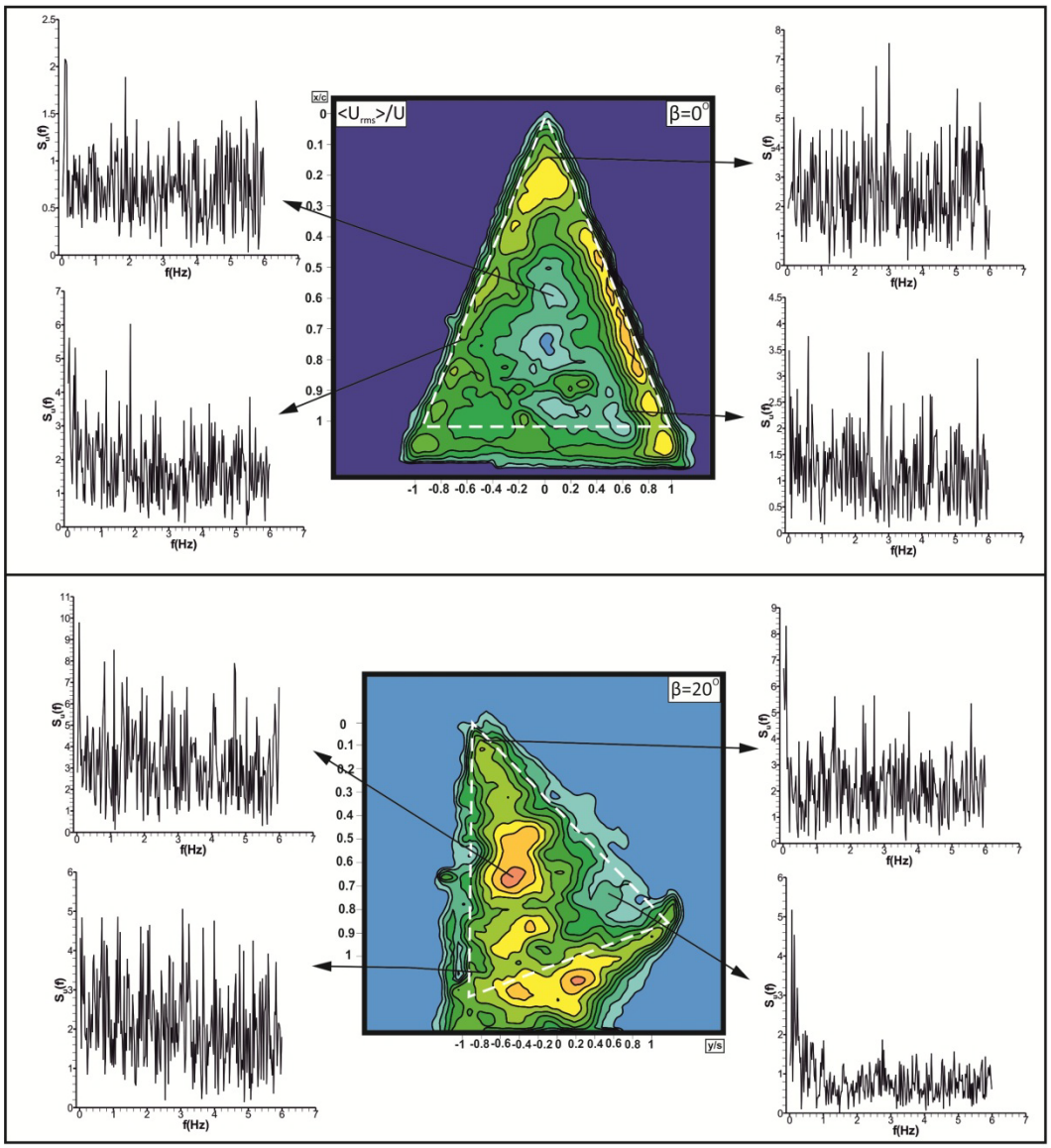

Figure 4.38. Spectra S_u of velocity fluctuations at selected locations, on $<u_{rms}>/U$ at angle of attack α=30° and yaw angles β=0° and β=20°.

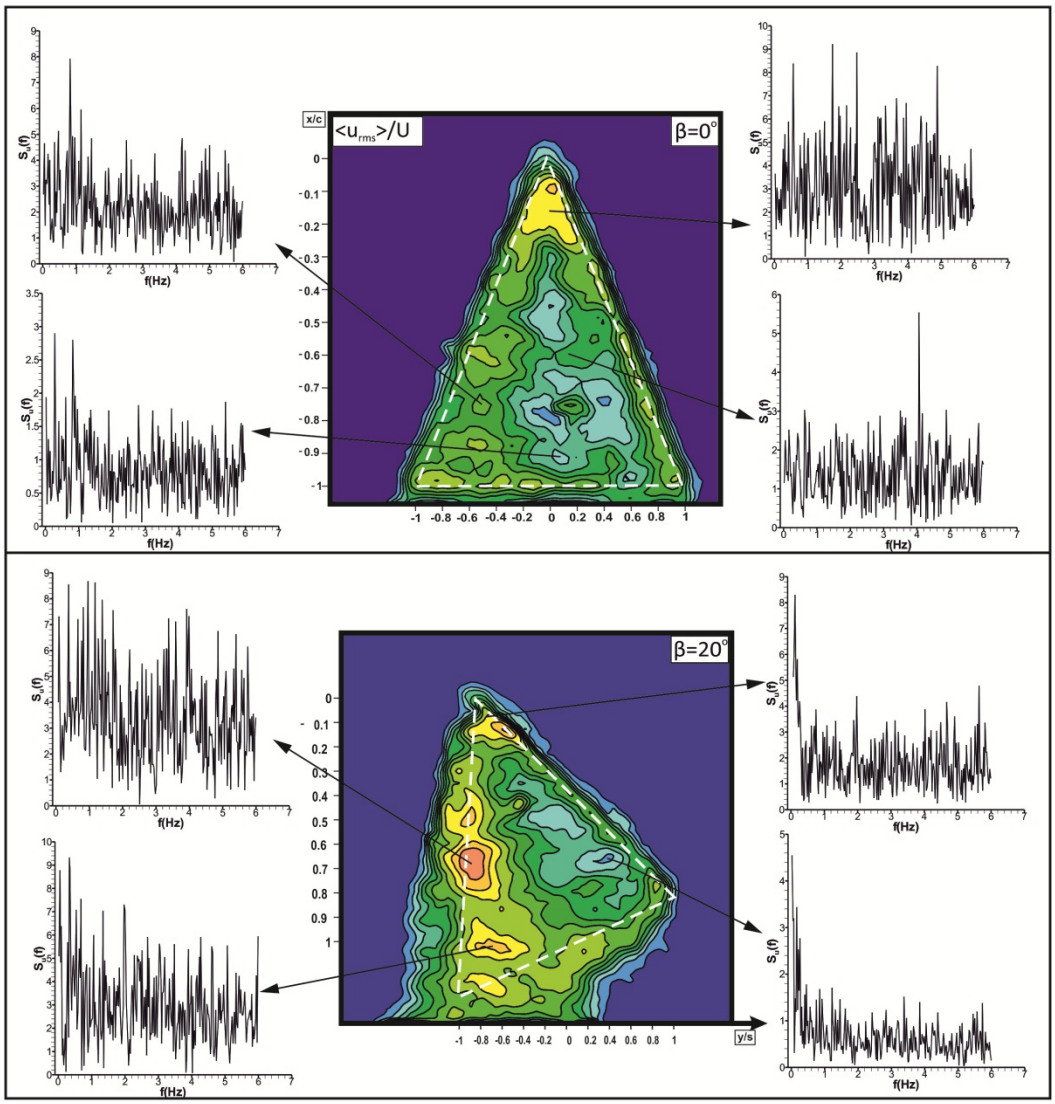

Figure 4.39. Spectra S_u of velocity fluctuations at selected locations, on $<u_{rms}>/U$ at angle of attack α=35° and yaw angles β=0° and β=20°.

4.3.1.5. Reynolds Stresses and Turbulent Kinetic Energy

Reynolds normal stresses $<u'u'>/U^2$, $<v'v'>/U^2$ and $<w'w'>/U^2$ normalized by the square root of the free-stream velocity, U^2 are presented in figures 4.40-4.42, figures 4.43-4.45 and figures 4.46-4.48 respectively. Generally speaking when the yaw angle, β increases values of $[<u'u'>/U^2]_{max}$ also increase. While windward side vortices broaden and pass the center of the delta wing, leeward side vortices shrink in size in lateral direction. For angle of attack α=25°, at yaw angle β=0° $[<u'u'>/U^2]_{max}$ is 0.12 when taking the yaw angle, β as 20° the maximum value of $[<u'u'>/U^2]_{max}$ reach 0.38. At an angle of attack α=30°, for yaw angle β=0°, the maximum value of $[<u'u'>/U^2]_{max}$ is 0.15, and for yaw angle of β=20° it reach the level of 0.2 on leeward side.

Contours of the normalized transverse velocity $[<v'v'>/U^2]_{max}$ behaves like $<v_{rms}>$ magnitude of this Reynolds normal stress increase up to a certain value then fall suddenly on leeward side. At 25° angle of attack, α, the maximum value of $[<v'v'>/U^2]_{max}$ is equal to 0.08, it reaches maximum value which is 0.24 at yaw angle β=8°. For β=12° it suddenly falls to a value of 0.12 then it takes place over 0.1 for β=16° and β=20°. At 30° angle of attack α, for 0° yaw angle, $[<v'v'>/U^2]_{max}$ is equal to 0.1, at yaw angle β=4° this value becomes 0.11. Finally, for the yaw angle β=20° the Reynolds normal stress $[<v'v'>/U^2]_{max}$ is equal to 0.07. At an angle of attack α=35° for yaw angle β=0°, the Reynolds normal stress, $[<v'v'>/U^2]_{max}$ is very low such as 0.02, for yaw angle β=20° it is equal to 0.04.

At an angle of attack α=25° for yaw angle β=0° the Reynolds normal stress $[<w'w'>/U^2]_{max}$ has a value of 0.225. When the yaw angle, β is set to12° it can be seen that fluctuations in velocity components dramatically. This flow characteristics is demonstrated by the numerical value of Reynolds normal stress $[<w'w'>/U^2]_{max}$ that is equal to 0.375. On the other hand, increasing the yaw angle, β to a higher level such as β=20° the experimental results show that the numerical value of Reynolds normal stress $[<w'w'>/U^2]_{max}$ decreases to a lower value such as 0.225. These results demonstrate that the region of flow separation enlarges over the surface of delta wing and reduces the level of fluctuations. In summary, at an angle of attack

$\alpha=30°$ for yaw angle $\beta=0°$ the value of $[<w'w'>/U^2]_{max}$ is equal to 0.28. For yaw angle $\beta=4°$, the value of $[<w'w'>/U^2]_{max}$ is equal to 0.32 then it starts to fall suddenly and at yaw angle $\beta=20°$ the value of $[<w'w'>/U^2]_{max}$ is equal to 0.2. At angle of attack $\alpha=35°$ for yaw angle $\beta=0°$ the value of $[<w'w'>/U^2]_{max}$ is equal to 0.18 at yaw angle $\beta=12°$ the value of $[<w'w'>/U^2]_{max}$ is equal to 0.27 and $\beta=20°$ the value of $[<w'w'>/U^2]_{max}$ is equal to 0.21.

Figures 4.49-4.51 demonstrate Reynolds stress correlations, $<u'v'>/U^2$. At yaw angle $\beta=0°$, $[<u'v'>/U^2]_{max}$ values can be seen in the leading edge vortices near the leading edges whereas in attached flow region close to the center of the delta wing minimum values of it can be seen. When delta wing is yawed, patterns of $<u'v'>/U^2$ get more complex. Patterns of Reynolds stress correlations, $<u'v'>/U^2$ behaves like $<v_{rms}>/U$; it increases up to a certain value then falls down abruptly.

Contours of the turbulence kinetic energy normalized by square of the freestream velocity, $<TKE>/U^2$ are presented in figures 4.52-4.54. In general, when yaw angle, β is given to delta wing, while on windward side $<TKE>/U^2$ value decreases, on the leeward side it increases. At an angle of attack $\alpha=25°$, for yaw angle $\beta=0°$, the values of $[<TKE>/U^2]_{max}$ is 0.24, for yaw angle $\beta=8°$ the $[<TKE>/U^2]_{max}$ takes the value of 0.44 and all yaw angles higher than 12° the $[<TKE>/U^2]_{max}$ values becomes almost 0.3. At angle of attack $\alpha=30°$, for yaw angle $\beta=0°$, the $[<TKE>/U^2]_{max}$ is equal to 0.20, for yaw angle $\beta=4°$ the $[<TKE>/U^2]_{max}$ gets a higher value for example, 0.30 and all yaw angles, β which are higher than 8° the $[<TKE>/U^2]_{max}$ gets almost 0.2 numerical value. At an angle of attack $\alpha=35°$, for yaw angle $\beta=0°$, the $[<TKE>/U^2]_{max}$ has 0.22 value. But in the case of yawing delta wing cause higher velocity fluctuations over delta wing in some regions, for example for yaw angle $\beta=4°$ the value of $[<TKE>/U^2]_{max}$ is 0.32 and all yaw angles higher than 8° the $[<TKE>/U^2]_{max}$ value is almost equal to 0.24.

Lower TKE values on the windward side take place because of low fluctuations of velocity components in this region. Even, If contours of time-averaged velocity components $<u>/U$, $<v>/U$ are examined carefully, it can be seen that these values are also very low.

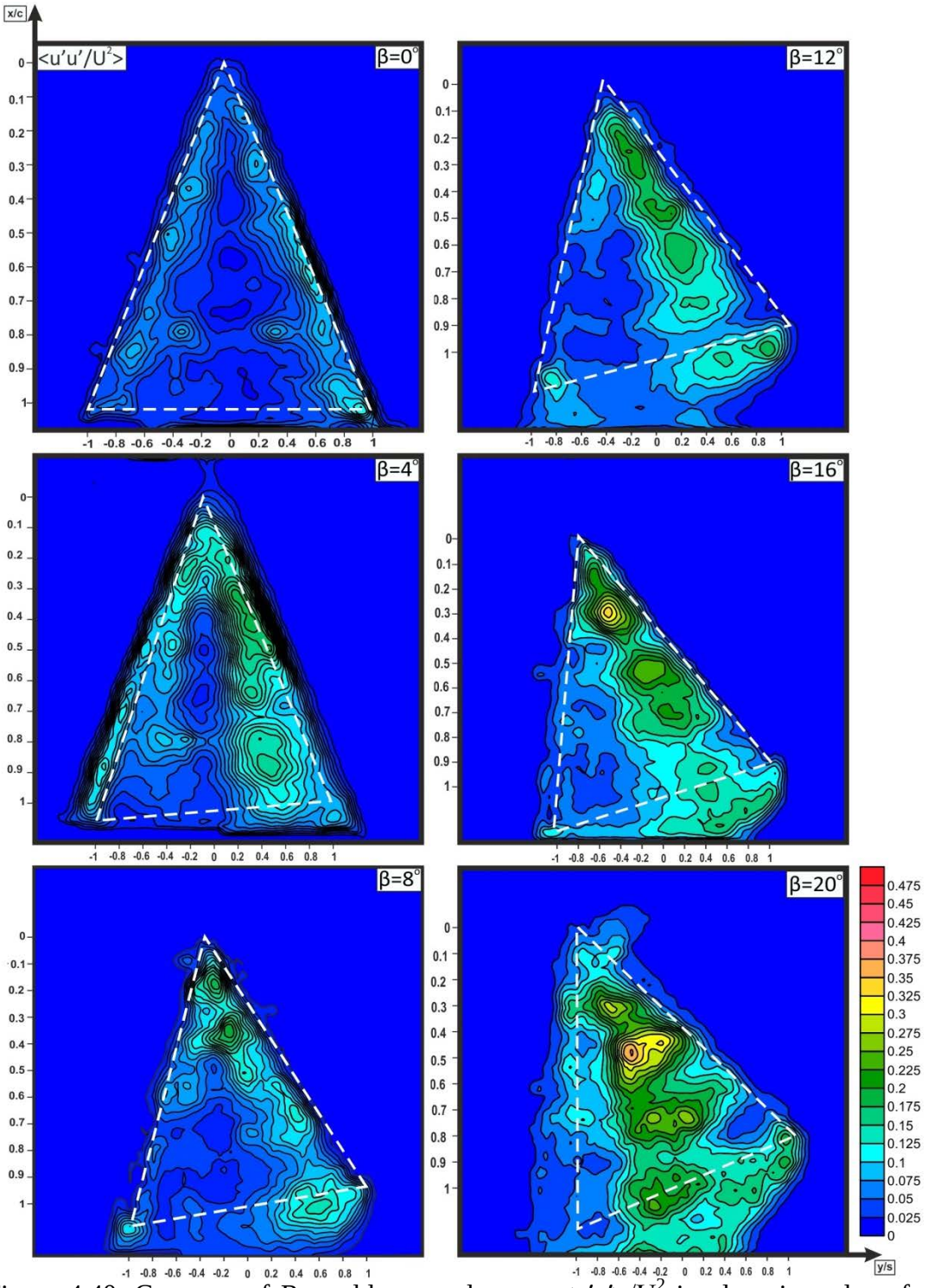

Figure 4.40. Contours of Reynolds normal stress $\langle u'u' \rangle / U^2$ in plan-view plane for angle of attack $\alpha=25°$ and yaw angle within the range of $0° \leq \beta \leq 20°$. Minimum and maximum values, $[\langle u'u' \rangle / U^2]_{min}=0.025$ and $\Delta[\langle u'u' \rangle / U]=0.025$ respectively.

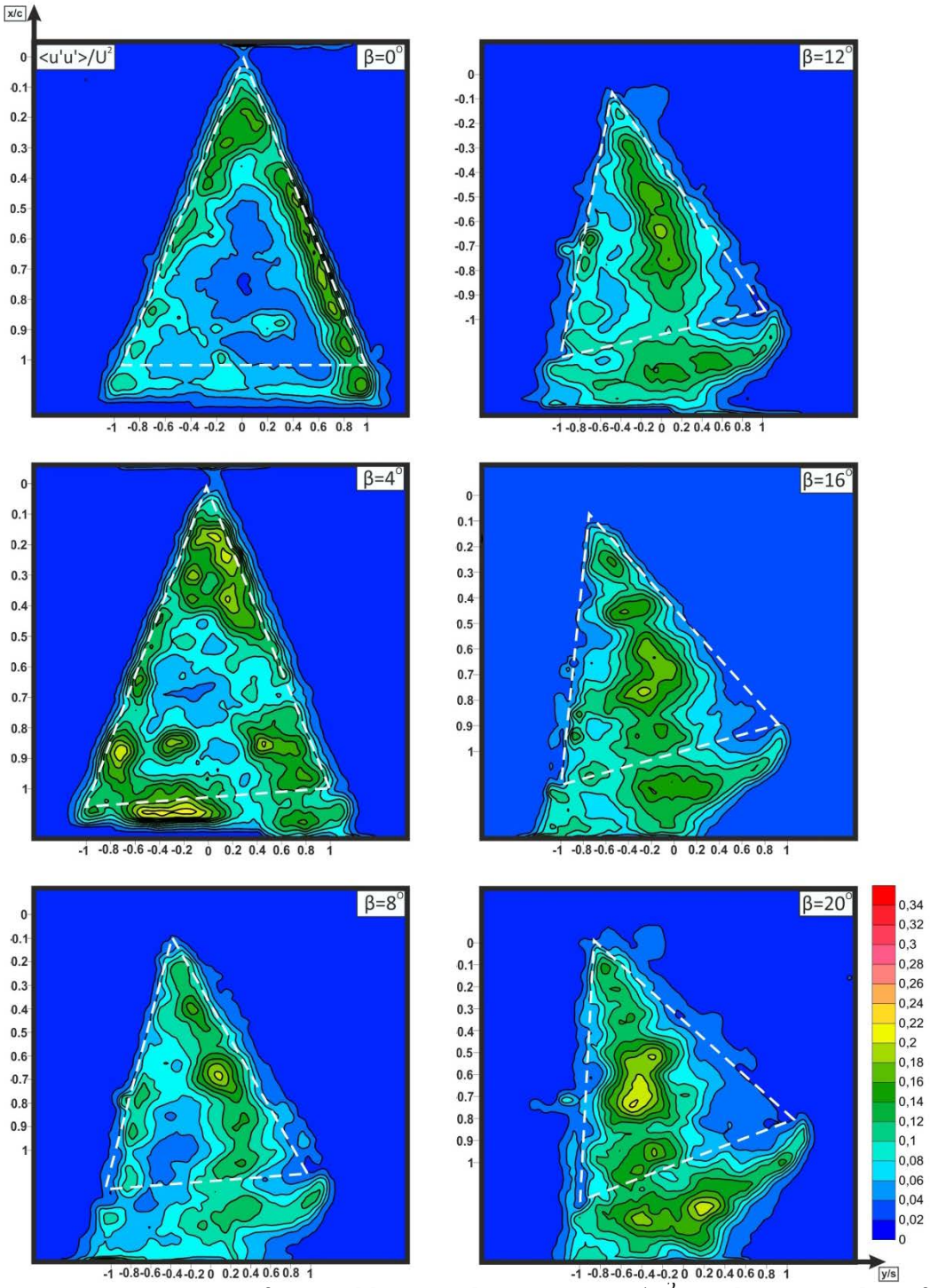

Figure 4.41. Contours of Reynolds normal stress $\langle u'u' \rangle / U^2$ in plan-view plane for angle of attack $\alpha=30°$ and yaw angle within the range of $0° \leq \beta \leq 20°$. Minimum and maximum values, $[\langle u'u' \rangle / U^2]_{min}=0.02$ and $\Delta[\langle u'u' \rangle / U^2]=0.02$ respectively.

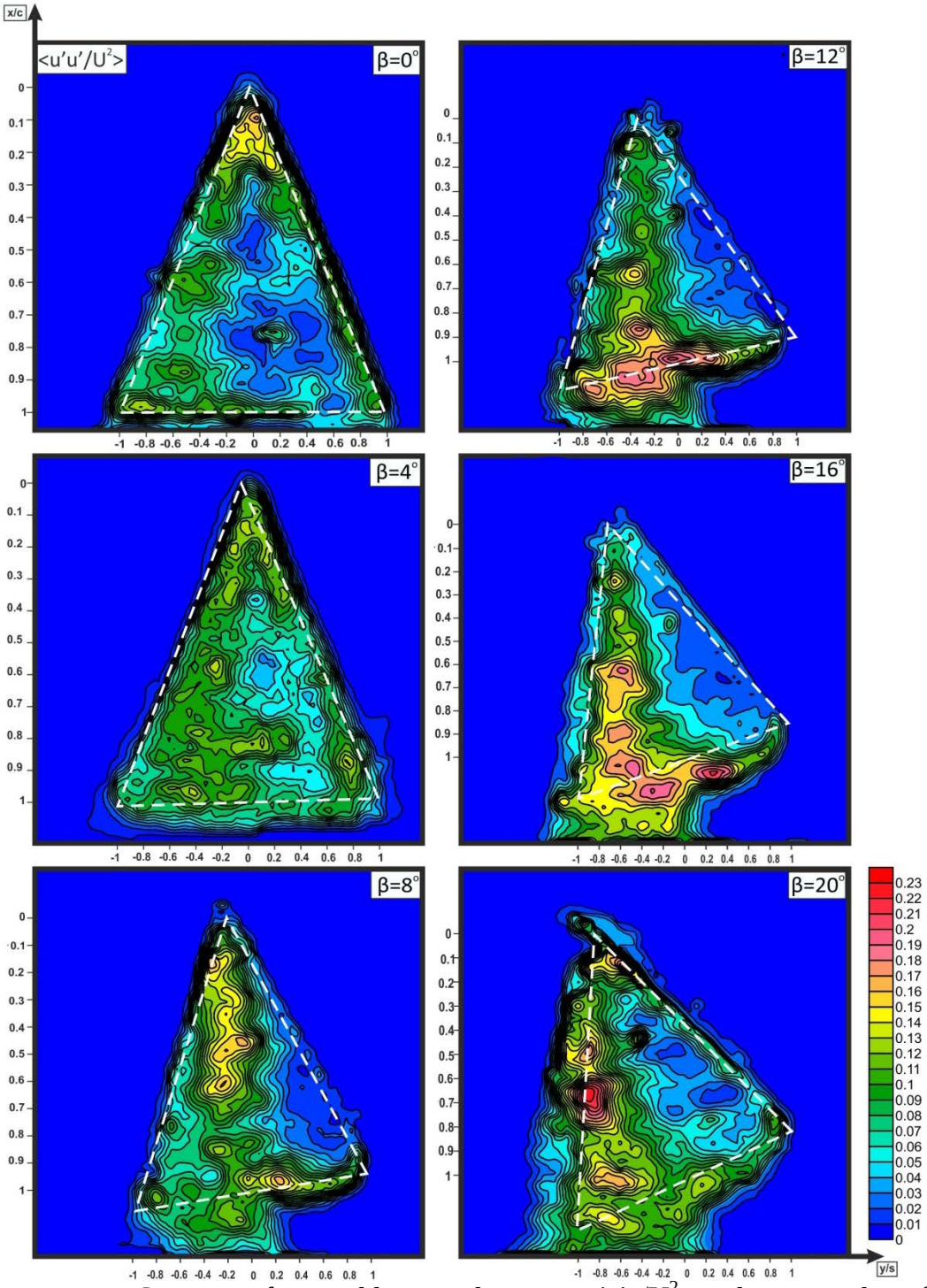

Figure 4.42. Contours of Reynolds normal stress $\langle u'u' \rangle / U^2$ in plan-view plane for angle of attack $\alpha=35°$ and yaw angle within the range of $0° \leq \beta \leq 20°$. Minimum and maximum values, $[\langle u'u' \rangle / U^2]_{min}=0.01$ and $\Delta[\langle u'u' \rangle / U^2]=0.01$ respectively.

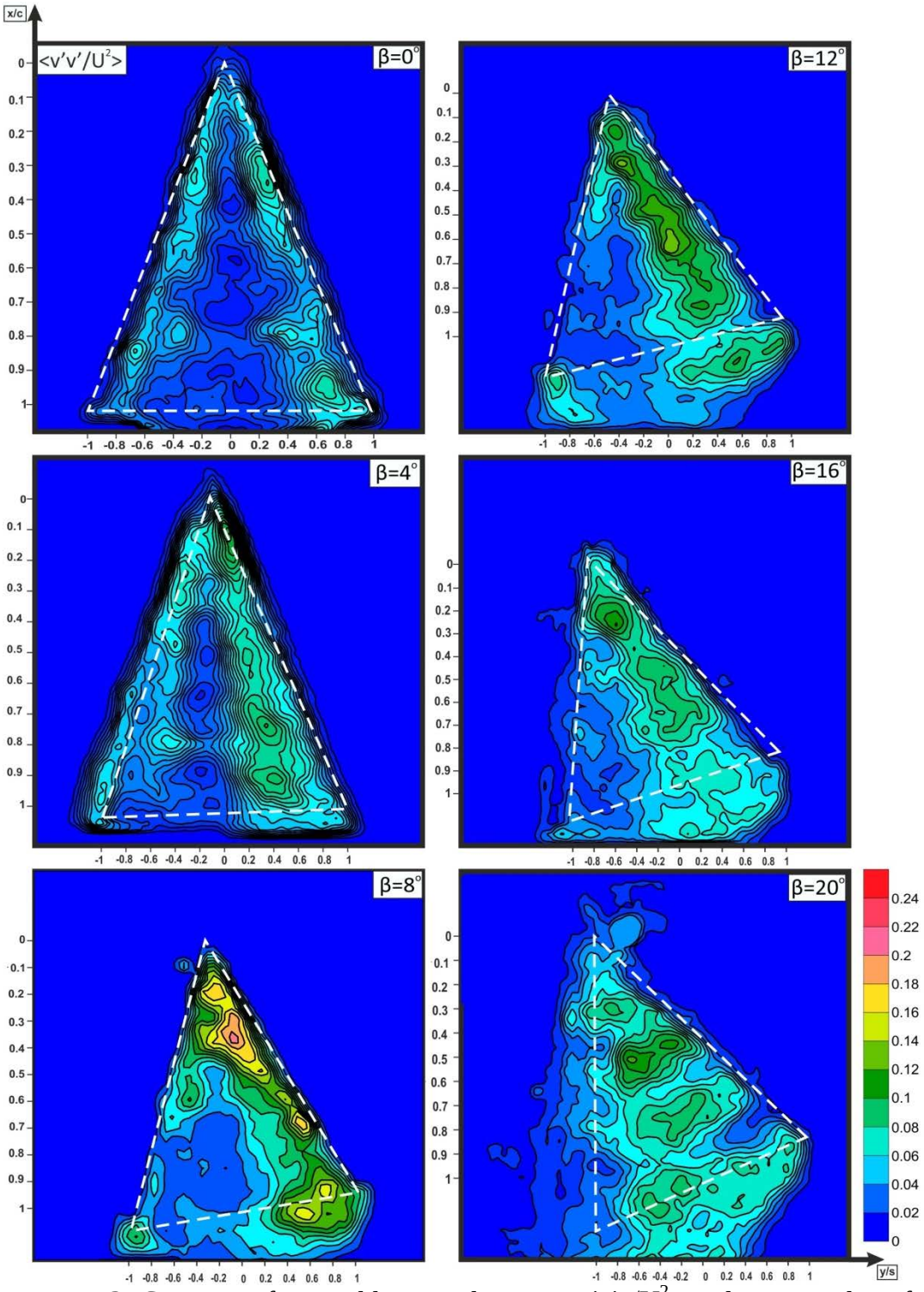

Figure 4.43. Contours of Reynolds normal stress $\langle v'v' \rangle / U^2$ in plan-view plane for angle of attack $\alpha=25°$ and yaw angle within the range of $0° \leq \beta \leq 20°$. Minimum and maximum values, $[\langle v'v' \rangle / U^2]_{min}=0.02$ and $\Delta[\langle v'v' \rangle / U^2]=0.02$ respectively.

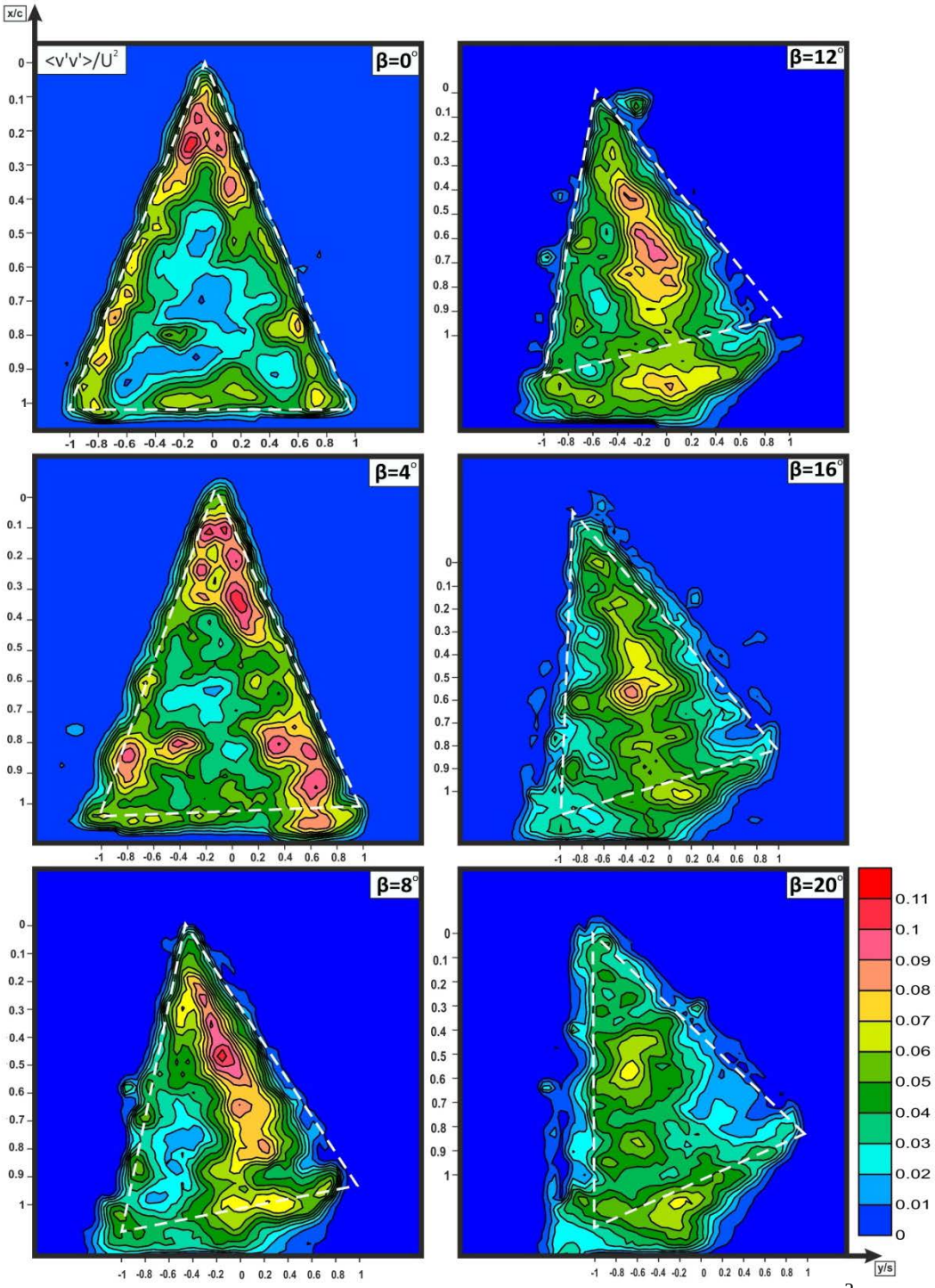

Figure 4.44. Time-averaged contours of Reynolds normal stress $\langle v'v' \rangle / U^2$ in plan-view plane for angle of attack $\alpha=30°$ and yaw angle within range of the $0° \leq \beta \leq 20°$. Minimum and maximum values, $[\langle v'v' \rangle / U^2]_{min}=0.01$and $\Delta[\langle v'v' \rangle / U^2]=0.01$ respectively.

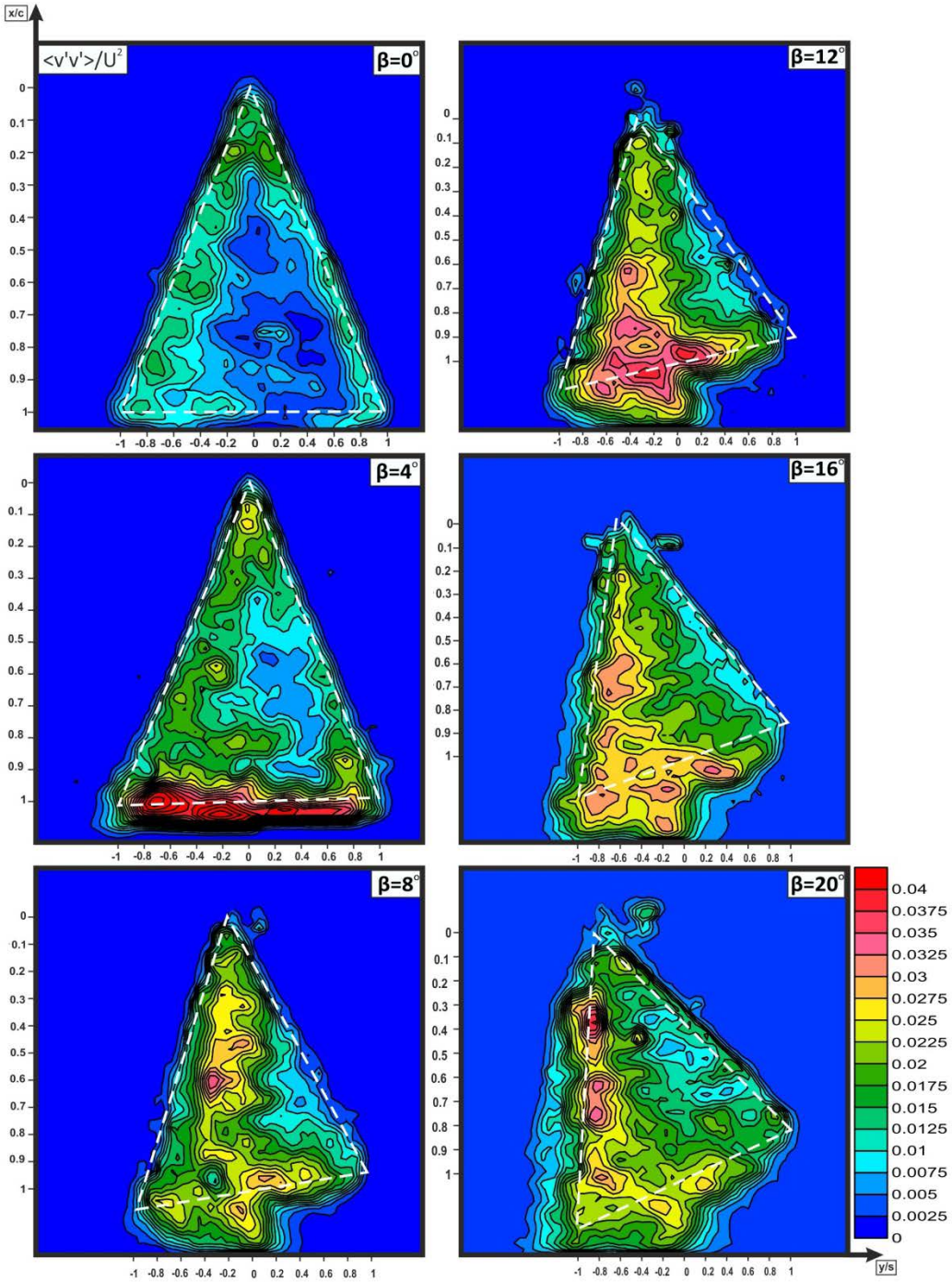

Figure 4.45. Time-averaged contours of Reynolds normal stress $\langle v'v' \rangle / U^2$ in plan-view plane for angle of attack $\alpha=35°$ and yaw angle within the range of $0° \leq \beta \leq 20°$. Minimum and maximum values, $[\langle v'v' \rangle / U^2]_{min}=0.0025$ and $\Delta[\langle v'v' \rangle / U^2]=0.0025$ respectively.

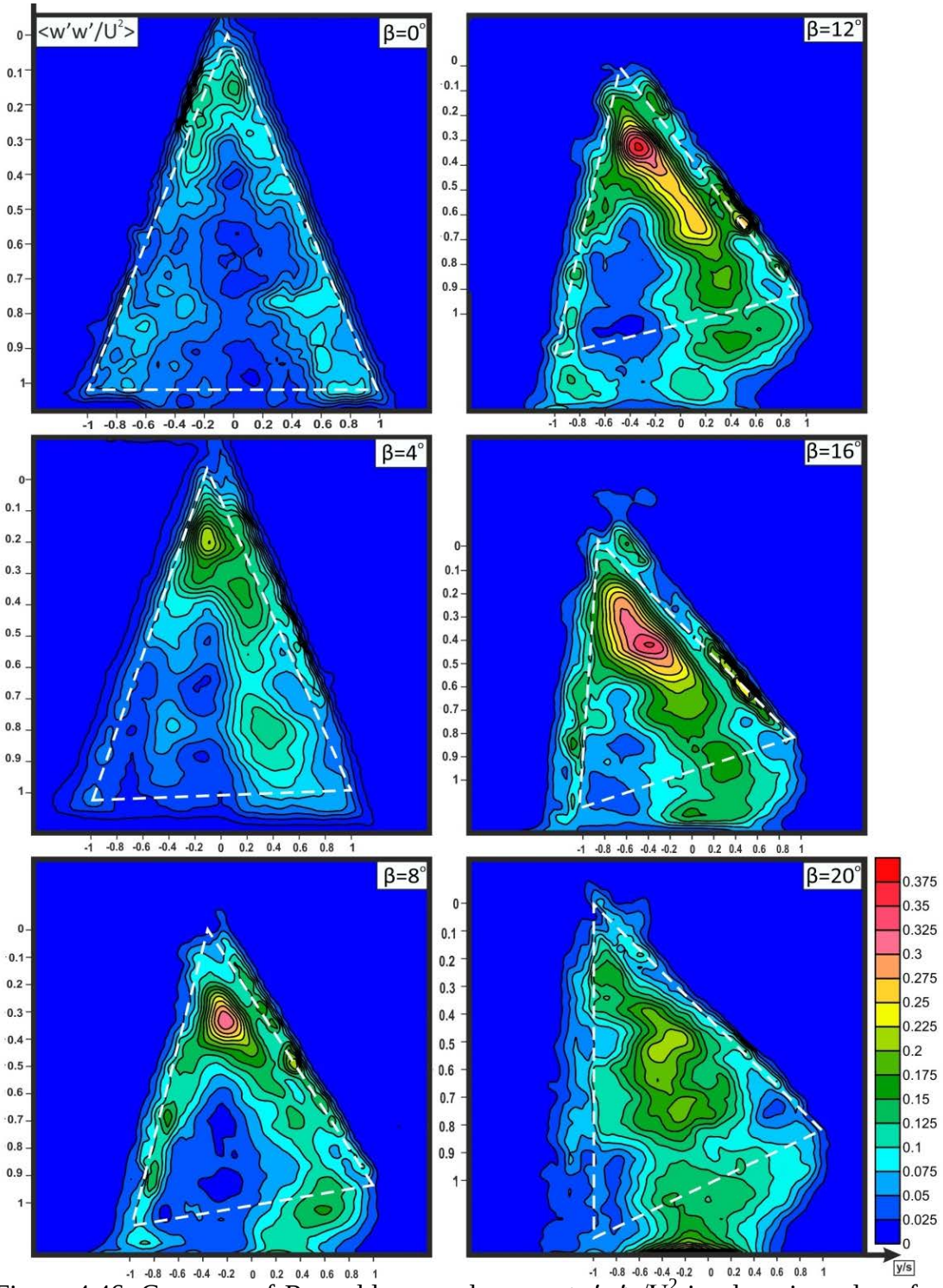

Figure 4.46. Contours of Reynolds normal stress $\langle w'w'\rangle/U^2$ in plan-view plane for angle of attack $\alpha=25°$ and yaw angle within the range of $0°\leq\beta\leq20°$. Minimum and maximum values, $[\langle w'w'\rangle/U^2]_{min}=0.025$ and $\Delta[\langle w'w'\rangle/U^2]=0.025$ respectively.

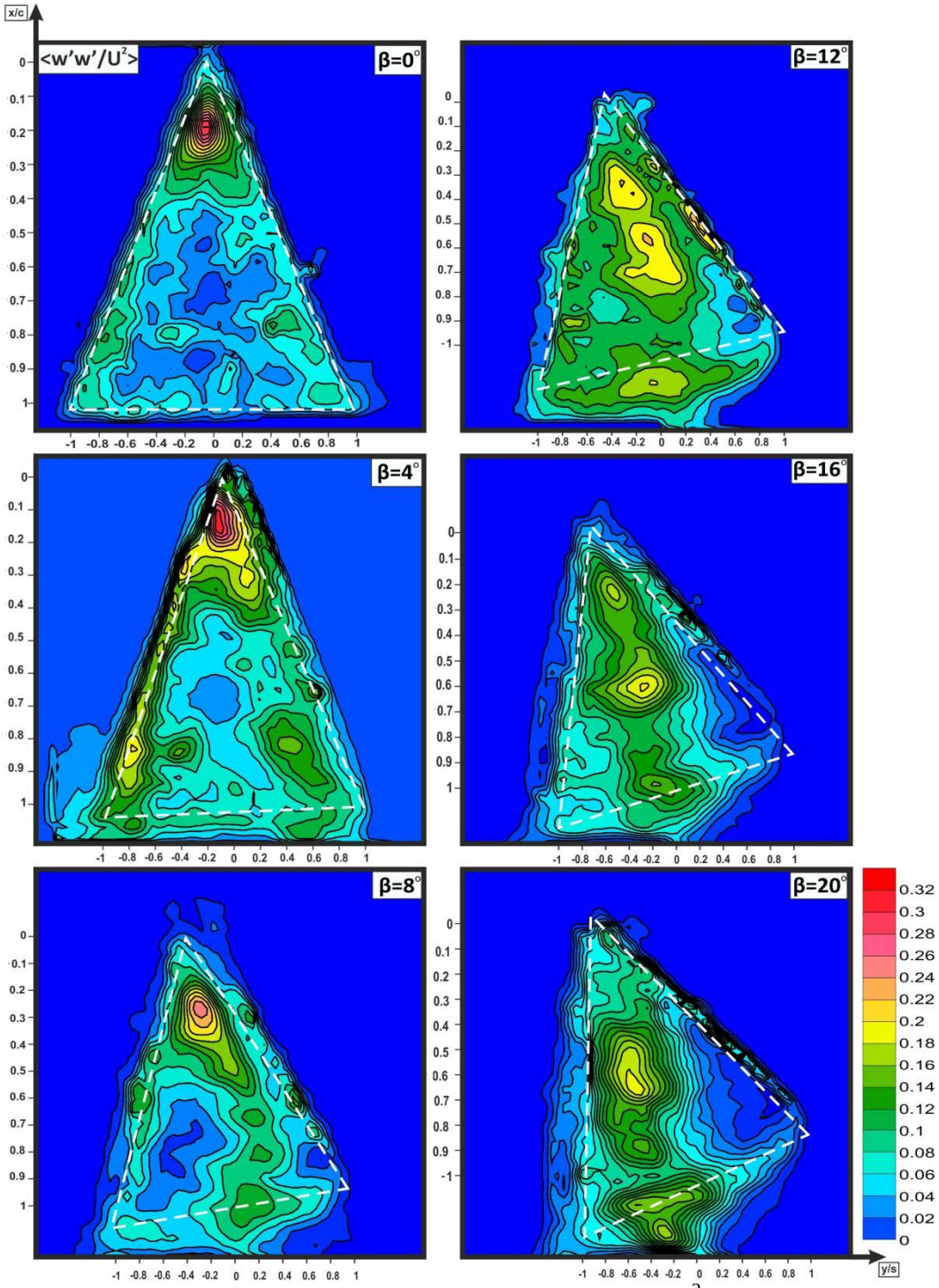

Figure 4.47. Contours of Reynolds normal stress $\langle w'w' \rangle / U^2$ in plan-view plane for angle of attack $\alpha=30°$ and yaw angle within the range of $0° \leq \beta \leq 20°$. Minimum and maximum values, $[\langle w'w' \rangle / U^2]_{min}=0.02$ and $\Delta[\langle w'w' \rangle / U^2]=0.02$ respectively.

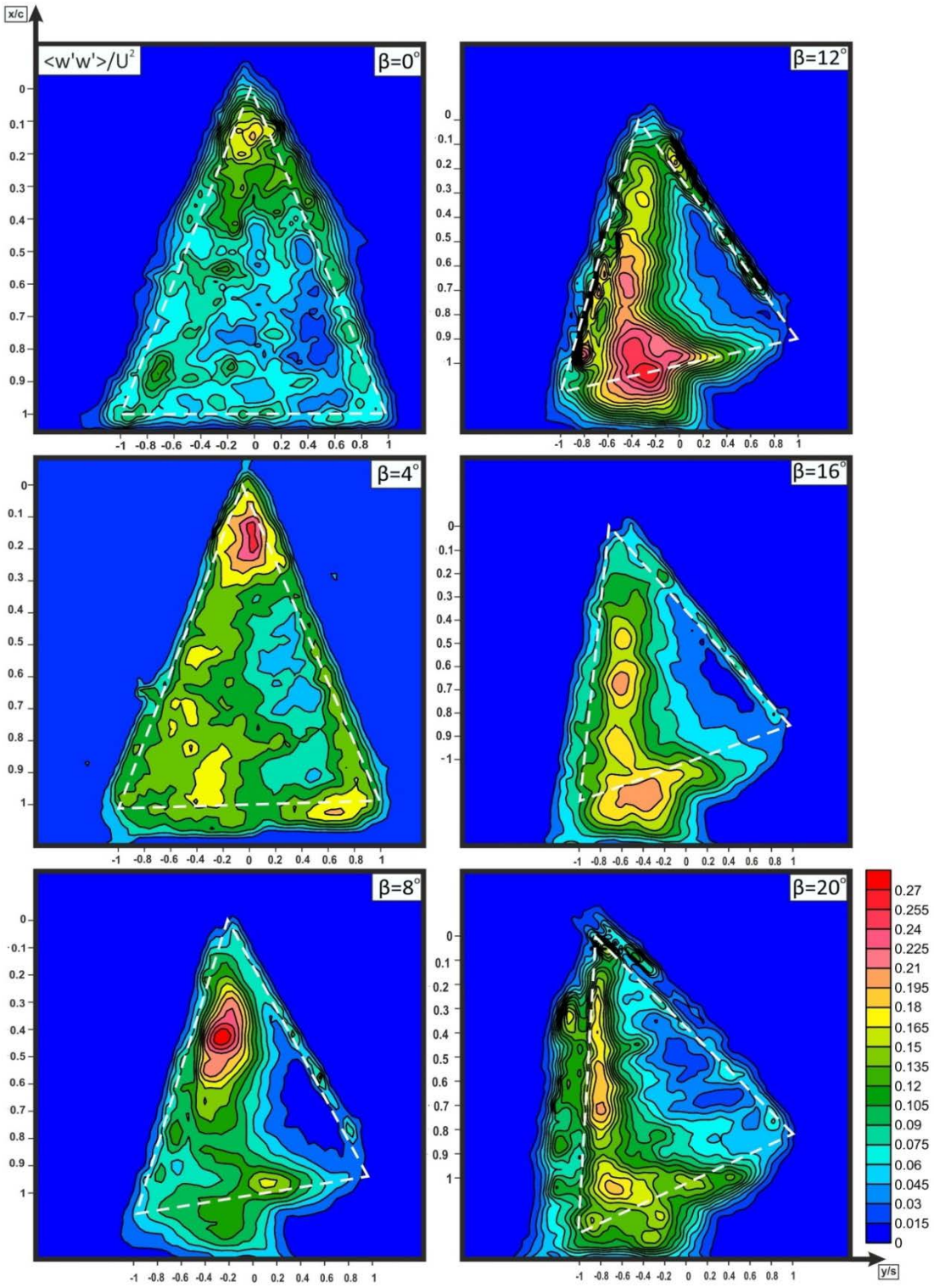

Figure 4.48. Contours of Reynolds normal stress $\langle w'w' \rangle / U^2$ in plan-view plane for angle of attack $\alpha=35°$ and yaw angle within the range of $0° \leq \beta \leq 20°$. Minimum and maximum values, $[\langle w'w' \rangle / U^2]_{min}=0.015$ and $\Delta[\langle w'w' \rangle / U^2]=0.015$ respectively.

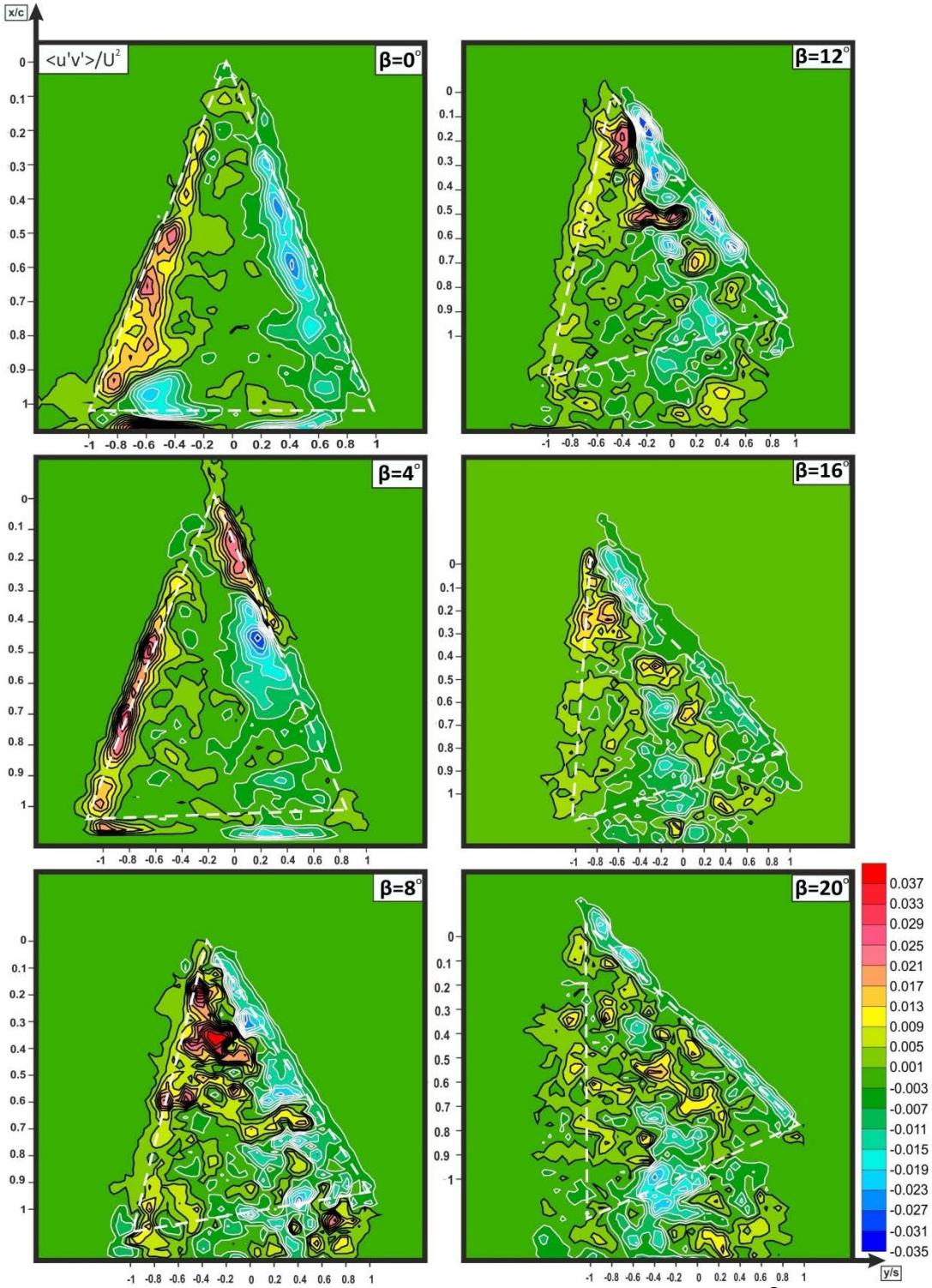

Figure 4.49. Time-averaged contours of Reynolds stress $\langle u'v' \rangle / U^2$ in plan-view plane for angle of attack $\alpha=25°$ and yaw angle within the range of $0° \leq \beta \leq 20°$. Minimum and maximum values, $[\langle u'v' \rangle / U^2]_{min}=0.001$ and $\Delta[\langle u'v' \rangle / U^2]=0.004$ respectively.

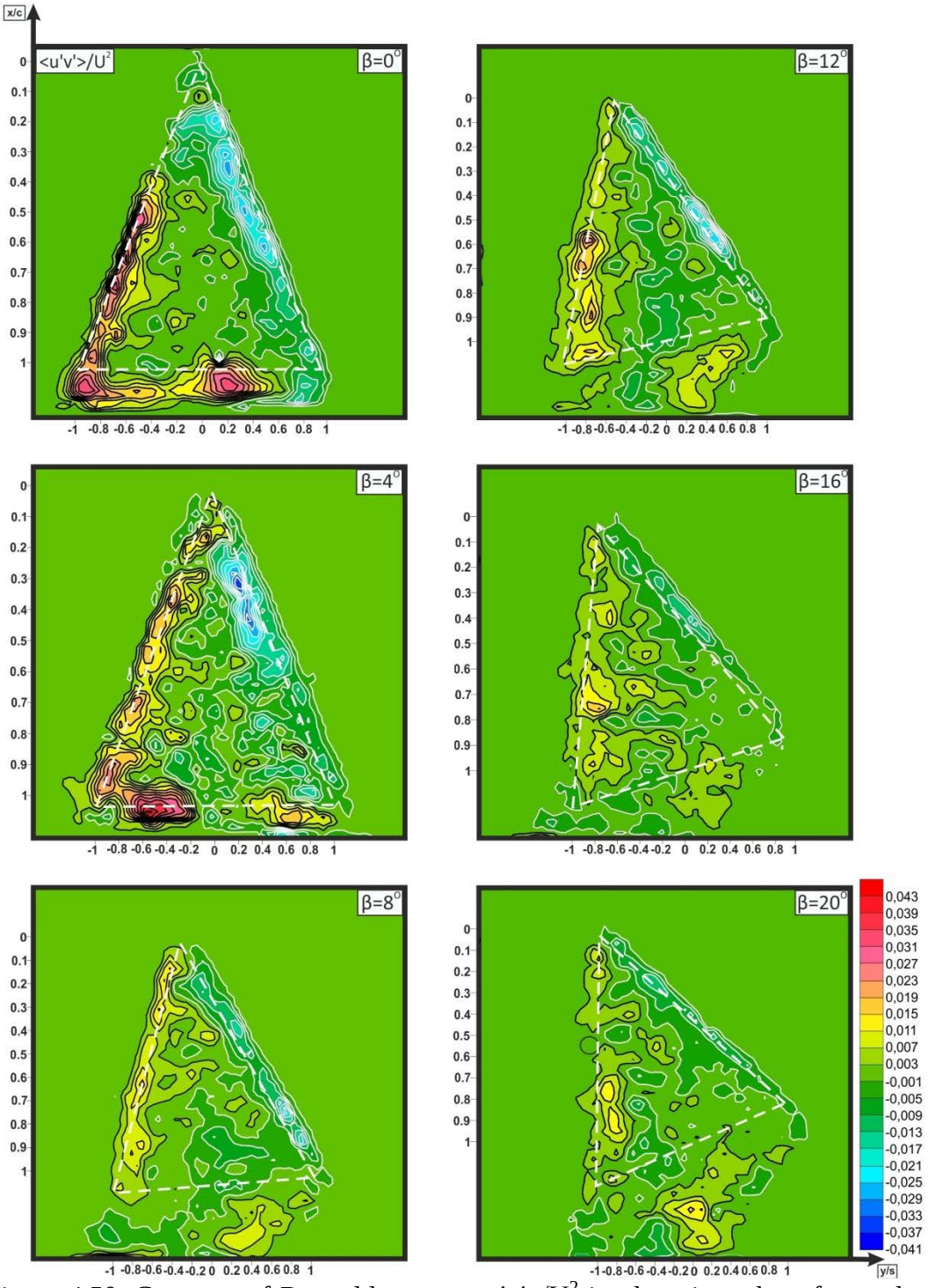

Figure 4.50. Contours of Reynolds stress $\langle u'v' \rangle / U^2$ in plan-view plane for angle of attack $\alpha=30°$ and yaw angle within the range of $0° \leq \beta \leq 20°$. Minimum and maximum values, $[\langle u'v' \rangle / U^2]_{min}=0.003$ and $\Delta[\langle u'v' \rangle / U^2]=0.004$ respectively.

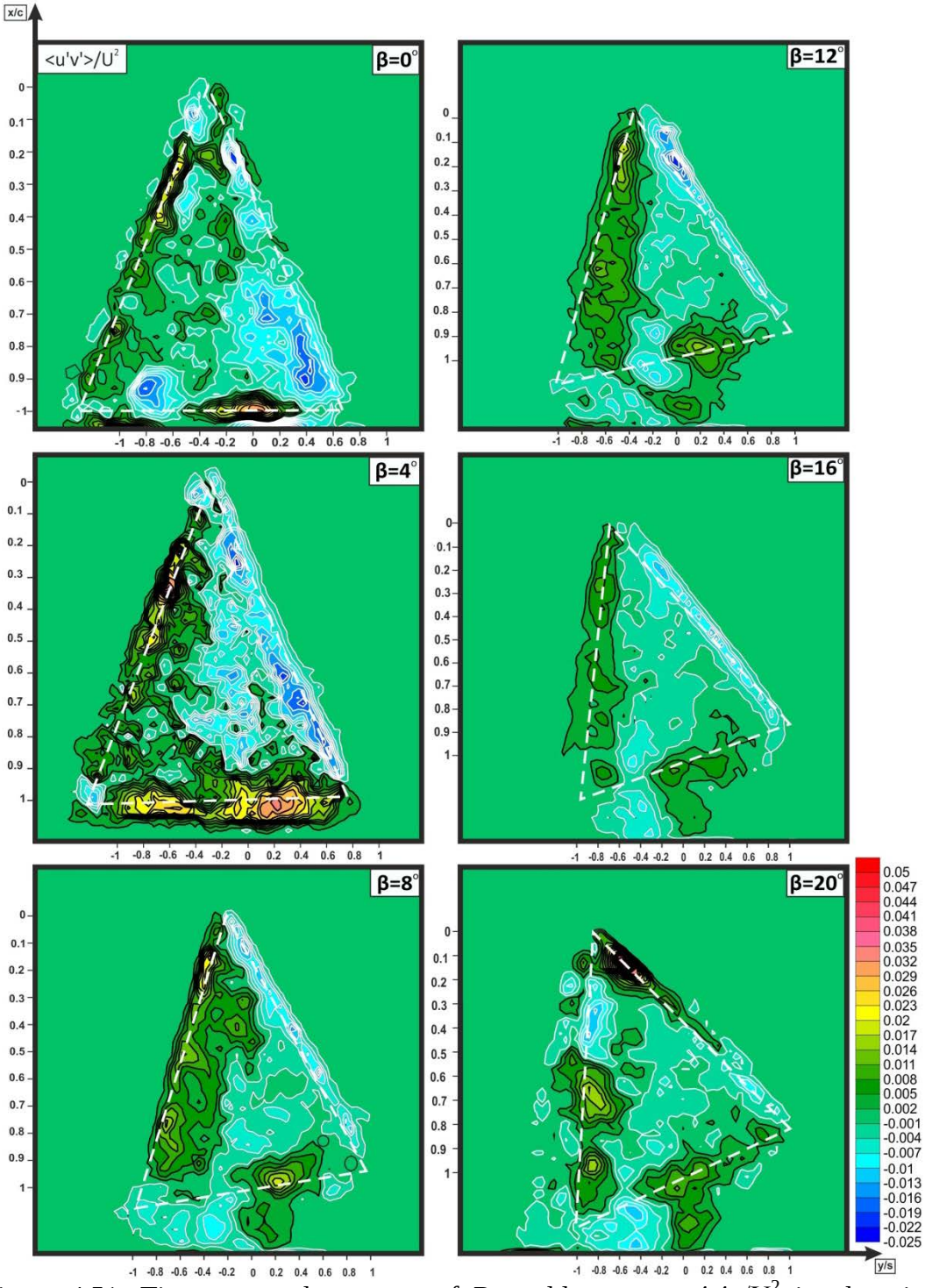

Figure 4.51. Time-averaged contours of Reynolds stress $\langle u'v' \rangle / U^2$ in plan-view plane for angle of attack $\alpha=35°$ and yaw angle within the range of $0° \leq \beta \leq 20°$. Minimum and maximum values, $[\langle u'v' \rangle / U^2]_{min}=0.002$ and $\Delta[\langle u'v' \rangle / U^2]=0.003$ respectively.

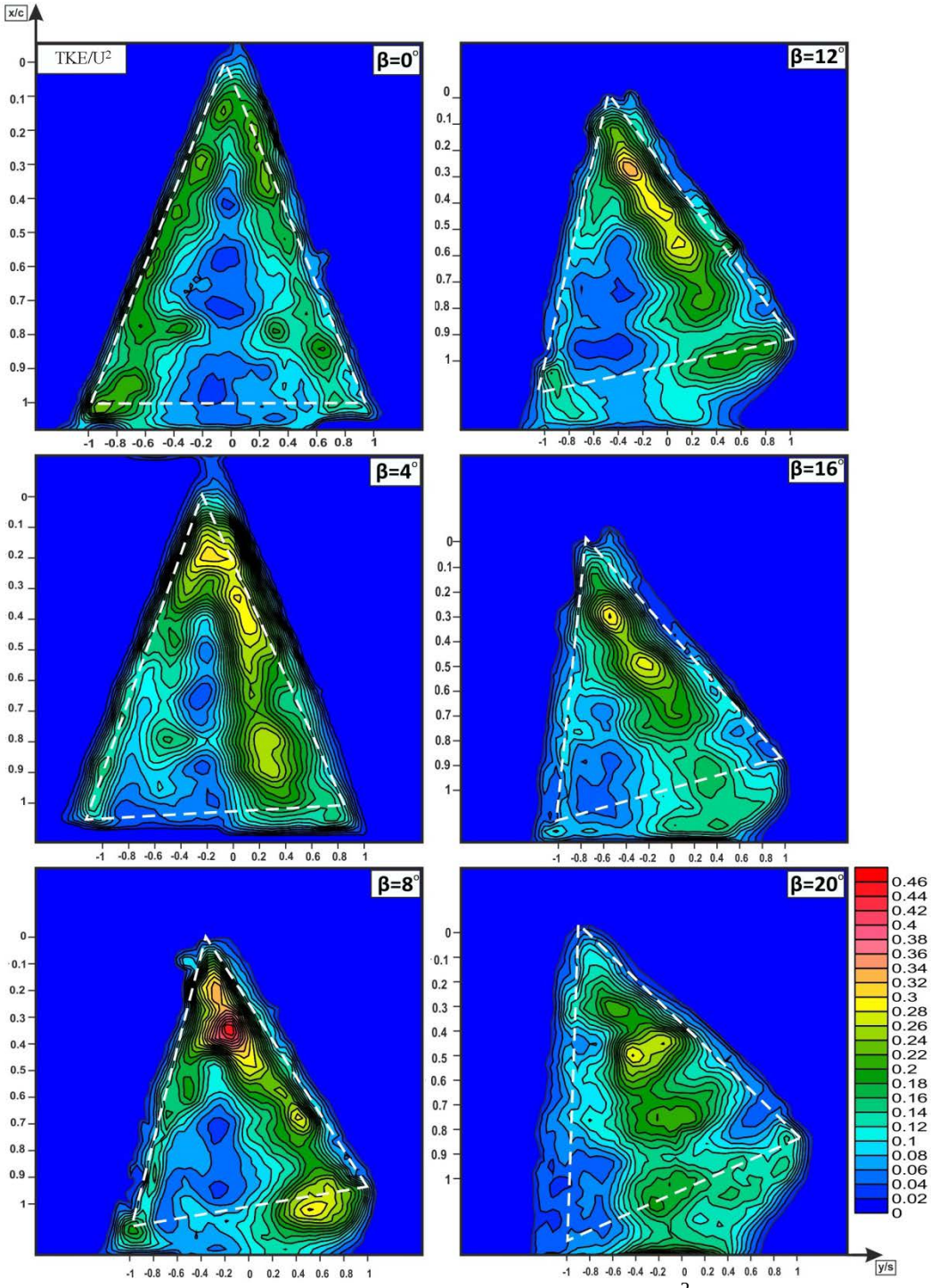

Figure 4.52. Contours of turbulence kinetic energy $\langle TKE \rangle / U^2$ in plan-view plane for angle of attack $\alpha=25°$ and yaw angle within the range of $0° \leq \beta \leq 20°$. Minimum and maximum value of $[\langle TKE/U^2 \rangle]_{min}= 0.02$ and $[\langle TKE/U^2 \rangle]= 0.02$ respectively.

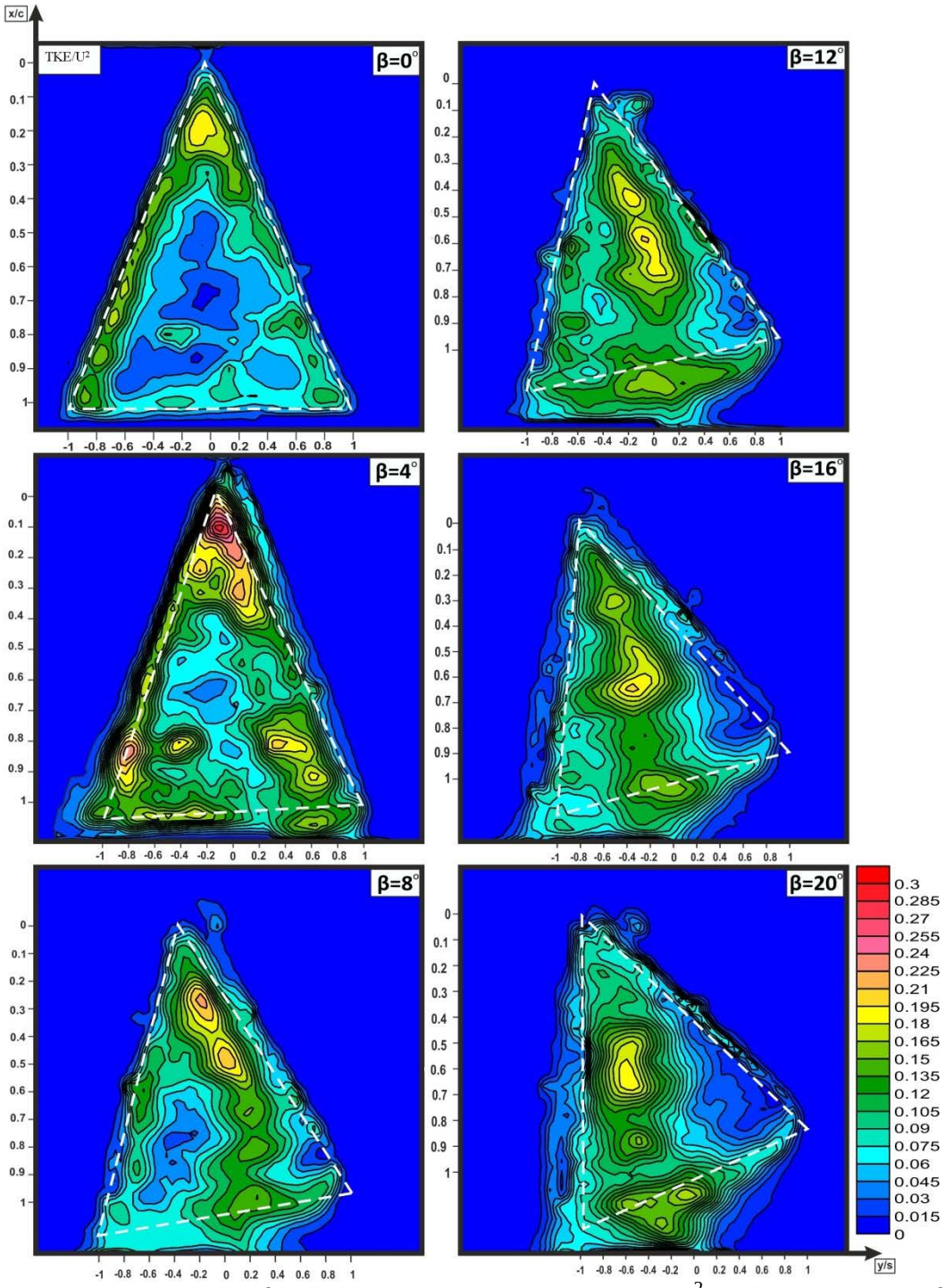

Figure 4.53. Contours of turbulence kinetic energy $\langle TKE \rangle / U^2$ in plan-view plane for angle of attack $\alpha=30°$ and yaw angle within the range of $0° \leq \beta \leq 20°$. Minimum and maximum value of $[\langle TKE/U^2 \rangle]_{min} = 0.015$ and $[\langle TKE/U^2 \rangle] = 0.015$ respectively.

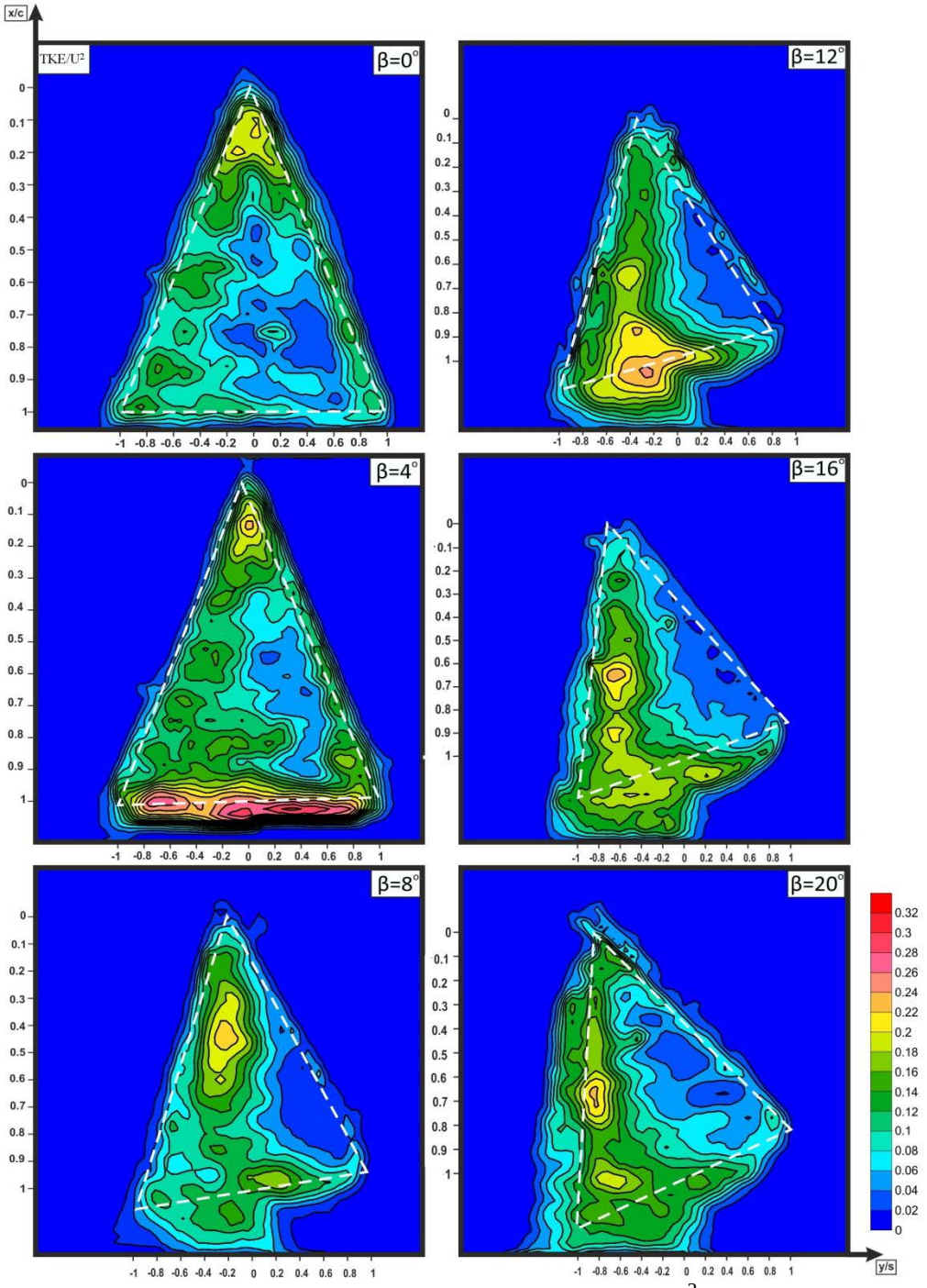

Figure 4.54. Contours of turbulence kinetic energy $\langle TKE \rangle / U^2$ in plan-view plane for angle of attack $\alpha=35°$ and yaw angle within the range of $0° \leq \beta \leq 20°$. Minimum and maximum value of $[\langle TKE/U^2 \rangle]_{min}= 0.02$ and $[\langle TKE/U^2]= 0.02$ respectively.

4.3.2. Side view plane experiments

In this chapter, effects of yaw angle, β on windward side leading edge vortex were investigated in side-view plane. As angles of attack, α were chosen as 30° and 35° and yaw angles, β were selected as 0°,4°,12° and 20°. Laser reflection region near the apex of the delta wing was masked in order to avoid misreading.

In this section time-averaged velocity vectors, <V>, streamlines, <Ψ>, vorticity <ω>, and u and w velocity components and velocity fluctuations of the windward side leading edge vortex were examined. In addition to plan-view plane experiments, side-view experiments revealed that large scale vortices occurred in windward side after onset of vortex breakdown interacts with leeward leading edge vortex to cause 3-Dimensional flow structures.

4.3.2.1. Time-Averaged Vectors, Streamlines, and Vorticity Patterns

Figures 4.49 and 4.50 present time-averaged velocity vectors <V>, figures 4.55 and 4.56 show time-averaged streamlines <Ψ> and figures 4.57 and 4.58 show time-averaged vorticity contours. As can be seen in figures, streamlines with varying yaw angle, β flow characteristics changes dramatically in this plane. Moreover, leading edge vortex-delta wing interaction can be seen in this plane also. In this plane vortex breakdown takes place where positive and negative vorticity interchange the locations.

At an angle of attack α=30° and yaw angle β=0°, a divergent bifurcation line, L_i a saddle point, S and a foci, F take place. At yaw angle β=4°, a divergent bifurcation line, L_i, at yaw angle β=12° two divergent bifurcation lines L_i, at yaw angle β=20° a bifurcation line, a saddle point S and a focus F also occurs in the measurement plane.

At an angle of attack α=35° and yaw angle β=0°, a divergent bifurcation line L_i, moves towards a saddle point S or stagnation point where velocity along the axis of leading edge vortex becomes zero , and downstream of this saddle point focus F is developed. At a yaw angle β=4°, a convergent bifurcation line L_0 which indicates

that vortex breakdown moves towards the apex of delta wing and a focus F takes place. At higher yaw angles, β critical points cannot be seen over the cross section of measurement.

The numerical value of positive vorticity, $<\omega>$ which is indicated by a solid line is higher than negative vorticity values, $<\omega>$ which is designated with a dash line. As can be seen from figures maximum vorticity takes place along the in the forward region or close to the apex of the delta wing before onset of vortex breakdown. But downstream of this vortex breakdown a negative vorticity take place. As yaw angle, β $[<\omega>]_{max}$ is increased this onset of vortex breakdown moves towards the leading edge causing a large region of stall flow region which is indicated by a negative vorticity $[<\omega>]_{max}$

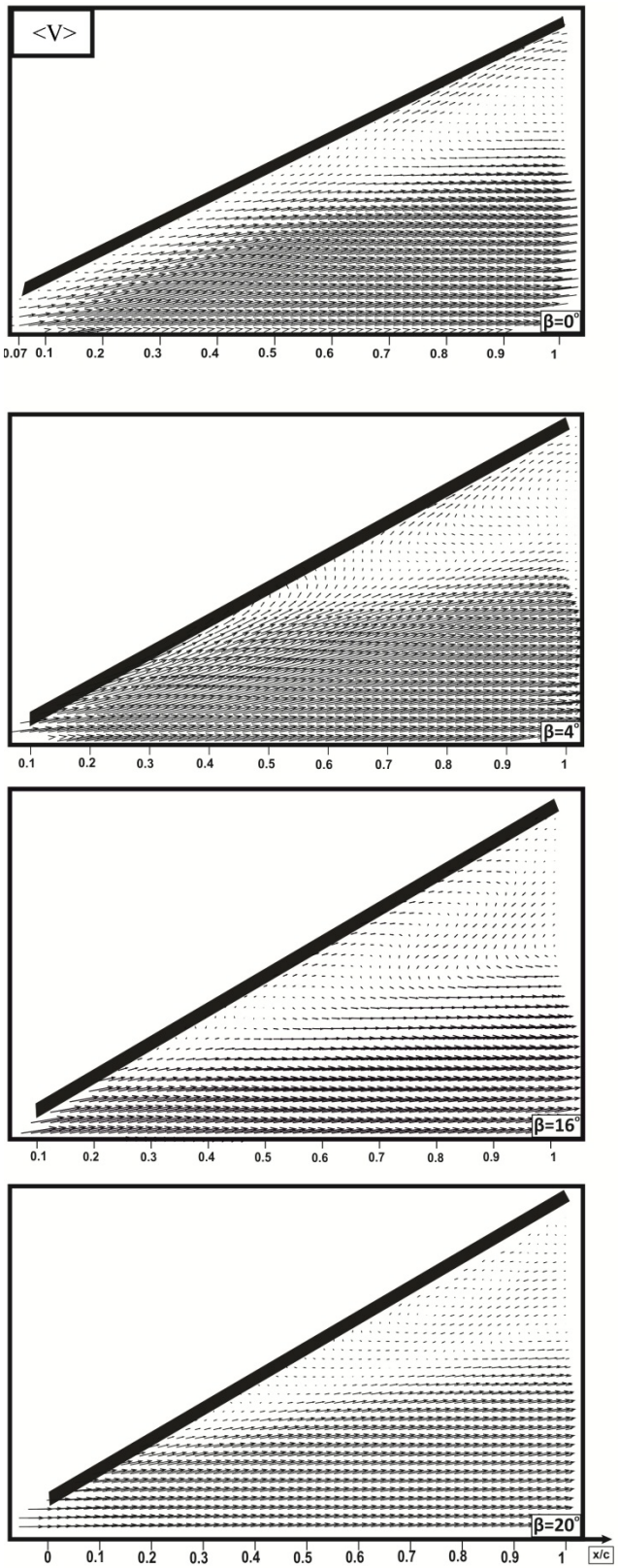

Figure 4.55. Patterns of time-averaged velocity vectors, <V> in side-view plane for angle of attack, α=30° and yaw angles within the range of 0°≤β≤20°.

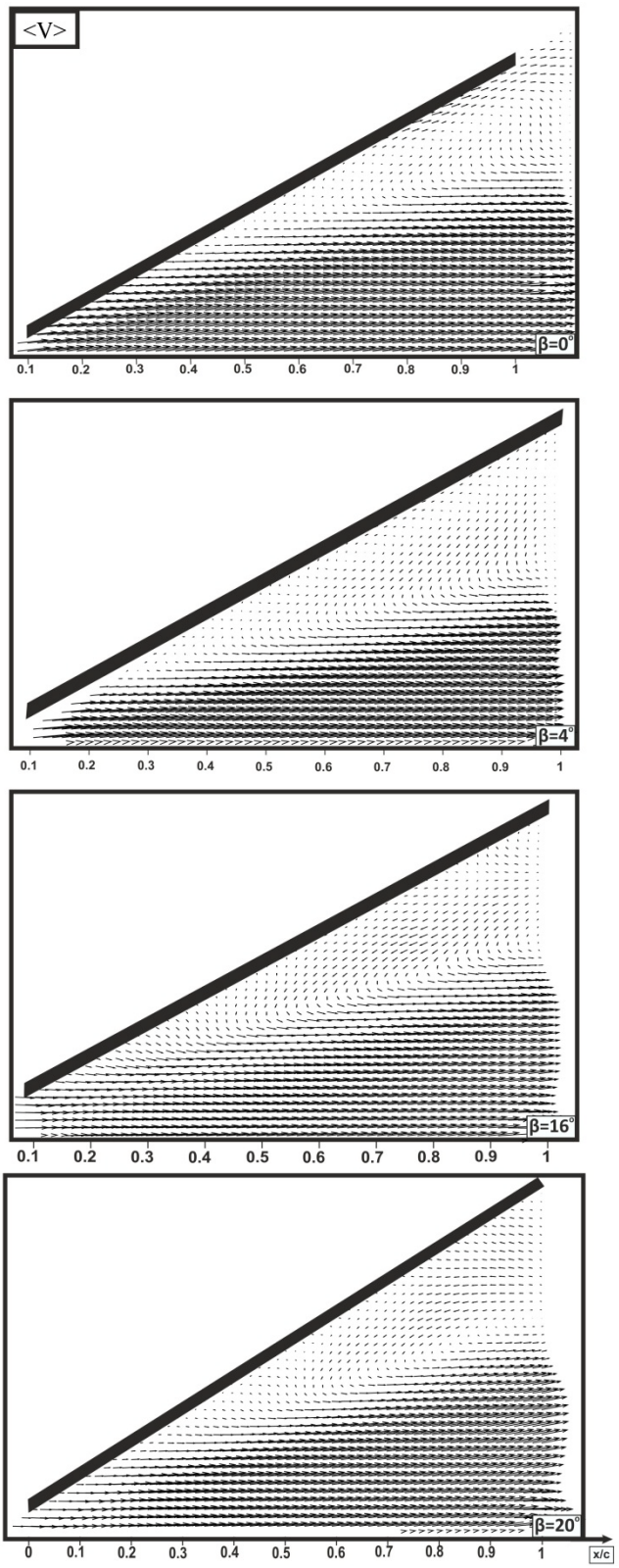

Figure 4.56. Patterns of time-averaged velocity vectors, <V> in side-view plane for angle of attack α=35° and yaw angles within the range of 0°≤β≤20°.

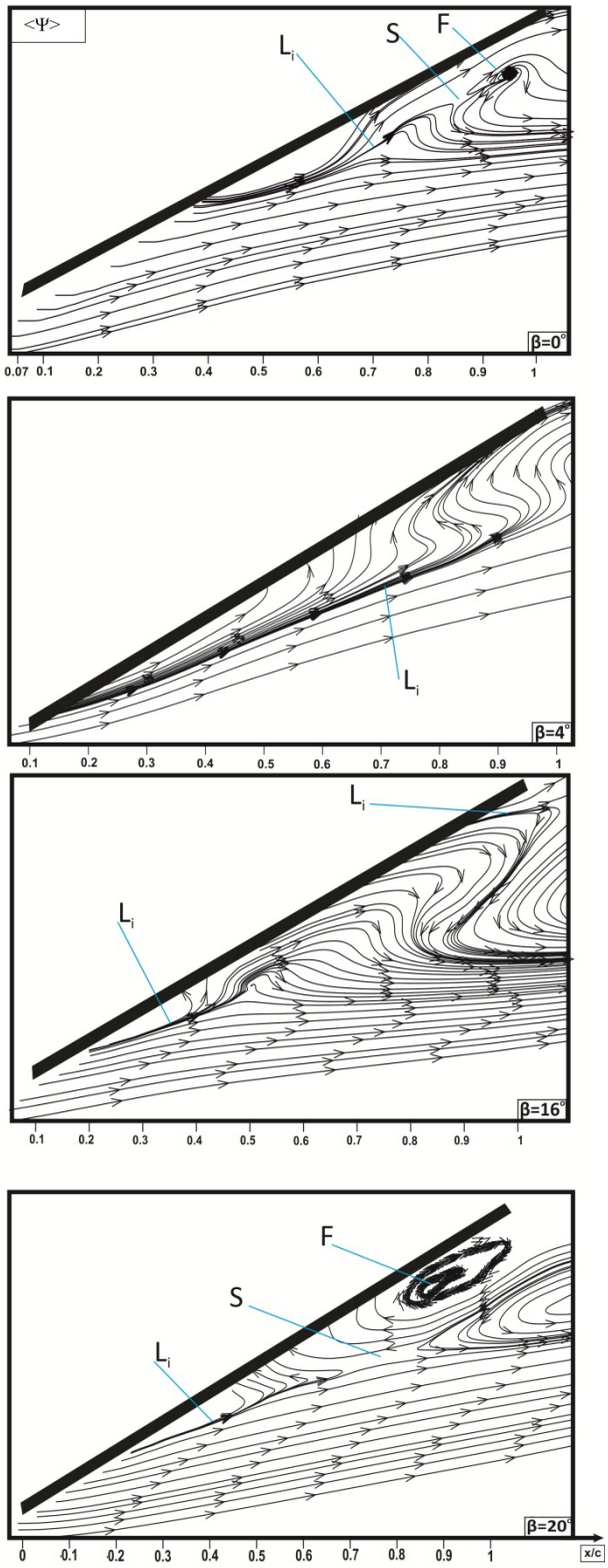

Figure 4.57. Patterns of time-averaged streamline <Ψ> in side-view plane for angle of attack α=30° and yaw angles within the range of 0°≤β≤20°.

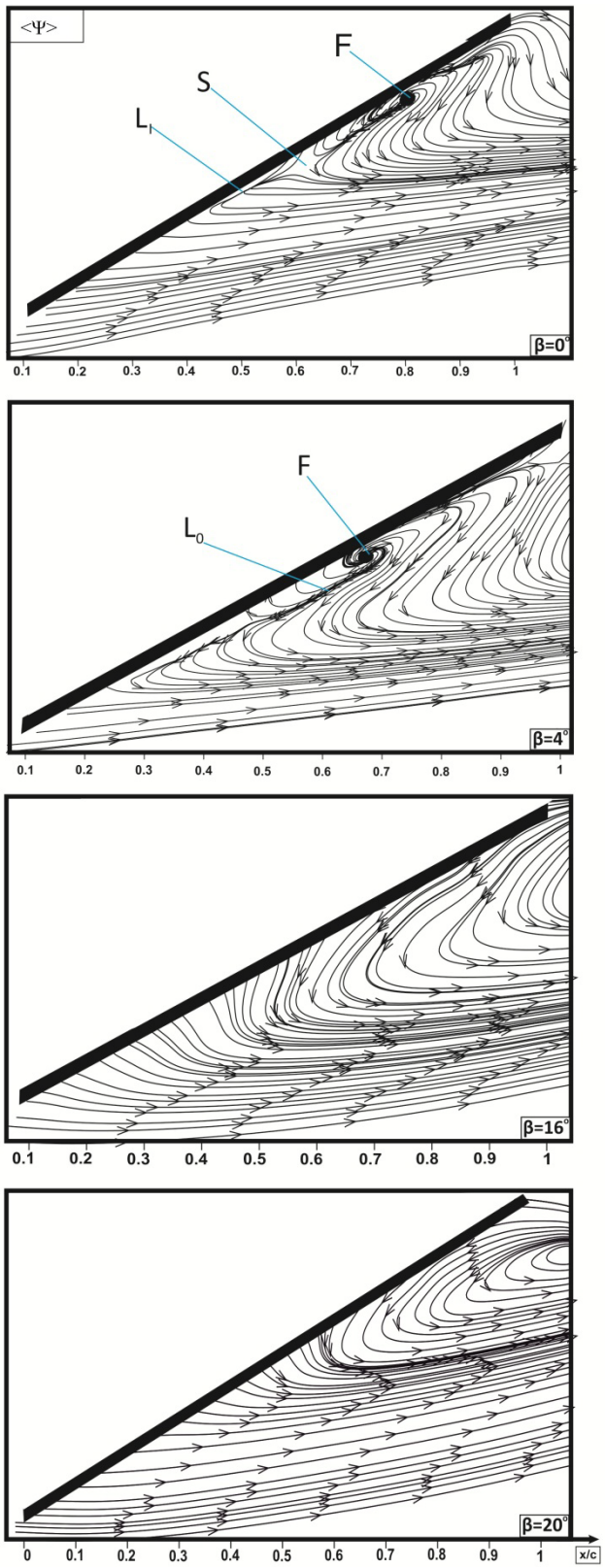

Figure 4.58. Patterns of time-averaged streamline, <Ψ> in side-view plane for angle of attack α=35° and yaw angles within the range of 0°≤β≤20°.

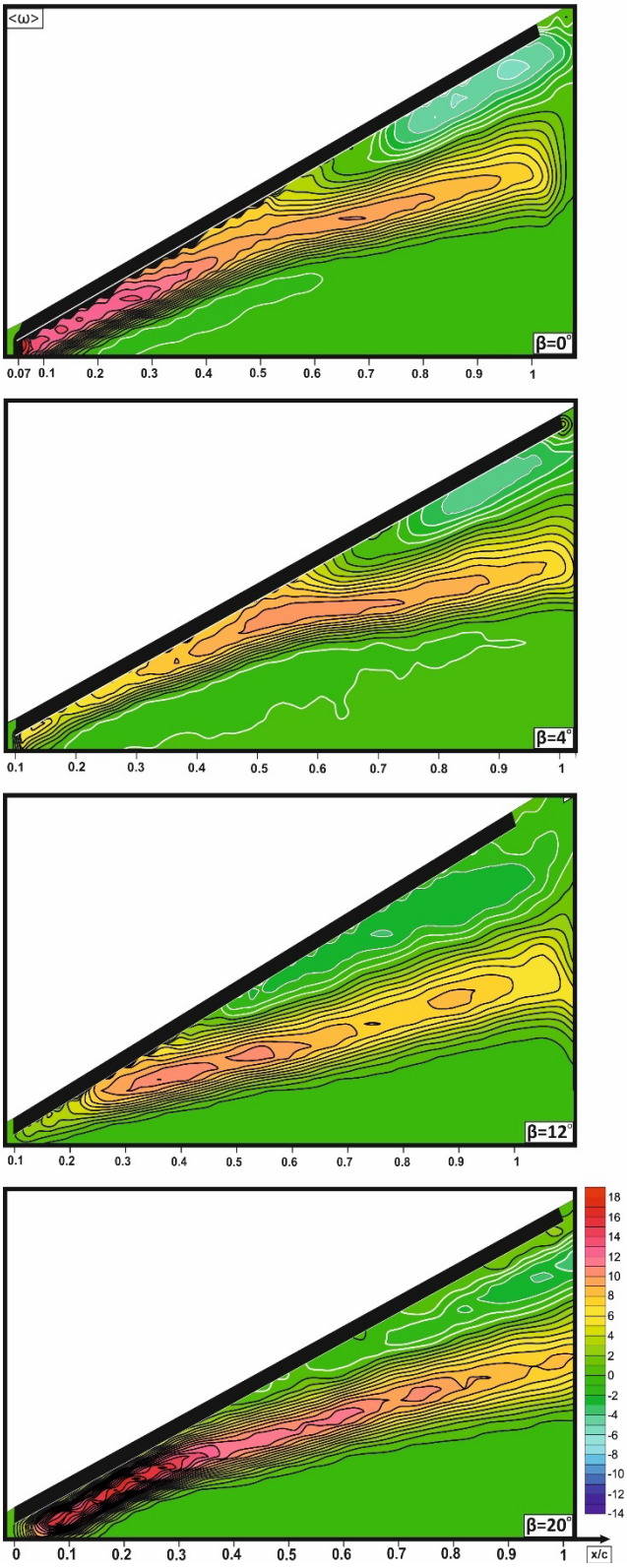

Figure 4.59. Contours of time-averaged vorticity, <ω> in side-view plane for angle of attack α=30° and yaw angles within the range of 0°≤β≤20°. Minimum and incremental values are $[<\omega>]_{min}=1$ and $\Delta[<\omega>]=1$.

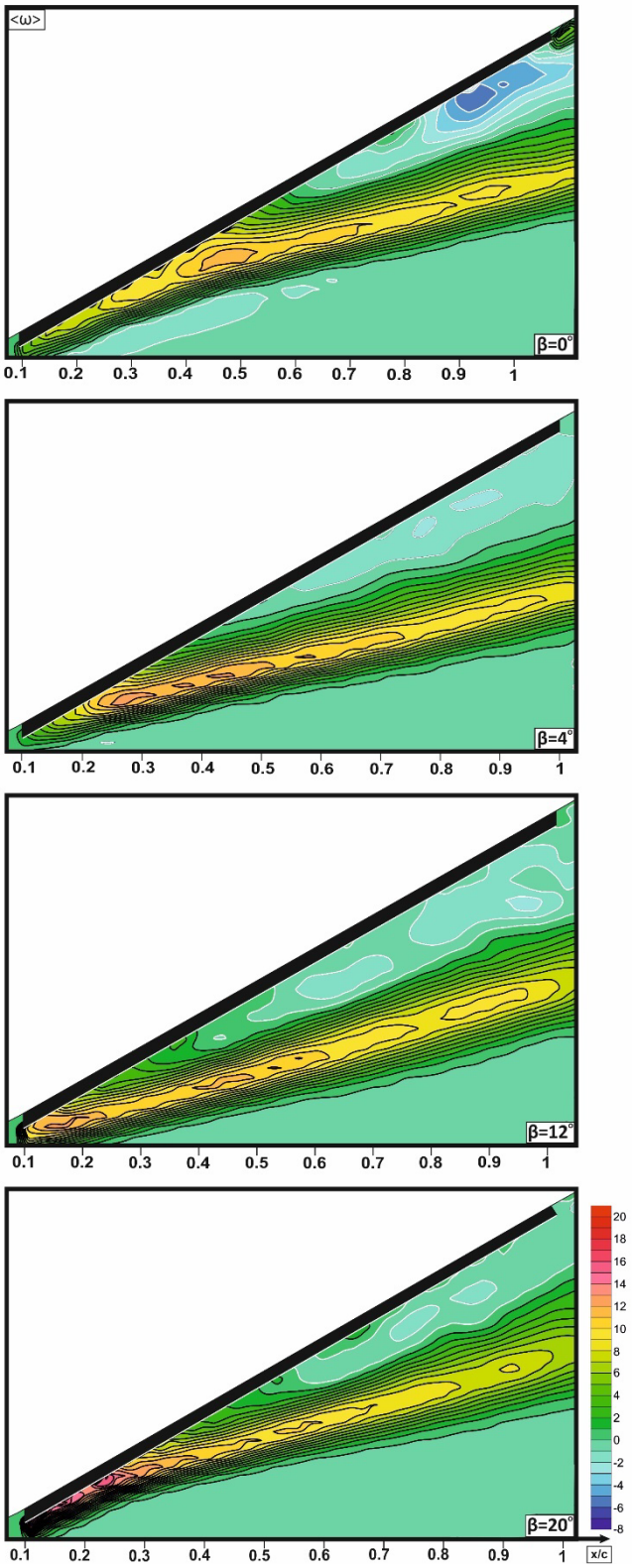

Figure 4.60. Contours of time-averaged vorticity, <ω> in side-view plane for angle of attack α=35° and yaw angles within the range of 0°≤β≤20°. Minimum and incremental values are $[<\omega>]_{min}=1$ and $\Delta[<\omega>]=1$.

4.3.2.2. Velocity Components

Figures 4.61 and 4.62 represent streamwise velocity component, <u/U> and figures 4.63 and 4.64 represent vertical velocity, <w/U> component. In the figures in addition to colourful contours, black lines present positive values and white lines present negative values. As can be seen from these figures maximum values of <u/U> are taken please a lower region of images. Downstream of vortex breakdown region a negative values <u/U> are seen but magnitude of negative <u/U> values are smaller than the positive values of <u/U> as a result wake flow regions that occurs downstream of onset of vortex breakdown. With increasing yaw angle, β, streamwise velocity, <u/U>] component decreases and these low values of velocities are seen near the apex. Figures of <u/U> clearly show recirculation zone. Vertical velocity component, <w/U> values are lower than streamwise velocity component <u/U> with increasing yaw angle, β in wake region $[<w/U>]_{max}$ increases.

At an angle of attack α=30°, for yaw angle of β=0°, streamwise velocity $[<u/U>]_{max}$ component is equal to1.2 and for yaw angle of β=20°, streamwise velocity, $[<u/U>]_{max}$ component has lower value such as1.1. At an angle of attack α=35°, for yaw angle of β=0°, streamwise velocity component increase to higher value of $[<u/U>]_{max}$=1.4 ,on the other hand, for yaw angle of β=20°, streamwise velocity, $[<u/U>]_{max}$ component has a smaller magnitude of angle of attack of α=30° and yaw angle of β=0° which is equal to1.1.

Values of the <w/U> decrease with yaw angle, β in the wake region or downstream of onset of vortex breakdown and numerical values of <w/U> is negative. These negative transverse velocity, <w/U> components cover a larger area with varying yaw angle, β near the surface of the delta wing which demonstrate occurrence of flow separation. At an angle of attack of α=30° and yaw angle of β=0°, transverse velocity component is $[<w/U>]_{max}$=0.24, at a yaw angle of β=4° transverse velocity component $[<w/U>]_{max}$ gets a highest value such as0.4 . A further increase, for example, at a yaw angle of β=20° transverse velocity component $[<w/U>]_{max}$ is equal to 0.2. In the case of angle of attack α=35° and for all values of

yaw angle transverse velocity component $[<w/U>]_{max}$ gets smaller values. These distributions of velocity contours reveal the effectiveness of separations.

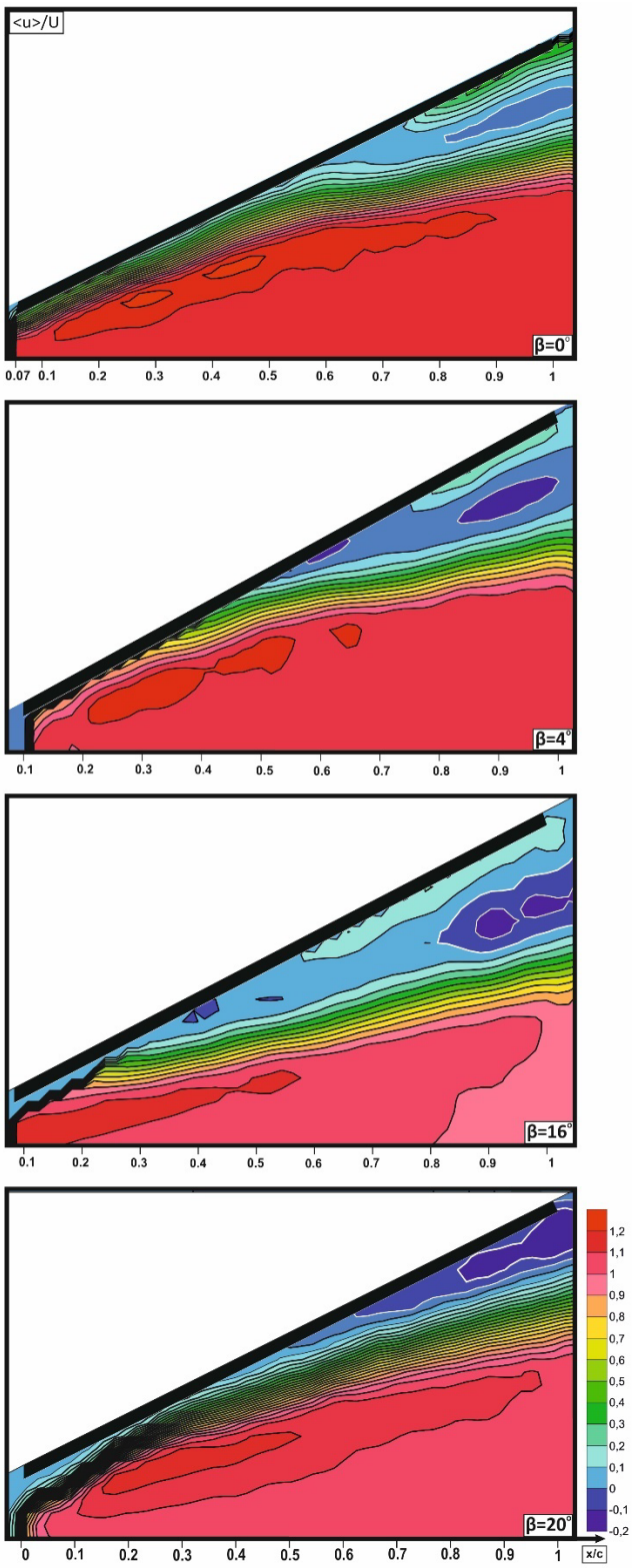

Figure 4.61. Contours of time-averaged streamwise velocity, <u>/U component in side-view plane for angle of attack α=30° and yaw angle within the range of 0°≤β≤20°. Minimum and incremental values are; $[<u>/U]_{min}$=0.1 and Δ[<u>/U]=0.1.

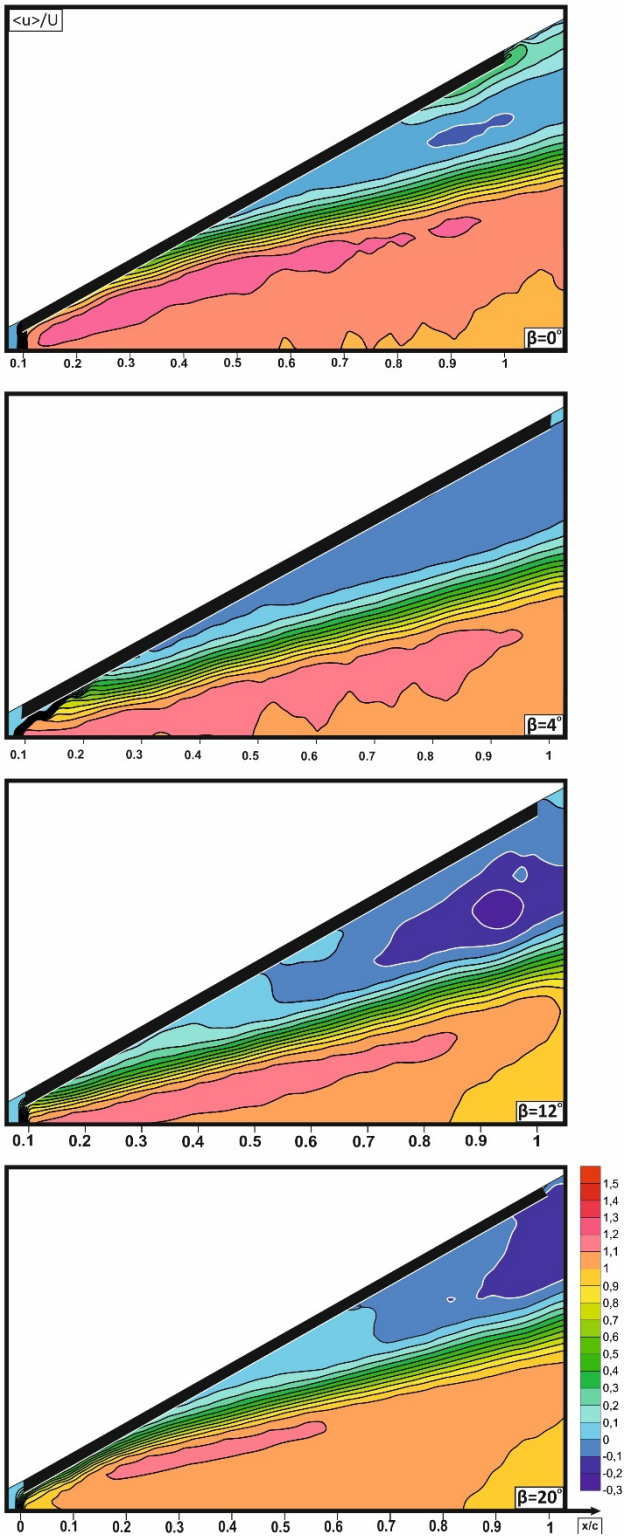

Figure 4.62. Contours of time-averaged streamwise velocity component, <u>/U in side-view plane for angle of attack of α=35° and yaw angles within the range of 0°≤β≤20°. Minimum and incremental values are $[<u>/U]_{min}$=0.1 and Δ[<u>/U]=0.1 respectively.

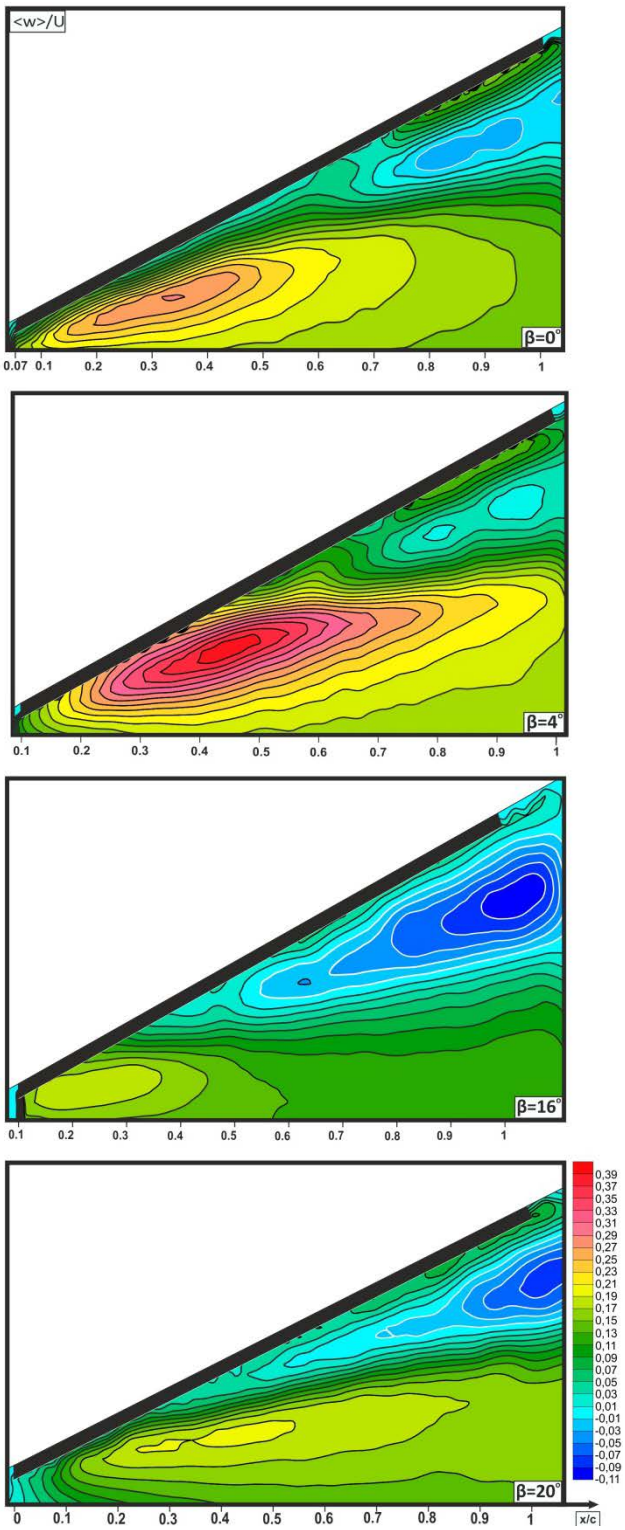

Figure 4.63. Contours of time-averaged transverse velocity component, <w>/U in side-view plane for angle of attack α=30° and yaw angles within the range of 0°≤β≤20°. Minimum and incremental values, $[<w>/U]_{min}$=0.01 and Δ[<w>/U]=0.02 respectively.

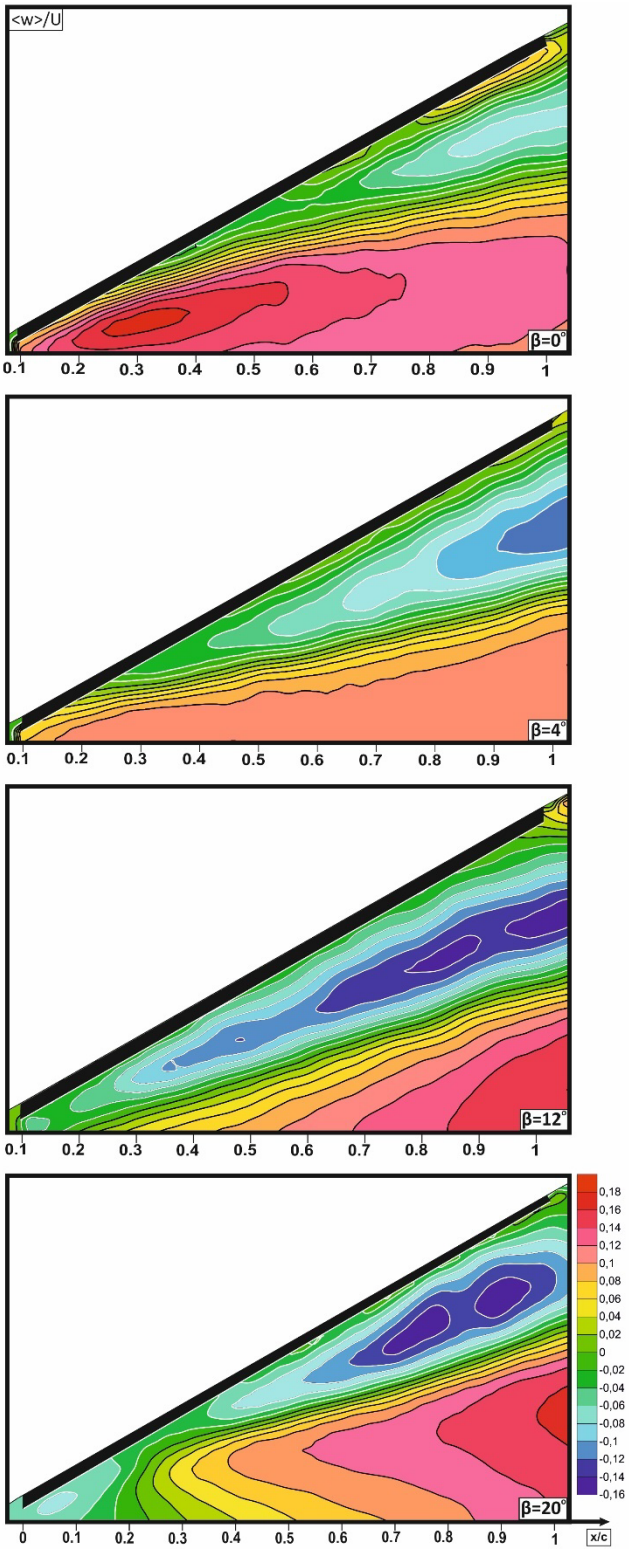

Figure 4.64. Contours of time-averaged transverse velocity component, <w>/U in side-view plane for angle of attack of α=35° and yaw angles within the range of 0°≤β≤20°. Minimum and incremental values are $[<w>/U]_{min}$=0.02 and Δ[<w>/U]=0.02 respectively.

4.3.2.3. Velocity Fluctuations

Figures 4.65 and 4.66 demonstrate root mean square, rms of streamwise velocity component, $<u_{rms}/U>$, figures 4.67 and 4.68 demonstrate rms of vertical velocity component, $<w_{rms}/U>$. In general, turbulent flow structures, enlargement of wake regions, turbulent quantities such as Reynolds stress correlations and the root mean square of the velocity components vary as a function angles of attach and yaw angles. As can be seen from figures, with increasing yaw angle velocity fluctuations increase in stall regions. For example, at an angle of attack of $\alpha=30°$ and yaw angle of $\beta=0°$ the magnitude of $[<u_{rms}/U>]_{max}$ is equal to 0.18 , at a yaw angle of $\beta=4°$, this magnitude of $[<u_{rms}/U>]_{max}$ is equal to 0.22. In the case of angle of attack of $\alpha=35°$ and yaw angle of $\beta=0°$ the magnitude of $[<w_{rms}/U>]_{max}$ riches the value of 0.38 and at yaw angle $\beta=20°$ $[<u_{rms}/U>]_{max}$ is 0.14. At an angle of attack $\alpha=30°$ and yaw angle of $\beta=0°$ $[<w_{rms}/U>]_{max}$ is almost 0.165 and at yaw angle of $\beta=20°$ $[<w_{rms}/U>]_{max}$ is 0.45. At angle of attack $\alpha=35°$ and yaw angle $\beta=0°$ $[<w_{rms}/U>]_{max}$ is almost 0.18 and at yaw angle $\beta=20°$ $[<w_{rms}/U>]_{max}$ is almost 0.18 also. It can be concluded that there are similarly between data that are obtained in side view and plan view planes. Generally, velocity fluctuations and related parameters are higher downstream of vortex breakdown in wake flow regions.

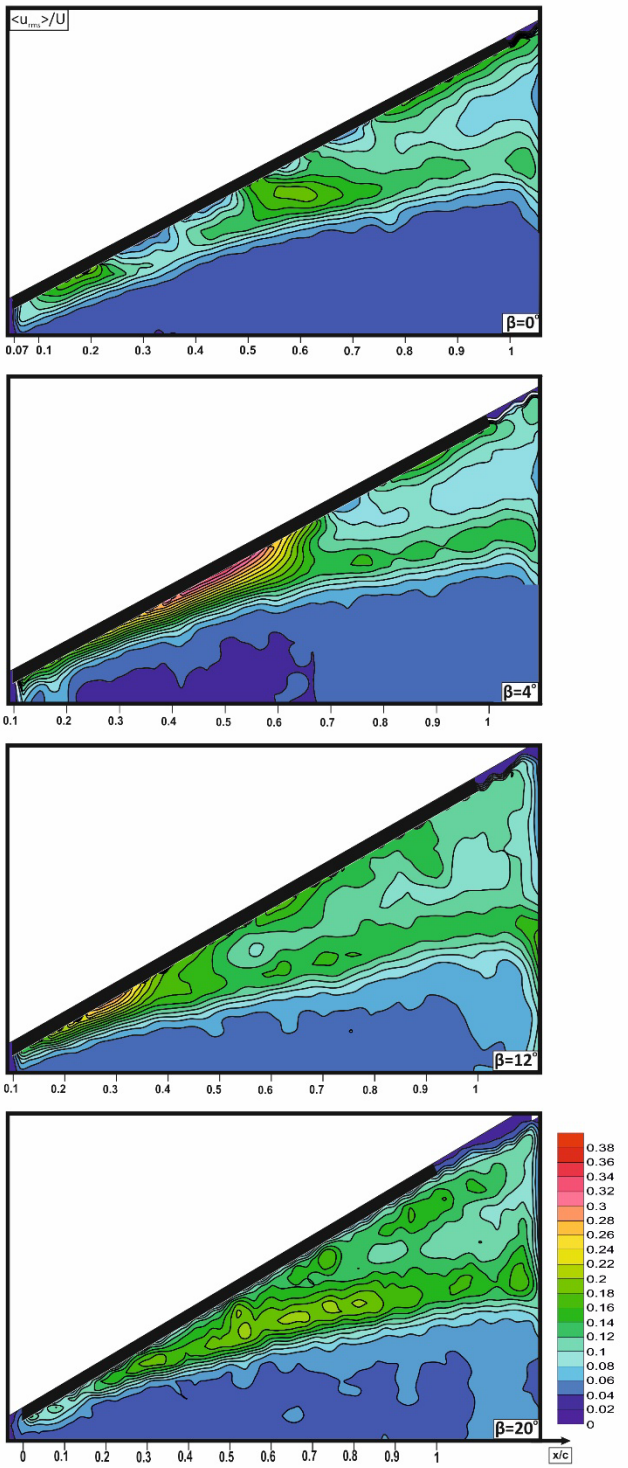

Figure 4.65. Contours of rms of streamwise velocity component, $\langle u_{rms} \rangle / U$ in side-view plane for angle of attack $\alpha=30°$ and yaw angles within the range of $0° \leq \beta \leq 20°$. Minimum and incremental values are $[\langle u_{rms} \rangle / U]_{min}=0.02$ and $\Delta[\langle u_{rms} \rangle / U]=0.02$ respectively.

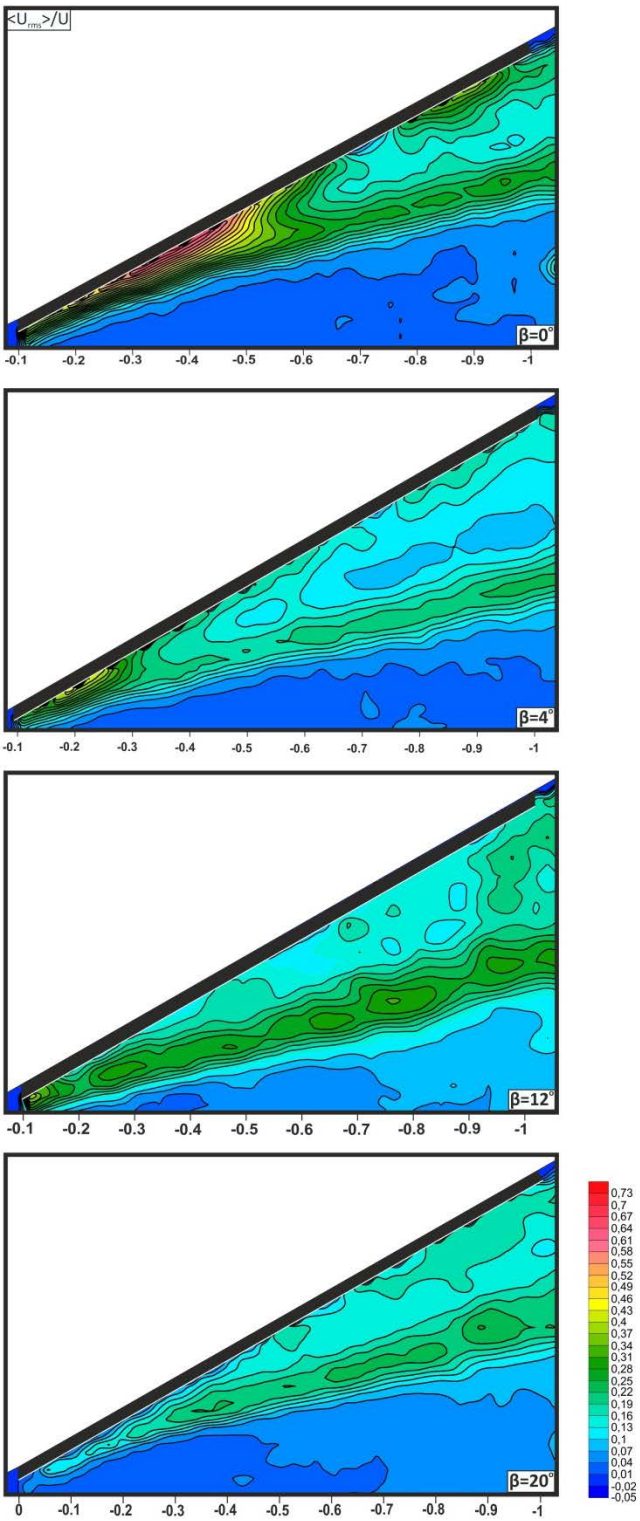

Figure 4.66. Contours of rms of streamwise velocity component, $\langle u_{rms} \rangle / U$ in side-view plane for angle of attack $\alpha=35°$ and yaw angles within the range of $0° \leq \beta \leq 20°$. Minimum and incremental values are $[\langle u_{rms} \rangle / U]_{min}=0.01$and $\Delta[\langle u_{rms} \rangle / U]=0.03$ respectively.

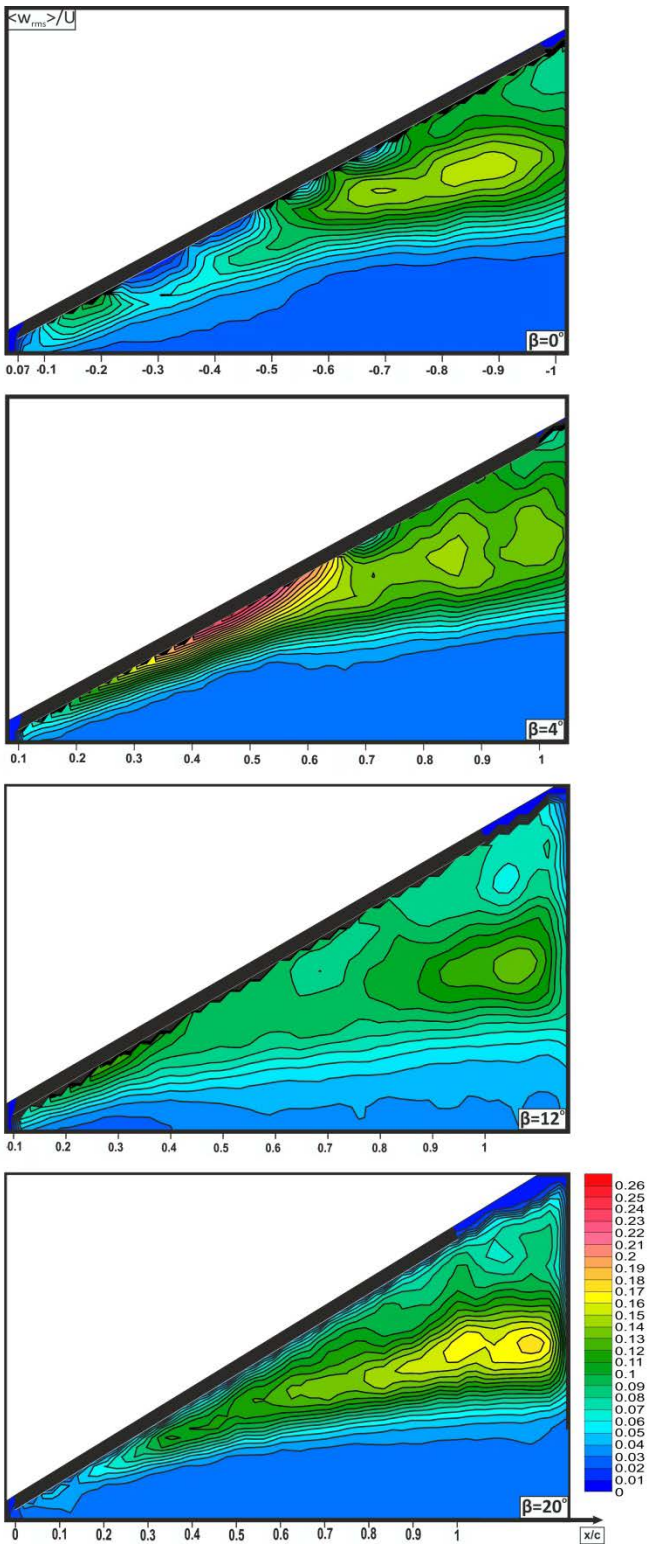

Figure 4.67. Contours of rms of vertical velocity component, $<w_{rms}>/U$ in side-view plane for angle of attack $\alpha=30°$ and yaw angles within the range of $0°\leq\beta\leq20°$. Minimum and incremental values are $[<w_{rms}>/U]_{min}=0.01$ and $\Delta[<w_{rms}>/U]=0.01$ respectively.

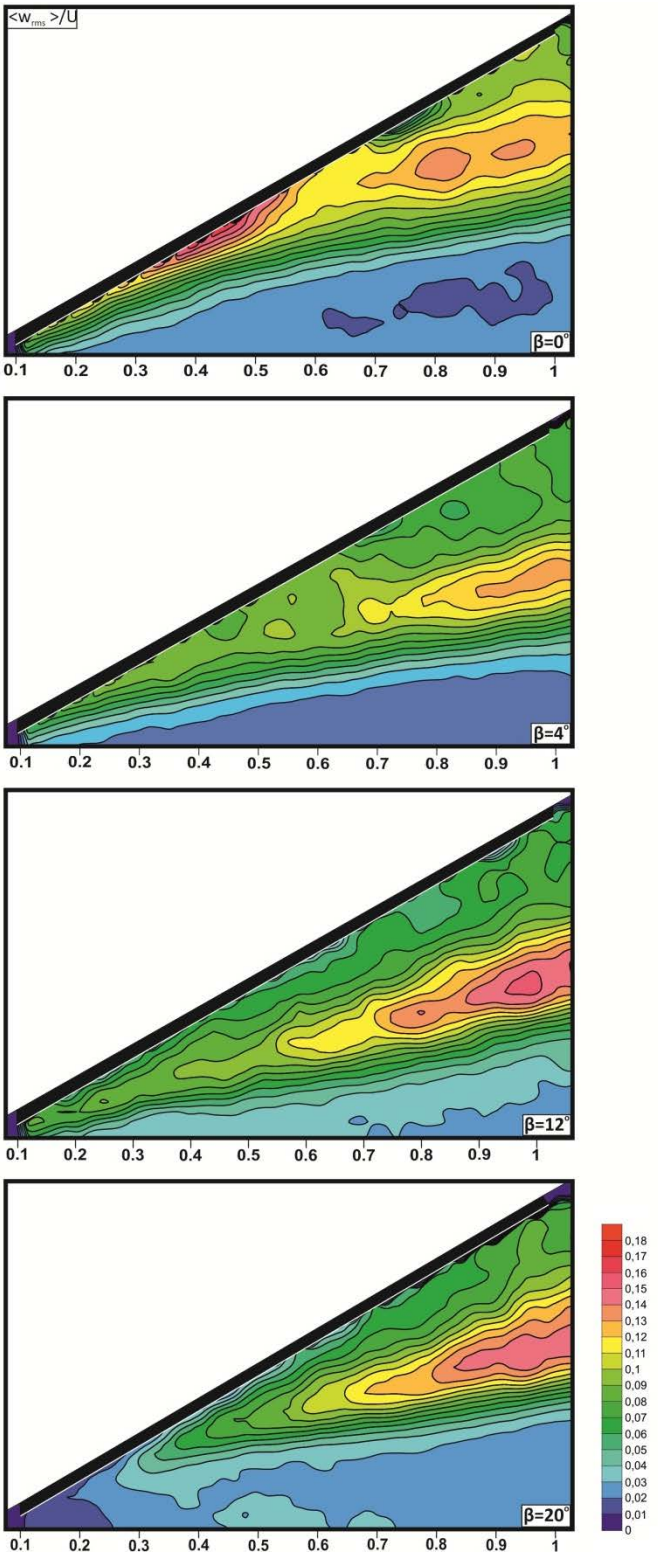

Figure 4.68. Contours of rms of vertical velocity component, $<w_{rms}>/U$ in side-view plane for angle of attack $\alpha=35°$ and yaw angles within the range of $0° \leq \beta \leq 20°$. Minimum and incremental values are $[<w_{rms}>/U]_{min}=0.01$ and $\Delta[<w_{rms}>/U]=0.01$ respectively.

4.4. Surface Pressure Measurement

Static pressure distribution over the delta wing is presented in figures 4.69-4.83. X axis show local dimensionless chords of the delta wing corresponding stations and Y axis shows static pressure distributions for yaw angles, in the range of $0^0 \leq \beta \leq 20^0$. In order to examine coefficient of pressure, $-C_p$ distribution in detail for each angles of attack new graphic for $-C_p$ distributions were presented. As can be seen in figures related to the pressure distributions, varying yaw angle, β from 0 degree to a higher degree, coefficient of pressure, Cp increases which induce more suction. At x/c 0.7 and 0.9 secondary vortices are clearly seen. When delta wing is yawed pressure distributions over the surface of the delta wing alter suddenly. Generally speaking as can be seen from figures with yaw angle, β, pressure coefficient, C_p on the windward side decrease in all x/c stations but this pressure coefficient, C_p on the leeward side do not show a regular variation, in some cases an increase are detected and in some cases a reduction are detected.

At an angle of attack of α=25°, the value of pressure coefficient, C_p on the windward side of the delta wing decreases for all stations. In distributions of pressure coefficient, C_p regular variation cannot be seen, at locations x/c 0.2 and 0.3 on leeward side. But, increasing yaw angle, β, pressure coefficient, C_p increases gradually, but at further stations close the central axis of wing pressure coefficient, C_p values decrease suddenly and get lower value than β=0° but higher than those results that occur on the windward side. As mentioned in the surface oil visualization section, at an angle of attack α=25°, on leeward side secondary vortices does not vanish so secondary vortices have influence on pressure distribution over the surface of the delta wing. At an angle of attack α=30°, C_p values of the windward side decrease in all stations just as angle of attack α=25°. On leeward side at x/c 0.2 up to 12 yaw angle, β but for 20° yaw angle, β at a location y/s=0 however it increases, and gets lower value than 16, at y/s=0.43, after 12° yaw angle β, pressure coefficient, C_p starts to fall and gets higher value than 8° yaw angle, β. At other station, for example, at x/c stations with yaw angle, β on the leeward side pressure coefficient, C_P values decrease gradually. For the angle of attack α=35°, generally, on the

windward side pressure coefficient, C_p values decrease with yaw angle, β at all stations. For the leeward side, at x/c 0.2 stalled pressure distribution takes place without variations which indicates the occurrence of typical separation at yaw angle of β=20°. When yaw angle, β is increased, suction peak values of pressure fall and at this angle of attack, α, on both leeward and windward side similar results are obtained. As can be seen from figures at higher angles of attack, α adverse effects are higher on pressure distribution on both sides.

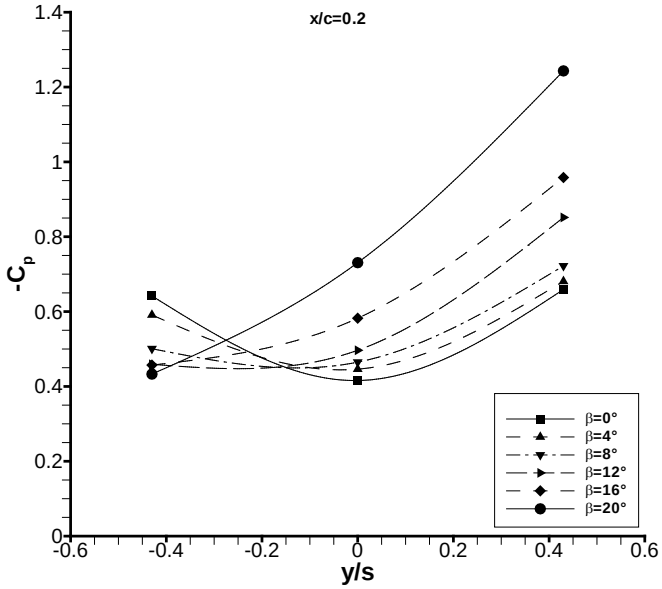

Figure 4.69. Distributions of pressure coefficient, ($-C_p$) over surface of the delta wing at x/c 0.2 at an angle of attack, α=25° and yaw angles within the range of 0°≤β≤20°.

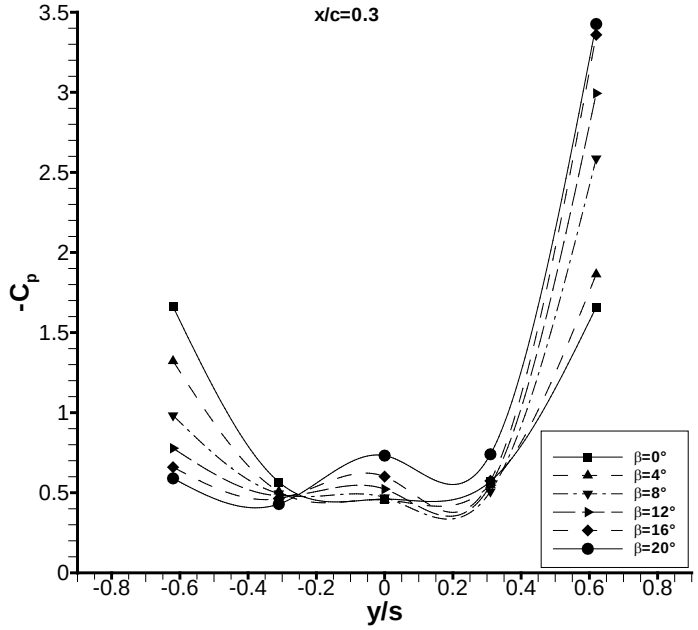

Figure 4.70. Distributions pressure coefficient, $-C_p$ over surface of the delta wing at x/c 0.3 at an angle of attack, α=25° and yaw angles within the range of 0°≤β≤20°.

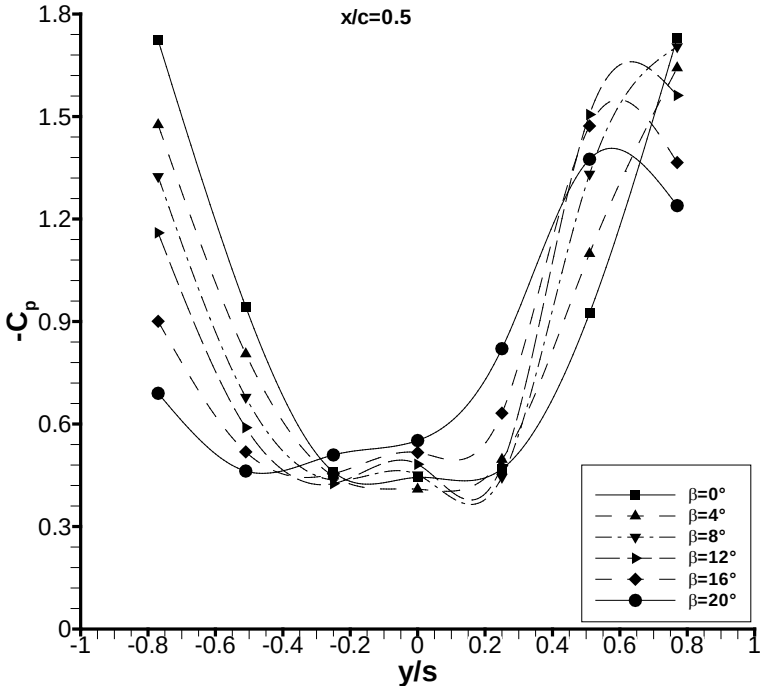

Figure 4.71. Distributions of pressure coefficient, $-C_p$ over surface of the delta wing at x/c 0.5 at angle of attack, $\alpha=25°$ and yaw angles within the range of $0°\leq\beta\leq20°$.

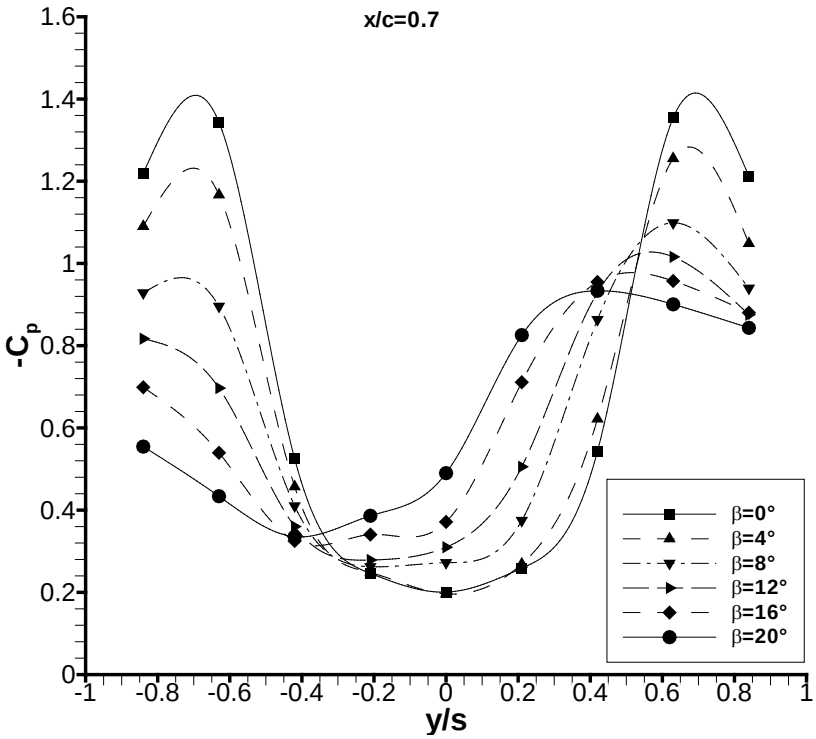

Figure 4.72. Distributions of pressure coefficient, $-C_p$ over surface of the delta wing at x/c 0.7 at an angle of attack, $\alpha=25°$ and yaw angles within the range of $0°\leq\beta\leq20°$.

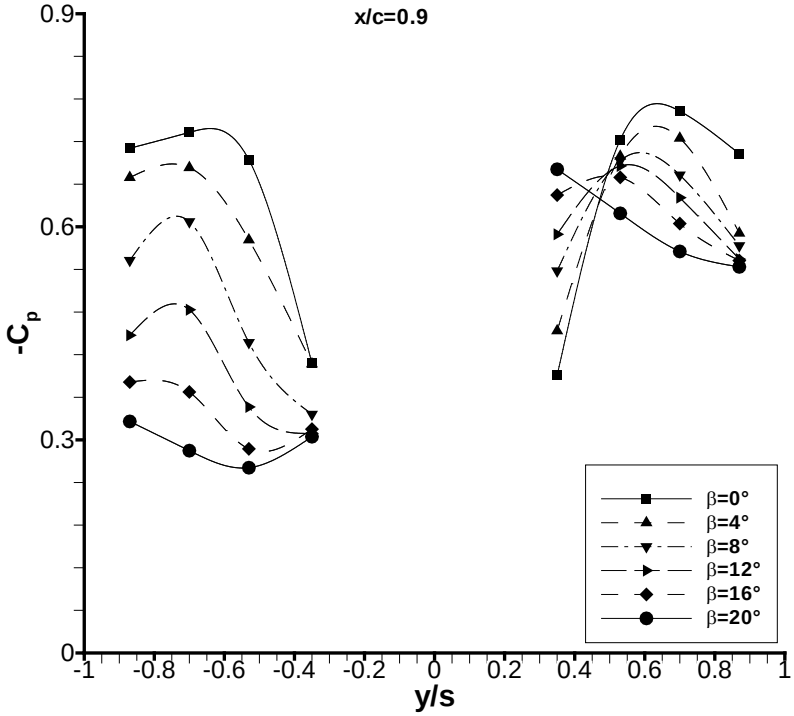

Figure 4.73. Distributions of pressure coefficient, $-C_p$ over surface of the delta wing at x/c 0.9 at angle of attack, $\alpha=25°$ and yaw angles within the range of $0°\leq\beta\leq20°$.

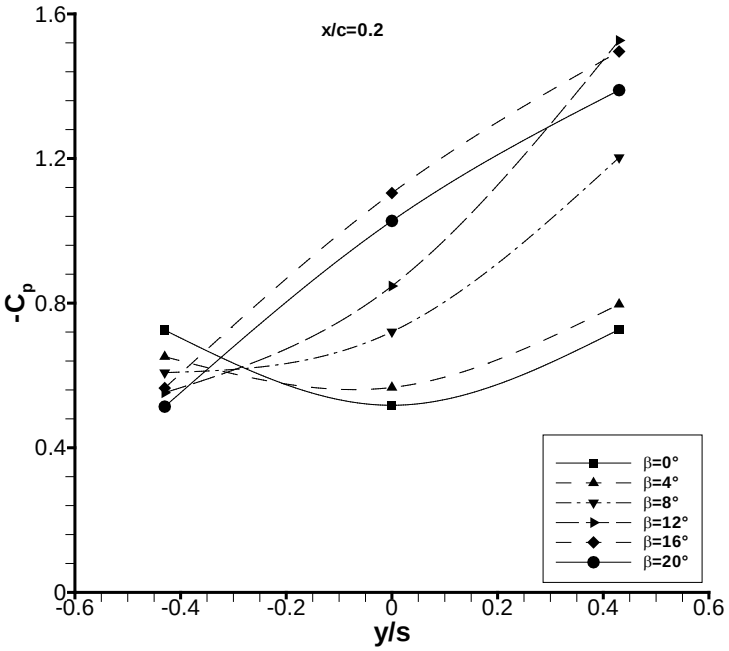

Figure 4.74. Distributions of pressure coefficient, $-C_p$ over surface of the delta wing at x/c 0.2 at an angle of attack, $\alpha=30°$ and yaw angles within the range of $0°\leq\beta\leq20°$.

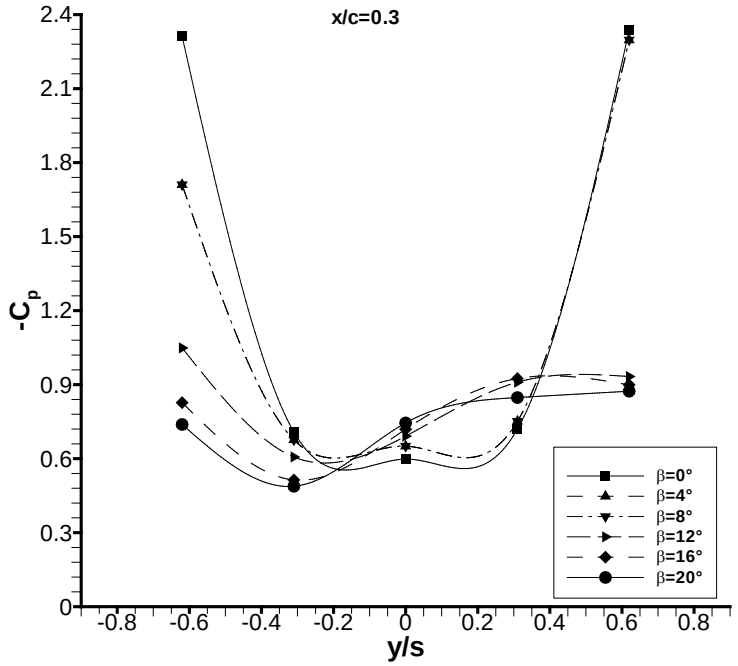

Figure 4.75. Distributions of pressure coefficient, $-C_p$ over surface of the delta wing at x/c 0.3at an angle of attack, $\alpha=30°$ and yaw angles within the range of $0°\leq\beta\leq20°$.

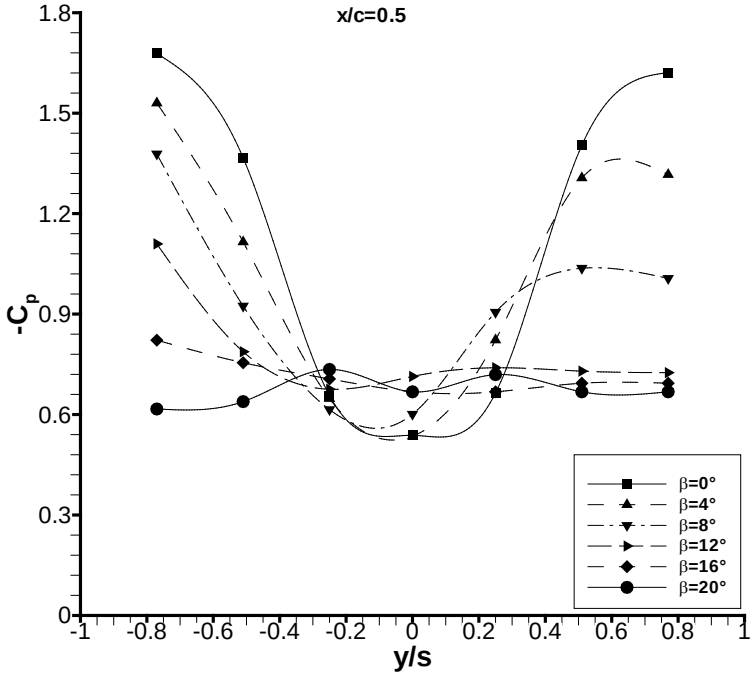

Figure 4.76. Distributions of pressure coefficient, $-C_p$ over surface of the delta wing at x/c 0.5 at an angle of attack, $\alpha=30°$ and yaw angles within the range of $0°\leq\beta\leq20°$.

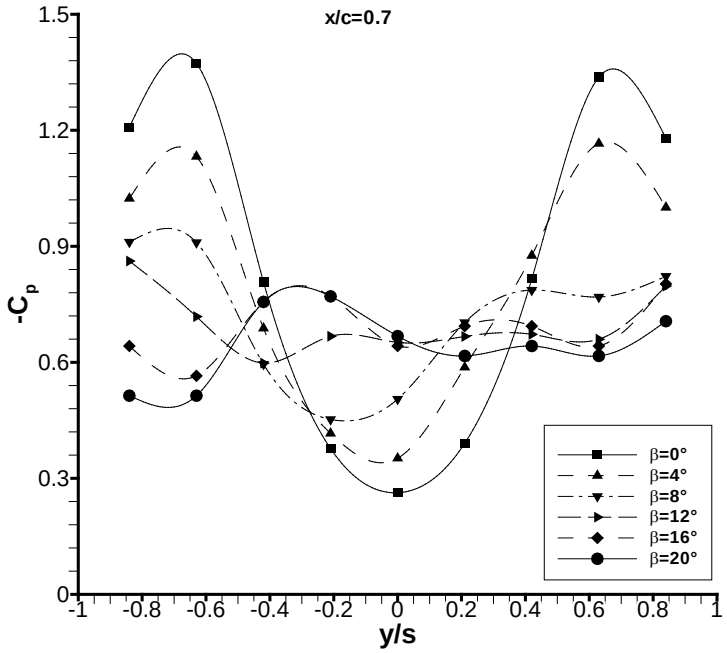

Figure 4.77. Distributions of pressure coefficient, $-C_p$ over surface of the delta wing at x/c 0.7 at an angle of attack, α=30° and yaw angles within the range of 0°≤β≤20°.

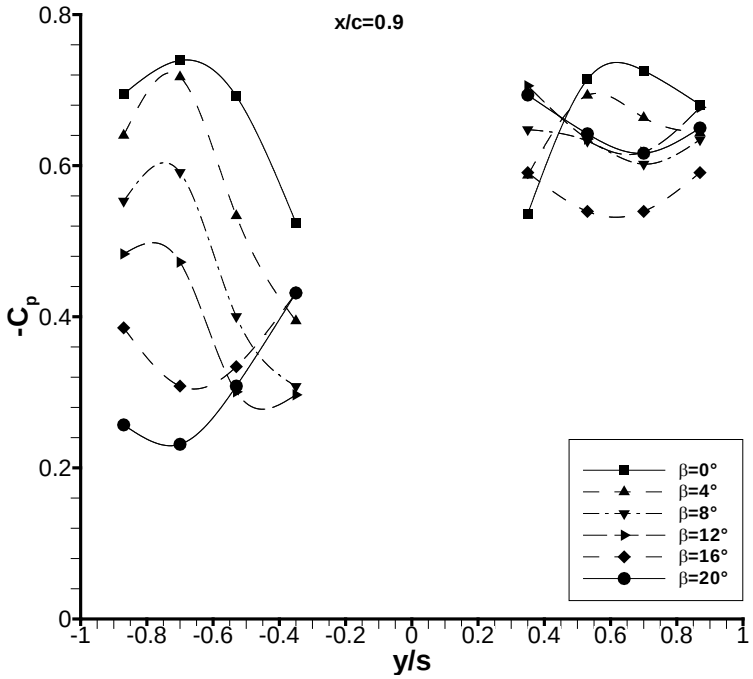

Figure 4.78. Distributions of pressure coefficient, $-C_p$ distribution over surface of the delta wing at x/c 0.9 at an angle of attack, α=30° and yaw angles within the range of 0°≤β≤20°.

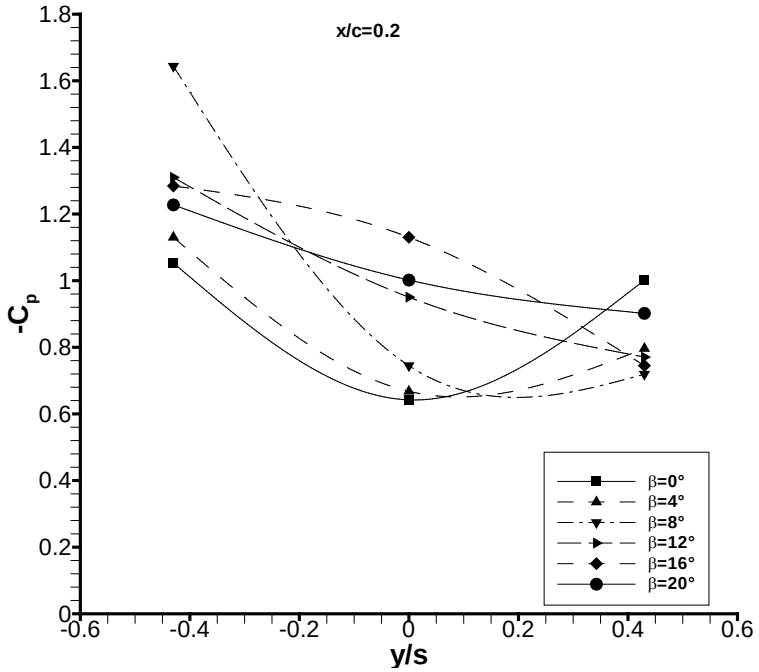

Figure 4.79. Distributions of pressure coefficient, $-C_p$ distribution over surface of the delta wing at x/c 0.2 at an angle of attack, α=35° and yaw angles within the range of 0°≤β≤20°.

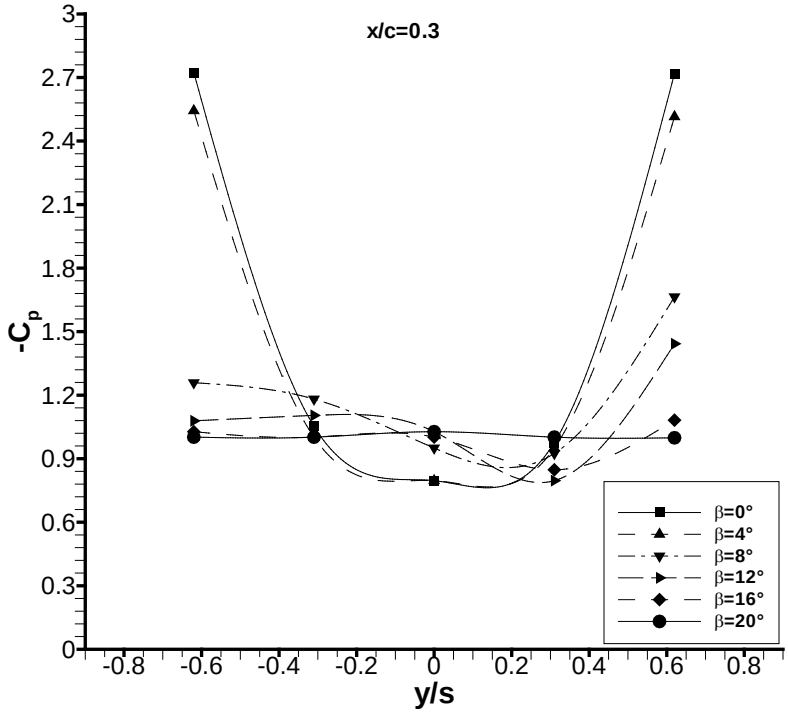

Figure 4.80. Distributions of pressure coefficient, $-C_p$ distribution over surface of the delta wing at x/c 0.3 at an angle of attack, α=35° and yaw angles within the range of 0°≤β≤20°.

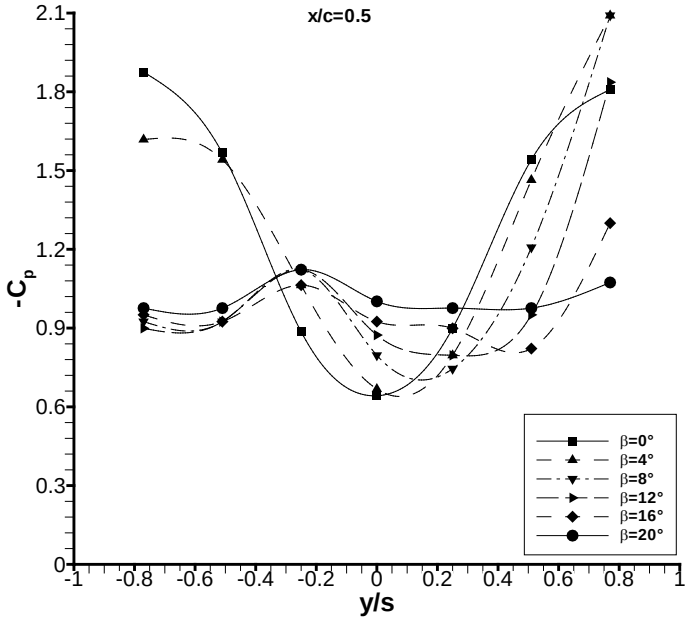

Figure 4.81. Distributions pressure coefficient, $-C_p$ over surface of the delta wing at x/c 0.5 at an angle of attack, $\alpha=35°$ and yaw angles within the range of $0°\leq\beta\leq20°$.

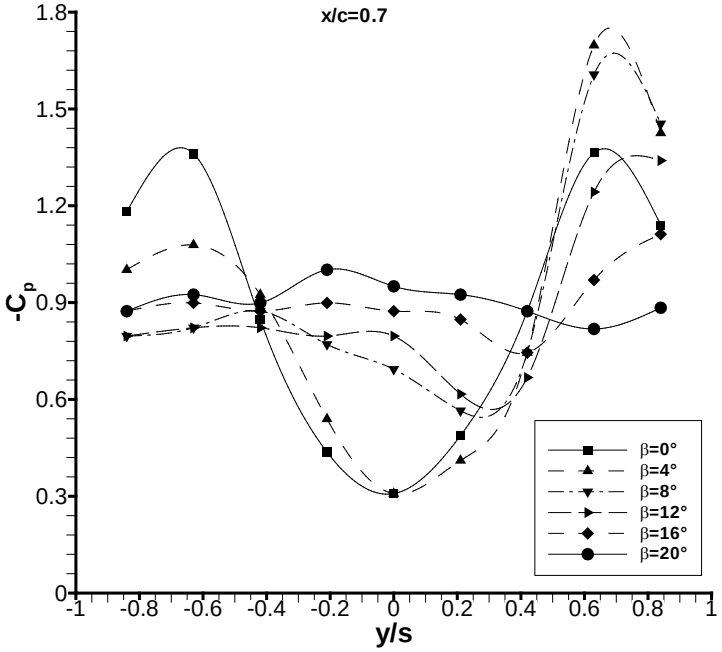

Figure 4.82. Distributions pressure coefficient, $-C_p$ distribution over surface of the delta wing at x/c 0.7 at an angle of attack, $\alpha=35°$ and yaw angles within the range of $0°\leq\beta\leq20°$.

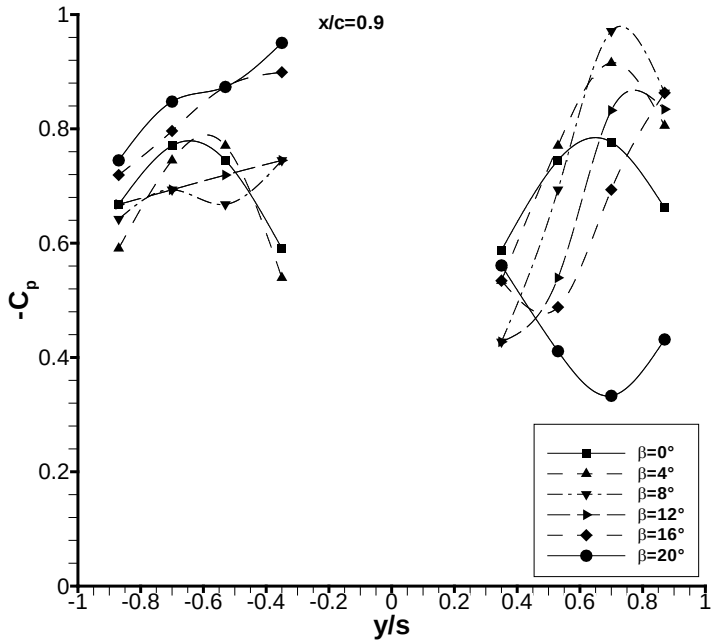

Figure 4.83. Distributions of pressure coefficient, $-C_p$ distribution over surface of the delta wing at x/c 0.9 at an angle of attack, $\alpha=35°$ and yaw angles within the range of $0°\leq\beta\leq20°$.

5. CONCLUSIONS AND RECOMMENDATIONS

5.1. Conclusions

In the present experimental investigation; vortex formation, development and breakdown over a flat plate delta having with 70° sweep angle, Λ for different flight conditions are investigated qualitatively and quantitatively using different experimental techniques. As a qualitative experiments, dye visualizations and surface oil experiments and as a quantitative experiments a stereo PIV technique and experiments of surface pressure measurements were conducted. Dye visualizations and stereo PIV experiments were performed in a water channel at the Reynolds number, $Re=20x10^3$. Experiments of surface oil visualization and surface pressure measurement were performed in a wind tunnel at the Reynolds number, $Re=10x10^4$. Angles of attack, α varying within the range of $25°\leq\alpha\leq35°$ and yaw angles, β within the range of $0°\leq\beta\leq20°$ are selected for whole experiments.

Experimental results reveal that symmetrical flow structures alter as a function of yaw angle, β. Furthermore at high angles of attack, α and under variations of yaw angle, β these changes in symmetrical flow structures are remarkable. Yaw angle, β has strong effect on the fluctuations of velocity components u, v and w, Reynolds stresses, $<u'u'>/U^2$, $<v'v'>/U^2$, $<w'w'>/U^2$ and pressure coefficients, C_p over the surface of the delta wing.

In terms of dye visualization, detailed experiments were conducted in plan-view and side-view planes in order to demonstrate vortical flow structures under the effect of yaw angles, β. In order to specify vortex breakdown locations, trajectories of the leading edge vortices and interactions of these leading edge vortices were qualitatively examined. These experiments revealed that with increasing yaw angle, β symmetrical flow structures deteriorate continuously. For instance, breakdown location of the windward leading edge vortex moves towards the apex of the delta wing, leeward vortex breakdown location moves far away from the trailing edge of the delta wing. Disorganised vortices occurred downstream of onset of vortex breakdown in the windward region spreads over majority of the delta wing surface

while in the leeward side an ordered leading edge vortex shrinks in size and onset of vortex breakdown moves towards the leading edge. Dye visualizations in side-view plane demonstrate that with increasing angle of attack, α and yaw angle, β a strong Kelvin-Helmholtz vortices form and interactions between leading edge vortices and the surface of the delta wing are magnified which may lead to unsteady loading of delta wing such as buffeting.

At an angle of attack of $\alpha=25^0$ with yaw angle of β=0°, windward side vortex breakdown takes place at a location of x/c=0.95, on the other hand, having same angle of attack of $\alpha=25^0$ and increasing yaw angle to a value of β=20° this windward side vortex breakdown takes place at a location of x/c=0.45 close to the midpoint of cord axis. For larger angle of attack such as $\alpha=35^0$ with zero yaw angle, β, this windward side vortex breakdown takes place at a location of x/c=0.57 ,but, providing a yaw angle of β=20° this windward side vortex breakdown moves upward direction close to the apex, x/c=0.1.

The experiments for quantitative observations, stereo PIV and surface pressure measurements were performed. In terms of instantaneous velocity data measured , in plan-view plane by means of the stereo PIV technique , time-averaged velocity vector, $\langle V \rangle$, patterns of streamline, $\langle \Psi \rangle$, vorticity contours, $\langle \omega \rangle$, velocity components, $\langle u \rangle/U$, $\langle v \rangle/U$, $\langle w \rangle/U$, rms of velocity fluctuations, $\langle u_{rms} \rangle/U$, $\langle v_{rms} \rangle/U$, $\langle w_{rms} \rangle/U$, Reynolds stresses $\langle u'u' \rangle/U^2$, $\langle v'v' \rangle/U^2$, $\langle w'w' \rangle/U^2$ and turbulence kinetic energy, TKE are determined.

In Plan-view plane vorticity distributions show that at yaw angle, β=0° there are three pairs of vortices in the measurement plane. These vortices are; main vortices, M, secondary vortices, S and outer vortices O. With increasing yaw angle, β secondary vortices diminish and windward side leading edge vortex breakdown in an earlier stage caused disordered vortices occupying a large area of the delta wing whereas leeward side leading edge vortices keep whirling in narrow gaps without developing onset of vortex breakdown over the wing surface.

In plan-view plane time-averaged streamline patterns, $\langle \psi \rangle$, reveal that flow becomes more complicated and windward side leading edge vortex spread over the delta wing. At angle of attack α=25° any important critical points are detected. At

angle of attack of α=30° important critical points are not detected up to yaw angle of β=12°. At yaw angle, β=20°, a convergent bifurcation line, L_0 , then a saddle point, S, and a foci point F take place. At angle of attack, α=35° important critical points are not detected up to 8°, at yaw angle, β=20° a foci points, F is developed then a convergent bifurcation line, L_0 and a saddle point, S are detected.

In side-view plane at angle of attack, α=30° for yaw angles β=0° and β=20° , a divergent bifurcation L_i a saddle point, S and a foci point, F take place. At yaw angle, β=20° these points take place further upstream of the delta wing and foci point F is enlarged. At angle of attack, α=35° and yaw angle, β=0°, a divergent bifurcation L_i then a saddle point, S and a foci point F take place and at yaw angle, β=20° important critical points are not detected.

On one hand, an increase of yaw angle, β causes to decrease time-averaged streamwise velocity component, <u>/U in windward region on the other hand, it provokes to increase this time-averaged streamwise velocity component, <u>/U in leeward region close to the leading edge. In additions, dimensionless <u>/U does not take negative values at an angle of attack of α=25° but in the cases of angles of attack of α=30° and α=35°, dimensionless <u>/U take negative values. Furthermore, with increasing yaw angle, β to a higher level of magnitudes of negative <u>/U get higher numerical values. In summary, the experimental results reveal that values of <u>/U vary with in the range of 0.05≤[<u/U>]≤1.2 at an angle of attack of α=25° in plan-view plane, but, for highest angles of attack, α for example, α=35°, the values of <u>/U vary with in the range of -0.3≤ [<u>/U] ≤1.6 at yaw angles, β in the range of 0°≤β≤20°

In side-view plane, <u>/U with increasing yaw angle, β magnitudes of <u>/U component decreases and these low values of velocities are seen near the apex, furthermore, with increasing yaw angle, β absolute value of negative streamwise velocity component, <u>/U.

Positive and negative values of transverse velocity component, <v/U> take places over the plane-view plane for all experiments. But, increasing yaw angle, β magnitudes of <v/U> decrease. At an angle of attack of α=25° and yaw angle, β=0°, the magnitudes of <v>/U vary from -0.9 to 0.9 but taking the yaw angle as β=20° the

magnitudes of $\langle v \rangle/U$ vary between -0.26 and 0.35. For larger angles of attack, $\alpha=35°$ and yaw angle, $\beta=20°$ values of $\langle v \rangle/U$ take place.

Magnitude of rms of streamwise velocity component $[\langle u_{rms} \rangle/U]_{max}$ increase gradually on leeward side while on windward sides these values decrease gradually. Magnitudes of rms of the cross-stream velocity $[\langle v_{rms} \rangle/U]_{max}$ increase for a certain degree then decrease gradually, moreover, maximum values of $[\langle v_{rms} \rangle/U]_{max}$ are seen on windward side.

Magnitudes of maximum value of vertical velocity component $\langle w_{rms} \rangle/U$ generally increase with yaw angle, β. Fluctuations in the root-mean-square of vertical velocities, $\langle w_{rms} \rangle/U$, increase because of the disintegration of a coherent leading edge vortices in the region downstream of onset of vortex breakdown.

When the yaw angle, β increases values of magnitude of $\langle u'u' \rangle/U^2$ increase as well. Magnitudes of the $\langle v'v' \rangle/U^2$ and $\langle w'w' \rangle/U^2$ increase up to a certain value then decrease suddenly. Turbulent kinetic energy $\langle TKE \rangle/U^2$ values decreased on windward side where very low magnitude of streamwise velocity components, $\langle u \rangle/U$ take place whereas it increased on leeward side.

By means of surface pressure measurements, pressure coefficients, C_P over the suction surface of delta wing are also determined. Surface pressure distributions reveal that to a certain level of yaw angle, β, pressure suction peak increases in the leeward side but at a high yaw angles, β pressure suction peak decreases suddenly. In windward side, generally, these pressure coefficients, C_p decrease gradually.

Although large scale vortices are developed with certain natural frequency after the collapsing point of leading edge vortices, these large scale vortices interacts with each other to produce randomly fragmented vortices. Swirling intensity of vortices calm down in the case of high yaw angle, β at a high angles of attack, α due to the direction of free-stream flow. Namely, some part of oncoming fluid drains over the pressure surface from the windward side to the leeward side of the delta wing causing high rate of flow separation in the suction side. But, swirling intensity of leading edge vortices on leeward side is magnified due to the large amount of fluid emanating from the windward side because of redirecting of fluid by the striking surface of delta wing exposed to the free-stream flow.

Asymmetric flow structure over the delta wing can lead adverse effects on aerodynamic performance and stability derivatives. Side view experiments reveal that leading edge vortices cause unsteady loading on the surface of delta wing when onset of vortex breakdown takes place as a function of yaw angles, β.

5.2. Recommendations for Future Studies

In the present study, force measurements were not conducted. In order to provide further information about effects of yaw angle, β on the aerodynamic parameters of delta wing, force measurements or calculations on two halves of the delta wing is inevitably necessary. Obtaining lift information over the surface of the delta wing, it can provide further information related to the stability problems of wings such as spin characteristics or tail optimization.

In order to improve aerodynamic performance of the delta wing, control techniques for both leading edge vortices must be applied. Control of disorganized vortices can be investigated in more detail. For windward side leading edge vortices which burst earlier, a selected control technique must be focused on delaying vortex breakdown. Windward side leading edge vortex may be controlled using active or passive control techniques in order to delay onset of vortex breakdown. Delaying of vortex breakdown can improve aerodynamic performance and lessen unsteady loading on the surface of delta wing. Blowing, suction or perturbation can be applied as a control technique. For leeward side leading edge vortices, an appropriate control method can be focused on moving the core of the vortex towards the central axis of wing in order to obtain symmetrical flow structures over the delta wing.

REFERENCES

AKILLI, H., SAHIN, B., ROCKWELL, D., 2001. Control of Vortex Breakdown by a Transversely-Oriented Wire. Physics of Fluids, 13(2):452-463.

ANDERSON J. D., 1991.Fundamentals of Aerodynamics, .McGraw-Hill Higher Education, New York, 772 p.

BREITSAMTER, C., 2008. Unsteady Flow Phenomena Associated With Leading-Edge Vortices. Progress in Aerospace Sciences 44(1):48-65.

CAI, J., PAN, S., LI, W., ZHANG, Z. 2014. Numerical and Experimental Investigations of a Nonslender Delta Wing With Leading-Edge Vortex Flap. Computers & Fluids, 99:1-17.

CALDERON, D. E., WANG, Z., Gursul, I., 2012.Three-Dimensional Measurements of Vortex Breakdown. Experiments in fluids, 53(1):293-299.

CANPOLAT, C., 2009. Vortex Formation over a Nonslender Delta Wing. Department of Mechanical Engineering, Çukurova University Institute of Natural and Applied Sciences– MSc Thesis 101 pages.

CANPOLAT, C., YAYLA, S., SAHIN, B., AKILLI, H., 2009. Dye Visualization of the Flow Structure over a Yawed Nonslender Delta Wing. Journal of Aircraft, 46(5):1818–1822.

CIPOLLA, K. M., ROCKWELL D., 1998. Small-Scale Vortical Structures in Crossflow Plane of a Rolling Delta Wing. AIAA journal 36(12):2276-2278.

COTON, F., MAT, S., GALBRAITH, R., GILMOUR, R., 2008. Low speed wind tunnel characterization of the VFE-2 wing. 46th AIAA Aerospace Sciences Meeting and Exhibit 7-10 January, Reno, Nevada, USA.

CURRY, R. E., MEYER JR, R. R., O'CONNOR, M. 1983. The Use of Oil for In-Flight Flow Visualization. NASA Technical Memorandum No: 84915.

DANTEC DYNAMICS, "Particle Image Velocimetry "http://www.dantecdynamics.com/docs/support-and-download/research-and-education/piv.pdf, (Access Date: 1 June, 2015)

DANTEC DYNAMICS, 2002. Flowmap 3D-PIV System, Installation & User's Guide.

DANTEC DYNAMICS, 2011. Dynamic Studio V3.20 User's Guide,.

DANTEC DYNAMICS, 2006.3D Stereoscopic PIV Reference Manual.

DÉLERY, J. M, 1992. Physics of Vortical Flows. Journal of Aircraft, 29(5):856-876.

DÉLERY, J. M.,2001. Robert Legendre and Henri Werlé: toward the elucidation of three-dimensional separation. Annual review of fluid mechanics, 33(1):129-154.

DÉLERY, J. M. ,2013., Three-dimensional Separated Flow Topology, Critical Points, Separation Lines and Vortical Structures, Wiley Press, London, 155 p.

EARNSHAW, PB. , 1962. An experimental investigation of the structure of a leading-edge vortex. Aeronautical Research Council Reports and Memoranda, No. 3281, England.

ELKHOURY, M., 2014. Performance of Transition-Sensitive Models in Predicting Flow Structures over Delta Wings. Journal of Aircraft, 52(1):77-89.

ELSAYED, M., SCARANO, F., VERHAAGEN, N. G., 2007. Particle Image Velocimetry Study of the Flow over a Slender Delta Wing. 25th AIAA Applied Aerodynamics Conference, Miami FL, USA.

ERICKSON, G. E., 1982. Water-tunnel studies of leading-edge vortices. Journal of Aircraft, 19(6):442-448.

FISHER, D. F., RICHWINE, D. M., BANKS, D. W. 1988. Surface flow visualization of separated flows on the forebody of an F-18 aircraft and wind-tunnel model. NASA Technical Memorandum No: 100436.

FURMAN, A., BREITSAMTER, C., 2013. Turbulent and unsteady flow characteristics of delta wing vortex systems. Aerospace Science and Technology, 24(1):32-44.

GAD-EL-HAK, M., BLACKWELDER, R., F., 1985. The discrete vortices from a delta wing. AIAA journal, 23(6):961-962.

GATLIN, G., VICROY, D., CARTER, M., 2012. Experimental Investigation of the Low-Speed Aerodynamic Characteristics of a 5.8-Percent Scale Hybrid

Wing Body Configuration. 30th AIAA Applied Aerodynamics Conference, 25-28 June, New Orleans, Louisiana USA.

GENÇ, M. S., KARASU, I., AÇIKEL, H. H. 2012a. An experimental study on aerodynamics of NACA2415 aerofoil at low Re numbers. Experimental Thermal and Fluid Science, 39:252-264.

GENÇ, M. S., KARASU, I., AÇIKEL, H. H., & AKPOLAT, M. T. 2012b. Low Reynolds number flows and transition. Low Reynolds Number Aerodynamics and Transition (MS. GENC editor). InTech: Rijeka, Croatia, p1-28.

GORDNIER; R.E., VISBAL M.R.; GURSUL I.; WANG Z., 2009. Computational and experimental investigation of a nonslender delta wing. AIAA Journal 47(8):1811-1825.

GORUNEY, T., ROCKWELL, D., 2009. Flow past a delta wing with a sinusoidal leading edge: near-surface topology and flow structure. Experiments in fluids, 47(2):321-331.

GÖRTZ, S., 2005. Realistic simulations of delta wing aerodynamics using novel CFD methods. Royal Institute of Technology (KTH) Department of Aeronautical and Vehicle Engineering, Sweden-Phd Thesis, 69 pages.

GURSUL, I., 1994. Unsteady flow phenomena over delta wings at high angle of attack. AIAA Journal, 32(2):225-231.

GURSUL, I., ALLAN, M. R., BADCOCK, K. J., 2005. Opportunities for the integrated use of measurements and computations for the understanding of delta wing aerodynamics. Aerospace science and technology, 9(3):181-189.

GURSUL, I., WANG, Z., VARDAKI, E., 2007. Review of flow control mechanisms of leading-edge vortices. Progress in Aerospace Sciences, 43(7):246-270.

GURSUL, I., XIE, W., 1999. Buffeting flows over delta wings. AIAA journal 37(1):58-65.

GUY, Y., MORROW, J. A., MCLAUGHLIN, T. E., WYGNANSKI, I., 1999. Pressure measurements and flow field visualization on a delta wing with

periodic blowing and suction. 24th Atmospheric Flight Mechanics Conference, AIAA Paper: 99-4178.

HOLMAN J. P., 2011. Experimental Methods for Engineers, Eighth Edition, Mcgraw-Hill, ISBN 978-0-07-352930-1, 729 pages.

HONEYWELL, 2001, 160PC Series Pressure Sensors Low Pressure Differential, Gage, Vacuum Gage/Amplified, Catalogue.

HONKAN, A., ANDREOPOULOS, J., 1995.Instantaneous three-dimensional vorticity measurements in vortical flow over a delta wing. AIAA journal, 35(10):1612-1620.

IIHR- the University of Iowa—Hydroscience & Engineering, http://www.iihr.uiowa.edu/blog/2011/08/02/understanding-the-flapping-wing/wake-v3/ (Access Date 6th August 2015).

IT-INSTUMENTATION TODAY "Strain Gage", http://www.instrumentationtoday.com/strain-gauge/2011/08/" (Access Date: 12 June, 2015).

HOLMAN J. P., 2011, Experimental Methods For Engineers, Eighth Edition, Mcgraw-Hill. New York. 739 pages.

JEANS, T., MCDANIEL, D., CUMMINGS, R., MASON, W., 2008. Aerodynamic Analysis of a Generic Fighter with a Chine Fuselage/Delta Wing Configuration Using Delayed Detached-Eddy Simulation. 26th AIAA Applied Aerodynamics Conference, 18 - 21 August, Honolulu, Hawaii, USA

JOHNSON, Jr., JOSEPH, L., GRAFTON, S. B., Long P. 1980,Exploratory investigation of the effects of vortex bursting on the high angle-of-attack lateral-directional stability characteristics of highly-swept wings. A Collection of Technical Papers—AIAA 11th Aerodynamic Testing Conference. 3rd March, Colorada Springs, CO, USA.

KARASU, İ., ŞAHİN, B., AKILLI, H, CANPOLAT, Ç., 2015. Dye Visualization of a Yawed Slender Delta Wing. Journal of Thermal Engineering, 1(7):647-654.

KARASU, I, 2011. Düşük Reynolds Sayılı Akışlarda Kanat Profili Üzerinde Türbülansa Geçisin Ve Laminer Ayrılma Kabarcığının Deneysel ve Sayısal İncelenmesi- Erciyes University Mechanical Engineering Master Thesis-82 pages.

KASTANTIN, Y., VEY, S., NAYERI, C. N., PASCHEREIT, C. O., 2010. Sharp Leading Edge Delta wing Control at Low Reynolds Number. 40th Fluid Dynamics Conference and Exhibit 28 June -1 July 2010, Chicago, Illinois, USA.

KAWAZOE, H., KATO, S., 2006. Effects of leading edge separation vortex of flexible structure delta wing on its aerodynamic characteristics. JSME International Journal Series B, 49(4):1049-1055.

KAWAZOE, H., NAKAMURA, Y., ONO, T., USHIMARU, Y., 1994. Static and Total Pressure Distributions around a Thick Delta Wing with Rounded Leading Edge, 25th AlAA Plasmadynamics and Lasers Conference, June 20-23,Colorado Springs, CO, USA.

LAMBOURNE, N. C., BRYER D. W., 1961. The Bursting of Leading Edge Vortices--Some Observations and Discussion of the Phenomenon, Aeronautical Research Council Reports And Memoranda, Reports and Memoranda No. 3282.

LANDRETH, C.C., ADRIAN, R.J., 1988. Measurement and Refinement of Velocity Data Using High Image Density Analysis in Particle Image Velocimetry. Applications of Laser Anemometry: Proceedings of the 4th International Symposium, Springer-Verlag, Berlin,Germany

LEE, K.Y., SOHN, M. H., 2003.The vortical flow field of delta wing with leading edge extension. KSME international journal, 17(6): 914-924.

LEE, M., CHIANG S., CHIH-MING H., 1987.Response of a delta wing in steady and unsteady flow. Proc. Forum on Unsteady Flow Separation, ASME FED. 52:19-24

MEINHART and SOLOFF, 1999 “Cleanvec” software, Turbulence Laboratory, University of Illinois at Urbana-Champaign

MERZKIRCH, W. 1987, Flow visualization. Academic Press. Orlando. 260 pages.

MITCHELL, A. M., BARBERIS, D., MOLTON, P., lery D.J., (2000). Oscillation of vortex breakdown location and blowing control of time-averaged location. AIAA journal, 38(5), 793-803.

MUNRO, C. D., KRUS P., and JOUANNET C., 2005. Implications of Scale Effect for the Prediction of High Angle of attack Aerodynamics. Progress in Aerospace Sciences 41(3):301-322.

NAKAMURA, Y., YAMADA T., 2002. Aerodynamic characteristics of spin phenomenon for delta wing. 23rd International Congress of Aeronautical Sciences ICAS 2002, 8-13 September,Toronto, Canada

NASA, "NASA Armstrong Fact Sheet: X-48 Hybrid / Blended Wing Body" https://www.nasa.gov/centers/armstrong/news/FactSheets/FS-090-DFRC.html, (Access Date 3 June, 2015).

NELSON R. C., VISSER K. D., 1990. Breaking down the delta wing vortex: The role of vorticity in the breakdown process. AGARD Symposium on Vortex Flow Aerodynamics, October 1–4, Scheveningen, Netherlands.

NELSON, RC. PELLETIER A., 2003. The unsteady aerodynamics of slender wings and aircraft undergoing large amplitude maneuvers. Progress in Aerospace Sciences 39(2):185-248.

ÖZGOREN M., SAHIN B., ROCKWELL D., 2002.Vortex Structure on a Delta Wing at High Angle of Attack. AIAA JOURNAL Vol. 40(2):285-292.

ÖZGOREN, M., SAHIN, B., ROCKWELL, D., 2001. Perturbations of a Delta Wing: Control of Vortex Breakdown and Buffeting. Journal of Aircraft, 38(6)1040-1050.

ÖZGÜR ANSIKLOPEDI Wikipedia https://www.wikipedia.org/, Erisim Tarihi, Eylül 2015

ÖZTURK, N. A., AKKOCA A., SAHIN, B., 2008. Flow details of a circular cylinder mounted on a flat plate", Journal of Hydraulic Research, 46(3):334-355,

PAYNE, F. M., NELSON R.C., 1986. An experimental investigation of vortex breakdown on a delta wing. NASA Technical Report, N86-27196.

PAYNE, F. M. NELSON, R.C., 1986. An experimental investigation of vortex breakdown on a delta wing. NASA Technical Report, N86-27196.

PAYNE, F. M., NG, T., NELSON, R. C., SCHIFF, L. B., 1988. Visualization and wake surveys of vortical flow over a delta wing. AIAA journal, 26(2):137-143.

PEVITT, C., and ALAM F., 2014. Static Computational Fluid Dynamics simulations around a specialized delta wing. Computers & Fluids 100:155-164.

REDINIOTIS, O. K., STAPOUNTZIS, H., TELIONIS, D. P. 1993. Periodic vortex shedding over delta wings. AIAA journal, 31(9):1555-1562.

ROOSENBOOM, M., KONRATH, E. W, SCHRÖDER, R., A., 2012. Stereoscopic particle image velocimetry flowfield investigation of an unmanned combat air vehicle. Journal of Aircraft, 49(6):1584-1596.

SARPKAYA, T., 1971. On stationary and travelling vortex breakdowns.Journal of Fluid Mechanics 45(03):545-559.

SCHÜTTE, A., LÜDEKE H., 2013. Numerical investigations on the VFE-2 65-degree rounded leading edge delta wing using the unstructured DLR TAU-Code." Aerospace Science and Technology (24.1):56-65.

SHIELDS M., MOHSENI K., 2012.EFFECTS OF SIDESLIP ON THE AERODYNAMICS OF LOW-ASPECT-RATIO LOW-REYNOLDS-NUMBER WINGS. AIAA JOURNAL 50(1):85-99.

SHIH, C., DING Z., 1996.Unsteady structure of leading-edge vortex flow over a delta wing. 34th Aerospace Sciences Meeting and Exhibit, 15-18 January, Reno, NV, USA.

SIDORENKO, A., BUDOVSKY, A., PUSHKAREV, A., MASLOV, A. 2008. Flight testing of DBD plasma separation control system. 46th AIAA Aerospace Sciences Meeting and Exhibit, 7-10 January, Reno, NV, USA.

SOHN, M. H., and CHANG J. W., 2010. Effect of a centerbody on the vortex flow of a double-delta wing with leading edge extension. Aerospace Science and Technology 14(1):11-18.

SOHN, M.H., LEE K. Y., CHANG J. W., 2004. Vortex flow visualization of a yawed delta wing with leading edge extension." Journal of Aircraft 41(2):231-237.

SUÁSTEGUI L.M. 2012. Overview on Stereoscopic Particle Image Velocimetry, Advanced Methods for Practical Applications in Fluid Mechanics, (S. JONES editor). INTECH Open Access Publisher, ISBN: 978-953-51-0241-0, p.1-20.

SAHIN, B., AKILLI, H., LIN, J. C., ROCKWELL, D., 2001. Vortex breakdown-edge interaction: consequence of edge oscillations. AIAA Journal, 39(5), 865-876.

TAYLOR, G. S., SCHNORBUS T., GURSUL I., 2003. An investigation of vortex flows over low sweep delta wings.33rd AIAA Fluid Dynamics Conference and Exhibit, 23-26 June, Orlando, Florida, USA.

TOBAK M., PEAKE D. J., 1982. Topology Of Three-Dimensional Separated Flows. Ann. Rev. Fluid Mech, 14:61-85.

TRAUB, L. W., MOELLER B., REDINIOTIS O., 1998. Low-Reynolds-number effects on delta-wing aerodynamics." Journal of aircraft 35(4):653-656.

TUNAY, T., 2011, Experimental And Numerical Studies Of Flow Characteristics Around A Ground Vehicle, Department of Mechanical Engineering ,Çukurova University Institute of Natural and Applied Sciences, Phd Thesis-185 pages.

UWAL-University of Washington Aeronautical Laboratory, “Flow Visualization” http://www.uwal.org/uwalinfo/techguide/flowvis.htm (Access Date: 13 July, 2015).

VERHAAGEN N.G., 1999. Effect of Sideslip on the Flow over a 65-deg Delta Wing Final Report. 1999 EOARD Special Contract Program SPC 97-4067.

VERHAAGEN, N. G., 2010. Effects of Leading-Edge Radius on Aerodynamic Characteristics of 50o Delta Wings.AIAA Paper 323.

VERHAAGEN, N. G., NAARDING S.H.J. 1989. Experimental and numerical investigation of vortex flow over a sideslipping delta wing. Journal of Aircraft 26(11):971-978.

WALKER, J.F.C.., 2011. An Experimental Investigation of Roll and Yaw Coupled Oscillations of a Delta Wing. Auburn University, Mechanical Engineering Msc-Thesis.

WANG, J., and TU J., 2010. Effect of wing planform on leading-edge vortex structures.Chinese Science Bulletin 55(2):120-123.

WOODIGA, S. A., LIU T., 2009.Skin friction fields on delta wings. Experiments in Fluids 47(6):897-911.

YANIKTEPE B.,2006. Origin and Control of Vortex Breakdown of Unmanned Combat Air Vehicles. Department of Mechanical Engineering, Institute of Natural And Applied Sciences University of Çukurova- Phd Thesis, 129 pages.

YANIKTEPE B., ROCKWELL D., 2005. Flow Structure on Diamond and Lambda Planforms: Trailing-Edge Region. AIAA Journal, 43:(7): 1490-1500.

YAVUZ, M. M., ELKHOURY M., ROCKWELL D., 2004. Near-surface topology and flow structure on a delta wing." AIAA journal 42(2):332-340.

YAVUZ, M.M., 2006, Origin and control of the flow structure and topology on delta wings, Lehigh University Mechanical Engineering. Phd Thesis.

YAVUZ, M.M., ROCKWELL D., 2006.Control of Flow Structure on Delta Wing with Steady Trailing-Edge Blow." AIAA journal 44(3):493-501.

YAYLA, S., CANPOLAT, C., SAHIN, B., AKILLI, H.,2013. The Effect of Angle of Attack on the Flow Structure over the Nonslender Lambda Wing. Aerospace Science and Technology, 28(1):417-430.

YAYLA S., 2009. Flow Characteristics of Diamond and Lambda Wings at Different Flight Conditions. Department of Mechanical Engineering, Çukurova University Institute of Natural and Applied Sciences, Phd Thesis, 132 pages.

YAYLA, S., CANPOLAT, Ç. SAHIN, B., AKILLI, H., 2010. Yaw angle effect on flow structure over the nonslender diamond wing. AIAA Journal, 48(10):2457-2461.

APPENDIX

Vorticity Evaluation

For 2-D flows, the out-of-plane component of vorticity is expressed as: (Yayla,2009,Yanıktepe,2006):

$$\Omega = \frac{1}{2}\left(\frac{\partial v}{\partial x} - \frac{\partial u}{\partial y}\right)$$

This expression can be computed by using finite difference method in order to solve numerically. Using central differences at an interior point:

$$\Omega_{ij} = \frac{1}{2}\left(\frac{v(i+1,j) - v(i-1,j)}{2\delta_x} - \frac{u(i,j+1) - u(i,j-1)}{2\delta_y}\right)$$

The stokes theorem can be formulated as:

$$\iint \left(\vec{\nabla} \times \vec{u}\right) d\vec{s} = \oint \vec{u} d\vec{l}$$

Assuming that the vorticity is constant at all unit surface formed by the four grid cells surrounding a given point, the vorticity of that point can be written as:

$$\Omega = \frac{1}{4\delta_x \delta_y} \oint \vec{u} d\vec{l}$$

In this expression, the integral is the circulation of the velocity around the path formed by the sides of the unit surface.

Bilinear Interpolation

A bilinear least square fit technique can be used in order to fill the gaps left in the data grid by the interrogation system NFILVB (Yayla,2009,Yanıktepe,2006).

Knowing the data values u_1,….., u_n at the N nearest neighbor location of a point where the data u is missing, the important point is to find a value for u that does not deviate too much from these known values. Due to realize this purpose, merit function needs to be minimized as:

$$\chi^2 = \sum_{k=1}^{N} \frac{|u_k - u|^2}{\sigma_k}$$

As suggested by Adrian et al., NFILVB applies this method to a linear model of the u and v components of velocity:

$$u = a_0 + a_1 x + a_2 y$$

$$v = b_0 + b_1 x + b_2 y$$

using the 5 nearest neighbors of a missing data. When the measurement errors σ_k on each data of u_k, they are set to 1. The minimum of the merit function:

$$\chi^2 = \sum_{k=1}^{5} |u_k - (a_0 + a_1 x + a_2 y)|^2$$

occurs when:

$$\frac{\partial \chi^2}{\partial a_0}(x_k, y_k) = \frac{\partial \chi^2}{\partial a_1}(x_k, y_k) = \frac{\partial \chi^2}{\partial a_2}(x_k, y_k) = 0 \ \textit{for}\ \text{k=1,…..,5}$$

This is a linear system which consists of 15 equations and 3 unknowns that is solved using the Singular Value Decomposition (SVD) technique which is described in Numerical Recipes books.

Gaussian Smoothing

In order to reduce the measurement noises in the velocity data from PIV, a local weighted averaging technique is used in NFILVB. The weights used are Gaussian (Yayla, 2009, Yanıktepe,2006):

$$u(x_i, y_j) = \sum_{m=-4}^{4} \sum_{k=-4}^{4} w_{km} u(x_{i-k}, y_{j-m})$$

where:

$$w_{km} = \frac{\omega_{km}}{\sum_{k=-4}^{4} \sum_{m=-4}^{4} \omega_{km}}$$

$$\omega_{km} = e^{\frac{2(k^2+m^2)}{\sigma^2}}$$

The parameter σ is the smoothing parameter that the user is asked for when running NFILVB. It controls how fast the Gaussian ω is decaying which determines the contributions of the surrounding points to the average value.

Averaged Flow Structure

Averaged quantities calculation was made according to the equations listed in the following table. Each averaged parameter was calculated at each spatial coordinate (x,y) considering the average of all instantaneous values (x,y). The terminology for each averaged parameters and the dimensionless equation employed to determine the averaged parameter as follows: (Yayla,2009,Yanıktepe,2006)

<V>≡ averaged (or mean) total velocity

$$< V >\equiv \frac{1}{N}\sum_{n=1}^{N} V_n(x,y)$$

<u>= averaged value of streamwise component of velocity

$$< u >\equiv \frac{1}{N}\sum_{n=1}^{N} u_n(x,y)$$

<u>= averaged value of transverse component of velocity

$$< \nu >\equiv \frac{1}{N}\sum_{n=1}^{N} \nu_n(x,y)$$

<ω>= mean value of vorticity

$$< \omega >\equiv \frac{1}{N}\sum_{n=1}^{N} \omega_n(x,y)$$

u_{rms}= root-mean-square of u component fluctuation

$$u_{rms} \equiv < u >_{rms} \equiv \left[\frac{1}{N}\sum_{n=1}^{N} \left[u_n(x,y) - < u(x,y) > \right]^2 \right]^{1/2}$$

v_{rms}= root-mean-square of v component fluctuation

$$\nu_{rms} \equiv < \nu >_{rms} \equiv \left[\frac{1}{N}\sum_{n=1}^{N} \left[\nu_n(x,y) - < \nu(x,y) > \right]^2 \right]^{1/2}$$

<u'v'> = averaged value of Reynolds stress correlation

$$< u'\nu' >= \frac{1}{N}\sum_{n=1}^{N} \left[u_n(x,y) - < u(x,y) > \right]\left[\nu_n(x,y) - < \nu(x,y) > \right]$$

TKE= a mean Turbulent Kinetic Energy (TKE) value

$$TKE = \frac{1}{2}\left(\overline{u'^2} + \overline{v'^2} + \overline{w'^2} \right)$$

Spectral Analysis

Spectral analysis can be expressed as fllowing procuders (Yanıktepe,2006).

$$S_{xy}(\overline{\omega}) = \frac{1}{2\pi}\int_{-\infty}^{\infty} R_{xy}(\tau)e^{-i\overline{\omega}\tau}d\tau$$

$$S_{yx}(\overline{\omega}) = \frac{1}{2\pi}\int_{-\infty}^{\infty} R_{xy}(\tau)e^{-i\overline{\omega}\tau}d\tau$$

their accompanying transform relations are expressed as follow:

$$R_{xx}(\tau) = \frac{1}{2\pi}\int_{-\infty}^{\infty} S_{xy}(\omega)e^{i\omega\tau}d\omega$$

$$R_{yx}(\tau) = \frac{1}{2\pi}\int_{-\infty}^{\infty} S_{yx}(\omega)e^{i\omega\tau}d\omega''$$

In order to cross-correlation functions are related by $R_{xy}(\tau) = R_{yx}(-\tau)$, $S_{xy}(\omega)$ is given as in the form of:

$S_{xy}(\omega) = \frac{1}{2\pi}\int_{-\infty}^{\infty} R_{yx}(-\tau)e^{-i\omega\tau}d\tau$ by substituting $\tau' = -\tau$:

$$S_{xy}(\omega) = \frac{1}{2\pi}\int_{-\infty}^{\infty} R_{yx}(\tau')e^{-i\omega\tau'}d\tau'$$

can be obtained. Since FFT originally works with complex data to write this equation in the complex form, let x(t) is a fuction of time, with period T,

$$x(t) = a_0 + \sum_{k=1}^{\infty}\left(a_k \cos\frac{2\pi kt}{T} + b_k \frac{\sin 2\pi kt}{T}\right)$$

where a_0 , a_k and b_k are constant Fourier coefficients given as:

$$a_0 = \frac{1}{T}\int_{-T/2}^{T/2} x(t)dt$$

$$a_{\substack{k\\k\geq 1}} = \frac{2}{T}\int_{-T/2}^{T/2} x(t)\cos\frac{2\pi kt}{T}dt$$

$$b_{\substack{k\\k\geq 1}} = \frac{2}{T}\int_{-T/2}^{T/2} x(t)\sin\frac{2\pi kt}{T}dt$$

Substituting for $a_0=0$;

$$x(t) = \sum_{k=1}^{\infty}\left\{\frac{2}{T}\int_{-T/2}^{T/2} x(t)\cos\frac{2\pi kt}{T}dt\right\}\cos\frac{2\pi kt}{T} + \sum_{k=1}^{\infty}\left\{\frac{2}{T}\int_{-T/2}^{T/2} x(t)\sin\frac{2\pi kt}{T}dt\right\}\sin\frac{2\pi kt}{T}$$

Next substituting for $\omega_k = \frac{2\pi kt}{T}$ and $\Delta\omega = \frac{2\pi}{T}$;

$$x(t) = \sum_{k=1}^{\infty}\left\{\frac{\Delta\omega}{\pi}\int_{-T/2}^{T/2} x(t)\cos\omega_k t dt\right\}\cos\omega_k t + \sum_{k=1}^{\infty}\left\{\frac{\Delta\omega}{\pi}\int_{-T/2}^{T/2} x(t)\sin\omega_k t dt\right\}\sin\omega_k t$$

When the period $T\to\infty, \Delta\omega\to d\omega$ and the sum sign becomes an integral with the limits $\omega = 0$ to $\omega = \infty$. In this case;

$$x(t) = \int_{\omega=0}^{\infty}\frac{d\omega}{\pi}\left\{\int_{-\infty}^{\infty} x(t)\cos\omega_k t dt\right\}\cos\omega_k t + \int_{-\infty}^{\infty}\frac{d\omega}{\pi}\left\{\int_{-\infty}^{\infty} x(t)\sin\omega_k t dt\right\}\sin\omega_k t$$

or putting

$$A(\omega) = \frac{1}{2\pi}\int_{-\infty}^{\infty} x(t)\cos\omega t dt$$

$$B(\omega) = \frac{1}{2\pi}\int_{-\infty}^{\infty} x(t)\sin\omega t dt$$

gives $x(t) = 2\int_0^\infty A(\omega)\cos\omega t dt + 2\int_0^\infty B(\omega)\sin\omega t dt$

This equation is a s a representation of x(t) by a Fourier integral of inverse Fourier transform and the terms *A*(ω) and *B*(ω) are the components of the Fourier transform of x(t) . In order to write *A*(ω) , *B*(ω) and x(t) in complex form making use of the result that;

$$e^{i\theta} = \cos\theta + i\sin\theta$$

Defining

$X(\omega) = A(\omega) + B(\omega)$ equations may be combined to give

$$X(\omega) = \frac{1}{2\pi}\int_0^\infty x(t)(\cos\omega t - i\sin\omega t)dt = \frac{1}{2\pi}\int_0^\infty x(t)e^{-i\omega t}dt$$

The latter equation is the formal definition of *X(ω)* which is called the fourier transform of x(t). $S_{xy}(\omega)$ can be written with respect to *A*(ω) , *B*(ω);

$$S_{xy}(\omega) = A(\omega) - iB(\omega)$$

And

$$S_{yx}(\omega) = C(\omega) - iD(\omega)$$

where *A(ω), B(ω), C(ω)* and *D(ω)* are real functions of ω. The amplitude of the any signal is calculated;

$$Amplt^2 = A^2 + B^2$$

$$Phase = \arctan(B/A)$$

CURRICULUM VITAE

İlyas KARASU was born in Sivas in 1986. He enrolled Erciyes University School of Civil Aviation in 2004 and graduated in 2008. He enrolled Mechanical Engineering in Erciyes University for Master of Science in 2009 and graduated in 2011. He began PhD education in Mechanical Engineering in Çukurova University in 2011. He works in Gaziantep University Aeronautics and Aerospace faculty as a lecturer. He is married with Merve KARASU.